Measurement of the Cosmic Ray Spectrum with the Pierre Auger Observatory

Zur Erlangung des akademischen Grades eines

Doktors der Naturwissenschaften

an der Fakultät für Physik des
Karlsruher Instituts für Technologie (KIT)

genehmigte

Dissertation

von

M.Sc. Daniela Mockler
aus Bietigheim-Bissingen

Tag der mündlichen Prüfung: 30.11.2018

Referent: Prof. Dr. Dr. h.c. Johannes Blümer

Korreferent: Prof. Dr. Günter Quast

Betreuer: Dr. Markus Roth

Remember to look up at the stars and not down at your feet.
Try to make sense of what you see
and wonder about what makes the Universe exist.
Be curious.

Stephen Hawking

Abstract

Cosmic rays combine the two subjects astrophysics and particle physics. The first deals with the very large, the second with the very small. Ultra-high energy cosmic rays act as messengers, informing us of the most violent and energetic processes happening in the Universe. Their discovery dates back to the beginning of the 20th century, and since then great discoveries have been made through the study of these particles. Cosmic rays allowed for the discovery of the first known particles of anti-matter and further particles such as the muon and pion. Even though our technological possibilities and understanding of particle physics have vastly improved over these years, the energy of the highest-energetic cosmic rays ($E \sim 10^{20}$ eV) remains unattainable to the Large Hadron Collider. Particle interactions and cross-sections at these energies are only accessible with ultra-high energy cosmic rays. From the astrophysical point of view, we want to determine the origin of these particles, which is closely related to understanding the acceleration and transport mechanisms. While we have ideas for potential sources, such as active galactic nuclei, gamma-ray bursts, or supernova remnants, the only consistent observation is that the origin of cosmic rays is both galactic and extragalactic. The mass composition and energy spectrum of ultra-high energy cosmic rays are two of the key observables in the studies of their origin. This work will focus on the energy spectrum. A precise measurement of the spectrum and its characteristics is an important ingredient to the fits of astrophysical models describing cosmic rays at the highest energies and the determination of a transition from galactic to extragalactic cosmic rays.

Due to the low flux of around one particle per square kilometer per century at 10^{20} eV, indirect measurements on ground are required. Ground-based detectors exploit the phenomenon of extensive air showers. As an ultra-high energy cosmic ray hits the Earth's atmosphere, it will interact with the atmospheric nuclei and create secondary particles. These particles will interact themselves, which leads to the generation of electromagnetic and hadronic cascades. The thus created extensive air showers are sampled by an array of surface detectors on ground. The surface detector of the Pierre Auger Observatory covers more than 3000 km^2 of the Argentine pampas near the city of Malargüe. The employed fluorescence detector yields a complementary measurement of the air showers by measuring the longitudinal profile of the showers.

The analyses presented in this work are focused on determining the energy spectrum from measurements obtained with the surface detector. The detector samples the extensive air showers at a limited number of distances. An empirical description of the observed lateral signal distribution is used to derive an expected signal at a certain distance to the shower axis. For each event, the expected signal gives a first estimator of the primary energy. The estimator is affected by atmospheric attenuation, such that the relation between the estimator and the primary energy depends on the incident angle of the primary particle. A zenith-independent estimator is achieved by means of the Constant Intensity Cut method, which gives an average correction. Within this work, a novel correction approach was studied, which accounts for a change of the attenuation with energy. After the correction, the energy estimator is calibrated by the measurements of the fluorescence detector using a subset of events that are measured with both detectors. In the course of this work, the energy spectrum was derived for both the standard surface detector and a nested detector array, which extends the measurements to lower energies. The combined energy spectrum covers three decades in energy and is compatible with previous results. The energy spectrum obtained with the standard surface detector is compared to the spectrum reported by the Telescope Array experiment. Both experiments are located at about the same latitude on opposite hemispheres. A clear difference in the overall energy scale is apparent when comparing the energy spectra of both experiments. Above an energy of about $10^{19.5}$ eV, the difference in the spectra is significant. To understand whether the discrepancy is due to the different sky coverage or differences in the analyses and experimental set-up, the energy spectra were studied in a common declination band. As a novel approach, the energy spectrum was derived with an anisotropy-insensitive approach. The studies revealed that the flux differences in the common declination band have to come from instrumental effects. Based on this result, future analyses within Auger and Telescope Array will have to carefully determine the (energy-dependent) systematic uncertainties to bring the spectra in agreement.

A new search for possible imprints of anisotropy in the energy spectrum was performed. Motivated by the large-scale dipolar anisotropy reported by Auger, the energy spectrum was derived in declination bands which include the extremes of the dipole. The analysis of the cumulative spectra showed a higher flux from the excess region, while the flux from the deficit region is lower. The results are consistent with what is expected for a dipolar anisotropy in the arrival direction of the particles.

Zusammenfassung

Die kosmische Strahlung stellt ein Bindeglied zwischen der Astrophysik und der Teilchenphysik dar. Die Teilchen der kosmischen Strahlung dienen als Boten und geben Auskunft über die energiereichsten Prozesse im Universum. Ihre Entdeckung zu Beginn des zwanzigsten Jahrhunderts führte zu bedeutenden Ergebnissen in der Teilchenphysik. So wurden das erste Antiteilchen, sowie schwere Teilchen wie Myonen und Pionen mithilfe der kosmischen Strahlung entdeckt. In den letzten Jahren haben sich unser Verständnis der zugrunde liegenden physikalischen Prozesse, sowie unsere technologischen Möglichkeiten stetig weiterentwickelt. Dennoch bleiben Energien, wie sie die höchstenergetischsten Teilchen der kosmischen Strahlung besitzen ($E \sim 10^{20}$ eV), für Teilchenbeschleuniger wie den LHC unerreichbar. Aussagen über Teilchenwechselwirkungen und Wirkungsquerschnitte bei den höchsten Energien sind daher nur durch Untersuchungen der kosmischen Strahlung möglich. Der Ursprung der kosmischen Strahlung stellt eine zentrale Frage der Astrophysik dar. Anhand der Quellen können sich Rückschlüsse auf Propagationseffekte und die Beschleunigungsmechanismen der Teilchen ziehen lassen. Es gibt jedoch lediglich Quellkandidaten, die tatsächlichen Quellen sind bisher unbekannt. Fest steht jedoch, dass die kosmische Strahlung sowohl galaktischen, als auch extragalaktischen Ursprungs ist. Die Untersuchung der Massenzusammensetzung und des Energiespektrums liefert wichtige Aussagen über mögliche Quellen. Die präzise Messung des Energiespektrums und dessen Merkmale dient als Basis zur astrophysikalischen Modellbeschreibung der höchstenergetischen kosmischen Strahlung.

Bei den höchsten Energien liegt der Fluss der kosmischen Strahlung nur noch bei einem Teilchen pro Quadratkilometer und Jahrhundert. Um eine Messung des Flusses mit ausreichender Statistik zu ermöglichen, bedarf es daher einer enormen Detektorfläche. Das Pierre-Auger-Observatorium in Argentinien ist mit einer Fläche von $3000\,\mathrm{km}^2$ der bis dato größte Detektor zur Messung der höchstenergetischen kosmischen Strahlung. Trifft ein Teilchen der kosmischen Strahlung auf die Erdatmosphäre, so wechselwirkt es mit den Atomkernen und erzeugt Sekundärteilchen, welche ihrerseits wiederum wechselwirken. Dies führt zur Bildung ausgedehnter Luftschauer, welche mittels Oberflächendetektoren am Boden gemessen werden können. Zusätzlich dazu messen Fluoreszenzteleskope die longitudinale Schauerentwicklung in der Atmosphäre.

Der Fokus dieser Arbeit liegt auf der Bestimmung des Energiespektrums mittels Daten des Oberflächendetektors. Aus einer empirischen Beschreibung der beobachteten lateralen Signalverteilung wird ein erwartetes Signal in einem bestimmten Abstand zur Schauerachse abgeleitet. Dieses Signal stellt für jedes Ereignis eine erste Schätzung der Primärenergie dar. Die Schätzung ist jedoch zenitwinkelabhängig, da der Schauer mit zunehmendem Einfallswinkel durch Wechselwirkungen in der Atmosphäre abgeschwächt wird. Eine zenitwinkelunabhängige Schätzung ergibt sich mithilfe der Constant-Intensity-Cut-Methode. Im Rahmen dieser Arbeit wurde eine neuartige Zenitwinkelkorrektur untersucht, die eine Abhängigkeit der atmosphärischen Abschwächung von der Primärenergie berücksichtigt. Anschließend wird die korrigierte Schätzung mit den Energiemessungen des Fluoreszenzdetektors kalibriert. Im Zuge dieser Arbeit wurde das Energiespektrum sowohl für den Standardoberflächendetektor, als auch für eine Erweiterung mit dem halben Detektorabstand bestimmt. Durch den verkleinerten Detektorabstand können niedrigere Energien gemessen werden. Das kombinierte Energiespektrum umfasst drei Dekaden in Energie und ist mit den bisherigen Ergebnissen kompatibel. Das mit dem Standardoberflächendetektor erhaltene Energiespektrum wurde mit dem gemessenen Spektrum des Telescope-Array-Experiments verglichen. Beide Experimente befinden sich auf etwa gleicher Breite auf gegenüberliegenden Hemisphären. Beim Vergleich der Energiespektren beider Experimente zeigte sich ein deutlicher Unterschied in der rekonstruierten Energieskala. Oberhalb einer Energie von etwa $10^{19.5}$ eV ist der Unterschied in den Spektren signifikant. Um zu verstehen, ob die Diskrepanz auf die unterschiedliche Himmelsabdeckung oder auf Unterschiede in der Analyse und im Detektoraufbau zurückzuführen ist, wurden die Energiespektren in einem gemeinsamen Deklinationsband untersucht. Als neuartiger Ansatz wurde das Energiespektrum mit einem Ansatz bestimmt, der unempfindlich gegenüber Anisotropien ist. Die Studien zeigten, dass die Flussunterschiede im gemeinsamen Deklinationsband auf instrumentale Effekte zurückführbar sind. Basierend auf diesem Ergebnis müssen sich zukünftige Analysen innerhalb des Pierre-Auger-Observatoriums und Telescope-Array-Experiments auf eine sorgfältige Bestimmung der (energieabhängigen) systematischen Unsicherheiten fokussieren, um die Spektren in Übereinstimmung zu bringen.

Eine neue Suche nach möglichen Auswirkungen der Anisotropie auf das Energiespektrum wurde durchgeführt. Motiviert durch die von dem Pierre-Auger-Observatorium nachgewiesene großskalige Dipolanisotropie wurde das Energiespektrum in Deklinationsbereichen bestimmt, die jeweils die Extreme des Dipols beinhalten. Die Analyse der kumulativen Spektren zeigt einen höheren Fluss aus der Region des Überschusses, während der Fluss aus der Region des Defizits geringer ist. Die Ergebnisse stimmen mit der Erwartung einer Dipolanisotropie in der Einfallsrichtung der Teilchen überein.

Contents

Acronyms

This is a list of acronyms used within this work sorted alphabetically according to the short version.

ADST	Advanced Data Summary Tree	71
AERA	Auger Engineering Radio Array	17
AMIGA	Auger Muon Detectors for the Infill Ground Array	16
CDAS	Central Data Acquisition System	13
c.d.f.	cumulative distribution function	54
CIC	Constant Intensity Cut	52
CLF	Central Laser Facility	15
CMB	cosmic microwave background radiation	4
Co	Coihueco	69
CR	cosmic ray	4
FADC	flash analog to digital converter	12
FD	Fluorescence Detector	11
FoV	field of view	33
GOES	Geostationary Operational Environmental Satellites	138
GPS	Global Positioning System	13
GZK	Greisen-Zatsepin-Kuzmin	3
HEAT	High Elevation Auger Telescopes	15
HeCo	virtual FD by combining Coihueco and HEAT	15
LDF	lateral distribution function	24
LHC	Large Hadron Collider	2
MD	Muon detector	16
MoPS	Multiplicity of positive steps	20

p.d.f.	probability density function	67
PE	photo-electron	27
PMT	photo-multiplier tube	12
SD	Surface Detector	11
SD-433	433 m SD infill	14
SD-1500h	1500 m SD horizontal	88
SD-1500	1500 m SD vertical	12
SD-750	750 m SD vertical	13
SSD	Surface Scintillator Detector	17
TA	Telescope Array	6
Thr	threshold trigger	21
ToT	time-over-threshold trigger	20
ToTd	time-over-threshold deconvoluted trigger	20
UHECR	ultra-high energy cosmic ray	1
VAOD	vertical aerosol optical depth	138
VCT	vertical centered through-going	27
VEM	vertical-equivalent muon	13
WCD	water-Cherenkov detector	12
XLF	eXtreme Laser Facility	15

CHAPTER

1

Introduction

Since their discovery over a century ago, cosmic rays have been the subject of intense scientific research. These charged subatomic particles extend over roughly eleven orders of magnitude in energy, from sub-GeV up to 10^{20} eV, with the energy spectrum following a steeply falling power law. The bulk of the particles, being low-energy, originate from the Milky Way itself. Particles at the lowest energies are produced by ordinary stars, such as the Sun, and are ejected during solar flares. The sources for energies above approximately 10^{9} eV are still unknown. Candidates for these cosmic rays are shocks within supernova remnants, gamma-ray bursts, active galactic nuclei or, most recently, starburst galaxies. With increasing energy, the particles are less confined and diffuse out of the galaxy. The most energetic particles are therefore thought to be of extragalactic origin.

The energy range of UHECRs[1], which is studied in this work, is of particular interest. Somewhere in the range of 10^{17} eV to 10^{19} eV the transition between the galactic and extragalactic cosmic rays takes place. The energy spectrum is not a single power law but exhibits distinct features. Two of the features, the ankle and the suppression, are accessible through the energy range analyzed in this work. In combination with the study of the mass composition of UHECRs, these features help to elucidate the origin of cosmic rays, and ultimately the acceleration mechanisms which are able to create the highest-energy particles in the Universe.

UHECRs are measured with ground-based detectors, of which the largest one to-date is the Pierre Auger Observatory. Due to the low flux of 1 particle per km^2 per year at 4 EeV and 1 particle per km^2 per century at 10^{20} eV, direct satellite-based measurements are no longer possible and indirect measurements using ground-based detectors are required. Ground-based measurements exploit the phenomenon of air showers produced by the incident cosmic rays. Once a UHECR enters the Earth's atmosphere, it will interact and produce secondary particles, which themselves produce further particles, leading to a cascade of secondary particles. These secondary particles are then measured at ground level.

Besides the astrophysical interest, the study of cosmic rays is also a study of particle physics at the highest energies. UHECRs initiate particle collisions with a center-of-mass

---

[1] ultra-high energy cosmic rays

energy of about one magnitude higher than the energies reachable at the LHC[2], allowing the study of hadronic interactions at the highest energies.

1.1 Ultra high energy cosmic rays

UHECRs are cosmic rays exceeding an energy of about $\sim 10^{18}$ eV. The low rate at which they arrive on Earth necessitates the usage of ground-based detectors in order to measure them. The first evidences for particles reaching Earth from outer space was found over 100 years ago as described in the following section. Innovations in detector design have made it possible to measure the flux of cosmic rays over several decades in energy. Precise measurements of the energy spectrum have revealed deviations from a simple steeply-falling power law. These features are addressed in the second section, followed by remarks on possible candidate sources. The last sections give an overview of extensive air showers and the mass composition.

1.1.1 Historical overview

The discovery of cosmic rays dates back over 100 years. At the end of the 19th century, Henri Becquerel discovered radioactivity and Earth itself was first assumed as the only source of ionizing radiation. This would be evidenced by a decrease in the measured radiation as a function of altitude. Domenico Pacini was one of the first physicists to test the ionization rates at various altitudes, including measurements underwater [1]. By observing a decrease in the ionization rate when placing an electroscope below the water surface, he contradicted the aforementioned assumption and concluded that part of the ionization stems from sources other than Earth itself. The broad acceptance of this claim came shortly afterwards with the balloon experiments of Victor Hess. During the flights, he measured the ionization rate not only at various altitudes, but also at different times of the day (as well as during a solar eclipse). He inferred from his measurements that the radiation had to enter the atmosphere from above and the source of this radiation was not necessarily the Sun alone [2]. In 1936, Hess received the Nobel Prize for the discovery of *cosmic radiation*.

In 1939, Pierre Auger observed coincident triggers in Geiger counters placed at different horizontal distances, and as such was the first to measure the lateral distribution of *air showers* [3]. The theoretical description of air showers was formulated by Heitler in 1954, who described the showers as *cascade* processes [4]. With the help of this model, the electromagnetic shower component can be described as an interplay between bremsstrahlung and pair production as explained in Section 1.1.4.

The first UHECR shower was detected by the M.I.T group at Volcano Ranch in New Mexico in the 1960s. Volcano Ranch was the largest detector array at this time. The array comprised 20 scintillation counters placed on a triangular grid and covered 12 km^2. In 1962, the first air shower with a reconstructed energy of about 10^{20} eV was recorded with this array [5].

Motivated by this discovery, bigger arrays were built to study cosmic rays in more detail. The theoretical prediction of a strong flux suppression at the highest energies was made shortly after by Kenneth Greisen as well as Georgiy Zatsepin and Vadim Kuz'min, known as the *GZK* cut-off [6, 7]. They predicted an upper limit for the spectrum of cosmic rays due to the interaction of UHECR protons with photons of the cosmic microwave background. The measurements by the first follow-up experiments provided contradictory evidence as to whether or not such a cut-off could be observed in the spectrum. The AGASA and Haverah Park experiments, both using an array of surface detectors, reported no visible steepening in

---

[2] Large Hadron Collider

their measured spectrum [8, 9]. However, data measured by the fluorescence telescopes of the High Resolution Fly's eye (HiRes) showed the first evidence of this suppression at the highest energies [10, 11].

By aiming for increased statistics at the highest energies, larger arrays with better detector techniques were proposed to finally elucidate the nature of the suppression. Being the largest detector array at present, with a running time of more than 10 years, the *Pierre Auger Observatory* (Auger) proved the existence of the suppression. The reason for the suppression remains yet unknown, as it could either be caused by the GZK[3]-cutoff alone or by the exhaustion of the accelerating sources. These scenarios are further discussed in the following sections.

1.1.2 The flux and its features

The all-particle spectrum of cosmic rays covers a vast range in energy, from less than 10^9 eV to more than 10^{20} eV, an energy that exceeds the rest mass energy of a proton by eleven orders of magnitude. The flux of cosmic rays is steeply falling with energy and roughly follows a power law $E^{-\gamma}$. In the search for structures and deviations from a single power law it is common to scale the flux by a power of energy as depicted in Fig. 1.1. Three spectral features immediately stand out. At an energy of about $3{\times}10^{15}$ eV to $5{\times}10^{15}$ eV a steepening of the flux occurs (*the knee*), followed by a flattening at around $5{\times}10^{18}$ eV (*the ankle*), and a strong suppression at highest energies, above $4{\times}10^{19}$ eV.

The current Auger data covers the ankle and the suppression region. The suppression is of particular interest for this work as a discrepancy between the measured suppression energies of various other experiments may give a handle on anisotropy studies as discussed in depth in Chapter 4. The aforementioned features are discussed here.

The knees

Several scenarios have been proposed to explain the knee-like structure in the all-particle spectrum. Up to the knee the particle energies arise most likely from diffuse acceleration in shock fronts of supernova remnants. The steepening at the knee may then reflect the maximum energy of galactic cosmic accelerators or alternatively a rigidity-dependent change in propagation. The result of both mechanisms is a change from a light toward a heavy composition in the knee region and is supported by the measurements of the KASCADE experiment and its extension KASCADE-Grande. The knee in the all-particle spectrum was measured at around $5{\times}10^{15}$ eV by KASCADE and it was shown that knee-like features appear in the flux of light elements [12, 13]. By splitting the data of KASCADE-Grande into electron-rich and electron-poor events representing the light and heavy elements, respectively, another steepening was observed. This *second knee* at $8{\times}10^{16}$ eV is attributed to a decrease of the flux in the heavy component, just as the knee is supposed to coincide with the extinction of the light component [14]. Most theories assume the knees to be intrinsic characteristics of the energy spectrum. Alternative theories explain the structures with new particle physics processes occurring in the interaction with the atmosphere, resulting in a mass-dependent cut-off in the spectra of the individual elements [15]. However, experimental results indicating a rigidity-dependent cut-off disfavor the alternative theories.

The ankle

All theories explaining the knees agree on the galactic origin of the particles measured in this energy range. With increasing energy, the gyroradius of the particles approaches the galactic

---

[3] Greisen-Zatsepin-Kuzmin

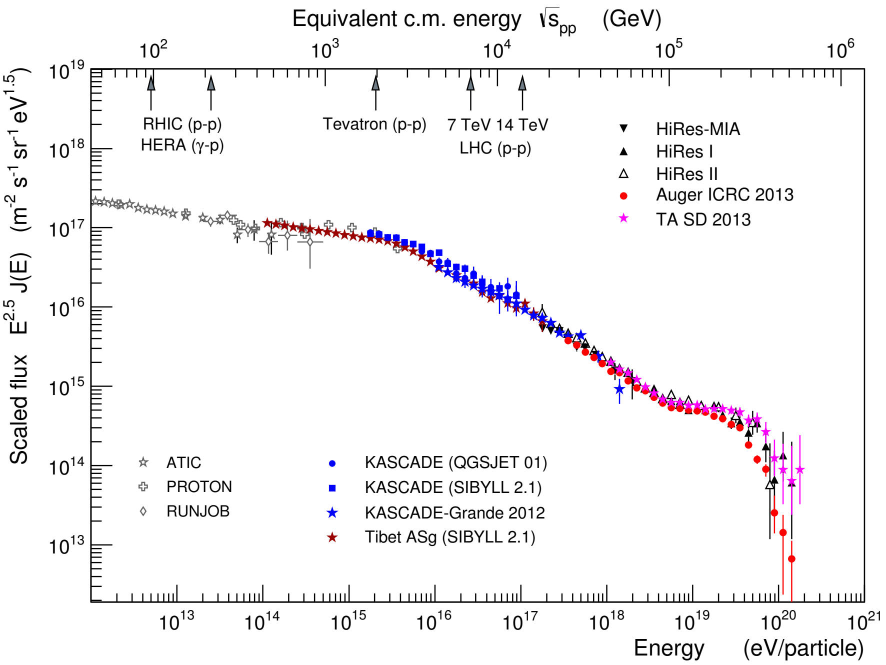

Figure 1.1: All-particle cosmic ray flux with data measured by various experiments and covering almost ten decades in energy (courtesy of Ralph Engel). The data are scaled by $E^{2.5}$ to highlight spectral features, of which the most prominent ones are discussed in more detail in this section. The equivalent center of mass energies of several man-made accelerators are also depicted.

scale height (~1 kpc), and the probability that they escape the Galaxy increases. In return, particles originating from outside the Milky Way are likely to enter the Galaxy and reach Earth. The ankle region is as such supposed to be the region of transition from a galactic to an extragalactic CR[4] flux. Two prominent and competing models to explain the ankle are depicted in Fig. 1.2.

The first model to be discussed is the *dip model*, shown in Fig. 1.2a, which assumes an early onset of the extragalactic component and the transition to extragalactic CRs to be completed before the ankle, at an energy of about $1{\times}10^{18}$ eV [16]. The ankle is then a consequence of propagation effects of a proton-dominated extragalactic flux. The protons interact with photons from the CMB[5] producing e^+e^- pairs. The energy loss accompanying this interaction results in an accumulation of protons at the ankle, leading to a flattening of the spectrum. This model allows for an admixture of nuclei on the order of only 10 % to 15 %, and the bulk of the composition from the transition energy up to the highest energies must consist of protons only.

The *mixed composition model* is displayed in Fig. 1.2b. Here, the galactic component is dominant before the ankle and a smooth transition to extragalactic particles takes place at the ankle itself [17].

A more recent model explains the ankle as a result of the *photodisintegration of nuclei* in the area surrounding the accelerator [18]. The key idea of this model is that the disintegration processes act as a high-pass filter on the energy spectrum of the injected nuclei. The disintegration is supposed to occur outside of the source whereas the previous assumptions on disintegration are exactly the opposite - the processes occur mainly inside the accelerator, permitting the low energy particles to escape unscathed, with only the high energy nuclei

---

[4] cosmic ray

[5] cosmic microwave background radiation

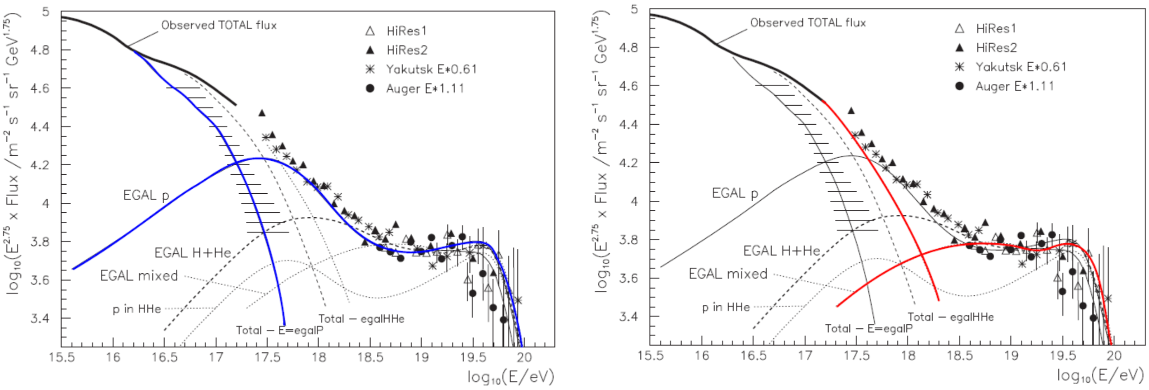

(a) Pair production dip **(b)** Mixed composition

Figure 1.2: Two scenarios to describe the ankle feature. In the dip scenario (a) the ankle is a signature caused by the interaction of an extragalactic proton component with the CMB photons producing electron-positron pairs. The mixed composition scenario (b) assumes a composition similar to the one of galactic CRs and the ankle is associated with the emergence of extragalactic particles.

suffering spallation. The new model assumes the nuclei are trapped in the turbulent magnetic field of the source environment. The escape time of the nuclei decreases with energy. Hence, the escape time of low-energy particles is higher than the interaction time, which increases the chances of interacting with the photons of the environment before escaping. The interaction generates nucleons whose energy is reduced by $1/A$ of the original nucleus of mass A. This gives a natural explanation to a lighter composition below the ankle evolving into a heavy composition above.

Flux suppression

Despite the confirmation of a suppression of the flux of CRs above an energy of about $4{\times}10^{19}$ eV, its origin remains unclear. The suppression can be understood in terms of propagation effects. Two processes are associated with propagation. Firstly, CRs interact with magnetic fields which alter their direction and travel time. Secondly, interactions with cosmic backgrounds take place, resulting in a change in composition and energy. Protons with energies above $6{\times}10^{19}$ eV interact with photons from the CMB and produce a Δ-resonance via the following processes:

$$\gamma_{\text{CMB}} + \text{p} \rightarrow \Delta^{+} \rightarrow \text{p} + \pi^{0}\,,$$
$$\gamma_{\text{CMB}} + \text{p} \rightarrow \Delta^{+} \rightarrow \text{n} + \pi^{+}\,.$$

The primary protons lose about 20 % of their energy in each of these interactions [6, 7]. This is the so-called GZK effect. A similar process occurs for heavier nuclei due to photodissociation processes, e.g giant dipole resonance. The interactions of protons and iron nuclei with photons of the CMB result in a comparable suppression energy as shown in Fig. 1.3. Apart from the energy loss, a consequence of the GZK effect is a constraint on the maximum propagation distance of extragalactic nuclei. Under the assumption of almost uniformly distributed sources across the Universe, the GZK horizon for protons with $E > 6{\times}10^{19}$ eV is of the order of 100 Mpc.

The propagation clearly affects the CRs on their way to Earth but the question is whether this is the main reason for the suppression. The rapid fall-off can also be an indication of the maximum energy of cosmic accelerators. The maximum acceleration energy differs for

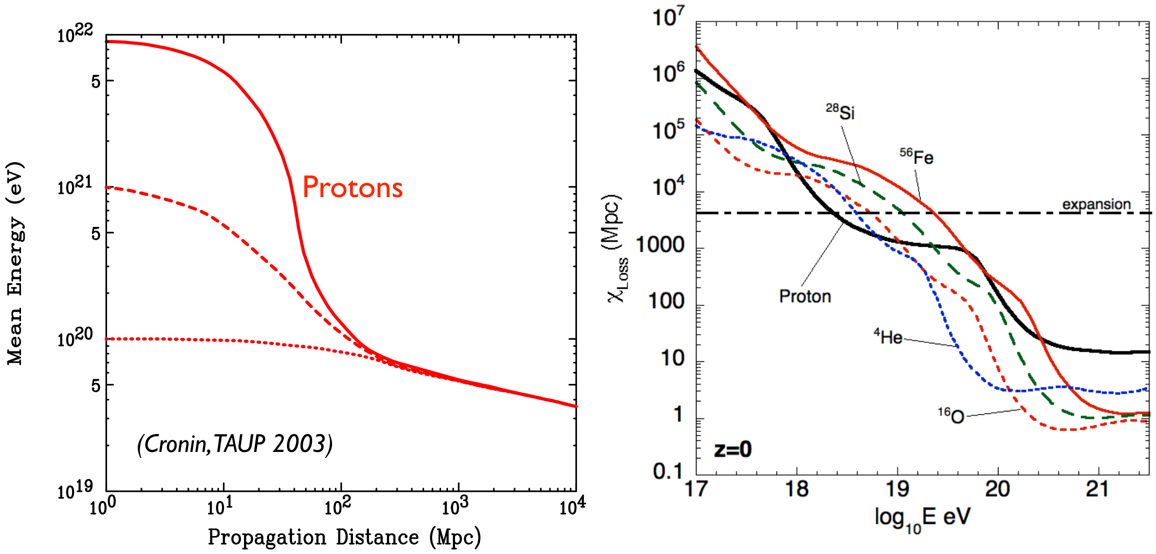

(a) **(b)**

Figure 1.3: Energy losses of nuclei during the propagation due to interactions with the photons of the CMB. In (a) the energy loss for proton primaries is shown (reference as stated in the plot) and in (b) the attenuation length of different nuclei is depicted over the energy [17]. Around 10^{20} eV the attenuation length for the heaviest nuclei are compatible with those of proton primaries leading to a similar suppression energy.

the various nuclei as it scales with the charge Z. The suppression is then a result of the superposition of the different cut-offs.

Two interpretations of the CR flux from the ankle up to the highest energies can be seen in Fig. 1.4. A pure proton composition is assumed for the fit to the TA[6] data reflecting a GZK-dominated suppression, whereas the Auger data is described by a mixed composition. In the latter case, the maximum energy for the components is rigidity-dependent and scales with $Z \times 10^{18.7}$ eV.

1.1.3 Possible source candidates and anisotropy

In contrast to the detection of sources for gamma-rays (see e.g [23]), no point sources of UHECRs have so far been discovered. Point source studies are suited to a light composition or neutral primary particles. Compared to heavier elements, these particles suffer less or even no deflection by magnetic fields. Due to the GZK horizon, particles with energies exceeding the GZK energy are limited to about 50 Mpc to 100 Mpc. This limit diminishes the number of possible sources and favors directional correlations of the source locations and the CR arrival directions. Besides the spatial source limitation, there are only a few potential sources that are thought to be able to accelerate CRs up to the highest energies. The candidate sources are summarized in the Hillas plot in Fig. 1.5. The sources are arranged according to the size of their accelerating environment R and their inherent magnetic field strength B. The maximum energy a particle can gain depends on the aforementioned source characteristics as well as on its charge Z, and is roughly $E \approx Z\,B\,R$. The two diagonals show the source conditions that are needed to accelerate proton (solid line) and iron (dashed line) primaries to 10^{20} eV. Among the most powerful accelerators are active galactic nuclei (AGN), gamma-ray bursts (GRB) and shocks within the intergalactic medium (IGM).

---

[6] Telescope Array

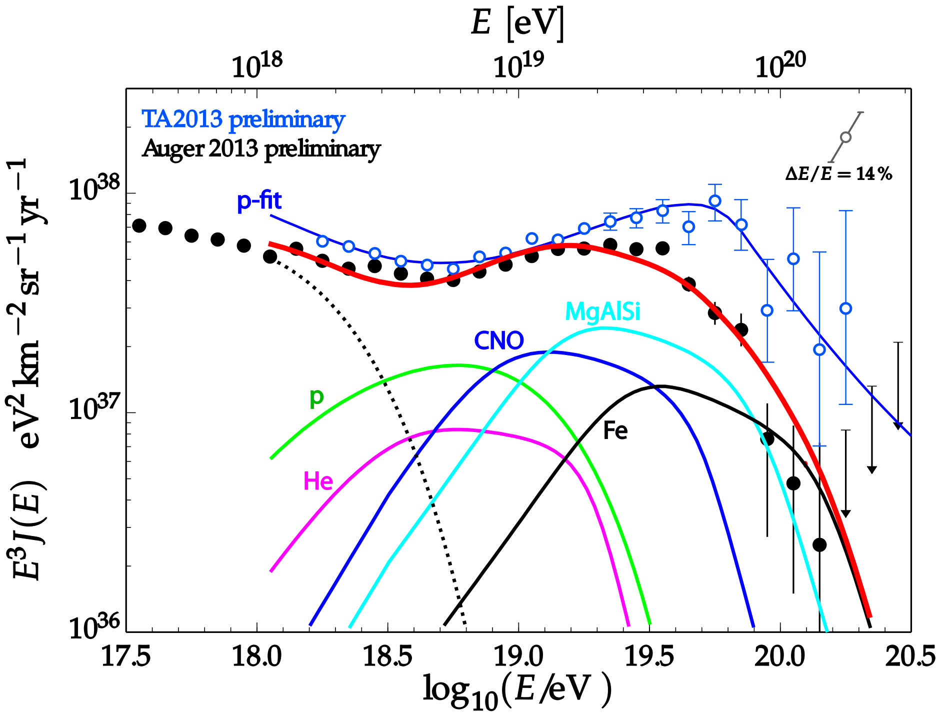

Figure 1.4: The flux of UHECRs as measured by TA and Auger [19, 20]. A model of extragalactic proton sources is used as input for the fit to the data measured by TA. The sources are distributed cosmologically according to $(1+z)^{4.4}$ and the particles are injected with a power-law distribution at the sources according to $E^{-3.9}$ (blue line). The data measured by Auger are compared to a model assuming a maximum acceleration energy $E_{\mathrm{max}} = 10^{18.7}\,\mathrm{eV} \times Z$ with injection spectra $\gamma = 1$ and an enhanced galactic CR composition from [21]. An additional galactic component is plotted as a dotted black line (plot and its description taken from [22]).

While no point correlation with one of these sources has been detected so far, inferences about the origin of UHECRs can still be drawn by performing anisotropy searches on medium and large scales. A recent study by Auger provides evidence of a correlation at an intermediate scale between the arrival directions of CRs above 39 EeV and starburst galaxies [24]. These galaxies undergo intense star formation and hence create extreme environments in which particles might be (re-)accelerated to the highest energies.

A clear, large-scale anisotropy in the arrival direction of CRs at a 5.2 σ level of significance was observed by Auger [25]. The direction of the reconstructed dipole is visualized in the sky map of Fig. 1.6. The cosmic-ray flux is shown for $E \geq 8\,\mathrm{EeV}$. The dipole points in the direction $\alpha_{\mathrm{d}} = 100 \pm 10^\circ$ in right ascension and $\delta = -24^{+12^\circ}_{-13}$ in declination. Hence, the dipole is pointing away from the galactic center which lies at the origin of the map, indicating an extragalactic origin of this anisotropy. A dipole in the arrival direction of CRs is predicted in case of the Compton-Getting effect [26] as a result of the Earth's motion with respect to the rest frame of the UHECR sources. However, the expected amplitude of 0.6 % is about ten times smaller than the observed one. Amplitudes in the range of 5 % to 20 % above the chosen threshold energy of 8 EeV arise from CRs originating either from a dominant source, suffering diffusion through the magnetic fields during their propagation, or from less prominent inhomogeneously distributed sources.

1.1.4 Extensive air showers

Cosmic rays entering the Earth's atmosphere interact with nuclei in the air, thereby producing secondary particles which themselves undergo interactions and create further particles. The

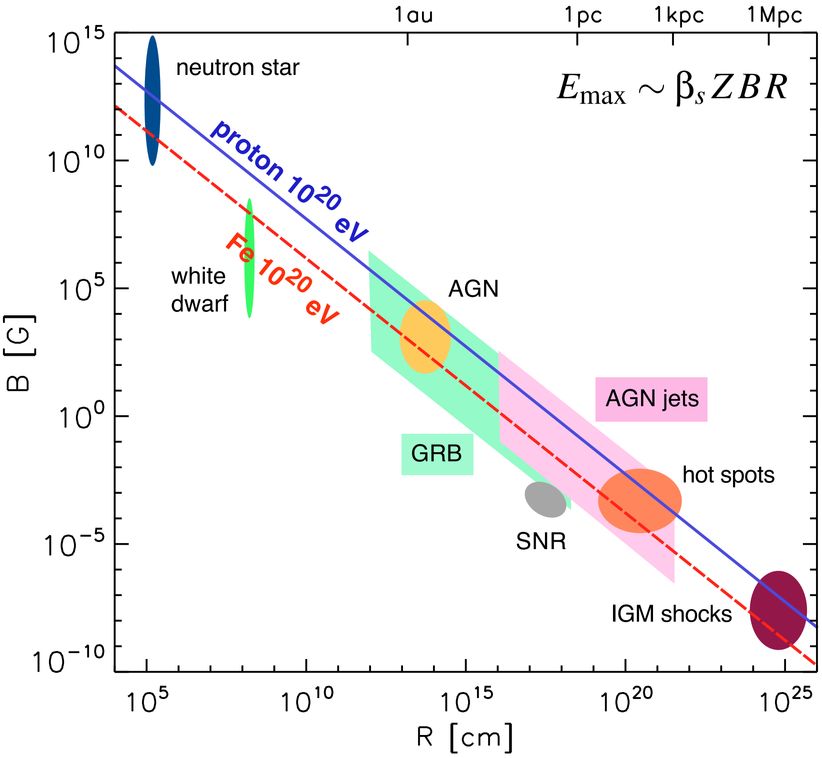

Figure 1.5: A Hillas-like plot sorting the potential sources for UHECRs according to their size and magnetic field strength. The lines correspond to proton (solid) and iron (broken) primaries accelerated up to 10^{20} eV. Based on [27], taken from [28] and modified.

processes continue until the energies of the individual particles reach a critical energy and the remaining interactions are due to ionization or scattering. The minimal energy for an incident primary particle to produce a cascade that reaches ground is about 10^{14} eV. With a starting energy of 10 EeV an extensive air shower consists of $\sim 10^{10}$ secondaries at ground level that are spread over an area of order 20 km^2. A shower can be divided into three components: the electromagnetic component ($e^{\pm}, \gamma$) contains the largest amount of energy within a shower ($\sim$ 90 %), the muonic component ($\mu^{\pm}$) undergoes almost no interactions before reaching the ground, and the hadronic component ($\pi^{\pm}$, π^0, p, n, $\mathrm{K}^{\pm}$, K^0) is dominant in the early shower development and supplies the other two components with energy. Based on the Heitler model, the three components are discussed in short below.

The electromagnetic component

Two physical processes are responsible for the development of the electromagnetic cascade as indicated on the right hand side of Fig. 1.7. A charged electromagnetic particle ($e^{\pm}$) is affected by the Coulomb field of a nucleus in the air and creates a photon via bremsstrahlung. The photon itself creates a $e^{\pm}$ pair when interacting with the nucleus. The radiation length for electromagnetic particles in air corresponds to $\lambda_r \approx 37\,\mathrm{g\,cm^{-2}}$, so on average two new particles will be created after a splitting length of $\mathrm{d} = \ln(2)\lambda_r$. Each of these interactions denotes a step in the simple Heitler model. The number of particles doubles with each step and the energy is assumed to be shared equally between the particles, leading to 2^n particles within the cascade after n steps. The splitting ceases abruptly when the energy of the individual particles reaches a critical energy E_c. Beyond this point, the particles lose energy due to ionization and scattering. The critical energy in air amounts to $\sim$ 87 MeV for electromagnetic particles. The total number of particles can be inferred from the incident

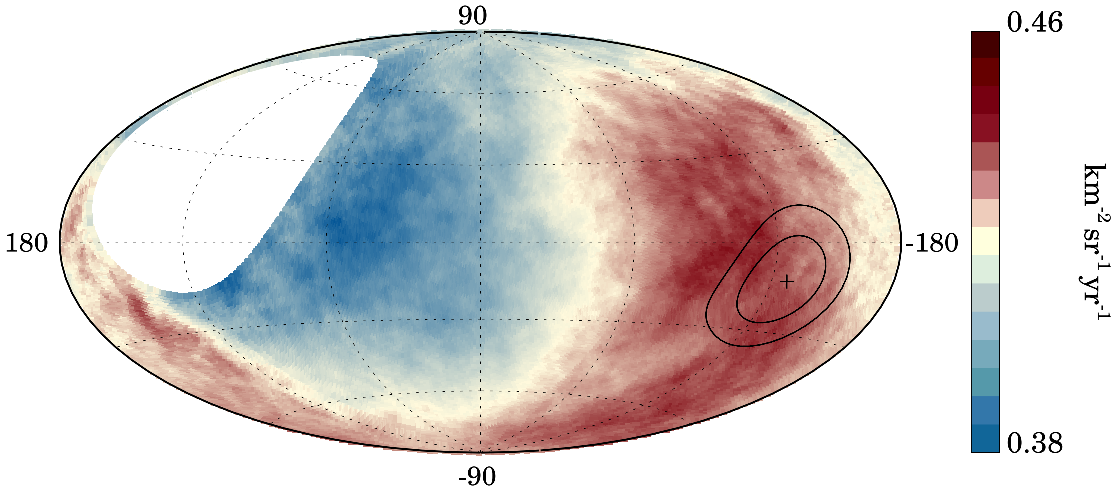

Figure 1.6: Sky map showing the CR intensity as observed by Auger in galactic coordinates. The reconstructed dipole direction is indicated by a cross and the 68 % and 95 % confidence-level regions are denoted by the contours. Modified, original from [25].

energy by the relation $N_{\text{max}} \propto E_0$ and the atmospheric depth of shower development scales as $X_{\text{max}} \propto \ln(E_0)$.

The hadronic component

Multiple particles are produced in each step of a hadronic interaction with an air nucleus. The most commonly produced particles are pions which occur in three states, two charged ($\pi^{\pm}$) and a neutral one (π^0). The states are produced with a ratio of about 1 : 1 : 1. After n generations, the incident energy E_0 is divided between the hadronic and electromagnetic component as follows:

$$E_{\text{had}} = \left(\frac{2}{3}\right)^n E_0 \qquad E_{\text{em}} = \left[1 - \left(\frac{2}{3}\right)^n\right] E_0 \tag{1.1}$$

The neutral particles almost immediately decay into two photons ($\pi^0 \rightarrow \gamma\gamma$) which themselves create electromagnetic sub showers, feeding the electromagnetic component. The charged hadrons suffer further interactions until the individual particle energy reaches a critical value ($E_c^{\pi} \sim 30\,\text{GeV}$). At this point, the decay length of the particle becomes comparable to the interaction length and decay dominates over the creation of new particles. Charged pions decay into a muon and neutrino:

$$\pi^- \longrightarrow \mu^- + \bar{\nu}_\mu \tag{1.2}$$
$$\pi^+ \longrightarrow \mu^+ + \nu_\mu \tag{1.3}$$

These decay products build the muonic shower component. The number of muons produced in a shower is approximated by:

$$N_\mu = \left(\frac{E_0}{E_c}\right)^\alpha \qquad \alpha = \frac{\ln n_{\text{ch}}}{\ln n_{\text{tot}}} \approx 0.82...0.9, \tag{1.4}$$

taking into account the number of charged particles (n_{ch}) as well as the total number of particles (n_{tot}). High-energy neutrinos and muons account for the invisible energy E_{inv} carried into the ground. This energy is of the order of 10 % to 15 % of the primary energy.

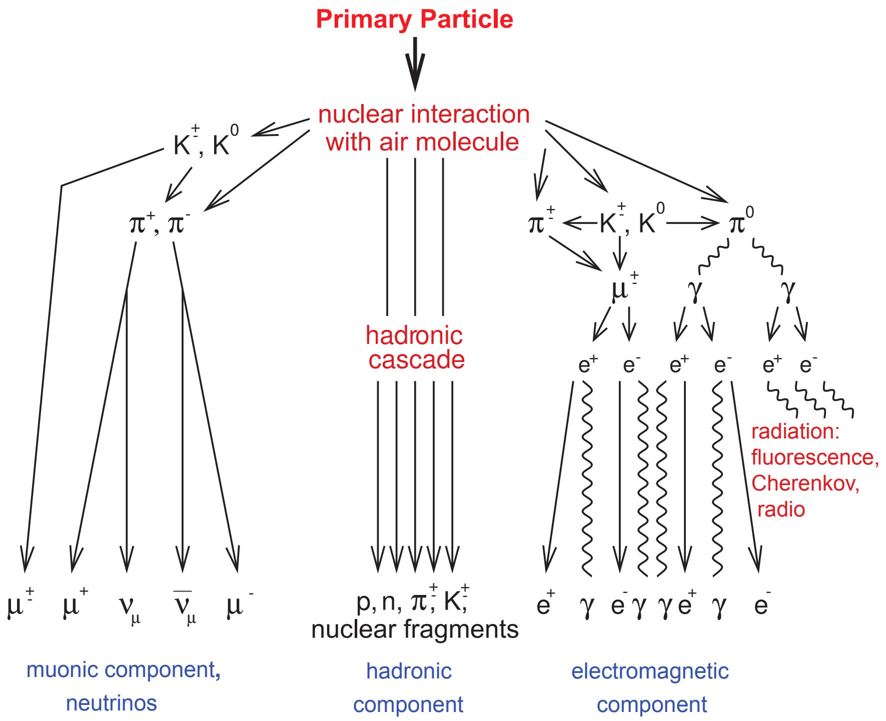

Figure 1.7: Illustration of the particle components created during the development of an air shower [29].

The properties of showers initiated by heavy nuclei are derived from proton showers using a superposition model. The binding energy per nucleon (~5 MeV) is much smaller than the average interaction energies. As a result, a nucleus of mass A can be approximated as A independent nucleons, each of them carrying a fraction of E_0/A of the incident energy. The impact on the number of muons contained in the shower is as follows:

$$N_\mu^A(E_0) = A \cdot \left(\frac{E_0/A}{E_c}\right)^\alpha = A^{1-\alpha}\left(\frac{E_0}{E_c}\right)^\alpha \tag{1.5}$$

The heavier the nucleus, the more muons are expected for a certain primary energy. On average, iron induced showers contain about 40 % more muons than proton showers. The position of the maximum shower development depends as well on the mass $X_\mathrm{max}^A = X_\mathrm{max}(E_0/A)$ and hence lies higher in the atmosphere for heavier particles. Compared to proton showers, iron showers with the same energy reach their maximum about 80 g cm^{-2} to 100 g cm^{-2} higher in the atmosphere.

1.1.5 Mass composition

The mass composition is a key observable used to understand the features present in the energy spectrum. As the depth of the shower maximum, X_max, differs for different primary species, it is well-suited to discriminate particles by their primary mass. However, fluctuations in the early state of the air-shower development prevent an event-by-event discrimination. Thus, the mass composition has to be inferred from the distribution of the average depth of shower maximum. The evolution of $\langle X_\mathrm{max}\rangle$ with energy as measured by Auger is depicted in Fig. 1.8. The relationship of the mean X_max with respect to energy E is [30]:

$$\langle X_\mathrm{max}\rangle = X_0 + D\,\lg\left(\frac{E}{E_0 A}\right), \tag{1.6}$$

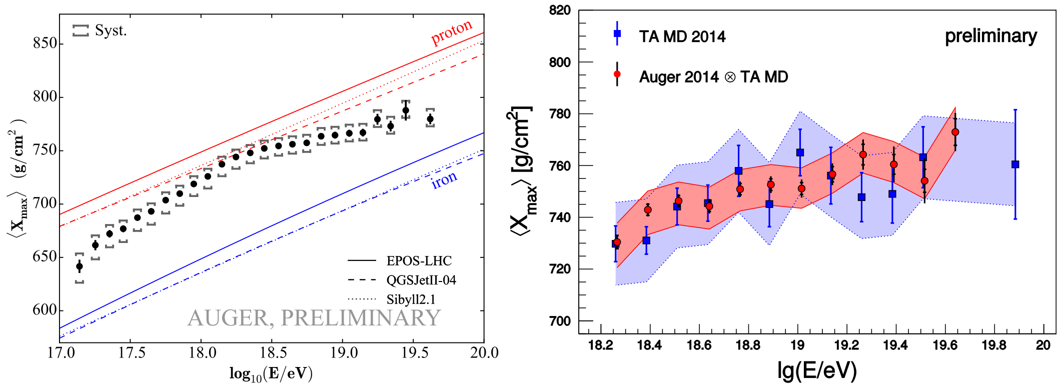

(a) **(b)**

Figure 1.8: Energy evolution of the average depth of the shower maximum. (a) The Auger data is compared to air-shower simulations using current hadronic interaction models [32]. (b) The mean $X_{\max}$ as measured with the Middle Drum detector of TA is compared to the Auger data folded with the MD acceptance. The measurements agree within their uncertainties [33].

with X_0 being the mean depth of proton showers at energy E_0 and D being the elongation rate, which refers to the change of $X_{\max}$ with $\lg E$. Describing the evolution of the mean $X_{\max}$ as function of logarithmic energy with a simple linear function leads to unsatisfying results (see [31]). A sound description is obtained with a change in the elongation rate at a certain break energy $E_0 = 10^{18.27}$ eV. This change in elongation rate indicates a deviation from a pure composition. The Auger data implies an evolution towards lighter masses up to the break energy, followed by a reversed trend towards heavier nuclei.

1.2 The Pierre Auger Observatory

The Pierre Auger Observatory is the world's largest observatory to measure ultra high energy cosmic rays [34]. It was originally designed to study the properties of the flux of cosmic rays at the highest energies, above 10^{18} eV [35], where the particle flux is very low. As such, its basic array layout consist of a Surface Detector (SD[7]) covering an area of about $3000\,\mathrm{km}^2$. A suited place to build the observatory was found in Argentina, in the Pampa Amarilla, near the town Malargüe. A layout of the observatory is depicted in Fig. 1.9. As visible from this map, the region is generally flat, with a maximum deviation of 270 m in altitude, making it possible to measure air showers at the same shower age over the whole array. The mean altitude is at about 1400 m or $875\,\mathrm{g\,cm^{-2}}$ in atmospheric overburden and therefore resides close to the maximum of air-shower development within the atmosphere. Another advantage of the location are the weather and atmospheric conditions. With hardly no rain, a clear atmosphere, and minimal light pollution due to the sparse population, it was possible to extend the observatory by a Fluorescence Detector (FD[8]). This detector consists of 27 telescopes and observes the light in the atmosphere above the SD. These two complementary detectors form a hybrid detector that is used for cross-calibration and as such enables the reconstruction of cosmic ray properties without a heavy use of simulations, making the analyses robust against changes of hadronic interaction models.

---

[7] Surface Detector

[8] Fluorescence Detector

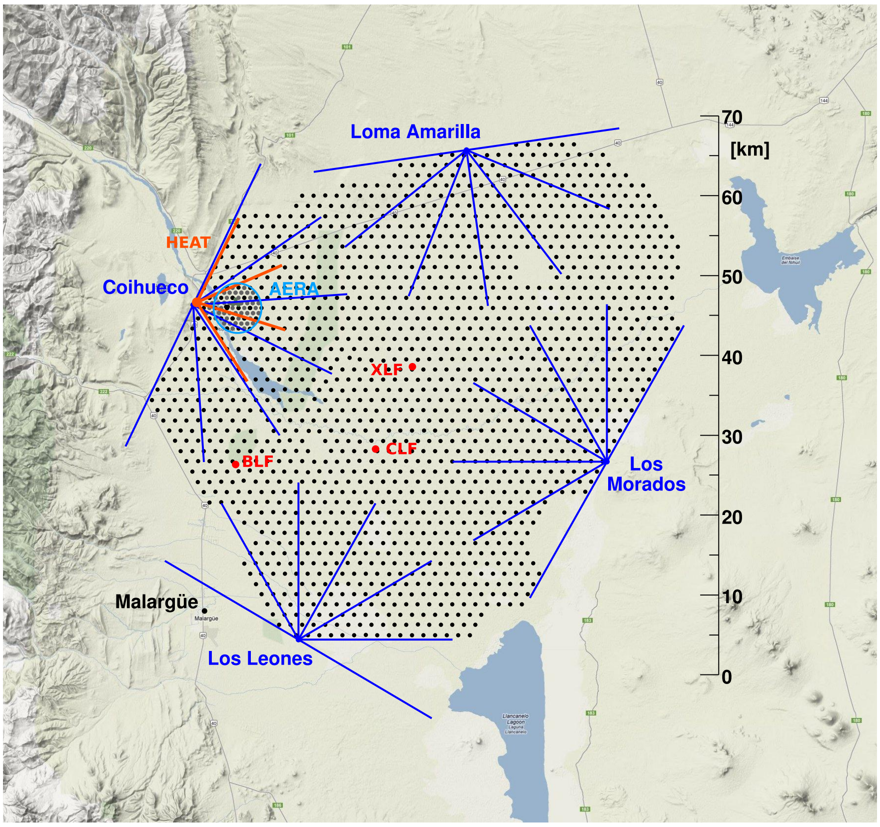

Figure 1.9: Map of Auger with SD stations as black dots and FD buildings shown in blue. Additionally, essential facilities for atmospheric monitoring as well as detector extensions are depicted (adapted from [36]). Details on the various facilities of the observatory are given in the text.

1.2.1 Surface detector

The original layout of the detector consists of a triangular grid of more than 1600 WCDs[9] with a distance of 1500 m amongst each other and is denoted as SD-1500[10]. Stable data taking was possible from January 2004 on but the construction of the SD-1500 was only completed in June 2008. Due to its tessellated grid and its spacing, the SD-1500 reaches the threshold of full efficiency for primary energies above $3{\times}10^{18}$ eV, as described in Section 3.3. Each WCD has a base of 10 m^2 and is filled with 12 tons of purified water up to a height of 1.2 m. The water volume is contained in a Tyvek reflective liner and monitored by three 9 inch diameter PMTs[11] mounted at the top of the tank looking vertically downward into the detector volume, as depicted in Fig. 1.10. They record the Cherenkov light produced by charged particles traversing the station faster than the phase velocity of light in water. Two signals are read out from each PMT, one directly from the anode, the other one from the last dynode after being inverted and amplified by a factor of 32 in nominal total signal as compared to the anode signal. This readout strategy provides a dynamic signal range suited to measure close to the core where the density of secondary particles increases to about 1000/µs as well as far away at a density as low as 1/µs. Each signal is digitized by 40 MHz 10-bit FADCs[12], with each FADC bin covering 25 ns. The calibration of each detector is performed in situ by normalizing

---

[9] water-Cherenkov detector s

[10] 1500 m SD vertical

[11] photo-multiplier tubes

[12] flash analog to digital converters

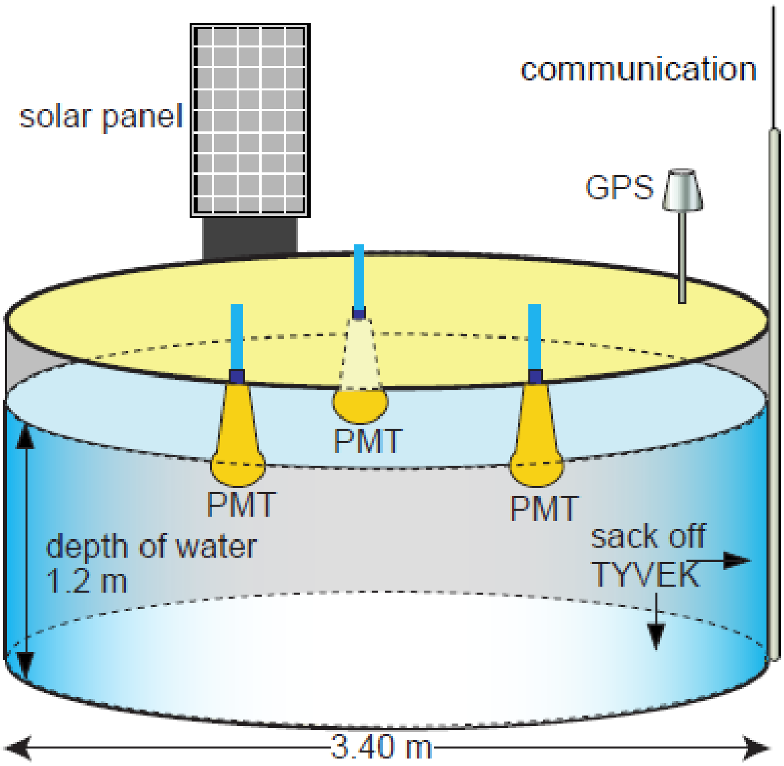

Figure 1.10: Schematic of an SD station with its internal components (from [37]).

the PMT signals to the signal a vertical through-going muon would induce in the detector (VEM[13]). All stations are equipped with solar panels and batteries as autonomous power supply for the PMTs, their electronics and for the communication with CDAS[14]. Fig. 1.11 shows a station in the field with its solar panel on top and the antennas for communication and GPS[15]. In the event of a trigger, all three PMT signals are transferred to CDAS. A detailed explanation of the trigger system is given in Section 2.1.

750 m array extension

The standard SD was extended by a nested array of 750 m spacing to decrease the energy of observations by one decade down to $3{\times}10^{17}$ eV. The SD-750[16] consists of 71 WCDs out of which 49 have been deployed in addition to the SD-1500 stations and the rest are shared stations amongst the two arrays [38]. The deployment location was chosen close to the FD sites Coihueco and HEAT, the low-energy extension for FD, having as such the possibility to measure low energetic showers in hybrid mode. The first data were taken in September 2007 with only one hexagon deployed and the final setup was completed in September 2012. Infrastructures as the trigger logic and event selection modes were adopted from the SD-1500. With the implementation of additional software triggers in July 2013 over the whole SD array, the sensitivity of the individual stations towards small signals on the single VEM level increased. As a result, the threshold of full efficiency for the SD-750 is lowered to about $10^{17.2}$ eV, as shown in [39]. The local station triggers are discussed in more detail in Section 2.1.1.

---

[13] vertical-equivalent muon

[14] Central Data Acquisition System

[15] Global Positioning System

[16] 750 m SD vertical

Figure 1.11: SD station in front of the Los Leones FD building.

433 m array extension

A narrow hexagonal cell with a baseline of 433 m was completely deployed by January 2013 with the SD-750 station Id 1764 as central station. The aim of the SD-433[17] is to measure energies below 10^{17} eV. First results show even an extension down to an energy of about $6{\times}10^{16}$ eV [40].

1.2.2 Fluorescence detector

The standard FD surveys the SD area from four different sites at the periphery of the observatory [41]. Each site, called Los Leones, Los Morados, Loma Amarilla, and Coihueco, houses six fluorescence telescopes and covers in total a field of view of 180° in azimuth and 30° in elevation. A single telescope has a field of view of 30°×30° in azimuth and elevation and points inward to observe the atmosphere above the SD. As a shower develops within the atmosphere, charged particles excite the nitrogen molecules which then de-excite by the emission of fluorescence light in the ~300 - 430 nm range. The UV light reaching the telescope buildings first has to pass a UV-transmitting filter, which shields the inner housing from visible background light, before it is focused by a 10 m^2 mirror onto the camera. The camera consists of 440 hexagonal PMTs arranged on a 22×20 grid and each PMT represents one pixel of the camera. A schematic of the setup is shown in Fig. 1.12, together with a photo showing the FD building at Los Leones.

The FD cameras are highly sensitive so that the operation of the telescopes is limited to clear and almost moon-less nights. Another limitation is given by the weather. The operation of the telescopes is put on hold in case of rain, snow or high wind speeds to avoid damages to the detector. This results in an FD duty cycle of around 15 %.

---

[17] 433 m SD infill

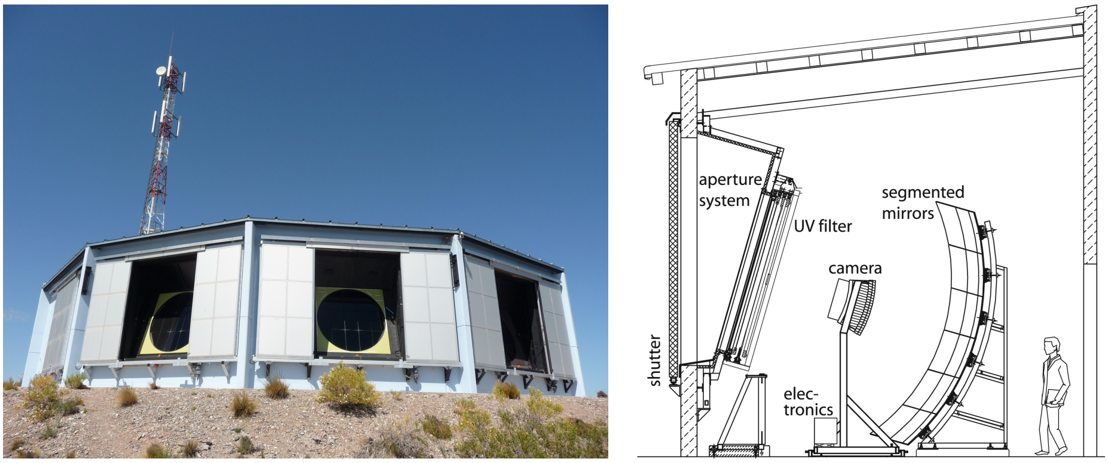

(a) **(b)**

Figure 1.12: (a) FD building at Los Leones with its communication tower. (b) Schematic view of a FD telescope (from [41]).

HEAT

HEAT[18] is the FD equivalent to the SD-750 of the standard SD and extends the measurements down to about 10^{17} eV [42]. With decreasing energy the amount of emitted fluorescence light is reduced and the shower has to land closer to a telescope in order to be measured. The field of view shrinks when approaching the telescope and as a result the longitudinal profile is detected only partially. To overcome this downside HEAT consists of three telescopes with two operation modes. In addition to the horizontal mode of the standard FD telescopes, the HEAT telescopes can be tilted upward by 29°, as visible in Fig. 1.13a. By combining the three telescopes with the 180 m distant telescopes of Coihueco during the reconstruction, an additional virtual FD is built, called HeCo[19]. The first measurements were performed at the end of January 2009 and since 2010 stable data taking is possible.

Atmospheric monitoring

The atmosphere above the SD array serves as calorimeter and monitoring its state is a crucial ingredient for the FD measurements. Atmospheric parameters such as temperature, pressure, and humidity influence the longitudinal development of air showers, the amount of emitted fluorescence light and its propagation. The atmospheric aerosol scattering and absorption properties as well as the cloud properties are monitored by four lidar stations, one at each FD site [43]. Each lidar station is equipped with a high-repetition UV laser sending pulsed shots at various rates into the direction of interest. The optical depth of the atmosphere during the FD operation is estimated by measuring the backscattered signal with the station's own PMTs.

Two laser facilities are installed in the center of the SD array. The CLF[20] and XLF[21] periodically fire pulsed laser shots in the line of sight of each of the FD telescopes and are thus conducive to measure the aerosol content between the FD site and the facility.

---

[18] High Elevation Auger Telescopes

[19] virtual FD by combining Coihueco and HEAT

[20] Central Laser Facility

[21] eXtreme Laser Facility


(a) (b)

Figure 1.13: Extensions to the observatory. (a) The low-energy extension of the FD, called HEAT, in upward mode. (b) Antenna of the radio detector AERA.

Additional information about the atmospheric state on a 1°×1°, or 110 km×110 km respectively, latitude-longitude grid is provided by the Global Data Assimilation System (GDAS) with a time resolution of 3 h [44].

Besides the atmospheric influence on the FD data, moderate effects are visible in the SD measurements due to altered particle densities on ground. A more detailed discussion of the weather effects on the signals measured on ground is given in Section 4.3.

1.2.3 AMIGA muon detector

The main objective of the AMIGA[22] enhancement is the direct measurement of the muon content of air showers [45]. It is a joint system of the SD-750 and scintillator detectors, which are buried in a few meter distance to the stations, as depicted in Fig. 1.14a. The signal recorded in the stations is a combination of the electromagnetic and muonic components of air showers. As the scintillators are buried at a depth of 2.3 m, they are effectively shielded from the electromagnetic particles and are left with measuring the muonic component alone. The respective overburden of around 540 g cm^{-2} imposes a cutoff for vertical muons of 1 GeV.

All scintillators combined build the MD[23]. A unitary cell of 7 stations is currently deployed. The data taking started at the end of 2014 with the completion of the cell. Each MD station of this cell is made up of 30 m^2 scintillators segmented into four modules, two modules having an area of 10 m^2 and 5 m^2, respectively. Twin detectors were installed at two positions of the unitary cell to study the accuracy of the muon counting algorithm. Each MD station runs in a slave trigger mode and reads out data once it received a trigger of its associated SD station.

1.2.4 Radio detector

The radio emission of air showers can be measured with a duty cycle of almost 100 % and provides yet another handle to study the properties of air showers in addition to the ones from SD, FD and MD. The radio signals are solely produced by the electromagnetic component of the shower and provide complementary information to measurements of the all-particle and the muon dedicated detectors.

The radio emission is caused by two main mechanisms. The first mechanism is the geomagnetic effect, which accounts for 80 % to 90 % of the emission. The electrons and

---

[22] Auger Muon Detectors for the Infill Ground Array

[23] Muon detector

positrons in the shower are deflected in opposite directions by the Earth's magnetic field. The charge separation induces a drift current transverse to the shower axis, which varies with time as the number of electrons and positrons changes during the shower development. The second mechanism, called Askaryan effect, is due to a charge excess over time. During the shower development, the shower front develops a negative net charge excess, leaving a positively charged plasma behind. The induced current is along the shower axis. The Askaryan effect is subdominant in air and accounts for about 10 % to 20 %.

The AERA[24] was incorporated into the observatory in 2009 at the location of the SD-750. The array currently consists of 153 antennas and covers an area of 17 km^2 [46]. Different antenna types operate in the frequency range of 30 to 80 MHz and various spacings and trigger systems are studied at the moment. One of the antenna realizations, a butterfly antenna, is shown in Fig. 1.13b. The detector is operated in hybrid mode with the other detectors and current results are found in [47–49].

1.2.5 Upgrades to the Observatory

The general goal of the ongoing upgrade to AugerPrime is the improvement of the mass composition sensitivity. The best option to achieve this improvement is the usage of SD measurements due to the high duty cycle of almost 100 %. A decomposition of the all-particle signal as measured with the SD stations into electromagnetic and muonic components on a shower-to-shower basis enables the extension of the composition measurement into the region of the flux suppression as well as the enhanced estimation of the primary mass on a single event basis. Improvements are also expected for composition-based anisotropy studies, the discrimination between hadronic primary particles and neutrinos/photons and for understanding the discrepancy of the muon content in data with respect to simulations. The upgrade includes four components.

In the first component, the existing WCDs will be equipped with scintillator detectors (SSD[25]) atop, as is shown in Fig. 1.14b. While the WCDs are most sensitive to the muons in the shower, the SSD detector will be sensitive to the electromagnetic shower component. The difference in the detector responses enables the determination of the signal contributions from muons and electromagnetic particles and thus the reconstruction of the muon number. The installation of the scintillators started in October 2016 and the engineering array consists of 12 upgraded stations to date.

Another method to derive the muon number is the usage of buried detectors as already realized by the MD. Due to the shielding by the soil, the electromagnetic shower component is absorbed and the signal measured by the MD is the pure muonic signal. The muon number is measured directly and can be compared to the results obtained from the SSDs. Therefore, the second upgrade component is the expansion of the MD to 61 detectors.

In the third part of the upgrade, each WCDs will be equipped with a fourth PMT. The installation of this *small PMT* will extend the dynamic range from 600 VEM to 30 000 VEM [50]. The larger dynamic range will reduce the number of events with saturated stations at the highest energies from about 40 % to 2 %. This will improve the reconstruction accuracy of the shower-size estimator S_{1000} (see Section 2.5) and ultimately the event selection based on energy.

The last planned upgrade is dedicated to the FD. The current duty cycle is limited to about 19 % for perfect operating conditions. Due to bad weather, power cuts or malfunctioning, this nominal value is reduced to 15 %. The aim of the upgrade is the extension of the FD operations into hours of increased night sky background. The operation during times with

---

[24] Auger Engineering Radio Array

[25] Surface Scintillator Detector

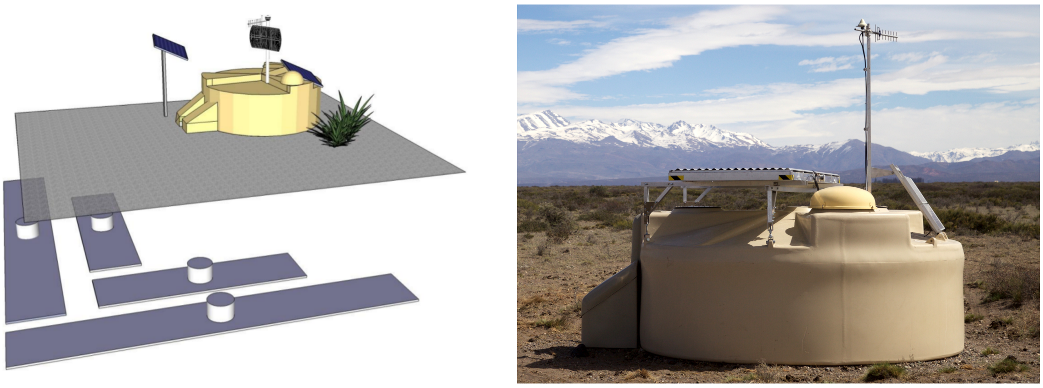

(a)

(b)

Figure 1.14: (a) Schematic of the AMIGA setup. An SD station is paired with underground muon detectors. (b) Scintillator on top of a water-Cherenkov station as part of the upgrade to AugerPrime.

higher PMT illumination will be achieved by lowering the PMT gain to prevent irreversible damages. The current setup is already suited to switch between different gains, allowing the operation of the PMTs at both the nominal and the adjusted gain.

CHAPTER

2

Reconstruction of Air Showers of UHECRs

The Pierre Auger Observatory applies a hybrid technique to record air showers. As introduced in Section 1.2, the hybrid approach utilizes a surface detector (SD) and a fluorescence detector (FD). The signals of the SD are calibrated to the energies measured by the FD in a marginal simulation-dependent way. Using the FD measurements for calibration sets the overall energy scale. More details on the calibration are given in Section 4.5. Although the calibration uses hybrid events denoting events that are well reconstructed by both, the SD and FD, the reconstruction procedures of air showers for the two detectors are completely independent of each other. For this work, the SD reconstruction method is the important one and will be introduced in the following.

When an air shower hits the ground, it leaves a footprint of SD signals on the array, as displayed in Fig. 2.7a. This footprint is dependent on the energy of the primary particle as well as on its incident angle. The higher the energy and the higher the zenith angle, the larger the footprint will be. The individual SD stations are equipped with hardware as well as software triggers to identify signals produced by candidate showers. Background signals produced mainly by random single atmospheric muons stemming from low energetic showers are discarded by the spatial and temporal combination of the individual station triggers. The different trigger algorithms implemented on each SD station are described in Section 2.1.1. The combination of the local station triggers to an array trigger validating a physics event is detailed in Section 2.1.3. The last level of the trigger hierarchy is comprised by a fiducial trigger as outlined in Section 2.2. This trigger ensures a high quality reconstruction and its application depends on the performed analysis. Extensions were performed as part of this work to its hitherto implementation in the $\overline{\text{Off}}\underline{\text{line}}$ software and are presented in Section 2.2.2. The $\overline{\text{Off}}\underline{\text{line}}$ framework was developed within the Pierre Auger Collaboration to reconstruct and simulate air showers using the Observatory's layout. Emphasis is laid on the application to the SD as this is the most important detector used within this work. First, the impact point on the ground and the arrival direction of the air showers are determined by means of approximating the shower geometry with a simple plane, as described in Section 2.4. Afterwards, the measured signals of the selected event stations are fit with a lateral distribution function (LDF), as outlined in Section 2.5. With the help of the LDF, the expected signal can be inferred at any given point from the shower axis except very close to the core. The expected signal at a particular distance to the reconstructed shower axis is then used as an estimator for the energy of the primary particle. Details on this are stated in Chapter 4.

2.1 Trigger and event selection

A hierarchical trigger structure is implemented on the array in order to distinguish air shower events from chance events [51]. Individual stations need to fulfill certain spatial and temporal selection criteria to form an event or be considered as part of such. The different level of the trigger and their associated selection criteria will be described in the following sections.

2.1.1 Local station triggers

The lowest trigger level is built by the hardware triggers implemented on each local station. This T1 trigger is realized by four, partially complementary, modes.

- Threshold trigger (Thr1): requires a coincident signal of at least 1.75 VEM in all three PMTs and selects mainly short signals coming from muons. It is therefore relevant for very inclined showers.

- time-over-threshold trigger (ToT[1]): asks for 13 FADC bins above 0.2 VEM in a time window of 3 µs in at least two PMTs. Due to its selection on signals spread in time, it is more sensitive to the electromagnetic component of a shower. It is the relevant trigger for nearby but low energy showers or high-energetic showers with a distant core.

- ToT-deconvoluted trigger (ToTd[2]): improved ToT using a deconvolution of the time traces [52, 53]. A single short peak always has an exponential tail with a decay constant of about 70 ns and therefore a non-negligible probability to fulfill the condition of a time-dispersed signal exceeding a certain threshold. To limit the amount of background signals wrongly counted as true shower signals a deconvolution of the exponential tail is performed. The deconvoluted trace d_i is obtained from the FADC trace a_i by

  $$d_i = \frac{a_i - f a_{i-1}}{1 - f} \qquad \text{with} \quad f = \exp(\Delta t/\tau),$$

  where Δt denotes the time unit of an FADC bin and τ is the decay time. This method deconvolutes the signal produced by several particles spread in time to a sequence of short peaks, whereas a background signal is converted to one or two FADC bins over threshold. Hence, a counting algorithm of how many bins exceed a certain threshold can be used after the deconvolution to trigger only on real shower signals.

- multiplicity-of-positive-steps trigger (MoPS[3]): the trigger algorithm counts the number of subsequent positive steps within an FADC trace that exceed a certain threshold within a sliding time window [54]. To discard background signals stemming from through-going muons, an upper limit of 30 FADC units is chosen for the step height. To avoid false-positive step counts introduced by fluctuations in the tail of large signal peaks, a veto is implemented after a large step. These trigger conditions allow for the detection of signals below the VEM level as introduced by electromagnetic particles.

---

[1] time-over-threshold trigger

[2] time-over-threshold deconvoluted trigger

[3] Multiplicity of positive steps

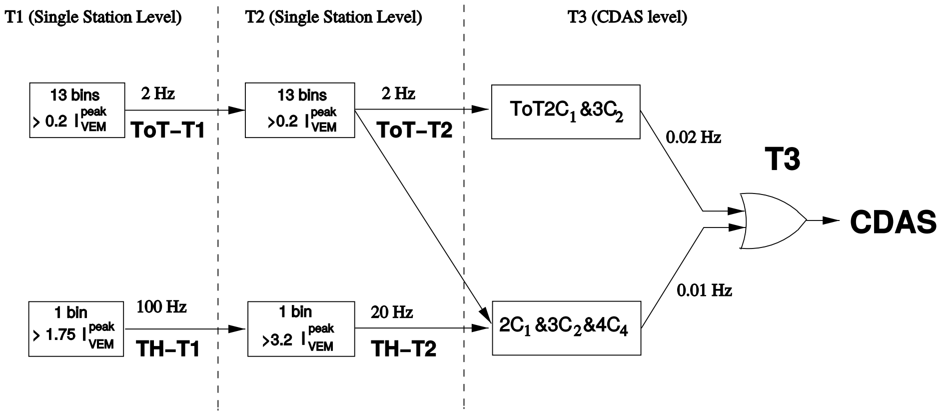

Figure 2.1: Schematic of the SD trigger hierarchy. An array trigger is obtained by the spatial and temporal combination of the local station triggers [51].

The two latter trigger modes have been designed to be most sensitive to the electromagnetic part of the shower. The primary background for the signal measurement in individual stations is made of accidental muons, which are not part of the recorded shower. Being insensitive to this background, the new triggers are able to record smaller signals. This allows for measuring low energetic showers and the energy spectrum can be extended towards energies around the second knee [55]. The two new trigger modes have been fully implemented on the array since June 2013 and stable trigger rates have been measured since January 2014.

Although the new triggers are listed in the following general description of the event recording, they are not used as candidate stations for the shower reconstruction in this work. Within this work, the stations which only fulfill a ToTd, a MoPS or both but no ToT or Thr[4] trigger in addition are treated as silent stations. The new triggers are not established as standard triggers throughout Auger at present. Nevertheless, they are of great potential for lowering the threshold of full efficiency of the SD-750 array and the SD-433 array.

The next trigger level (T2) is a stricter version of the T1 trigger. In order to promote a T1-Thr to a T2-Thr all three PMTs must exceed a signal threshold of 3.2 VEM, whereas all other T1 triggers are promoted directly. This criterion reduces the event rate of a station to an acceptable value of 20 Hz that is sufficient to cope with the bandwidth of the communication system. All T2 triggers are sent to the CDAS where the individual station triggers are evaluated to form an array trigger. The hierarchical trigger system is illustrated in Fig. 2.1.

2.1.2 Central data station triggers

The T3 trigger is formed at the CDAS and performs the spatial and temporal combination of the individual T2 station triggers to determine all stations that belong to a potential air shower event. In order to be sensitive to vertical ($\theta < 60°$) as well as to inclined ($\theta > 60°$) showers, two station patterns are allowed:

- 3-fold mode: requires the coincidence of three stations that fulfill a minimum of compactness, namely, selecting a central station, the two neighboring stations must be part of the first two crowns around it. The distance of the stations determines the permitted time window. Each T2 has to happen within $(6+5C_n)$µs to the first one, with C_n denoting the crown number. Only ToT, ToTd and MoPS are allowed as individual station triggers. This mode is suited to mostly select vertical showers.

---

[4] threshold trigger

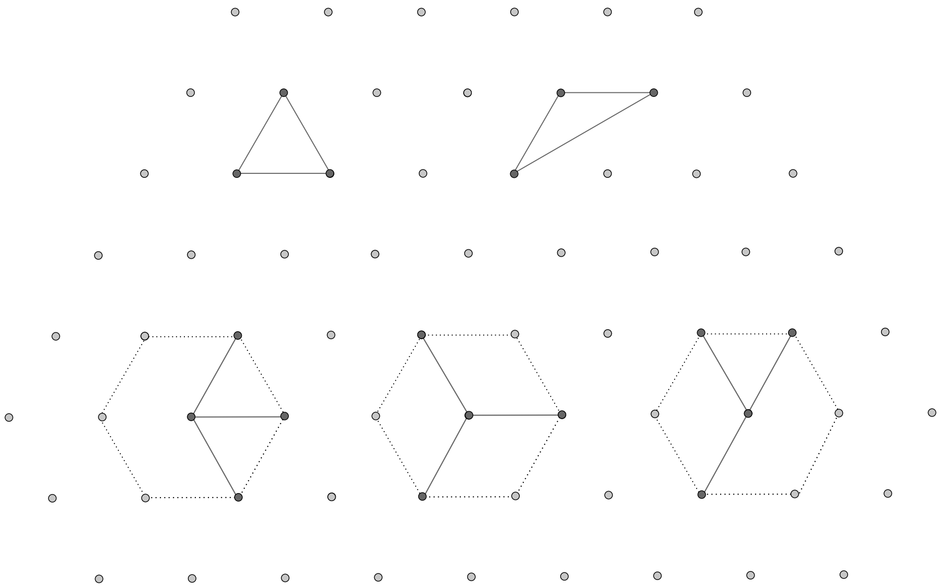

Figure 2.2: Example of T4 trigger configurations. The three-fold mode is shown in the upper part. The three stations have to build a non-aligned set with an equilateral or isosceles base triangle configuration. In the lower part the three minimal four-fold configurations are shown. Three stations have to trigger in the first crown around the central station in a non-aligned way (based on [56]).

- 4-fold mode: requires the coincidence of four stations fulfilling any kind of T2. The spatial compactness is more permissive, allowing the fourth station to be part of the fourth crown around the central station instead of the second crown. For the temporal condition the same logic is used as in the three-fold mode. Due to its looser distance requirements this trigger mode will select mainly inclined showers with zenith angles larger than 60°.

Once a T3 is found, all remaining T2 triggers are sent to the CDAS and stations only fulfilling a T1 trigger are read-out in addition if they triggered within 30 µs from the T3. Only events that pass one of the T3 criteria are stored for later analyses.

2.1.3 Physics event selection

To further distinguish between real air shower events and accidental or lightning events, a stricter version of the T3 trigger is applied on the stored data. The three-fold mode of this T4 trigger requires three nearby stations that either fulfill an equilateral or an isosceles base triangle configuration as depicted in the upper part of Fig. 2.2. All three stations must pass the T2-ToT. A less tight criterion requires four non-aligned stations with the central station being surrounded by three stations lying in the first crown. Three example configurations are shown in the bottom part of Fig. 2.2. The stations can fulfill any T2 trigger. In both modes the trigger times of the individual stations must fit to a planar shower front moving with the speed of light.

2.2 Quality trigger

The last trigger level is a fiducial trigger as it requires the station with the highest signal, also referred to as hottest station, to be surrounded by six active stations. Applying this trigger condition guarantees the selection of events that are well contained in the array. Even

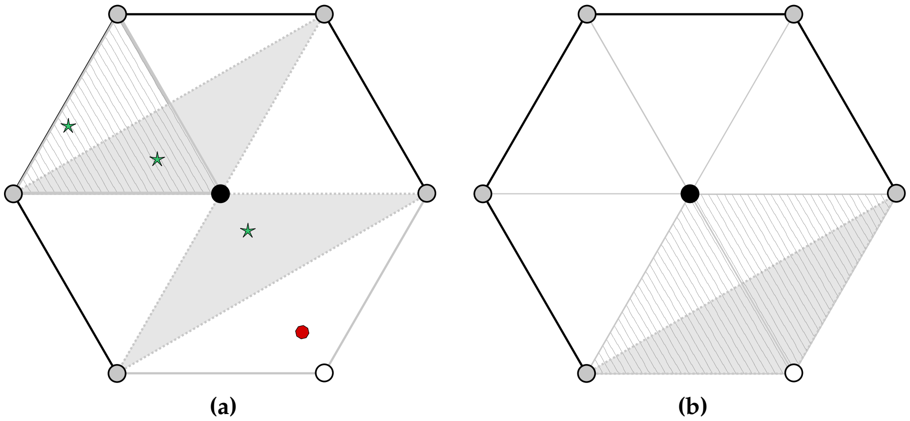

Figure 2.3: (a) Schematic of the T5 posterior configuration. The station with the largest signal (black) is here surrounded by 5 functioning stations (gray). The missing station is visualized with an unfilled marker. The reconstructed shower core of the event must fall either in an equilateral triangle (dashed area) or an isosceles triangle (shaded area) to be accepted (green stars), with the hottest station being always part of the triangle. Also allowed are T5 posterior triggers with only four surrounding stations. The core position indicated by the red polygon is not accepted. (b) Difference in excluded trigger area for a 5T5 trigger. The dashed area indicates the discarded trigger area prior to this work and the shaded area denotes the rejected area after the implementation of the isosceles triangles. Figures taken from [57].

though detector maintenance is provided on a regular basis, about 1 % of the stations are expected to be not functioning at any moment. Therefore, not only events that fall too close to the periphery of the array will be discarded by this trigger cut but also events including a malfunctioning station around the hottest station are rejected. Both event types show biases in the core reconstruction and their energy assignment as part of the signal information gets lost due to the missing or inactive stations. A side-effect of applying the quality trigger cut is the saturation of the effective detector area above a certain energy, hence becoming equal to the geometrical area. The shower footprint on ground scales with the primary energy. As a consequence, showers landing outside of the array can still trigger a sufficient amount of stations to allow for a reconstruction, leading to an increase of the detector acceptance with increasing energy without the cut. Two trigger modes have been realized in the past within the $\overline{\text{Off}}\underline{\text{line}}$ software. The first mode is a pre-reconstruction trigger, asking the hottest station to be the central station within an active hexagon, hence it is denoted as 6T5 trigger (*T5-prior*). The second mode implies conditions on the reconstructed core and as such works as a post-reconstruction trigger (*T5-pos*). This mode requires the reconstructed core to lie within an active equilateral triangle and the number of active stations within the surrounding hexagon of the station with the highest signal is allowed to decrease from six to four stations.

2.2.1 Station quality selection

The availability of each station is monitored by the rate of T2 triggers that are sent to CDAS. For an active station this rate is about 20 Hz. Only active stations are allowed in the reconstruction of events with $\overline{\text{Off}}\underline{\text{line}}$ as well as in the determination of the various trigger conditions. A proper rejection status is assigned on an event-by-event basis if a station is malfunctioning. While a station with a rejection status is not taken into account for the reconstruction of an event, there are some rejection statuses that are still acceptable for the fiducial trigger as the station is in principle operating:

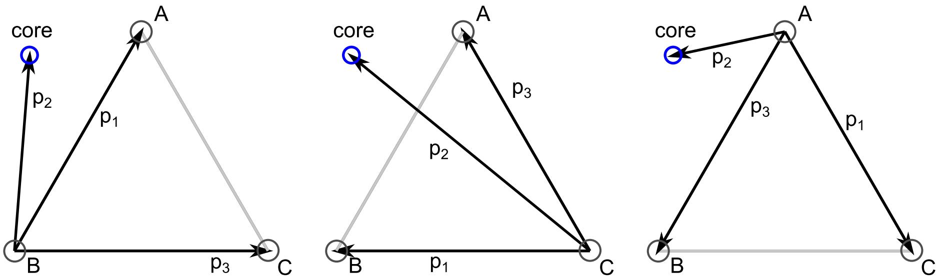

Figure 2.4: Schematic for calculating the active triangle [57]. Events with the reconstructed core position as shown here would be discarded as the core is not contained within the triangle.

- out of time: the trigger timing of the station does not fit to a shower plane moving with the speed of light
- random trigger
- lonely: the station exceeds certain distances to the next shower candidate station
- ToTd or MoPS: the station fulfills only a new trigger

The distinction between *T5-prior* and *T5-pos* is due to a rejection status that can only be assigned during the reconstruction. In general, stations that are considered to be active for an event and have no rejection status assigned are set to silent if they exhibit no trigger. During the fit of the lateral distribution function LDF[5] (described in Section 2.5) such a silent station is flagged as *bad silent* if it is closer to the core than a certain distance and its expected signal exceeds a fixed threshold. It is considered to be highly unlikely for the station to not observe a trigger, indicating a kind of malfunction that stayed undetected by CDAS.

2.2.2 Active triangles

To decide whether the reconstructed shower core lies within an allowed triangle, the hottest station and its surrounding hexagon have to be determined first. Afterwards, all possible triangles, either equilateral or isosceles, including the hottest station as one corner station are calculated. As the individual stations have a slightly different altitude, each triangle spans its own plane. The reconstructed core has to be projected onto this plane along the shower axis to check whether it is contained in the examined triangle. A schematic of the core position check with respect to the triangle is shown in Fig. 2.4. For all three station positions it is calculated whether the vector $\vec{p}_2$ from one station position to the core position lies in the plane spanned by the vector from this position to the remaining two station positions, i.e the plane spanned by $\vec{p}_1$ and $\vec{p}_3$. This is not the case for the core position drawn in Fig. 2.4. As part of this work, the isosceles base triangle has been added to $\overline{\text{Off}}\underline{\text{line}}$. An example for accepted core positions can be found in Fig. 2.3a, illustrated as star positions. The core position marked in red within the isosceles triangle that is spanned by two active and one missing hexagon stations is discarded.

2.3 Signal uncertainties

The measurement of air showers is always object to statistical and systematic uncertainties. A precise study of these uncertainties is necessary to guarantee a valid air shower reconstruction and to assign proper uncertainties to the reconstructed quantities.

---

[5] lateral distribution function

2.3.1 Shower-to-shower fluctuations

Any particle interaction is subject to statistical fluctuations. As a consequence, the showers induced by two primary particles with the exact same energy, mass and arrival direction will differ even though they were initiated with the same primary quantities and propagate through the very same atmosphere. The differences increase when dealing with a non-ideal detector as the atmosphere as well as the background radiation are constantly evolving. The typical size of these shower-to-shower fluctuations is estimated to 10 %. However, these fluctuations affect all stations within a shower in the same way and as such do not need to be considered on the level of the event reconstruction.

2.3.2 Sampling fluctuations

The signal measurements can only be performed up to a certain accuracy due to the sampling nature of the detector. An estimation of the accuracy is obtained by analyzing the signals as measured by so-called multiplet stations. These are stations that are only about 11 m apart which is a negligible distance when compared to the footprint of the whole shower. Except for events where the core lands close to such a multiplet and the particle density grows steeply when approaching the core, the multiplets are considered to measure the same spot in the shower. Following this assumption, the difference in their signals determines the uncertainty of the signal measurement for the whole array. The uncertainty is related to the number of particles hitting the station and therefore decreases with increasing signal. Furthermore, the uncertainty depends on the ratio of the electromagnetic to the muonic component. The same signal can either be induced by a few muons or a larger amount of electromagnetic particles as discussed in Section 2.5. The current parameterization relates to the changing ratio by its dependence on the secant of the zenith [58]:

$$f_S := \frac{\sigma[S]}{\sqrt{S}}(\theta) = 0.865(1 + 0.593(\sec\theta - 1.22)). \tag{2.1}$$

2.4 Geometry reconstruction

The aim of the reconstruction of air showers is the determination of the energy and the arrival direction of the primary UHECR. The latter is achieved by a fit of the shower geometry, whereas the energy is inferred from an expected signal at a certain distance to the shower axis that serves as an estimator for the primary energy, as explained in Section 2.5.

The standard reconstruction is based on a bottom up selection algorithm, starting with the selection of a seed of stations. First, all stations that fulfill either the three-fold or the four-fold mode of the T4 trigger (Section 2.1.3) are selected as possible seed stations. Secondly, the station set that maximizes the sum of the individual signals is used as seed. The trigger times of these stations are fit to the shower front propagating at the speed of light c along the shower axis $\hat{a}$:

$$c(t_0 - t) = (\vec{x}(t) - \vec{b})\hat{a}. \tag{2.2}$$

The weighted time average is used as time origin t_0 and the signal weighted barycenter of the stations determines the spatial origin $\vec{b}$. The signal start times of all stations not belonging to the seed are then compared to the expected time for the shower to arrive at the individual stations. Stations with times not compatible within a certain margin are flagged as *accidental* and are discarded in the following reconstruction steps.

If there are at least four triggered stations in the event and the fit of an LDF was successful, the more realistic model of a spherical shower front (depicted in Fig. 2.5a) is fit subsequently.

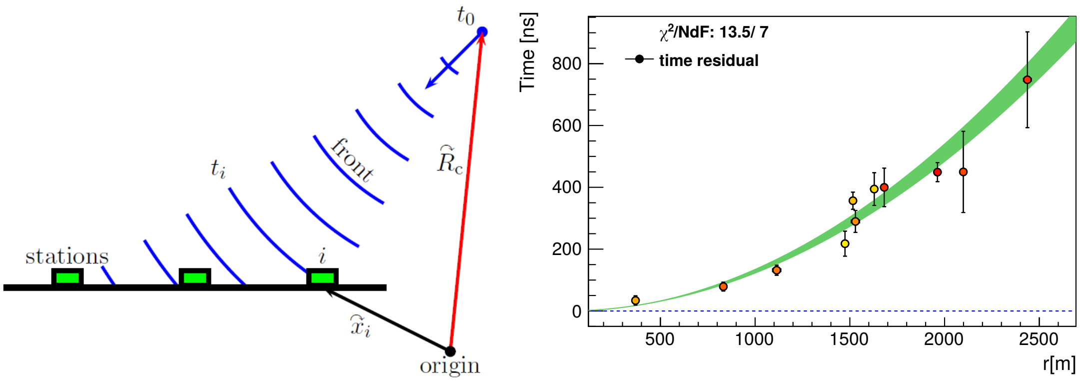

(a) **(b)**

Figure 2.5: (a) Schematic of the arrival of a spherical shower front at ground. (b) Time distribution fit of a curved shower front to the measured signal times (Event time: 02. January 2017, Auger Id: 170016437700).

A sphere develops after the first interaction of the primary particle in the atmosphere, originating from the virtual point $\vec{R}_c$ at the time t_0:

$$c(t_i - t_0) = |\vec{R}_c - \vec{x}_i|, \tag{2.3}$$

with $\vec{R}_c = \vec{c} + R_c\hat{a}$ and R_c being the radius of curvature. The impact point $\vec{c}$ of the shower axis on ground, in the following denoted as (shower) core, has to be estimated beforehand. The individual trigger times t_i and station positions $\vec{x}_i$ serve as input for the fit. The system of equations can be solved by a linear approximation, which then serves as input for a non-linear fitting routine using MINUIT-2.

2.5 Lateral distribution function

The SD array works as a sampling detector and to infer a proper estimate for the primary energy, the lateral distribution is fit. A first estimate inferred from the fit is the expected signal at an optimal radial distance, which depends on the actual spacing of the array. The optimal distance is determined as the distance that depends least on the functional form used for the LDF and hence the expected signal at this distance results in a robust estimate.

The lateral dependence of the signals measured on the ground is described by

$$S(r) = S(r_{\text{opt}}) f_{\text{LDF}}(r). \tag{2.4}$$

A modified Nishimura-Kamata-Greisen (NKG) function provides the best description of the data measured by Auger:

$$f_{\text{LDF}}(r) = \left(\frac{r}{r_{\text{opt}}}\right)^{\beta} \left(\frac{r + r_{\text{scale}}}{r_{\text{scale}} + r_{\text{opt}}}\right)^{\beta+\gamma}. \tag{2.5}$$

The distance parameter r_{opt} refers to the aforementioned optimal distance and is strongly dependent on the grid spacing. It was estimated to be 1000 m and 450 m for the SD-1500 and the SD-750, respectively [59, 60]. The signal estimate at the optimal distance $S(r_{\text{opt}})$ is also referred to as shower size and is denoted by S_{1000} for events measured with the SD-1500 or S_{450} in case of the SD-750. The parameters β and γ determine the slope of the LDF and depend on the zenith angle. The scale parameter r_{scale} is set to 700 m for both arrays. Besides the spectral index γ, it allows for more flexibility far from the core where the lateral distribution is mainly dominated by muons.

The likelihood function for estimating the LDF reads as follows:

$$\mathcal{L} = \prod_i f_P(n_i, \mu_i) \prod_i f_G(n_i, \mu_i) \prod_i F_{\mathrm{sat}}(n_i, \mu_i) \prod_i F_{\mathrm{zero}}(n_i, \mu_i) \tag{2.6}$$

with n_i being the effective particle number detected in a station and μ_i is the theoretical LDF expectation. The usage of an effective particle number is necessary as the WCD itself only provides information about PEs[6] that are induced by Cherenkov photons. The actual number of particles that induce a certain signal remains unknown. It is dependent on the type of the secondary particles, their incident angle as well as on the distance of the station to the shower core. At large zenith angles or far away from the core, the signal in a station is dominated by muons as the electromagnetic shower component suffers from attenuation in the atmosphere. The mean signal of one VCT[7] muon is 1 VEM and as a result the effective particle number to produce this signal approaches one. At low zenith angles, the electromagnetic component is important. However, about 20 particles are needed to produce an equivalent signal of 1 VEM, so the effective particle number increases as can be seen in Fig. 2.6b. The effective number is obtained by:

$$n_{\mathrm{eff}} = p(S/\mathrm{VEM}), \tag{2.7}$$

with the Poisson factor p described as:

$$p = t + \frac{1-t}{\sqrt{f_S}}. \tag{2.8}$$

Here, $t := 1/(1+e^z)$ and $z := 40\,(0.98 - f_S)$, depending on the signal uncertainty f_S which itself is parameterized as [58]:

$$f_S := \frac{\sigma[S]}{\sqrt{S}}\,(\theta) = 0.865\,(1 + 0.593\,(\sec\theta - 1.22)) \tag{2.9}$$

The three contributions of the function cover *non-saturated* signals, *saturated* signal and *non-triggered* signals. the non-saturated signals themselves are split into two cases:

- Small signals use Poissonian statistics, i.e. $f_P(n_i, \mu_i) = \frac{\mu_i^{n_i} e^{-\mu_i}}{n_i}$.
- Large signals make use of the central limit theorem that allows for the Gaussian approximation for signals with $S_i \geq S_{\mathrm{th}}^{\mathrm{G}} = 15\,\mathrm{VEM}$. As such, these signals are described by $f_G(n_i, \mu_i) = \frac{1}{\sqrt{2\pi}\sigma_i} \exp\left(\frac{(n_i-\mu_i)^2}{2\sigma_i^2}\right)$.
- Saturated signals can sometimes be recovered. The distribution of the recovered signals is shown in Fig. 2.6a. In such cases, the recovered signal is used in the Gaussian approximation and the uncertainty of the saturation recovery is added to the signal uncertainty. In cases where the recovery fails, the saturated signal, n_i, serves as lower limit on the actual signal. To obtain the probability of measuring a signal larger than the saturated one, the Gaussian approximation is integrated over all possible values larger than n_i, i.e. $F_{\mathrm{sat}}(n_i, \mu_i) = \frac{1}{2}\mathrm{erfc}\left(\left(n_i - \mu_i\right)/\sqrt{2}\sigma_i\right)$. Here, the complementary error function $\mathrm{erfc} = 1 - \mathrm{erf}(x)$ is used.

---

[6] photo-electrons

[7] vertical centered through-going

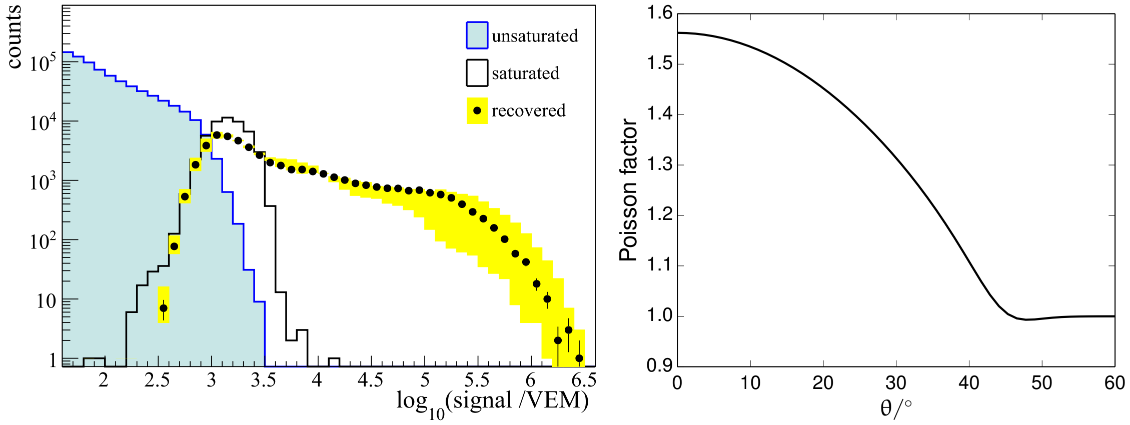

(a) **(b)**

Figure 2.6: (a) Spectrum of measured signals in 5T5 events. Shown are three different signal categories. The blue-shaded area corresponds to unsaturated signals and the black histogram gives the distribution of the saturated signals. The black circular markers denote the signals which could be recovered and the yellow band gives the systematic uncertainty. The recovered signal spectrum matches the spectrum of the unsaturated signal below 10^3 VEM [62]. (b) The Poisson factor as function of zenith angle [63]. This factor is used to convert the measured station signals into an effective particle number as explained in the text.

- Zero signal stations are stations whose signals do not exceed a certain threshold to form a trigger. For the standard triggers ToT and Thr this threshold is assumed to be 3 VEM. The later introduced triggers ToTd and MoPS are triggering at about 1 VEM. The non-triggered stations are included in the likelihood by summing up their Poissonian probabilities with an expected signal μ_i and an actual signal $n_i \leq n_{\text{th}}$: $F_{\text{zero}}(n_{\text{th}}, \mu_i) = \sum_{n=0}^{n_{\text{th}}} f_P(n, \mu_i)$.

The actual fit is done by minimizing the (negative) log-likelihood function:

$$\ln \mathcal{L} = \sum_i \ln f_P(n_i, \mu_i) + \sum_i \ln f_G(n_i, \mu_i) + \sum_i \ln F_{\text{sat}}(n_i, \mu_i) + \sum_i \ln F_{\text{zero}}(n_i, \mu_i). \quad (2.10)$$

Besides the three LDF parameters $S(r_{\text{opt}})$, β and γ, the impact point on ground and the arrival direction are fit. Hence, the number of parameters that need to be fit increases to at least eight. The convergence of the fit is improved by using an iterative procedure, splitting the fit into different stages in which some of the parameters are fixed either to estimates (e.g. $S(r_{\text{opt}})$ is estimated from the signal in the station closest to the optimal distance) or to values obtained in previous parameterizations. This reduces the number of free parameters that need to be fit. For this work, the slope parameters β and γ are always fixed to previous parameterizations. For the SD-1500, the slope parameters were obtained by analyzing a set of events with large station multiplicities [61], whereas the parameters for the SD-750 stem from a global event fit as described in [60]. However, it is possible to free the slope parameters within the $\overline{\text{Off}}\underline{\text{line}}$ reconstruction by changing the number of required candidate stations within an event. A minimum of four candidate stations is always required for a free slope fit.

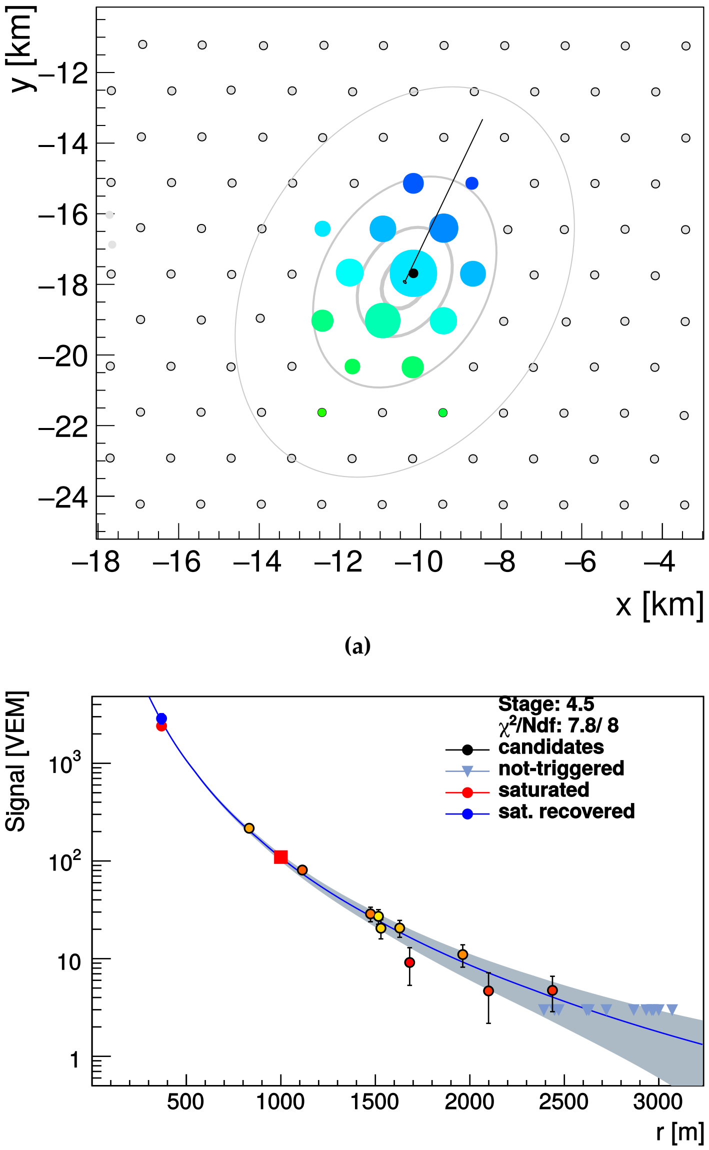

(a)

(b)

Figure 2.7: (a) Example footprint of an air shower as measured by the SD-1500. Triggered stations are visualized by colored circles with the timing ranging from blue for early trigger times to green for late ones. The signal size is encoded by the size of the circles. The x- and y-axes represent east and north, respectively. The reconstructed arrival direction is indicated by the solid black line. (b) Lateral distribution fit to the measured signals of an SD-1500 event with a reconstructed energy of 2.52×10^{19} eV and a zenith angle of 41.7° (Event time: 02. January 2017, Auger Id: 170016437700). The signal size at 1000 m, referred to as shower size, is visualized by the square marker in red. Both figures are taken from the EventBrowser of Offline.

CHAPTER

3

Monte Carlo Studies

The air shower simulations used within the scope of this work use the Monte Carlo framework Corsika [64]. This code handles the development of air showers in the atmosphere, simulating the interactions and decays of the particles. The models to describe the hadronic interactions in the context of cosmic rays differ depending on the energy of the interactions. For the low-energy interactions below 200 GeV the FLUKA model is used as standard model [65]. High-energetic interactions can be modeled by three different Monte Carlo event generators, namely QGSJet-II.04 [66], Epos-LHC [67], and Sibyll-2.3 [68], all of which have been tuned to the LHC data. The first two models are Regge-Pomeron based models, while the latter one uses a mini-jet approach [69] (and references therein). The use of interaction models is fraught with uncertainty as no man-made accelerator can reach the energies occurring in air showers. Nevertheless, the models describe the existing air shower data well and can be used as crosscheck for parameterizations derived from data alone. In this chapter the energy resolution of the detector as well as the trigger efficiency of the array are analyzed. The focus lies on the analysis of the SD-1500 array.

3.1 Reconstruction accuracy

The SD observable that is related to the energy as measured by the FD is the shower size $S(r_{\text{opt}})$. It is determined during the fit of the LDF together with the core position, as described in Section 2.5. A correct shower size estimation is dependent on a correct core reconstruction. The current implementation of the LDF within $\overline{\text{Off}}\underline{\text{line}}$ assumes a cylindrical symmetry around the shower axis. The detection of showers suffers from attenuation in the atmosphere as well as from geometrical projections on ground, both dependent on the zenith angle (see Fig. 3.1). These asymmetries push the reconstructed core towards the early part of the shower as the signal density is higher for this region. The bias in the core position increases with zenith angle as depicted in Fig. 3.2. Here, the bias in the reconstruction of the core position is shown for the two primaries proton and iron for energies of $10^{18.5}$ eV, 10^{19} eV, $10^{19.5}$ eV and two dedicated zenith angles. The core bias is inferred from the difference of the reconstructed core position to the Monte Carlo position. The showers are rotated in azimuth so that the incoming direction is to the right. The core shift towards the early part of the shower is

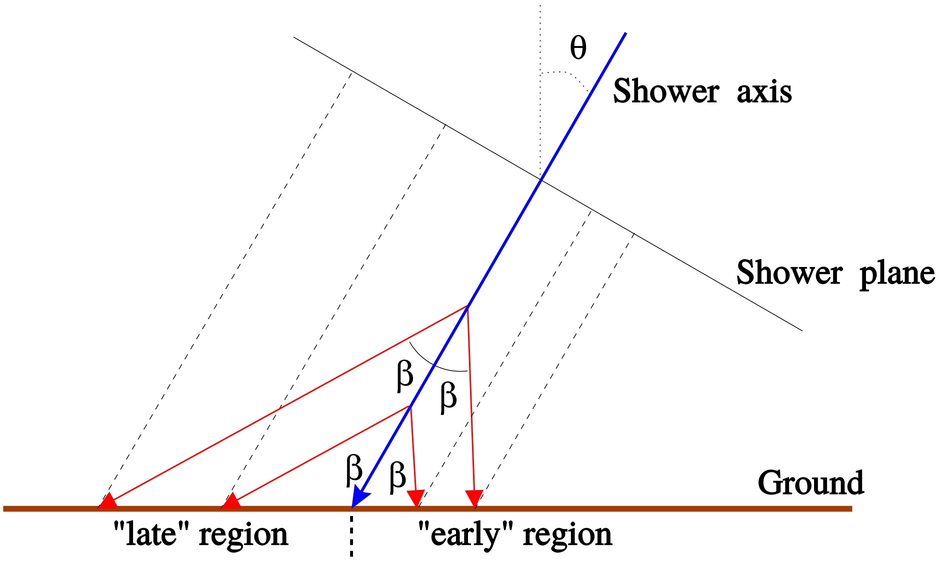

Figure 3.1: Schematic illustrating the geometrical asymmetry induced by the projection of the particle densities on ground onto the shower plane. Figure taken from [70].

visible for the higher zenith angle due to the increase of traversed atmosphere and hence the increase of attenuation.

The accuracy of the shower size is estimated using showers simulated with the fixed library as described in Appendix A.1. The reconstructed shower size as obtained from the LDF fit is compared to the mean signal of a set of stations located on a ring at 1000 m around the shower core in shower plane coordinates. The dense stations of the ring are not included in the event reconstruction. In Fig. 3.3 only the stations at 90° and 270° are chosen as their signal is affected least by the asymmetry. The relative difference between the reconstructed shower size and the estimate for the true shower size is shown as function of zenith angle and for three different energies. The lowest energy corresponds approximately to the threshold energy of full efficiency. The trend of an increase in the reconstructed shower size with higher zenith angle is a result of upward fluctuations at the trigger threshold. Only the signals that fluctuate upwards are recorded and fit in the LDF. The difference between the reconstructed shower size and the measured signals at 1000 m is affected by the way the LDF fit is set up. The slope parameters are fixed within the reconstruction of the simulated showers to the parameterizations determined from data. The underlying primary distribution in data is a mixed one, so applying this to a pure composition is likely to lead to small differences. Due to the lower muon numbers in proton showers compared to iron ones, the LDF of a proton shower will be slightly steeper than an average data LDF.

3.2 Direct energy calibration and migration matrix

A caveat of the interaction models is that the Monte Carlo energy is not directly comparable to the energy obtained in data. This discrepancy could be the consequence of a lack of muons produced in simulated air showers. The Monte Carlo energy of each interaction model differs not only from data but also from the energy of the other models as they have different approaches on how to model the various interactions in hadronic collisions. To overcome this mismatch between the energy scales and reduce the dependence on the interaction models, the efficiency study performed in this chapter uses the energy estimate instead of the Monte Carlo energy. As the energy estimate is a reconstructed observable, events that

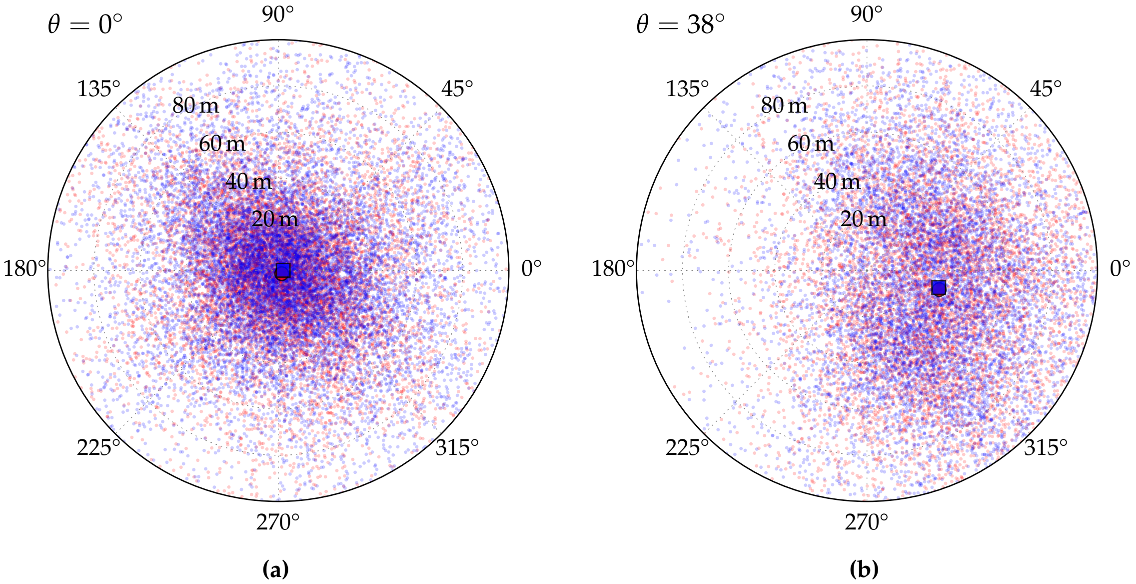

Figure 3.2: (a) Bias in reconstructed core position for proton (red) and iron (blue) primaries with a zenith angle of 0° and the energies $10^{18.5}$ eV, 10^{19} eV, $10^{19.5}$ eV. (b) Bias in the reconstructed core position for the same primaries and energies but a zenith angle of 38°. The bias increases for growing zenith angles due to the increase of traversed atmosphere.

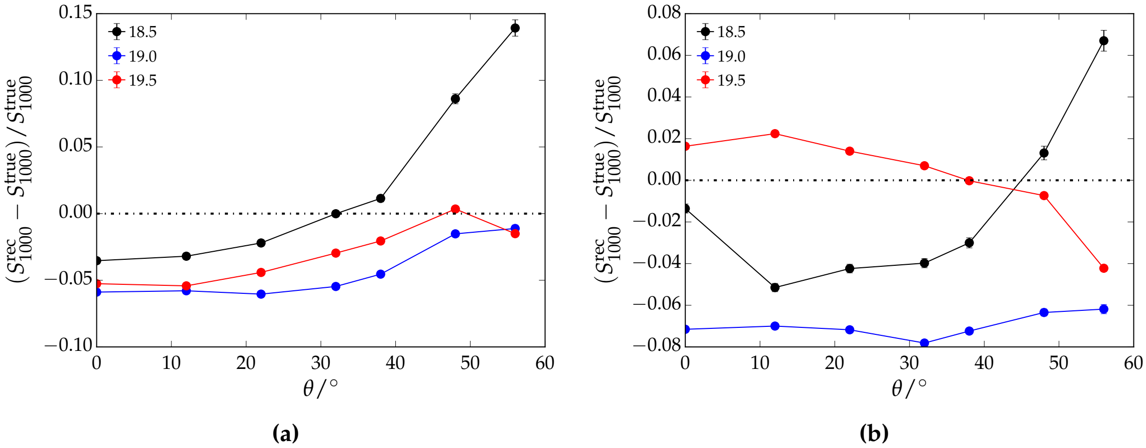

Figure 3.3: (a) Relative difference for the shower size derived from proton showers as function of zenith angle and for three different energies. (b) Relative difference for iron showers.

fail to trigger the array lack this information. Hence, an inverse energy calibration has to be performed in a first step to deduce the energy estimate from the true energy.

The events used in this analysis were selected with SD and FD quality cuts and in addition with a fiducial FoV[1] selection tuned with simulations. The FoV of a telescope is described in more detail in Section 4.5.1. Depending on the primary species, the shower maximum will develop deeper or shallower in the atmosphere. Due to the limited field of view of a telescope, a selection bias in the composition can arise. The FoV selection was introduced to overcome this bias. A result of this selection is that showers with low zenith angles are discarded. Each pure particle species is selected with the FoV cut derived for this species, whereas the 50/50

---

[1] field of view

mixed composition of proton and iron showers is selected with a cut deduced for a mixed composition. The applied FoV cuts were derived in a previous analysis within Auger. The FD energy of each event is calculated by taking the reconstructed calorimetric energy and multiplying it with the true invisible energy correction for this event. The resulting energy is denoted as $E^{\text{true}}_{\text{FD},i}$:

$$E^{\text{true}}_{\text{FD},i} = E^{\text{rec}}_{\text{cal},i} \frac{E_{\text{MC},i}}{E^{\text{MC}}_{\text{cal},i}}. \tag{3.1}$$

The reconstructed total FD energy in simulations is obtained by adding the missing invisible energy to the reconstructed calorimetric energy. However, the library of Appendix A.2, which is used in this analysis, uses an invisible energy correction derived for data. A correction of the pure primaries with the data model leads to an overestimation of the reconstructed energy for protons, whereas the energy of iron showers is slightly underestimated, as shown in Fig. A.6. To avoid this bias in the FD energy, the correction with the true invisible energy as stated in Eq. (3.1) is chosen.

The true energy estimate is inferred from the true energy, which refers either to the true FD energy $E^{\text{true}}_{\text{FD}}$ or the Monte Carlo energy E_{MC}. When using the true FD energy, any possible bias has to be studied first and corrected for. The bias study is performed by comparing the reconstructed calorimetric energy to the simulated calorimetric energy. As shown in Fig. 3.4, the bias is below 1 % for proton showers and below 2 % for iron showers. The bias is parameterized as function of the true calorimetric energy for energies above the full efficiency:

$$\Delta E = p_0 \left[\operatorname{erf} \left(\log_{10} E^{\text{MC}}_{\text{cal}} - p_1 \right)^2 - p_2 \right], \tag{3.2}$$

and the true reconstructed FD energy is corrected for this bias. Applying the correction function to the true FD energy leads to an unbiased FD energy as shown in Fig. 3.5 for the different compositions. The bias in the FD energy was first found in SD-750 simulations. As described in Section 4.5.3, the bias in the low FD energies is significantly larger and reaches about 5 % around the full efficiency threshold.

In the next step, only those events with $E_{\text{FD}} > 3\,\text{EeV}$ are selected for further analysis. These events enter the likelihood minimization, which is set up in the following way to simultaneously fit the inverse energy calibration and the resolution of the energy:

$$\log \mathcal{L} = \sum_i^n \log \mathcal{N} \left(E_{\text{rec,i}} | E_{\text{true,i}}, \sigma_{\text{tot}}(E_{\text{true,i}}) \right) \tag{3.3}$$

$$E_{\text{rec,i}} = A\, S^B_{\text{rec,i}} \qquad S_{\text{rec,i}} = S_{1000,i} / f_{\text{CIC}}(\theta_i) \tag{3.4}$$

$$E_{\text{true,i}} = A\, S^B_{\text{true,i}} \qquad S_{\text{true,i}} = a \left(E_{\text{t},i} / E_0 \right)^b , \tag{3.5}$$

with E_{t} either being the bias-corrected, true FD energy or the Monte Carlo energy. A normal distribution $\mathcal{N}$ is used and the sum runs over all n events of the simulated composition. A and B are the energy calibration parameters obtained from data, whereas the calibration parameters a and b are part of the fit. The reconstructed shower sizes are corrected for the attenuation in the atmosphere with f_{CIC}, which uses the same functional form as the attenuation function discussed in Section 4.4. The attenuation function is fit externally and is therefore not part of the global fit. The events entering the fit of the attenuation function are not selected with the fiducial FoV to not distort the zenith distribution. The validity of the fitted attenuation correction is checked in Fig. 3.8. Here, the two-dimensional event distribution for the attenuation-corrected energy estimate is shown. The color coding represents the deviation of the event number in a specific bin from the average number of events in a certain bin of the energy estimate. The deviation is given in units of standard

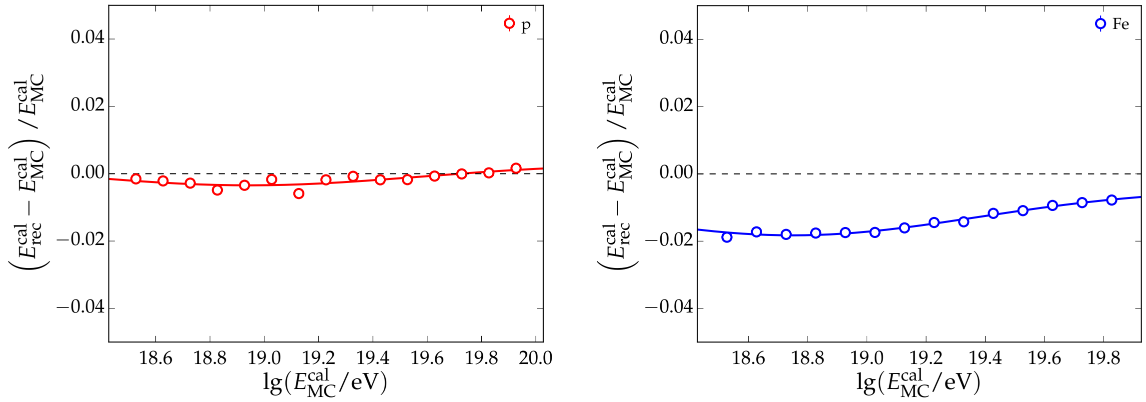

(a) proton **(b)** iron

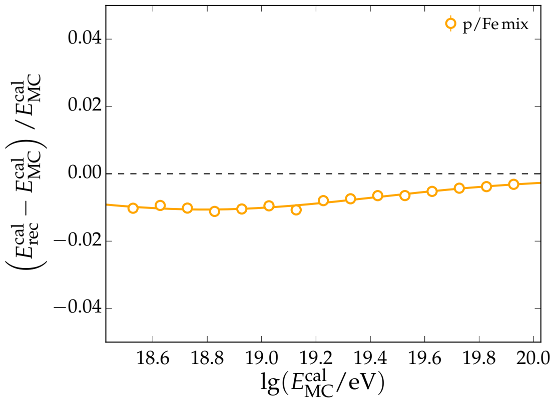

(c) p/Fe mix

Figure 3.4: Bias in the calorimetric energy estimated for (a) proton and (b) iron induced showers as well as for (c) a mixed composition.

deviation σ_{stat}. A detailed description of the attenuation correction is given in Section 4.4. The two-dimensional event distribution for the different primary species shows no significant deviation from a uniform distribution above the chosen threshold value of $S = 40\,\mathrm{VEM}$. The assumed model for the energy resolution included in the fit is the following:

$$\frac{\sigma(E)}{E} = d + e\sqrt{\frac{E_0}{E}}. \tag{3.6}$$

Here, E_0 is chosen to minimize the correlations of the fitted calibration parameters. The direct energy calibration is done for proton and iron primaries individually as well as for a 50/50 mix. The fit parameters for the energy calibration, resolution, and attenuation correction are summarized in Table 3.1. The energy resolution for the SD-750 array was studied with the simulation library described in Appendix A.3. The analysis follows the one described in this section. The resulting resolutions for proton and iron are shown in Fig. A.5a. The resulting parameters for the two pure compositions and a mixed composition are given in Eq. (A.6).

The direct energy calibration provides a check for possible biases in the reconstructed SD energy after the energy calibration has been performed. For this, the energy estimator S_{rec} as obtained after the attenuation correction is compared to the true energy estimator $S_{\mathrm{true}} := \hat{S}$:

$$\hat{S} = a\left(\frac{E_{\mathrm{true}}}{E_0}\right)^b. \tag{3.7}$$

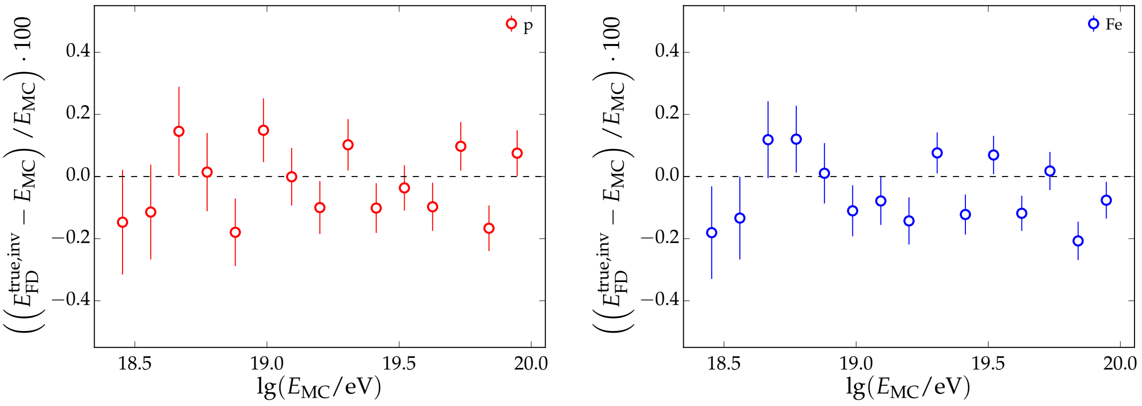

(a) proton **(b)** iron

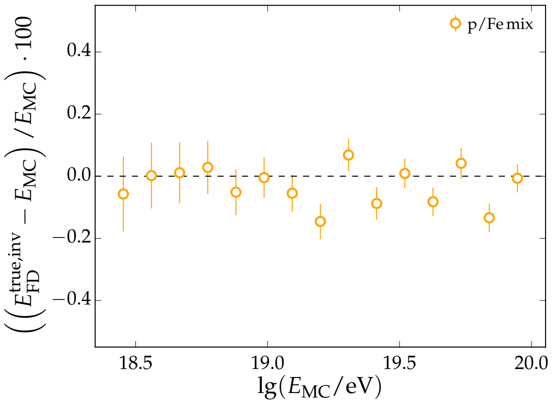

(c) p/Fe mix

Figure 3.5: The true reconstructed FD energy is corrected for the FD bias in the calorimetric energy and compared to the Monte Carlo energy. After the correction, the energies are compatible.

Table 3.1: Parameters for the energy calibration, attenuation function, and resolution as derived from SD-1500 simulations for different compositions.

Primary	proton	iron	p/Fe mix
A/EeV	0.2062 ± 0.0008	0.1849 ± 0.0004	0.1962 ± 0.0005
B	1.0611 ± 0.0008	1.0646 ± 0.0004	1.0607 ± 0.0005
a	0.972 ± 0.084	1.372 ± 0.084	1.153 ± 0.060
b	-2.506 ± 0.149	-1.169 ± 0.185	-1.922 ± 0.122
c	-0.395 ± 0.877	-3.242 ± 0.915	-1.683 ± 0.637
d	0.1093 ± 0.0011	0.0500 ± 0.0005	0.1003 ± 0.0007
e	0.431 ± 0.012	0.485 ± 0.006	0.442 ± 0.008

The relative difference in the energy estimate is shown in Fig. 3.6a and Fig. 3.6c for proton and iron induced showers, respectively. The reconstructed energy estimate of both primaries is below 2 % for energies above the threshold of full efficiency and shows an increasing bias towards lower energies. Such a bias in the reconstructed SD energy was already reported in [71]. Here, the authors studied the bias with the help of QGSJet-II.03 and a 50/50 mix of proton and iron showers. A maximum relative difference at the order of 2.5 % was found

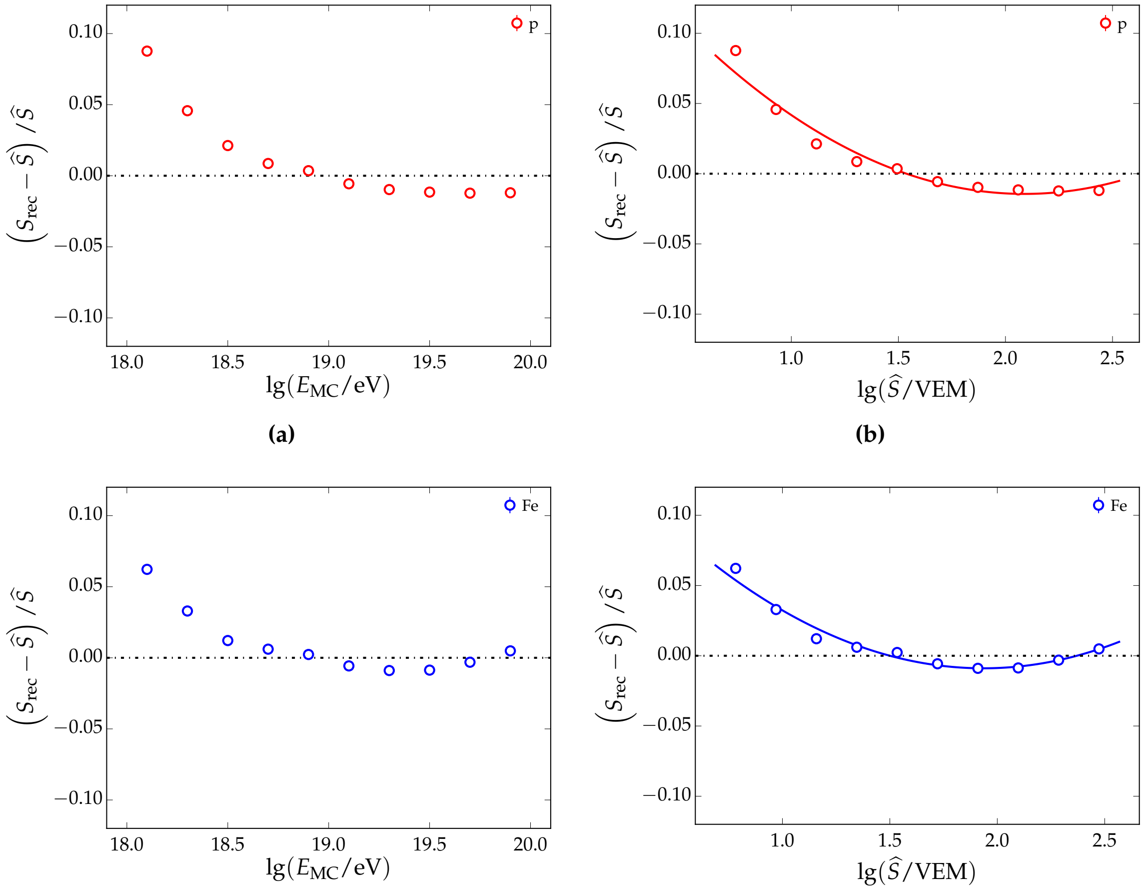

(a) **(b)**

(c) **(d)**

Figure 3.6: SD energy bias as described in the text for (a), (b) proton induced showers as function of the Monte Carlo energy and the true energy estimate, respectively. The same is shown in (c) and (d) for iron showers.

at the threshold of full efficiency. This has to be compared to Fig. 3.7 of this work, which shows the relative bias for a mixed composition but using the updated hadronic model of QGSJet-II.04. The bias at the threshold energy derived in this work is on the order of 2 %, which is in agreement with the bias found in the previous work.

Any positive bias at the threshold energy leads to upward fluctuations and as such to an overestimation of the flux at these energies. If the observed difference of the true energies is not related to an issue with the simulation using the Offline framework, the SD energies as observed in data have to be corrected for the bias. Therefore, a parameterization as function of the true energy estimate is performed. The resulting function for the mixed composition is:

$$\frac{\Delta S}{\hat{S}} = 0.21151831 - 0.22068261 \cdot \lg\left(\hat{S}/\text{VEM}\right) + 0.05456337 \cdot \lg\left(\hat{S}/\text{VEM}\right)^2. \tag{3.8}$$

The resulting fits are shown in Fig. 3.6b, Fig. 3.6d and Fig. 3.7b for the two primaries and their mix, respectively.

The imperfections of the detector accumulate in its resolution. If the resolution is too high, event migrations are affecting the measured cosmic ray flux in a non-negligible way as events migrate from one energy bin into another. Due to the steeply falling flux there is a spillover of events from low to high energies. The migration matrix gives the probability to observe an event with E_{rec} given its true energy E_{true}. As the showers were selected with SD

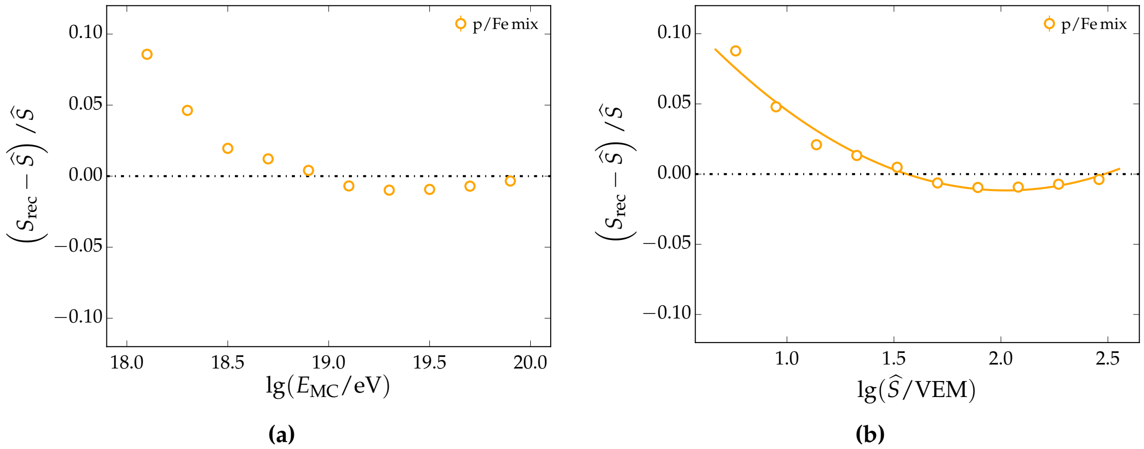

Figure 3.7: SD energy bias as function of the (a) Monte Carlo energy and (b) true energy estimate for a mixed composition.

quality cuts, they all fulfill a valid T4 trigger, such that the trigger probability is not included in the matrix. As the showers were simulated not with a real array mimicking bad periods and station inactivities but with an ideal array, the T5 trigger is always fulfilled once a T4 trigger was found (i.e no station is ever inactive). The migration matrix then reads as:

$$M_{ij} = P\left(E_{\mathrm{rec}}|E_{\mathrm{true}}\right) = \frac{n_i(E_{\mathrm{rec}})}{n_j(E_{\mathrm{true}})}, \tag{3.9}$$

with $n(E_{\mathrm{rec}})$ being the number of events with a measured energy E_{rec} and $n(E_{\mathrm{true}})$ refers to the number of simulated events with energy E_{true}. The width of the migration matrix is the energy resolution found in simulations. The result of the migration matrix for the mixed composition is depicted in Fig. 3.9d. The individual migration matrices for the pure compositions are given in Fig. A.3. The migration matrices obtained for the SD-750 simulations are depicted in Fig. A.4. In Fig. 3.9a, Fig. 3.9b, and Fig. 3.9c, a specific slice in energy E_{true} is selected for proton, iron, and a mixed composition, respectively. The relative energy differences are compared to the prediction obtained from a normal detector kernel as used in Eq. (3.3). The resolution for iron primaries is slightly better than for proton ones due to their higher number of muons in the shower and the fact that the stations are more sensitive to this shower component.

In Fig. 3.10, the energy calibration derived for simulations is compared to the one obtained for data. The energy assignment in data and simulations differs, which points to the report of external analyses of observing a lack of muons in simulations as compared to data. Taking as an example an energy estimate S_{38} of 40 VEM results in $E_{\mathrm{data}} = 8.31$ EeV, $E_{\mathrm{p}} = 10.33$ EeV, and $E_{\mathrm{Fe}} = 9.39$ EeV. The energy ratio of data and simulations results in $E_{\mathrm{p}}/E_{\mathrm{data}} = 1.24$ and $E_{\mathrm{Fe}}/E_{\mathrm{data}} = 1.13$. An energy estimate of 100 VEM gives the energies $E_{\mathrm{data}} = 21.60$ EeV, $E_{\mathrm{p}} = 27.33$ EeV, and $E_{\mathrm{Fe}} = 24.89$ EeV, with the energy ratios of $E_{\mathrm{p}}/E_{\mathrm{data}} = 1.27$ and $E_{\mathrm{Fe}}/E_{\mathrm{data}} = 1.15$. Hence, the difference in the energy scales is not constant. Taking the energy estimates of the golden hybrid events obtained in data and calibrating them with the parameters for proton and iron simulations gives the following mean differences:

$$\left\langle \frac{E_{\mathrm{SD}}^{\mathrm{p}}}{E_{\mathrm{FD}}^{\mathrm{data}}} \right\rangle = 1.23 \quad \text{and} \quad \left\langle \frac{E_{\mathrm{SD}}^{\mathrm{Fe}}}{E_{\mathrm{FD}}^{\mathrm{data}}} \right\rangle = 1.12. \tag{3.10}$$

For comparison, the Telescope Array experiment reports a difference of 1.27 using proton showers simulated with QGSJet-II.03 [72].

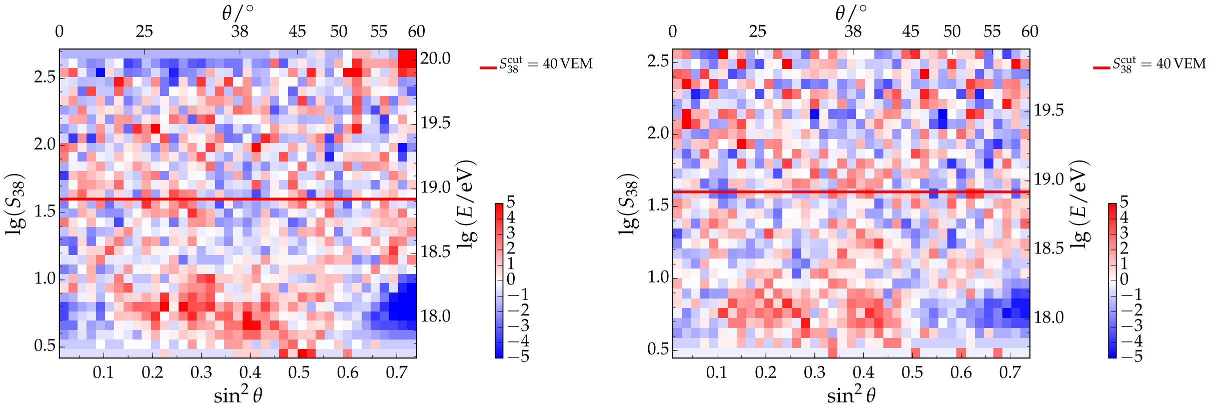

(a) proton **(b)** iron

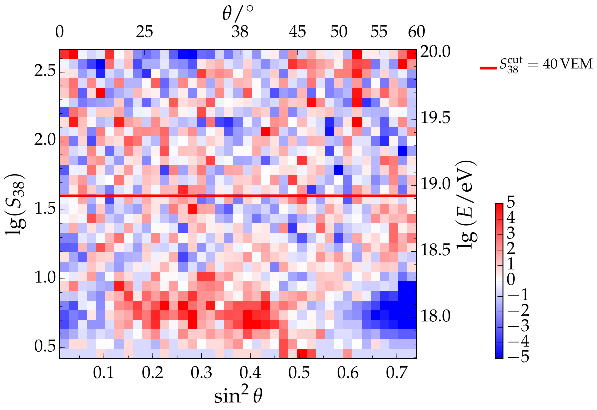

(c) p/Fe mix

Figure 3.8: Two-dimensional event distribution of the energy estimates as obtained after applying the attenuation correction to the shower sizes. the color coding gives the deviation of the number of events in a certain bin with respect to the average number of events within a bin in energy estimate. The differences are given in units of standard deviation σ_{stat}.

3.3 Trigger efficiency

The probability that an event with a certain energy and zenith angle triggers the array and passes the physics selection is studied with the help of simulations. Generally, the trigger efficiency for the array depends on the energy, mass, and zenith angle of the incident particle

$$\epsilon = \epsilon\left(E, A, \theta\right), \tag{3.11}$$

as the particle density on ground as well as the composition of the secondaries depend on these observables. To mimic the measured data as closely as possible, the detector simulation is part of the $\overline{\text{Off}}\underline{\text{line}}$ framework. In this way, the reconstruction chain for simulated and measured events is the same. The simulated events use randomly distributed impact points on the ground and are based on the simulation library stated in Appendix A.2. To determine the efficiency of the array, the ratio of the number of triggered events and the number of events thrown onto the array is calculated:

$$\epsilon = \frac{n_{\text{rec}}}{n_{\text{all}}}. \tag{3.12}$$

In the following, the trigger efficiency is determined as function of the true energy estimate rather than the Monte Carlo energy. This reduces the dependence of the efficiency

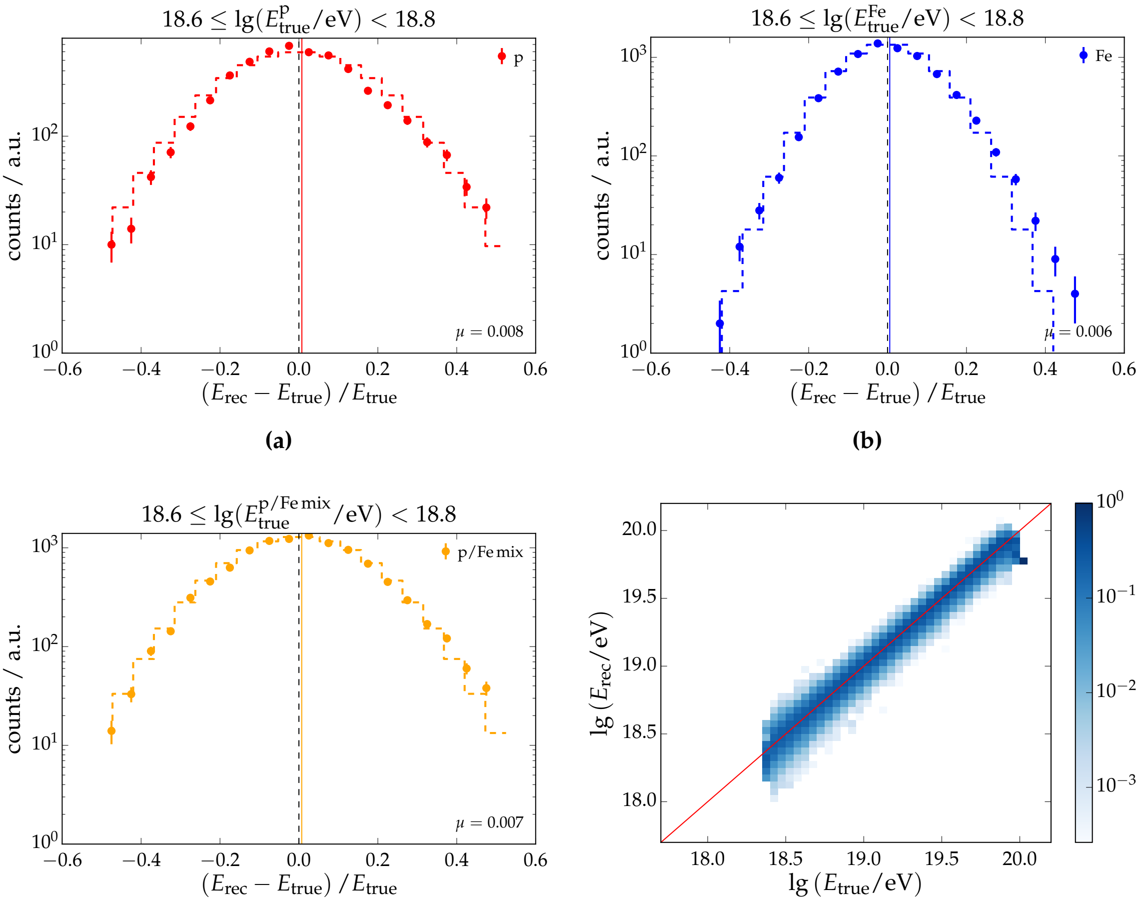

(a) **(b)** **(c)** **(d)**

Figure 3.9: (a), (b), (c) Relative energy differences in SD-1500 simulations for proton, iron, and a mixed composition. (d) Migration matrix for a mixed composition obtained in SD-1500 simulations.

parameterization on the actual hadronic interaction model used in the analysis. The true energy estimate is obtained by performing an inverse energy calibration on the Monte Carlo energy using the calibration parameters for a mixed composition as described in the previous section.

The following functional form is used to describe the efficiency:

$$\epsilon\,(S,\theta) = \frac{1}{2}\left(1 + \operatorname{erf}\left(\frac{\lg S - a(\theta)}{b}\right)\right), \tag{3.13}$$

with the parameters a and b and the error function $\operatorname{erf} := \frac{2}{\sqrt{\pi}} \int_0^x \mathrm{d}t e^{-t^2}$. The b parameter is constant, whereas a depends on the zenith angle as follows:

$$a(\theta) = a_0 + a_1 \cos^2\theta + a_2 \cos^4\theta + a_3 \cos^6\theta. \tag{3.14}$$

The parameterization of a is done empirically on the basis of the parameterization of the atmospheric attenuation, which is described in more detail in Section 4.4. Higher order terms of the angular dependence are introduced to improve the fit. The negative log-likelihood to be minimized is:

$$-\log\mathcal{L} = -\sum_i \log f\,(n_{\mathrm{rec}}; n_{\mathrm{all}}, \epsilon\,(S,\theta))\,, \tag{3.15}$$

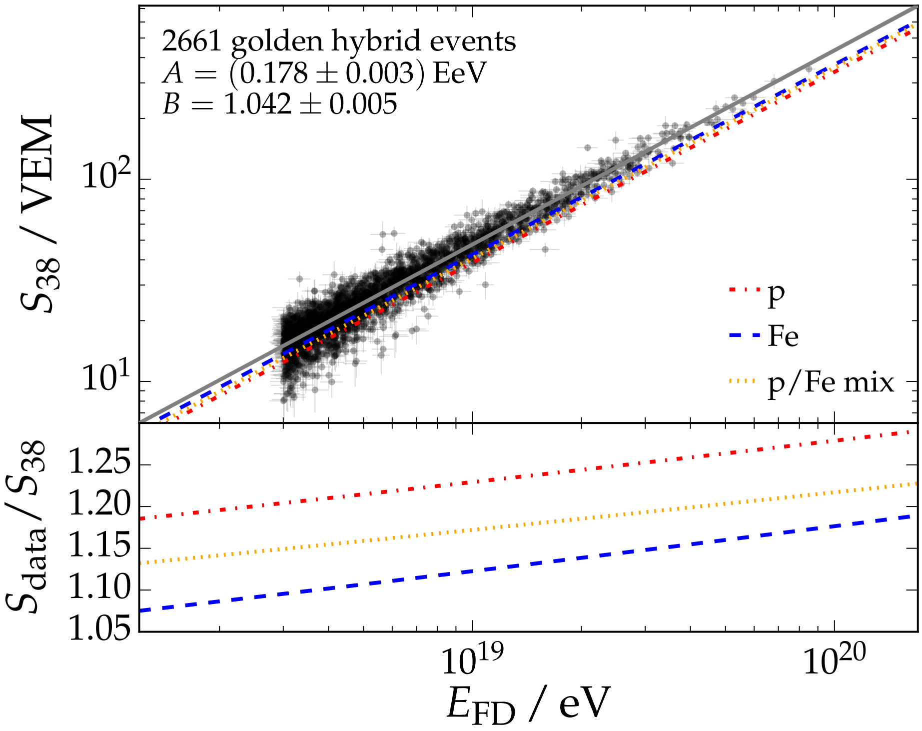

Figure 3.10: The energy calibration deduced for SD-1500 data is compared to the calibration obtained for simulations using the direct energy calibration. The calibration is performed for proton, iron, and a mixed composition.

with f denoting the binomial distribution. The minimization is performed separately for the individual primary species. The parameters for the efficiencies determined for the SD-750 and SD-1500 data using proton primaries are given in Table 3.2. The efficiency of the SD-750 array was studied in a previous work [39] and follow-up analyses. The results for the efficiency of the SD-1500 array are depicted in Fig. 3.11 for proton and iron primaries. The upper y-axis shows the energy using the energy calibration parameters obtained from data. A two-dimensional visualization is given in Fig. 3.12 for proton simulations. In Fig. 3.13, contour lines for three different efficiency thresholds are shown for the SD-750 and SD-1500 array. The contours correspond to the efficiencies derived from proton simulations. Due to the higher sensitivity of the WCDs to muons, the efficiency derived for proton showers is the most conservative efficiency, as the trigger efficiency of the array increases for primaries with $A > 1$. Therefore, the parameterization deduced for proton simulations is used further on.

The dependence of the trigger efficiency on the zenith angle is a mixture of atmospheric attenuation and geometrical projections. With increasing zenith angle, the shower suffers higher attenuation, leading to a reduction of the efficiency. However, at the same time, the muons entering the WCD cause a higher signal due to the increased track length in the station, which counteracts the attenuation. The interplay of these effects leads to a non-trivial dependence on the zenith angle. As can be seen from Fig. 3.13a, the trigger efficiency for the SD-750 array decreases faster with zenith angle than for the SD-1500 efficiency. The events recorded with the SD-750 array have lower energies and as such develop higher up in the atmosphere. The number of secondaries arriving on ground is less than for SD-1500 events. Hence, the attenuation with increasing zenith angle leads to a more rapid drop of the trigger efficiency.

Table 3.2: Parameters of the trigger efficiency for proton showers measured with the SD-750 and SD-1500 array.

Parameter	a_0	a_1	a_2	a_3	b
SD-750	2.39 ± 0.06	-4.86 ± 0.32	4.10 ± 0.56	-0.98 ± 0.31	0.249 ± 0.004
SD-1500	1.37 ± 0.08	-3.46 ± 0.46	4.13 ± 0.78	-1.47 ± 0.42	0.400 ± 0.007

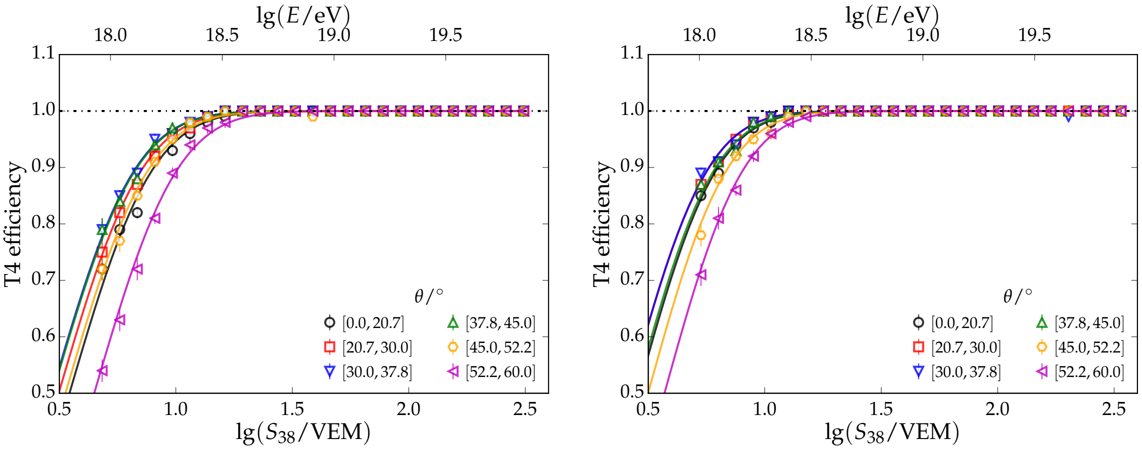

(a) proton

(b) iron

Figure 3.11: The efficiency model compared to the zenith-binned simulations as function of the energy estimate for (a) proton and (b) iron primaries. The energy scale obtained in data is shown for comparison.

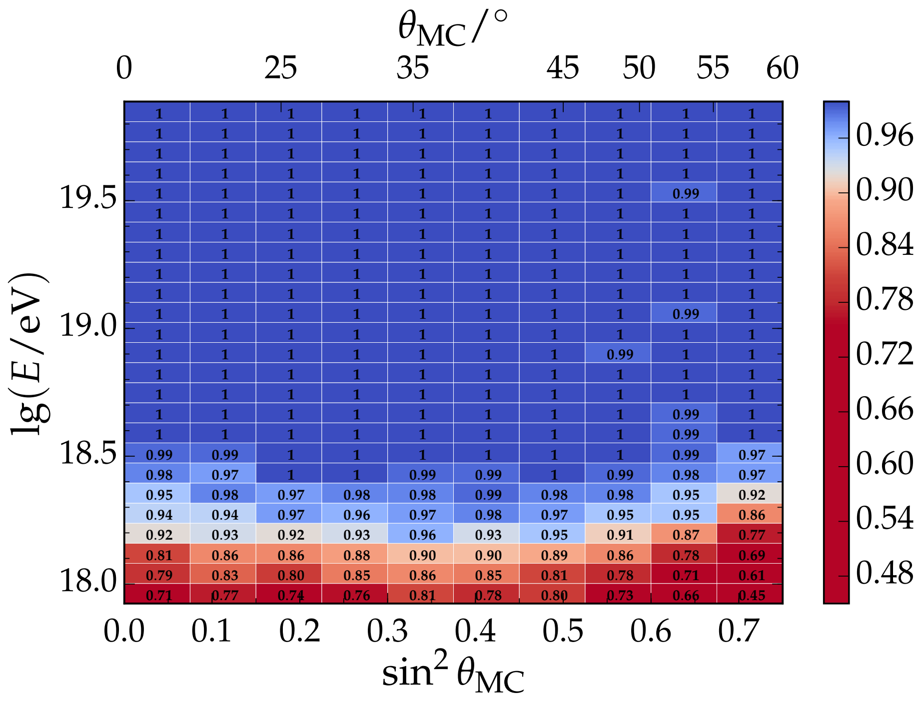

Figure 3.12: Two-dimensional efficiency as derived for proton primaries. The energy scale corresponds to the one obtained for data.

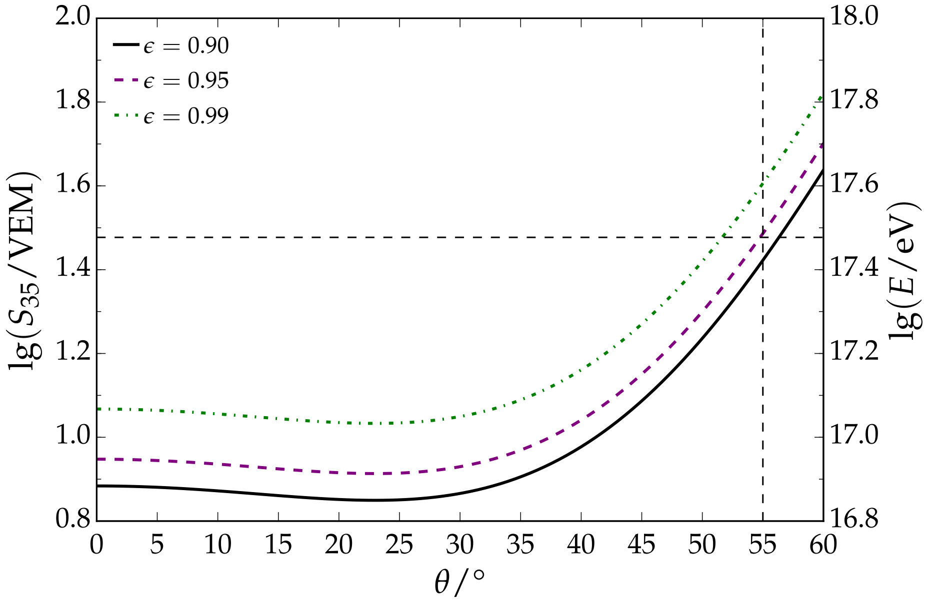

(a) SD-750 simulations

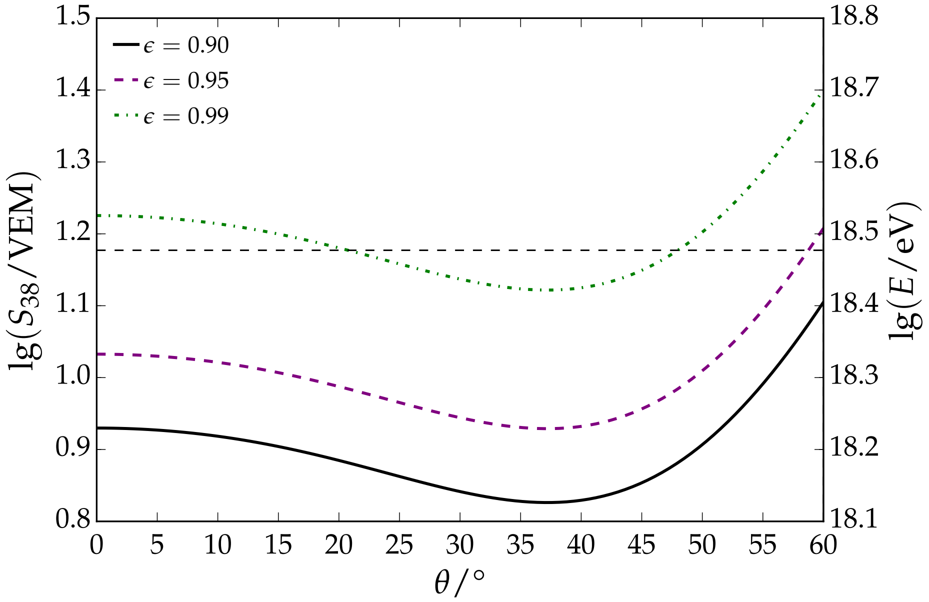

(b) SD-1500 simulations

Figure 3.13: Trigger efficiency lines derived from simulations using the hadronic interaction model of QGSJet-II.04 and proton primaries. The horizontal dashed lines correspond to the energies of full efficiency as used in the analysis of data. The vertical line in case of the SD-750 efficiency [63] represents the maximum zenith angle used in the standard analysis.

CHAPTER

4

Energy Spectrum

This chapter is dedicated to the study of the energy spectrum as measured with the surface detector of Auger. The SD provides three data sets, two formed by dividing the SD-1500 data into two zenith angle ranges, and one obtained from the SD-750 array. For the SD-1500 data the distinction is made between vertical ($\theta < 60°$) and inclined events ($\theta > 60°$). The focus of this work lies on the vertical events. Inclined showers traverse larger atmospheric depths than vertical showers and are therefore in a later shower development stage when reaching ground. The electromagnetic particles get absorbed in the atmosphere, such that the majority of the particles at ground level are energetic muons. These muons are highly deflected by the geomagnetic field, with the result that the event reconstruction described in Chapter 2 no longer applies. A detailed description of the reconstruction procedure of inclined events is given in [73] and the derived energy spectrum is presented in [74].

The analysis presented here uses vertical events with zenith angles below 60°. The SD provides an indirect measurement of the primary energy. A first energy estimate is obtained during the fit of the lateral distribution of the secondaries on ground, as described in Section 2.5. The estimate is referred to as shower size and corresponds to the expected signal at an optimal distance to the shower core at which the assumption of the functional form of the LDF has the least impact on the signal estimation. As the optimal distance depends on the grid spacing, the derived shower sizes are S_{450} and S_{1000} for the SD-750 and SD-1500 data, respectively. Seasonal changes in the atmosphere influence the shower development and lead to a change of the estimated shower size. The respective corrections are presented in Section 4.3. In Section 4.4, the dependence on the zenith angle is corrected with the Constant Intensity Cut method. A new approach to the attenuation correction is studied in Section 4.4.3. After the corrections, the energy estimates are calibrated to the calorimetric energy measurements of the fluorescence detector. The necessary steps and the derived calibrations are given in Section 4.5. The resulting SD-750 and SD-1500 spectra are presented in Section 4.6. The measured spectra are distorted by event migrations due to the finite energy resolution. In Section 4.7, the smeared spectra are corrected for this effect using a forward-folding method. The SD-1500 spectrum is further compared to the SD spectrum measured by the Telescope Array experiment in Section 4.10. The two experiments observe a difference in the measured flux at energies above 10^{19} eV. In order to investigate the origin of the discrepancy, the Auger spectrum is first checked for possible dependencies on the arrival direction in Section 4.9. In Section 4.10.2, the SD spectra of Auger and TA are then studied in a declination band in which the field of view of both detectors overlap.

4.1 Event selection

The events used for the analysis presented in this chapter are of high quality to determine the flux of the cosmic rays as precisely as possible. All events have to be reconstructed successfully, meaning that the lateral distribution was fit, and they have to fulfill the condition of the 6T5-prior trigger. As described in Section 2.2, the station with the highest signal has to be surrounded by a hexagon of active stations at the time of triggering. The neighboring stations themselves do not need to be triggered but can remain silent (i.e. having a signal below trigger threshold). The condition of the 6T5-prior is depicted in Fig. 4.1a. The *prior* add-on is important here as it refers to a selection prior to the reconstruction, whereas it is also possible to select events according to the criterion of the 6T5-posterior trigger. This selection is used for analyses based on inclined events. Here, the station closest to the reconstructed core is required to be surrounded by six active stations. In general, using the two 6T5 criteria to select vertical events will give almost the same data set as the station with the highest signal is also the one closest to the reconstructed core for most of the cases. For larger zenith angles, this agreement does not hold any more. To ensure a proper reconstruction, the data are also cut on the zenith angle, limiting the events to 55° and 60° for the SD-750 and SD-1500, respectively. Another cut is applied to the reconstructed energies taking only events above the full trigger efficiency into account. The threshold of full efficiency corresponds to $3{\times}10^{17}$ eV for the SD-750 and $3{\times}10^{18}$ eV for the SD-1500.

The event rate of the array is constantly monitored. To determine periods in which the array is unstable, a constant rate λ of T5 triggers is assumed and the probability for consecutive T5 triggers being separated by more than a time interval T is given by [75]:

$$P(T) = e^{-\lambda T}. \tag{4.1}$$

A time period is flagged as a bad period when the probability falls below a certain threshold. The duration of a bad period varies. The unstable data taking periods can be caused by short incidents such as thunderstorms or by long-lasting problems due to flaws in the communication among the stations. Any bad period is excluded for the event selection as well as for the exposure calculation as described in Section 4.2.1.

4.2 Calculating the exposure

4.2.1 Geometrical exposure

The exposure is a key ingredient to determine the flux of cosmic rays. Above the full efficiency of the detector, the calculation is solely based on the geometrical aperture and the uptime of the array. Due to the hexagonal grid, the aperture is determined by counting the number of active hexagonal cells. The cell area that contributes to the aperture is calculated as

$$A_{\text{cell}} = \frac{\sqrt{3}}{2} d^2. \tag{4.2}$$

Considering the different spacings of the SD-750 and SD-1500, this reads as follows

$$A_{\mathrm{cell}}^{750\,\mathrm{m}} = \frac{\sqrt{3}}{2}(0.75\,\mathrm{km})^2 = 0.487\,\mathrm{km}^2 \tag{4.3}$$

$$A_{\mathrm{cell}}^{1500\,\mathrm{m}} = \frac{\sqrt{3}}{2}(1.5\,\mathrm{km})^2 = 1.949\,\mathrm{km}^2. \tag{4.4}$$

The area of the cell varies with the zenith angle of the shower and needs to be projected into the shower plane to get the effective cell area. The integration over the solid angle leads to

$$\mathrm{d}A_{6\mathrm{T}5} = A_{\mathrm{cell}} \cos\theta \,\mathrm{d}\Omega \tag{4.5}$$

$$\begin{aligned} A_{6\mathrm{T}5} &= A_{\mathrm{cell}} \int_0^{2\pi} \mathrm{d}\Phi \int_{\cos\theta_{\max}}^{\cos\theta_{\min}} \mathrm{d}\cos\theta \cos\theta \qquad (4.6) \\ &= A_{\mathrm{cell}} \pi (\sin^2\theta_{\max} - \sin^2\theta_{\min}). \end{aligned}$$

Inserting finally the different spacings as well as the respective zenith ranges for SD-750 and SD-1500 results in

$$A_{6\mathrm{T}5}^{750\,\mathrm{m}} = 1.0269\,\mathrm{km}^2\,\mathrm{sr} \tag{4.7}$$

$$A_{6\mathrm{T}5}^{1500\,\mathrm{m}} = 4.5912\,\mathrm{km}^2\,\mathrm{sr}. \tag{4.8}$$

After the determination of the aperture, the exposure is obtained by integrating over time:

$$\mathcal{E}_{\mathrm{geom}} = \int_{t_0}^{t_1} \mathrm{d}t A(t) \tag{4.9}$$

$$= \int_{t_0}^{t_1} \mathrm{d}t N(t) A_{6\mathrm{T}5}, \tag{4.10}$$

with $N(t)$ denoting the active hexagons in the time period $[t - \mathrm{d}t, t + \mathrm{d}t]$. The information about the activity of individual stations is obtained from the so called T2 files. These files store the location of the stations as well as the activity at each second. With this information, the exposure calculation is simplified to a sum running over each second within the time range of interest:

$$\mathcal{E}_{\mathrm{geom}} = \sum_i A(t_i) t_i. \tag{4.11}$$

Due to changes in the array configuration, additional criteria besides the activity of individual stations have to be considered in the exposure calculation:

- Communication crisis: In 2009, data taking with the SD-1500 was unstable due to connection problems of the stations to CDAS. The short disconnections caused a tremendous event loss. The whole crisis lasted eight months, of which the time interval 16.04.2009 - 06.06.2009 has to be rejected completely. The rest of the bad period from 07.06.2009 - 15.11.2009 can be used with a special requirement for the 6T5 trigger, namely that the considered hexagon has to remain active for another 120 s after the initial trigger [76].

- Bad periods: From time to time, the array suffers from technical disturbances or bad weather conditions, such as heavy thunderstorms with lightnings. Data taken during such bad periods are excluded for the standard spectrum analysis.

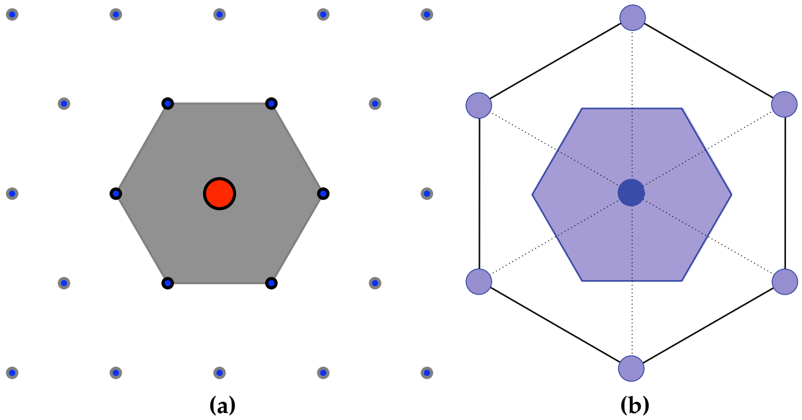

Figure 4.1: (a) Schematic view of the 6T5 criterion where the station with the largest signal must be surrounded by six active neighbors. (b) Depiction of an elementary hexagon cell. The shaded area corresponds to the area accounted for in the exposure calculation.

- Bad stations: Between May 2009 and May 2011, stations of the SD-750 have been equipped with additional communication systems, which were not always working properly. The affected stations are neglected in the exposure calculation and are flagged as bad stations during the event reconstruction by the SdBadStationRejectorKG module of Offline.

Within the scope of this work, the criterion for the T5-pos trigger was extended for the Offline framework as described in Section 2.2.2. Events where the reconstructed core is only contained in an active isosceles triangle but not in an equilateral one can be selected now as well. When working with *nT5-pos* events, the exposure has to be adjusted depending on the number of active stations (n) required around the station with the highest signal. The relaxed *nT5-pos* trigger is used in anisotropy analyses focused on the highest energies. Here, the high station multiplicity ensures a reliable reconstruction property even though the event falls close to the array border or to a malfunctioning station.

4.2.2 Directional exposure

The study of the CR flux in different regions of the sky necessitates the determination of a directional exposure. For a detector with a continuous operation, the exposure is independent of the right ascension and only depends on the declination as follows [77]:

$$\omega(\delta) \propto \cos l_0 \cos\delta \sin\beta + \beta \sin l_0 \sin\delta. \tag{4.12}$$

The exposure calculation is expressed in terms of equatorial coordinates. As visualized in Fig. 4.2a, the declination gives the angular distance of a point on the sphere to the celestial equator and the right ascension is the angular distance of a point measured eastward from the vernal equinox. In Eq. (4.12), l_0 refers to the latitude at which the considered detector is located and β is given by

$$\beta = \begin{cases} 0 & , \quad \xi > 1 \\ \pi & , \quad \xi < -1 \\ \cos^{-1}(\xi) & , \quad \text{else} \end{cases} \tag{4.13}$$

with

$$\xi = \frac{\cos\theta_{\max} - \sin l_0 \sin\delta}{\cos l_0 \cos\delta}. \tag{4.14}$$

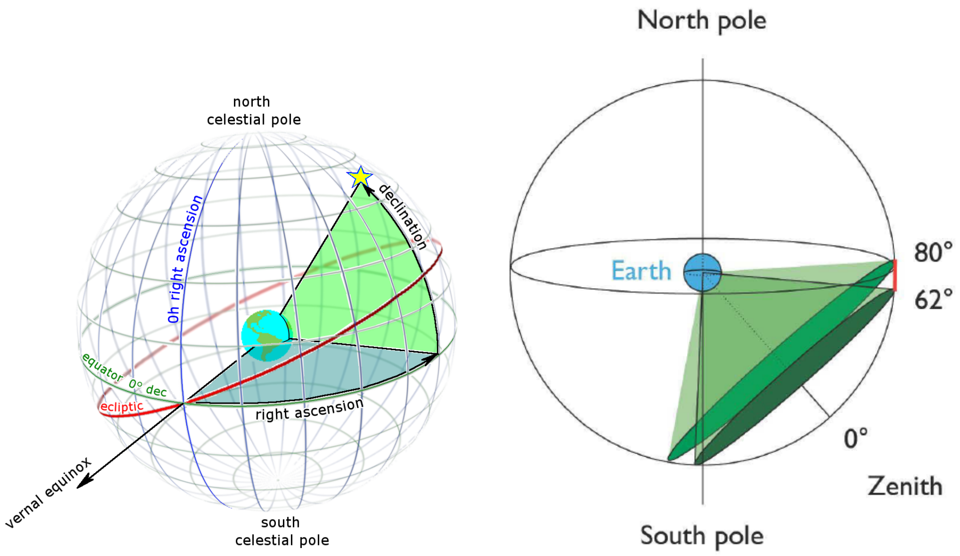

(a) **(b)**

Figure 4.2: Schematic of the (a) equatorial (from Wikipedia) and (b) local coordinate system. For the latter, the location of Auger is used.

The zenith angle θ_{max} represents the angle up to which the respective detector is fully efficient. The normalization is done by integrating over the sphere:

$$\mathcal{E}_{\mathrm{geom}} = \int \mathrm{d}\Omega\, \omega(\delta) = 2\pi \int_{-\pi/2}^{\pi/2} \mathrm{d}\delta\, \omega(\delta) \cos\delta, \tag{4.15}$$

such that the integrated exposure equals the geometrical exposure for the analyzed time range and data set.

An example for the relative directional exposure on the sphere is illustrated in Fig. 4.3, where the exposure $\omega(\delta)$ at a certain point is divided by the total exposure of the observed sky. Here, a maximum zenith angle of 60° is used and the exposure is calculated for the location of Auger. With an average latitude of $l_0 = -35.21°$, Auger is mainly sensitive in the southern hemisphere. The highest exposure is accumulated in the region of the south pole as the pole is always covered for $\theta < 60°$. The field of view can be increased towards the northern hemisphere by including events up to 80° as shown in Fig. 4.2b. In this case, the maximum declination increases from 24.79° to 44.79° as indicated by the dashed and dashed-dotted lines in Fig. 4.3. The directional exposure as function of declination is also shown in Fig. 4.47 in comparison to the one obtained for the Telescope Array experiment.

4.3 Corrections to the shower size

The shower development is affected by variations in the atmospheric conditions and by the geomagnetic field, resulting in modulations of the particle density and distribution on the ground. The shower sizes S_{450} and S_{1000}, as being dependent on the measured particle distributions, are thus altered by the modulations. As a consequence, the energies inferred from these estimators are affected as well. The effects of the atmospheric conditions and geomagnetic field comprise an angular dependence that leads to spurious anisotropies in the spectrum, if not corrected for. It is of crucial importance to include these corrections in the analysis of different declination bands as described in Section 4.9.

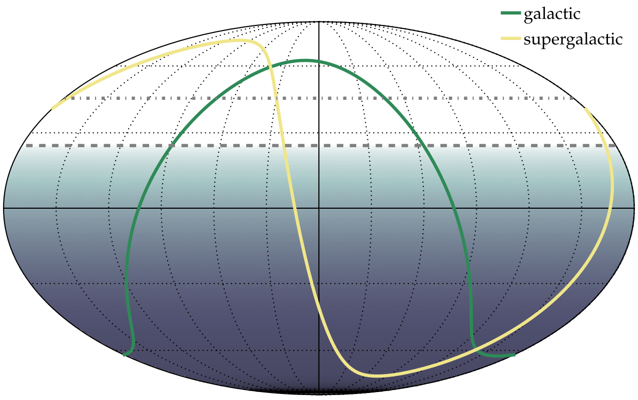

(a)

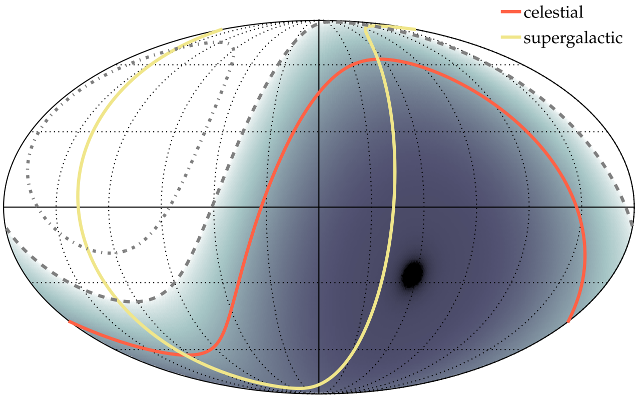

(b)

Figure 4.3: Directional exposure for events with $\theta < 60°$ in (a) equatorial and (b) galactic coordinates. The maximum field of view when using SD-1500 data and SD-1500h data ($\theta < 80°$) is shown by the dashed and dashed-dotted line, respectively. The planes for the other coordinates systems used in anisotropy studies are depicted in addition.

The modulations in the atmospheric conditions have two major effects. The first one is the variation of the longitudinal development of the shower as a result of the changes in the air pressure. A higher pressure corresponds to an increased matter overburden and therefore the first interaction takes place higher in the atmosphere and the shower is more advanced (i.e. older) when it reaches the ground. The second one is the effect on the lateral extent of the shower on the ground due to varying air densities. An increased density decreases the Molière radius (corresponding to a circle around the shower axis that contains 90 % of the energy content of the shower) and narrows the lateral distribution of the showers. The impact of the atmospheric variations on the shower size have been studied for both the SD-750 and the SD-1500 data and are of the order of ±1 %. The correction factor resulting from the weather effects is depicted in Fig. 4.4 in form of violin plots (see Appendix C.1 for further description). The modulation of the shower size can be parameterized with the help of the ground pressure and density at the time of the event [37, 44, 78–84]. The corrections applied within this work make use of the zenith-dependent parameterization of [85].

Any air shower developing in the Earth's atmosphere is spread in the direction of the Lorentz force that is given by the shower axis and the magnetic field vector. The spread of the shower leads to a change in the charged particle distribution on the ground and as such alters the estimate of the shower size. The geomagnetic field induces an azimuthal modulation

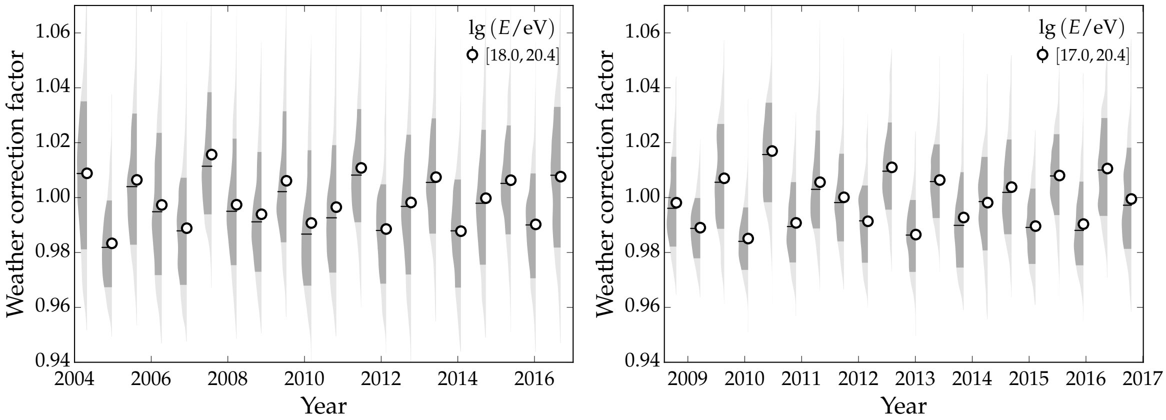

(a) SD-1500 **(b)** SD-750

Figure 4.4: Corrections applied to the measured shower sizes. Weather corrections are available for (a) SD-1500 and (b) SD-750 data. The circular markers indicate the mean of the bin, the median is depicted with a solid line. The distribution of the correction factor within each bin is visualized with a kernel density estimate (i.e violin). Here, the 1σ (dark gray) and 3σ (light gray) regimes are shown.

with an amplitude at a 2 % level for zenith angles approaching 60° as depicted in Fig. 4.5b. Any azimuthal dependence in the shower size translates into azimuthal variations of the event rate for a given shower size and consequently to an azimuthal dependence of the event rate at a given energy. As the modulation is also zenith dependent, the event rate is distorted in the declination distribution resulting in a fake dipolar pattern. As Fig. 4.5c implies, the reconstructed energies are higher for events coming from the southern sky without the correction applied. The correction gets smaller with increasing declination. The influence of the geomagnetic field is studied with the help of air shower simulations by switching off the field and comparing it to the observed shower size distribution in the presence of the field. This was done for S_{1000} in [86], the effect on S_{450} has not been studied yet. Therefore, the S_{1000} values are corrected for both the atmospheric and geomagnetic effects, whereas S_{450} is only corrected for weather effects. The total correction factor for the SD-1500 data is shown in Fig. 4.5d. The effect on the shower size is on the level of 1 % for vertical showers with a slight increase towards 60°. No dependence on the primary energy is observed.

4.4 Constant Intensity Cut

The shower sizes $S = \{S_{450}, S_{1000}\}$ for a fixed energy and primary depend on the zenith angle, as the attenuation changes with the amount of traversed atmosphere. The amount of traversed matter (slant depth) increases approximately with $1/\cos\theta$ with the result that a shower arriving at 60° traverses about twice the amount of matter compared to a vertical shower with a zenith angle of 0°. The number of interactions within the atmosphere increases with zenith angle. This is crucial for the electromagnetic component of the shower. The interaction probability of muons is lower than for electrons and photons and the decay probability depends on the traversed distance and not on the slant depth. Therefore, for showers below 60°, the attenuation of the muonic component is negligible, whereas the electromagnetic component decreases with zenith angle. This leads to a dependence on the zenith angle of the measured number of events in terms of the shower size. This dependence has to be corrected for to get an energy estimator solely dependent on the energy. The

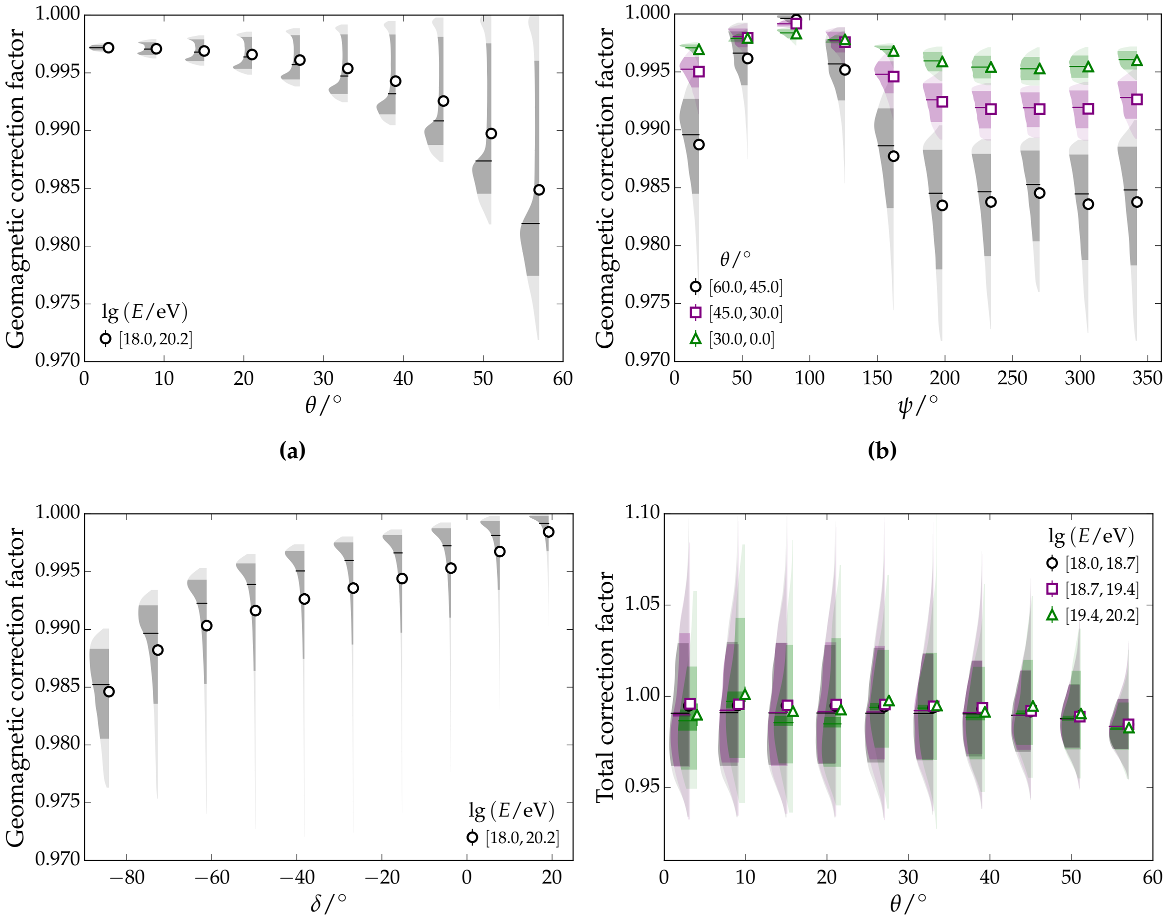

(a) **(b)**

(c) **(d)**

Figure 4.5: Corrections applied to the measured shower sizes. The geomagnetic correction factor shown as function of (a) zenith, (b) azimuth, and (c) declination angle is solely determined for the SD-1500 shower size S_{1000}. The combination of geomagnetic and weather correction factors as function of zenith angle is given in (d). Violin profiles are shown for different primary energies. The effect on S_{1000} is on the order of 2 %.

correction is performed with the help of the CIC[1] [87–96]. The empirical method assumes an isotropic arrival distribution for the primary particles above a certain energy threshold. As the detector measurement is symmetric in azimuth, the isotropy is expressed as:

$$\frac{\mathrm{d}J}{\mathrm{d}\theta} = 0. \tag{4.16}$$

Expressing the flux J as number of particles $\mathrm{d}N$ per energy $\mathrm{d}E$, detection area $\mathrm{d}A_{\mathrm{eff}}$, time $\mathrm{d}t$, and solid angle $\mathrm{d}\Omega$, this reads as:

$$\frac{\mathrm{d}}{\mathrm{d}\theta}\left(\frac{\mathrm{d}N}{\mathrm{d}A_{\mathrm{eff}}\,\mathrm{d}t\,\mathrm{d}E\mathrm{d}\Omega}\right) = \frac{\mathrm{d}}{\mathrm{d}\theta}\left(\frac{1}{\cos\theta}\,\frac{\mathrm{d}N}{\mathrm{d}A\,\mathrm{d}t\,\mathrm{d}E\,\mathrm{d}\cos\mathrm{d}\phi}\right). \tag{4.17}$$

---

[1] Constant Intensity Cut

The stations are located in the detector plane. The effective detector area $A_{\mathrm{eff}} = A\cos\theta$ corresponds to the projection of the stations into the plane perpendicular to the shower axis, called shower plane. Neglecting the zenith-independent variables results in:

$$\frac{\mathrm{d}N}{\mathrm{d}E\,\mathrm{d}\cos^2\theta} = \mathrm{const.} \tag{4.18}$$

Integrating over the energy above the chosen threshold energy leads to:

$$\frac{\mathrm{d}N}{\mathrm{d}\cos^2\theta} = -\frac{\mathrm{d}N}{\mathrm{d}\sin^2\theta} = \mathrm{const.} \tag{4.19}$$

A relative attenuation is obtained by comparing the measured shower size to the size a shower would produce at ground if it arrived at a certain reference angle:

$$f_{\mathrm{CIC}}(\theta) = S(E,\theta)/S(E,\theta_{\mathrm{ref}}). \tag{4.20}$$

From Eq. (4.20), the energy estimate $S(E,\theta_{\mathrm{ref}}) = S_{\theta_{\mathrm{ref}}}(E)$ follows as:

$$S_{\theta_{\mathrm{ref}}}(E) = S(E,\theta)/f_{\mathrm{CIC}}(\theta). \tag{4.21}$$

Strictly speaking, the shower size depends also on the primary mass. As the underlying composition is unknown, this dependency is dropped here. The reference angle θ_{ref} is chosen accordingly to the observable zenith angle range:

$$\begin{aligned} &\cos^2\theta_{\mathrm{ref}} = \langle\cos^2\theta\rangle \qquad (4.22)\\ \Longrightarrow\quad &\theta_{\mathrm{ref}} = \arccos\sqrt{\langle\cos^2\theta\rangle}. \end{aligned}$$

The zenith angle range covered by the SD-750 array is $[0°, 55°]$, resulting in a median zenith angle of 35°. The reference angle for the SD-1500 array is 38° as the maximum zenith angle is 60°. The current parametrization of the attenuation function f_{CIC} uses a third degree polynomial of the variable $x = \cos^2\theta - \cos^2\theta_{\mathrm{ref}}$, having tested other functional forms in the past, as done in e.g [59]. In the next step, the fitting procedure of the attenuation function is described using the example of the SD-1500 array to simplify the notation. The same procedure holds as well for the SD-750 array.

The approach used in this work to obtain the parameters for the attenuation function from data requires uniformity of the number of events above an a priori chosen threshold value for the shower size. The method is discussed in detail in [63, 92] and is compared to the previously used countdown approach. The previous method requires a certain number of events, i.e. intensity, within each $\sin^2\theta$ bin. This number is chosen a priori. Starting with the largest shower size in each angle bin, the sizes are iterated backwards until the required intensity is reached. Within each $\sin^2\theta$ bin, the shower size at which this intensity is reached, differs. By fitting this dependence, the parameters for the attenuation function and the S_{38}^{cut} value are obtained. The variable S_{38}^{cut} corresponds to the lowest shower size reached in the $\sin^2\theta$ bin that contains 38° when performing the backwards iteration. With the countdown method, the energy corresponding to the chosen intensity is unknown during the CIC analysis and is only obtained in the next step by performing the energy calibration as discussed in Section 4.5. The countdown method neglects possible Poissonian fluctuations as it requires an exact number of events within each bin. This downside is overcome by the method discussed in the following.

The uniformity method starts with a fixed value for S_{38}^{cut} and an initial guess for the parameters of the attenuation function. This gives a particular value for the shower size $S_i^{\mathrm{cut}} = S_{38}^{\mathrm{cut}} f_{\mathrm{CIC}}$ in each $\sin^2\theta$ bin i. The distribution of the number of events n_i having a shower size greater than S_i^{cut} should be uniform. The parameters of the attenuation function are thus fitted to optimize the uniform statistic of n_i. During the fit procedure, the shower sizes fluctuate in and out of the calculation of n_i as they either exceed or lie below the attenuation curve depending on the parameters. This discrete counting is smoothed by using a kernel function $K(S_i, S_i^{\text{cut}}, \sigma(S_{1000}))$. The number of the events in a bin i is now given as:

$$n_i = \sum_j K(S_i, S_i^{\text{cut}}, \sigma_i)\,, \tag{4.23}$$

where the sum is running over all events in the specific bin. The variable S_i is denoting the shower sizes S_{1000} in the bin i and $\sigma_i = \sigma_i(S_{1000})$. Assuming a normal distribution, the kernel function K is expressed as:

$$K(S_i, S_i^{\text{cut}}, \sigma_i) = \frac{1}{2}\left[1 + \text{erf}\left(\frac{S_i - S_i^{\text{cut}}}{\sqrt{2}\sigma_i}\right)\right]. \tag{4.24}$$

The calculation of the c.d.f.[2] on the right hand side is rather cumbersome as all events contribute to the n_i counts. Therefore, the following approximation was chosen and checked against the exact calculation to give the same results:

$$K(x, \Delta) = \int_{-\infty}^{x} \rho(x', \Delta)\,\mathrm{d}x' = \begin{cases} 0 & ;\quad \mathrm{x} < -\Delta \\ (1 + x/\Delta)^2/2 & ;\quad -\Delta \le x < 0 \\ 1 - (x/\Delta - 1)^2/2 & ;\quad 0 \le x < \Delta \\ 1 & ;\quad \Delta \le x \end{cases} \tag{4.25}$$

The fit is performed using the following χ^2 function:

$$\chi^2 = \sum_i^k \frac{(n_i - \langle n \rangle)^2}{\langle n \rangle} \tag{4.26}$$

$$\langle n \rangle = \frac{1}{k} \sum_{i=1}^{k} n_i, \tag{4.27}$$

where the sums run over the k zenith angle bins. The parameters of the attenuation function are implicitly included in both, the measured counts n_i and the expected counts $\langle n \rangle$. In the following, the CIC analysis is performed for the SD-750 and SD-1500 data sets. The data are selected according to the respective quality cuts as stated in Appendix B.1.

4.4.1 Attenuation correction for SD-750 data

The showers sizes S_{450} are normalized to the size the showers would have produced had they arrived at 35°. The normalized sizes are further on referred to as S_{35}. The attenuation function is determined by using the uniformity method as described in the previous section. For this work, I use events which fulfill $S_{35} > 40\,\text{VEM}$. The corresponding primary energy is $5.6{\times}10^{17}$ eV. The cut selects 22 580 events for the fit. The data are divided into 200 bins in $\cos^2\theta$, each bin holding 112 events. The minimization of Eq. (4.26) results in the following attenuation function:

$$f_{\text{CIC}}(x) = 1 + (1.634 \pm 0.028)\,x + (-1.404 \pm 0.075)\,x^2 + (-2.15 \pm 0.39)\,x^3, \tag{4.28}$$

---

[2] cumulative distribution function

with $x = \cos^2\theta - \cos^2\theta_{35}$. As the amount of traversed atmosphere is proportional to $\sec\theta$ for any shower with $\theta > 0$, the attenuation curve is shown as a function of $\sec\theta$ in Fig. 4.6a. The measured event distribution within each $\cos^2\theta$ bin is re-sampled and plotted in addition. The data points and the uncertainties resulting from the bootstrapping are compatible with the actual fit and support its validity. A visualization of the attenuation correction is shown in Fig. 4.6c and Fig. 4.6d. In Fig. 4.6c, the integrated number of events with a shower size above a certain value of S_{450} is depicted for four zenith angle bins. The higher attenuation with increasing zenith angle leads to a shift of the distributions towards lower sizes. At the lowest shower sizes, a plateau develops due to the trigger efficiency. For large shower sizes, the distributions become less smooth due to the decreasing statistic. After correcting for the attenuation, the event distributions lie on top of each other, as shown in Fig. 4.6d. The vertical line represents the cut value of 40 VEM that was chosen a priori. The size range below the cut, which is not part of the fit, is grayed out.

Another crosscheck for the correctness of the derived attenuation function is shown in Fig. 4.14a. Here, the distribution of the energy estimates is depicted in two dimensions. The deviation from uniformity is indicated by the color of each bin. The number of events within each bin of $(\Delta\sin^2\theta, \Delta\lg S_{35})$ is compared to the mean number of events for a specific $\Delta\lg S_{35}$ bin. The difference to the mean is stated in units of standard deviation σ_{stat}. The cut value S_{35}^{cut} of 40 VEM is depicted as a horizontal line. Above the threshold energy of 0.3 EeV the event distribution is rather uniform, apart from some fluctuations on the order of a few standard deviations. Strong deviations are observed below the threshold of full efficiency, with an overestimation of events at lower zenith angles and an underestimation of events at the highest zenith angles at the level of 5σ.

To study the impact of the weather corrections, the attenuation function is fitted to the uncorrected shower sizes. The resulting function is:

$$f_{\text{CIC}}^{\text{uncorr}}(x) = 1 + (1.64 \pm 0.03)\,x + (-1.40 \pm 0.08)\,x^2 + (-2.19 \pm 0.39)\,x^3. \tag{4.29}$$

The attenuation obtained for the uncorrected shower sizes is shown in Fig. 4.6a as red, dashed line. The relative residual of the two attenuation functions is shown in Fig. 4.6b. They are compatible within 0.1 % or 0.1σ. Hence, the weather corrections have a negligible effect on the attenuation function. The attenuation function obtained from the corrected shower sizes is used for the following analyses in this work.

4.4.2 Attenuation correction for SD-1500 data

Any shower size S_{1000} measured with the SD-1500 array is associated to a signal at the reference angle of 38°. The signal at the reference angle is the energy estimate S_{38}, which refers to the shower size corrected for attenuation effects:

$$S_{38} = \frac{S(1000)}{f_{\text{CIC}}(\theta)}. \tag{4.30}$$

The parameters of the attenuation function are determined using the uniformity method as described Section 4.4. The cut value S_{38}^{cut} is set to 40 VEM and the data are divided into 200 bins in $\cos^2\theta$. The chosen threshold for the energy estimate corresponds to a cut in primary energy above 8.3×10^{18} eV. 19 540 events are selected with this cut, resulting in about 97 events per bin in $\cos^2\theta$.

The minimization of Eq. (4.26) results in the following attenuation function:

$$f_{\text{CIC}}(x) = 1 + (0.966 \pm 0.039)\,x + (-1.659 \pm 0.072)\,x^2 + (-1.19 \pm 0.40)\,x^3, \tag{4.31}$$

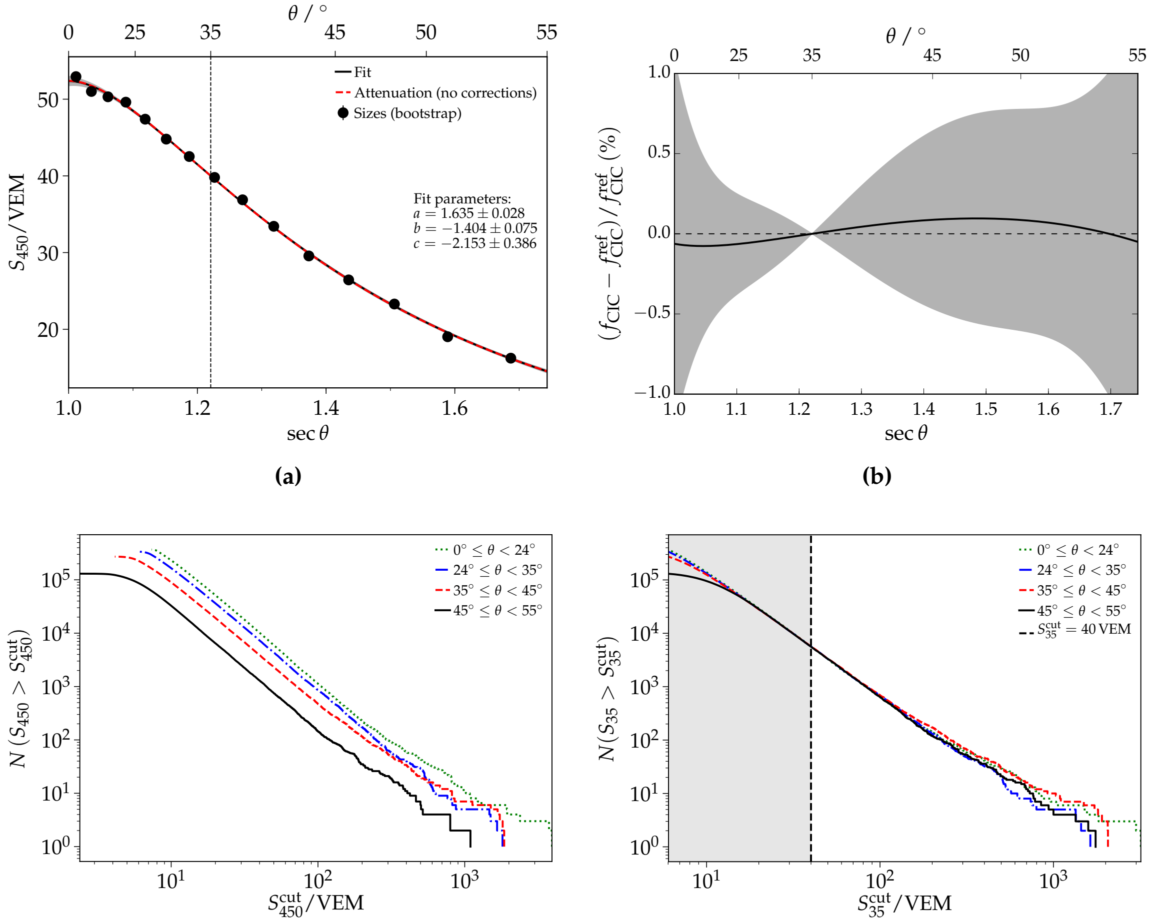

(a) **(b)**

(c) **(d)**

Figure 4.6: (a) The attenuation function obtained for events measured with the SD-750 and corrected for weather effects. The attenuation for the uncorrected shower sizes is plotted in addition. (b) Relative difference of the attenuation functions obtained for corrected and uncorrected sizes. The shaded area shows the 1σ uncertainty of the function using the corrected sizes. (c) The integral event distribution for a reduced number of zenith angle bins prior to the attenuation correction. (d) After applying the attenuation correction the event distributions lie on top of each other, confirming the fit result. The shaded are refers to the size range excluded in the fit.

with $x = \cos^2\theta - \cos^2\theta_{38}$. The attenuation function is shown in Fig. 4.7a, together with the data points using a bootstrap re-sampling. As done for the SD-750 events, the attenuation function is compared to the one obtained for the uncorrected shower sizes:

$$f_{\mathrm{CIC}}^{\mathrm{uncorr}}(x) = 1 + (0.954 \pm 0.039)\,x + (-1.65 \pm 0.07)\,x^2 + (-1.20 \pm 0.40)\,x^3. \tag{4.32}$$

The relative residual of the attenuation functions is depicted in Fig. 4.7b. In case of the SD-1500, the shower sizes are not only corrected for weather effects but also for geomagnetic effects due to the Earth's magnetic field. The impact of both corrections exceeds 1 % for the higher zenith angles. The larger difference necessitates the use of the attenuation function obtained from the corrected shower sizes when studying angular dependencies of the flux. All further analyses include the attenuation function obtained from the corrected shower sizes. As done for the SD-750, a visualization of the attenuation correction for a reduced number of zenith bins is shown in Fig. 4.7c and Fig. 4.7d. After applying the correction, the distributions of the shower sizes lie on top of each other in the size region of interest. The uniformity after applying the correction is checked with the two-dimensional event distribution shown

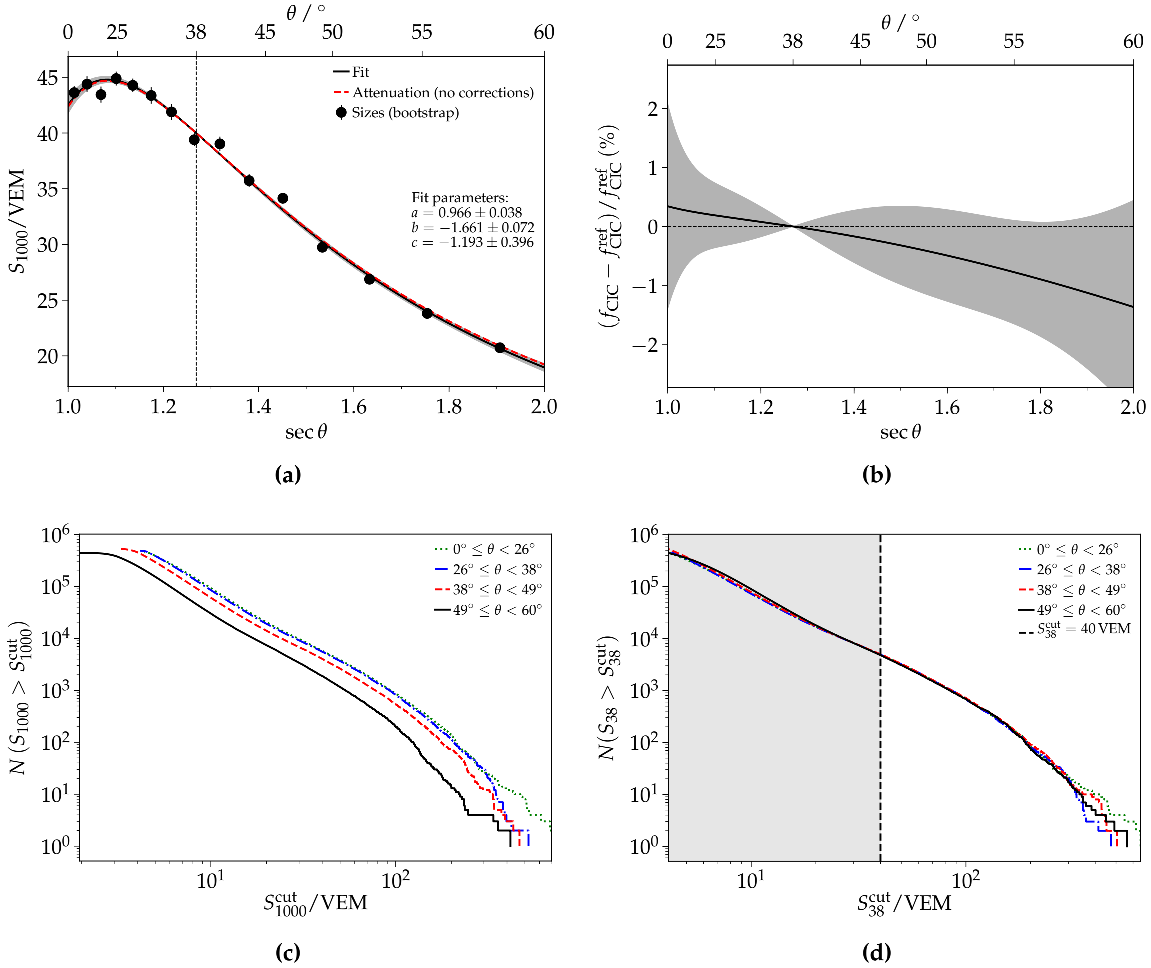

(a) **(b)** **(c)** **(d)**

Figure 4.7: The attenuation function obtained for events measured with the SD-1500 and corrected for weather and geomagnetic effects. The attenuation for the uncorrected shower sizes is shown for comparison. (b) Relative difference of the attenuation functions obtained from the corrected and uncorrected sizes. The shaded band represents the 1σ uncertainty of the model obtained for the corrected sizes. (c) The event distribution for a reduced number of zenith angles prior to the attenuation correction. (d) After the correction, the distributions lie on top of each other as being independent of the zenith angle.

in Fig. 4.14c. Above the S_{38}^{cut} value, the distribution is uniform, whereas below this cut the fluctuations reach a deviation on the order of 5σ in some parts of the $(\sin^2\theta, \lg S_{38})$ space. In order to reduce these fluctuation, an alternative method for determining the attenuation function is explored in the next section.

4.4.3 Energy dependence of the attenuation correction

Recent studies [93–96] indicate a non-negligible energy dependence of the attenuation function, being apparent for both SD-750 and SD-1500 data. Following the approach of the aforementioned authors, the evolution of the parameters of the attenuation function can be studied by performing the analysis for several values of S^{cut}. This analysis is done for both data sets, starting with the data measured with the SD-1500.

SD-1500 data

As suggested in [95], the threshold values are determined using:

$$S_n^{\mathrm{th}} = \alpha^{n-1} S_1^{\mathrm{th}}, \tag{4.33}$$

with $S_1^{\mathrm{th}} = 20\,\mathrm{VEM}$. With the energy calibration of [97], this size value corresponds to an energy around 4 EeV, including only events above full efficiency. The scaling factor is chosen as $\alpha = 1.13$. This results in gaps between the consecutive thresholds which are larger than the resolution of S_{1000}. With increasing size, the number of events exceeding the threshold decreases. To ensure a valid statistic, a maximum threshold energy of about 20 EeV is chosen. This also discards the energy range where anisotropy is starting to become important [24]. The chosen limits lead to 12 threshold values for S_{cut}. I consider 100 bins in $\cos^2\theta$ for zenith angles from 0° to 60°. For each of the S_{cut} values, the uniformity method as described in Section 4.4 is performed. The attenuation function is again a third degree polynomial in terms of the variable $x = \cos^2\theta - \cos^2\theta_{38}$. The resulting attenuation parameters are shown in Fig. 4.8a. For comparison, the parameters obtained with the single threshold of $S_{\mathrm{cut}} = 40\,\mathrm{VEM}$ as used in Section 4.4.2 are depicted as round markers. A trend with S_{cut} is visible for all three parameters, indicating an energy dependence. In the next step, each parameter is fit with a linear function, such as:

$$\xi\left(S_{38}\right) = \xi_0 + \xi_1 \log_{10}\left(\frac{S_{38}}{S_0}\right), \tag{4.34}$$

where S_0 denotes a reference value. Here, I choose a reference value of 40 VEM, which corresponds to the cut value of the standard attenuation fit. The resulting fits are shown in Fig. 4.8b, Fig. 4.8c, and Fig. 4.8d and the parameter values are summarized in Table 4.1. The attenuation correction of the shower sizes S_{1000} becomes an iterative process in the following. The first step is to determine an initial estimate S_{38}^* for the corrected shower size using a reference attenuation correction with $S_{38} = S_0$:

$$\begin{aligned} S_{38}^* = S_{1000}\Bigg[1 &+ x\left(a_0 + a_1\log_{10}\left(\frac{S_{38}}{S_0}\right)\right) + x^2\left(b_0 + b_1\log_{10}\left(\frac{S_{38}}{S_0}\right)\right) \qquad (4.35)\\ &+ x^3\left(c_0 + c_1\log_{10}\left(\frac{S_{38}}{S_0}\right)\right)\Bigg]^{-1} \\ = S_{1000}&\left[1 + a_0 x + b_0 x^2 + c_0 x^3\right]^{-1}, \qquad (4.36) \end{aligned}$$

recovering the standard attenuation function. The initial estimate S_{38}^* is used as input for S_{38} then instead of $S_{38} = 40\,\mathrm{VEM}$:

$$\begin{aligned} S_{38} = S_{1000}\Bigg[1 &+ x\left(a_0 + a_1\log_{10}\left(\frac{S_{38}^*}{S_0}\right)\right) + x^2\left(b_0 + b_1\log_{10}\left(\frac{S_{38}^*}{S_0}\right)\right) \\ &+ x^3\left(c_0 + c_1\log_{10}\left(\frac{S_{38}^*}{S_0}\right)\right)\Bigg]^{-1}. \end{aligned} \tag{4.37}$$

Due to the slow change of the attenuation function with energy, one iteration is sufficient to get an appropriate energy estimate S_{38}. The energy-dependent attenuation function was fixed to a size range of 20 VEM to 107 VEM. Below and above these limits, the attenuation parameters show strong correlations. Therefore, any shower size falling outside of this range is corrected with the respective attenuation function at the limit. For low shower sizes the attenuation parameters obtained for 20 VEM are used and for high shower sizes the parameters are fixed to the ones at 107 VEM. The distribution of events with $S_{38} > 20$ VEM is depicted in Fig. 4.9a for both the energy-dependent attenuation correction and the standard correction. A fit to the expected distribution of $\sin\theta\cos\theta$ is shown in addition. The event distribution for the standard approach follows the expectation up to an angle of about 45°. For higher zenith angles, there are more events than expected, indicating an overestimation of the energy. This overshoot of events is reduced by using the energy-dependent correction. Another check can by made by looking at the event distributions as function of $\sin^2\theta$ for different threshold values as depicted in Fig. 4.9b. A constant is fit to the distributions obtained with the energy-dependent attenuation correction. In addition, the distributions obtained from the standard attenuation function are plotted as dashed lines. The distributions using the energy-dependent approach are flat as expected in case of isotropy, whereas the ones determined from the standard attenuation correction show some deviations at the lowest and highest zenith angles. In Fig. 4.14d, the two-dimensional event distribution is checked for deviations from uniformity. The color code indicates the difference of the number of events within a bin in the $(\Delta\sin^2\theta, \Delta\lg S_{38})$ space to the mean number of events in a $\Delta\lg S_{38}$ bin in units of standard deviations. No significant deviations are observed above the threshold of 20 VEM.

In Fig. 4.10a, the size spectrum including all events above ~15 VEM (~3 EeV) as obtained with the energy-dependent correction is compared to the spectrum resulting from the standard approach. The iterative fit reduces the flux for the lower energy estimates in the vicinity of the ankle. The relative residual of the fluxes is shown in Fig. 4.10b. A maximum correction at the level of about 6 % is apparent for energy estimates below the ankle. With increasing size, the difference between the fluxes vanishes. To evaluate the impact on the energy spectrum, the energy estimates have to be calibrated with the energies measured by the FD. The energy calibration will be discussed in the next Section 4.5. Due to the differences in the energy estimates obtained with the two different attenuation corrections, each approach needs its own energy calibration.

Table 4.1: Parameters of the energy-dependent attenuation function obtained for SD-1500 data.

	a_0	a_1	b_0	b_1	c_0	c_1
Value	0.961	0.202	−1.608	−0.476	−1.148	−1.560
Uncertainty	0.012	0.054	0.022	0.100	0.120	0.553

SD-750 data

The work presented in [96] indicates an energy dependence of the attenuation correction for SD-750 data. As in the case of the SD-1500, the fit of the attenuation function is repeated for different values of S_{35}^{cut} and the resulting parameters are checked for a dependence on this cut. The different cut values are determined using Eq. (4.33), with a value of 1.15 for the scaling parameter α. The lowest threshold value S_1^{th} is set to 30 VEM. Using the energy calibration of [97], this is well above the full efficiency of 0.3 EeV ≈ 21 VEM, preventing any upward fluctuations due to inefficiencies. I consider $n = 10$ different cut values to ensure a valid number of events within each of the 100 bins in $\cos^2\theta$. Thus, the highest threshold is at 105.54 VEM. The procedure for the energy-dependent attenuation fitting is analog to the one for the SD-1500 data. For each cut value, the attenuation function is fit using the uniformity method. In Fig. 4.11a, the resulting attenuation parameters are compared to the one obtained with the standard approach, which uses only one cut at $S_{35} = 40$ VEM. Each parameter is then fitted with a linear dependence on the logarithm of the energy estimate as defined in Eq. (4.34).

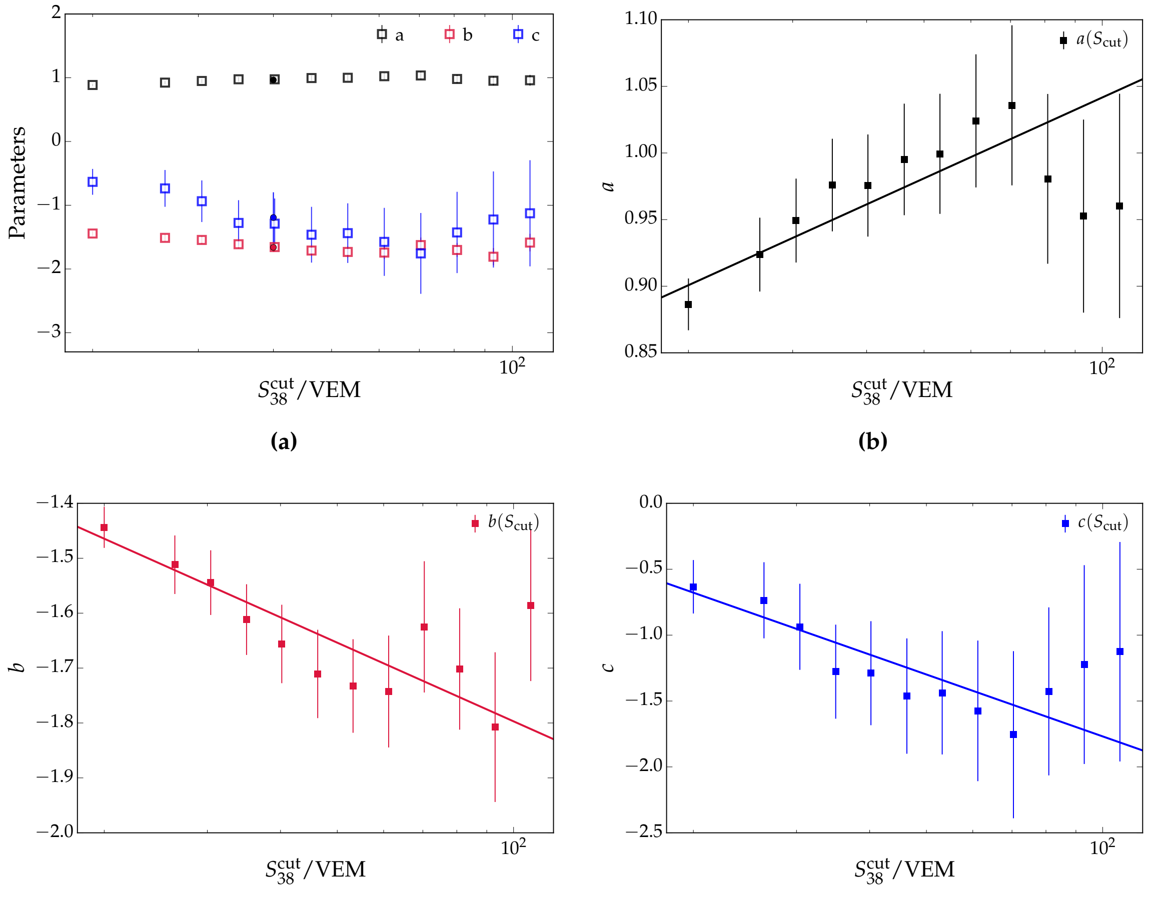

(a) **(b)**

(c) **(d)**

Figure 4.8: (a) Parameters for the SD-1500 obtained from the attenuation fit using different size thresholds. The parameters for a fixed cut of 40 VEM are shown in addition. (b), (c), (d) The energy dependence of each parameter is fitted assuming a logarithmic dependence on the energy estimate.

The individual fits to the parameters are depicted in Fig. 4.11b, Fig. 4.11c, and Fig. 4.11d and the fit values are stated in Table 4.2, together with their fit uncertainties. For each event with a shower size $S(450)$ and zenith angle θ, an initial estimate of S_{35} is calculated using a reference attenuation function with $S_{35} = S_0$. Hence, the attenuation function used for getting the first estimate is of the form of the standard attenuation function as the energy-dependent terms are canceling out. In the next step, the initial estimate S_{35}^* is then used instead of $S_{35} = S_0$. With this, a second estimate for S_{35} is obtained. As the attenuation function changes slowly with energy, the result of the second iteration is a valid estimate for S_{35}. In Fig. 4.12a, the angular distribution above 30 VEM as observed with the energy-dependent attenuation correction is compared to the one obtained with the standard correction. The overdensity of events at the highest zenith angles is reduced. A check for uniformity above different cut values is depicted in Fig. 4.12b. Besides the fluctuations visible for the lowest size cut, the distributions are compatible with uniformity. A two-dimensional check for uniformity is depicted in Fig. 4.14b. There is no significant deviation from uniformity apparent for energy estimates above the threshold of 30 VEM.

As the attenuation function is only explored from 30 VEM to 105.54 VEM, the parameters for any initial estimate of S_{35} below the lower limit are set to the ones at 30 VEM. Likewise, for any S_{35}^* values exceeding the upper limit, the parameters at 105.54 VEM are used. The

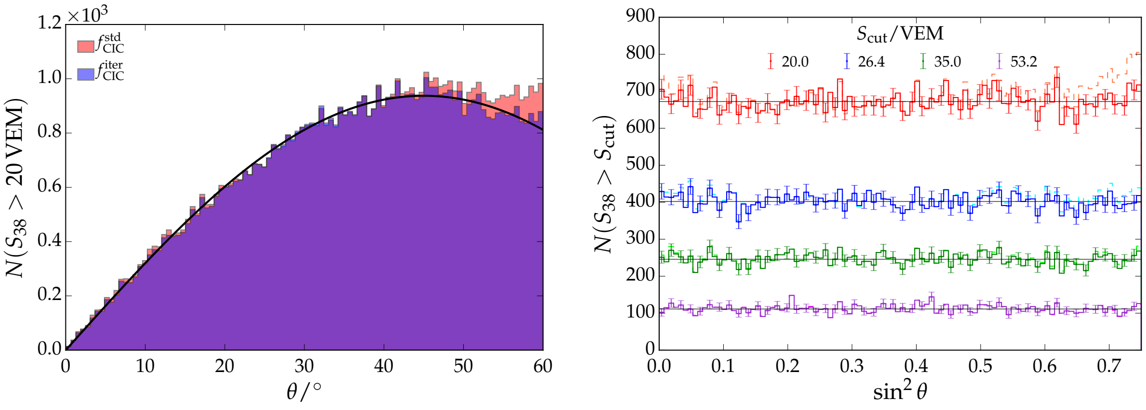

(a) **(b)**

Figure 4.9: (a) Angular distribution of events with $S_{38} > 20\,\mathrm{VEM}$. A fit to the expected $\sin\theta\cos\theta$ distribution is shown in black. (b) Event distribution for different threshold values as function of $\cos^2\theta$. The distributions for the energy-dependent attenuation correction (solid lines) are compared to the ones using the standard approach (dashed lines). The black lines show fits to a constant. Using the energy-dependent correction, the distributions are compatible with uniformity, whereas the standard method shows a increased number of events at the highest zenith angles.

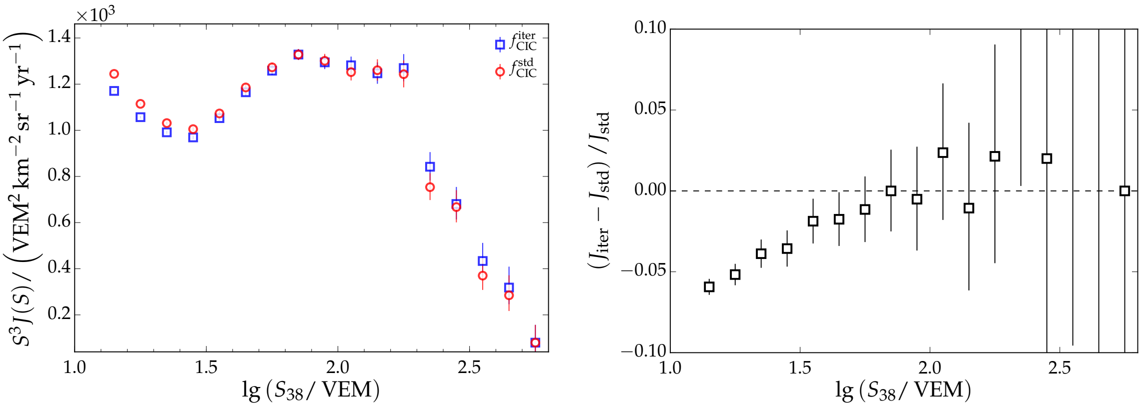

(a) **(b)**

Figure 4.10: (a) The spectrum of the energy estimates as obtained with the iterative energy-dependent attenuation correction and the standard correction using $S_{38}^{\mathrm{cut}} = 40\,\mathrm{VEM}$. Using the energy-dependent correction lowers the flux for energy estimates below the ankle. (b) Relative residual of the fluxes using the two different methods for correcting the attenuation.

resulting size spectrum is shown in Fig. 4.13a. The energy-dependent attenuation correction lowers the flux in the low size range. To further quantify the reduction of the flux, a relative residual with respect to the standard attenuation function is depicted in Fig. 4.13b. The maximum correction amounts to about 2 % at the lowest energy estimates. As expected, the difference vanishes when approaching the standard cut value of 40 VEM. The spectra are compatible within their uncertainties for higher size values. As in the case of the SD-1500, a separate calibration has to be performed on the energy estimator obtained with the energy-dependent attenuation correction to deduce the energy spectrum.

Table 4.2: Parameters of the energy-dependent attenuation function obtained for SD-750 data.

	a_0	a_1	b_0	b_1	c_0	c_1
Value	1.623	−0.355	−1.382	−0.719	−1.981	2.973
Uncertainty	0.011	0.079	0.030	0.211	0.150	1.078

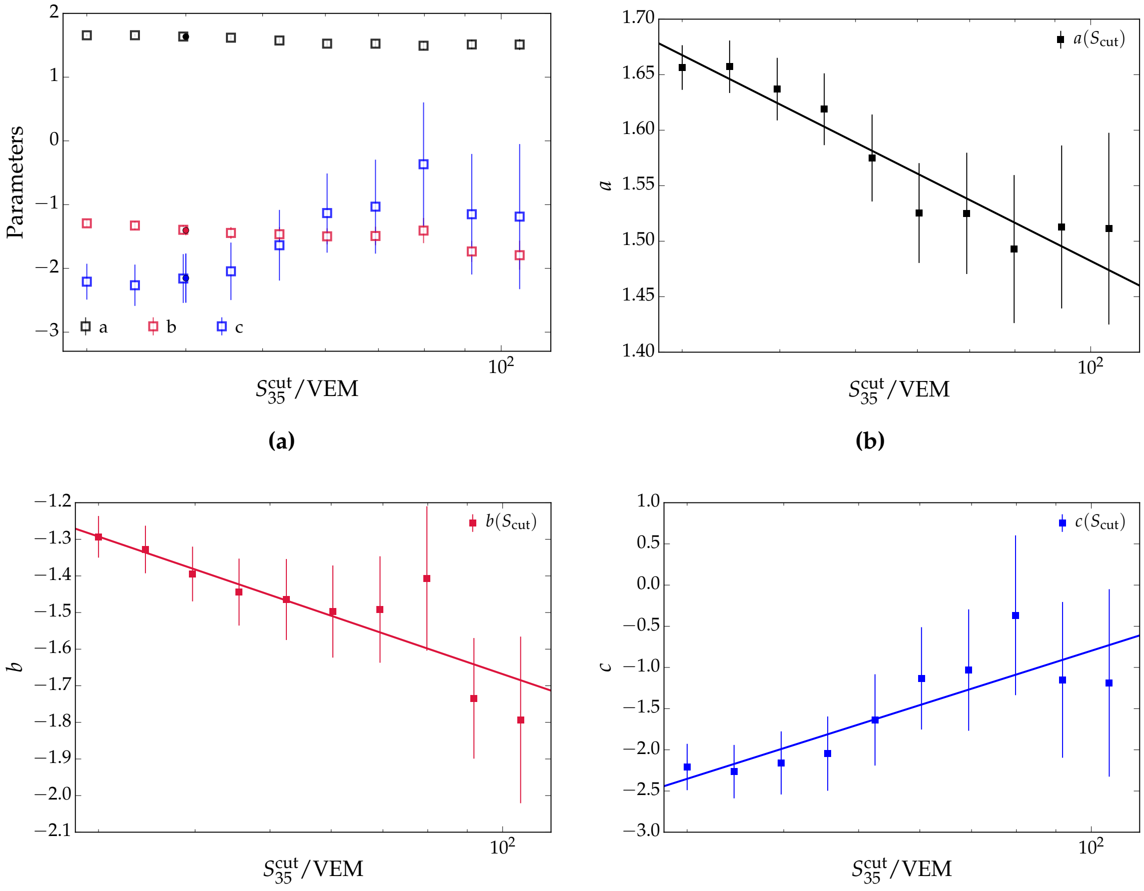

(a) **(b)**

(c) **(d)**

Figure 4.11: (a) Parameters for the SD-750 obtained from the attenuation fit using different size thresholds. The parameters for a fixed cut of 40 VEM are shown in addition. (b), (c), (d) The energy dependence of each parameter is fitted assuming a logarithmic dependence on the energy estimate.

Extended zenith range for the SD-750 data

Previous works [39, 60] showed that the fit quality of the attenuation correction for the SD-750 data worsens when the allowed maximum zenith angle is increased to 60°. A reasoning for this could be the change of the shower attenuation at higher zenith angles. With increasing zenith angle, the electromagnetic component vanishes and the muonic component starts to dominate. With the energy-dependent method, the attenuation function is fitted repeatedly, hence becoming more flexible.

In the following, SD-750 data up to 60° are used. The data selection follows the one described in Section 4.1, except for the cut on the zenith angle. The weather correction is applied to the shower sizes S_{450} and the same S_{35}^{cut} values are used. The standard method using a cut value of 40 VEM is repeated for the extended data set and compared to the

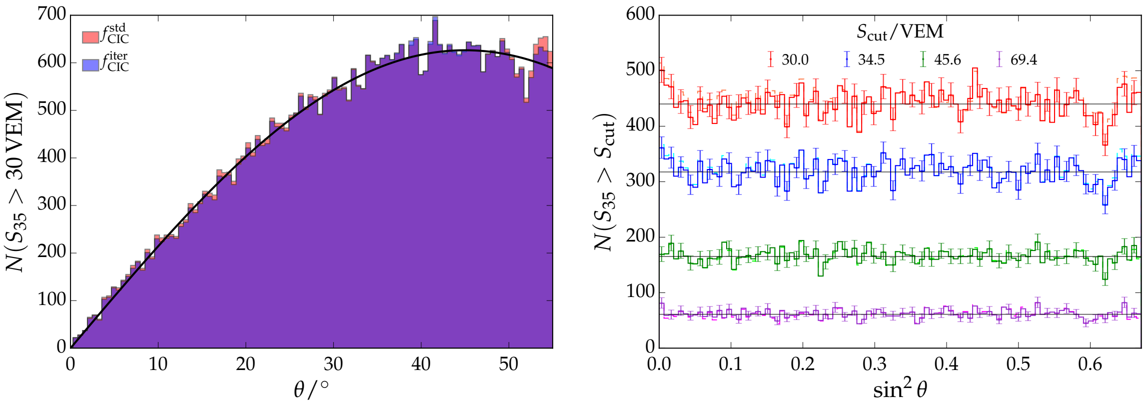

(a) **(b)**

Figure 4.12: (a) Angular distribution of events with $S_{35} > 30\,\mathrm{VEM}$. A fit to the expected $\sin\theta\cos\theta$ distribution is shown in black. (b) Event distribution for different threshold values as function of $\cos^2\theta$. The distributions for the energy-dependent attenuation correction (solid lines) are compared to the ones using the standard approach (dashed lines). The black lines show fits to a constant. Using the energy-dependent correction, the distributions are compatible with uniformity, whereas the standard method shows an increased number of events at the highest zenith angles.

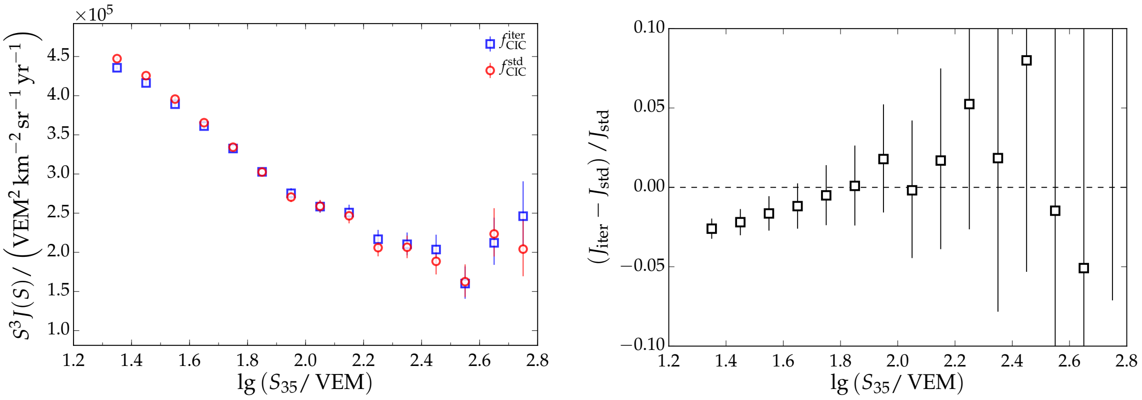

(a) **(b)**

Figure 4.13: (a) The spectrum of the energy estimates as obtained with the iterative energy-dependent attenuation correction and the standard correction using $S_{35}^{\mathrm{cut}} = 40\,\mathrm{VEM}$. Using the energy-dependent correction lowers the flux for energy estimates below the ankle. (b) Relative residual of the fluxes using the two different methods for correcting the attenuation.

iterative method. The results for the standard method are given in Appendix C.2. The resulting parameters for the iterative approach are shown in Fig. 4.15 and their values are stated in Table 4.3. The resulting zenith distributions are depicted in Fig. 4.16a. The upward fluctuation of events at highest zenith angle is reduced when using the energy-dependent correction. This can also be seen in the one-dimensional uniformity check shown in Fig. 4.16b. The resulting size spectrum is shown in Fig. 4.17a. Due to the increased zenith angle range, the exposure has to be corrected by a factor of 2.35 sr/2.1 sr. This corresponds to the ratio of the integral of $\mathrm{d}\Omega\cos\theta$ with a maximum zenith angle of 60° and 55°, respectively. A relative residual of the fluxes is depicted in Fig. 4.17b. The flattening at the lowest energies could be due to trigger effects, as full efficiency is reached at a higher energy for larger zenith angles. Further studies and tests of this method are necessary to investigate whether it will

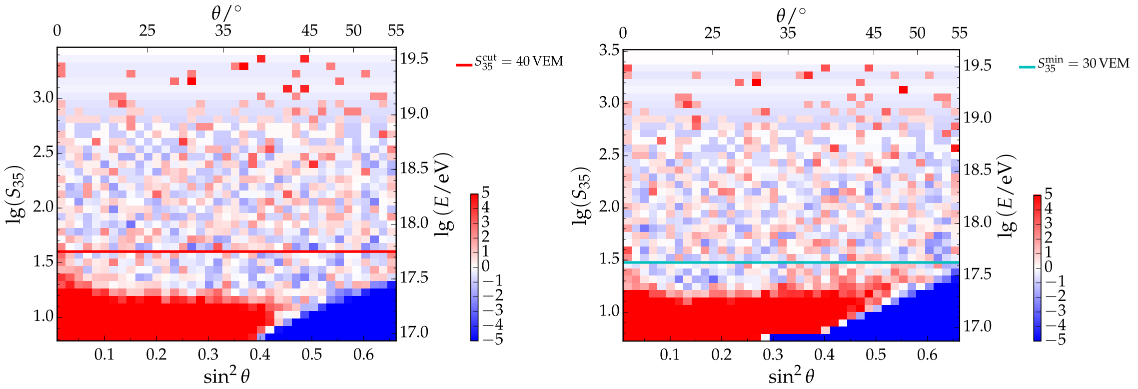

(a) SD-750 data

(b) SD-750 data

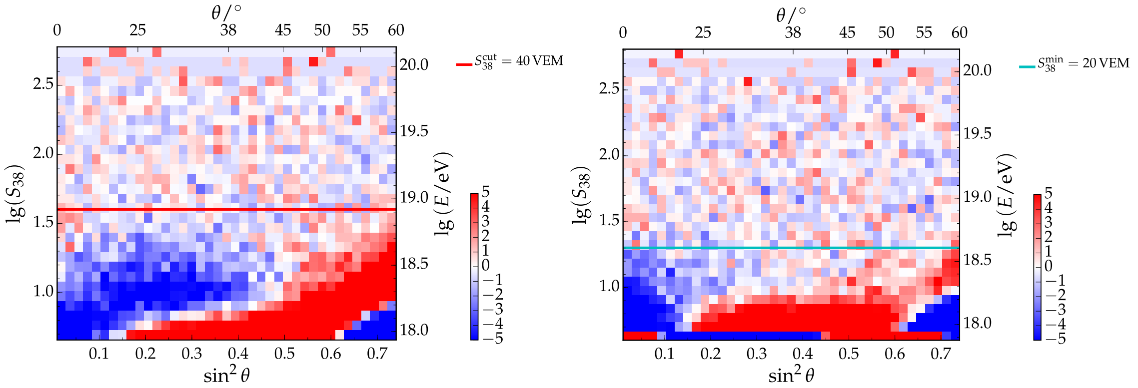

(c) SD-1500 data

(d) SD-1500 data

Figure 4.14: Two-dimensional event distribution of the energy estimates obtained with the (a), (c) standard attenuation correction and the (b), (d) energy-dependent attenuation correction for the SD-750 and SD-1500 data. The size thresholds above which events are used within the fit of the attenuation function are shown as horizontal lines. The color coding represents the deviation of the event numbers in a specific size and zenith angle bin from the mean number of events in the particular size bin. The deviation is given in units of standard deviation σ_{stat}. Using the energy-dependent correction reduces the fluctuations below the cut value, especially in case of the SD-1500.

be possible to extend the zenith range up to 60°, therefore closing the gap to the SD-1500 array. The analysis will benefit from the new triggers ToTd and MoPS due to their increased sensitivity at lower signals. These triggers have the potential to lower the threshold of full efficiency and increase the number of candidate stations for showers with higher zenith angles [39, 55].

Table 4.3: Parameters of the energy-dependent attenuation function obtained for SD-750 data up to 60°.

	a_0	a_1	b_0	b_1	c_0	c_1
Value	1.680	−0.136	−1.412	−0.713	−2.782	0.368
Uncertainty	0.007	0.049	0.029	0.210	0.086	0.616

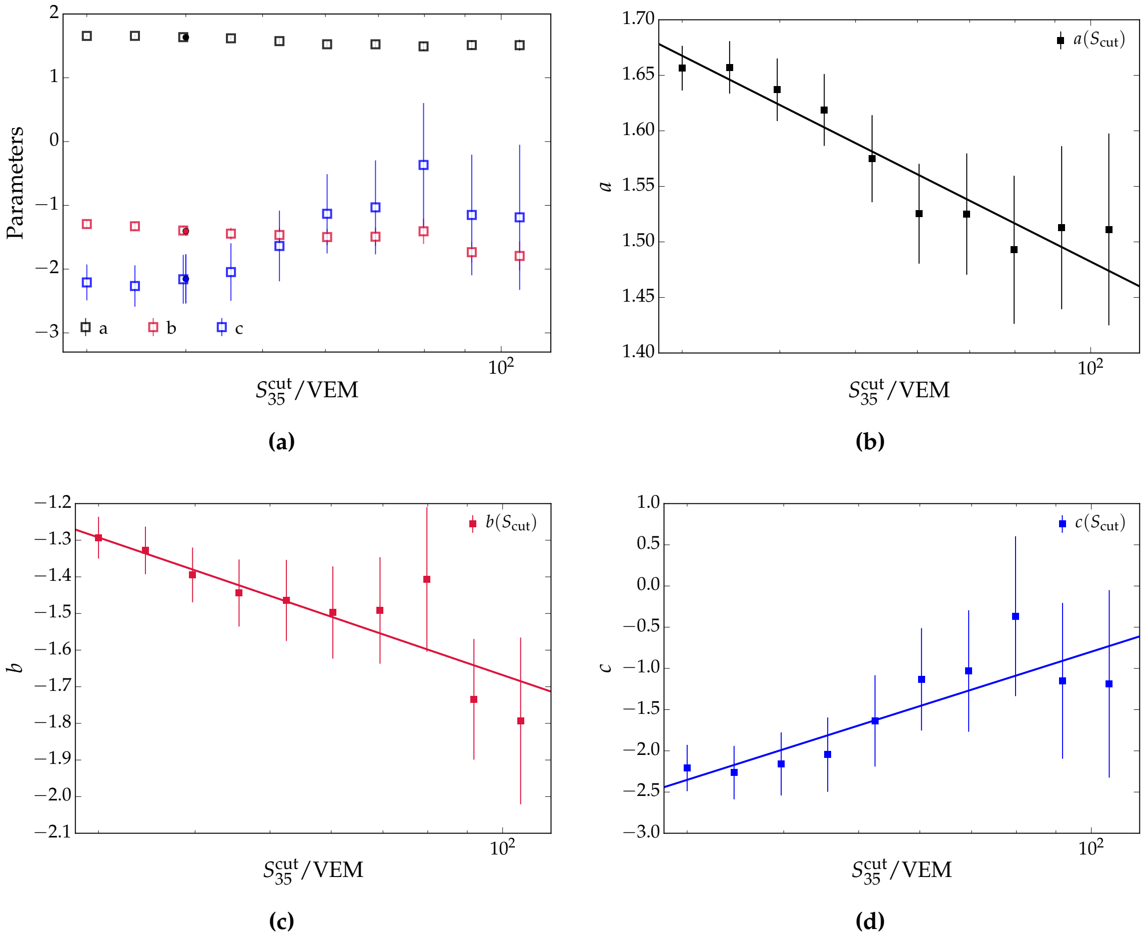

(a) **(b)**

(c) **(d)**

Figure 4.15: (a) Parameters for the SD-750 up to 60° obtained from the attenuation fit using different size thresholds. The parameters for a fixed cut of 40 VEM are shown in addition. (b), (c), (d) The energy dependence of each parameter is fitted assuming a logarithmic dependence on the energy estimate.

4.5 Energy calibration

In Section 4.4, the energy estimators $S = S_{SD}(\theta_{\mathrm{ref}}) = \{S_{35}, S_{38}\}$ for the SD were obtained after correcting the shower size estimators for their zenith dependence. In the next step, the energy estimators need to be calibrated to derive the energy of the incident primaries. As Auger employs a hybrid detector, it is possible to perform the calibration in an almost model-independent way by using the independent measurement of the FD. The SD is superior in its statistic due to its duty cycle of almost 100 % compared to 15 % of the telescopes but the FD sets the energy scale as it measures in a direct way the calorimetric energy of an air shower. A subset of events, called *golden hybrids*, is used for the calibration. This subset consists of events that were successfully reconstructed by both detectors independently. The shower size S is a function of the mass A of the primary. With the current detectors it is not possible to determine the mass on an event-by-event basis and hence the dependence on the mass cannot be taken into account. An unbiased calibration is ensured by applying an event selection that results in an unbiased mass composition within the golden hybrids. As the water-Cherenkov detectors are more sensitive to muons, the SD is slightly more efficient for iron induced showers due to the higher muon content. Therefore, selecting events with

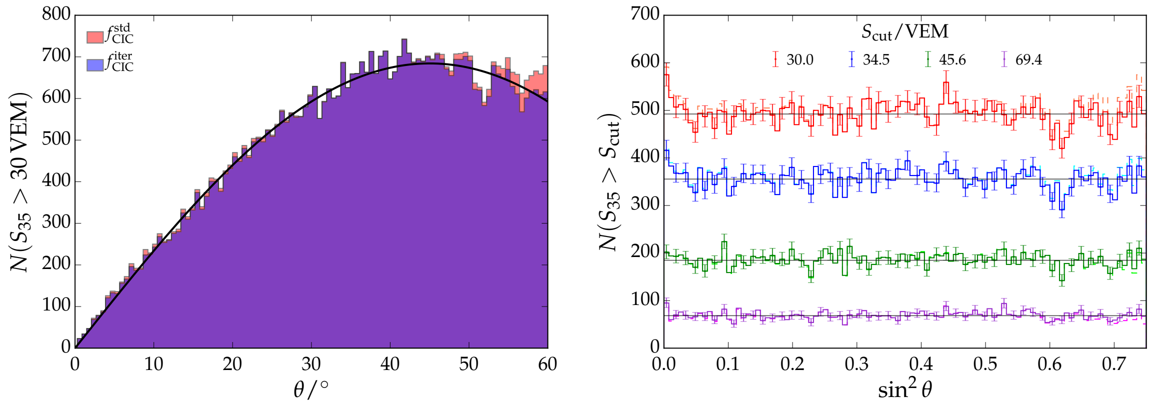

(a)

(b)

Figure 4.16: (a) Angular distribution of events with $S_{35} > 30\,\mathrm{VEM}$ and zenith angles up to 60°. (b) Event distribution for different threshold values as function of $\cos^2\theta$. The distributions for the energy-dependent attenuation correction (solid lines) are compared to the ones using the standard approach (dashed lines).

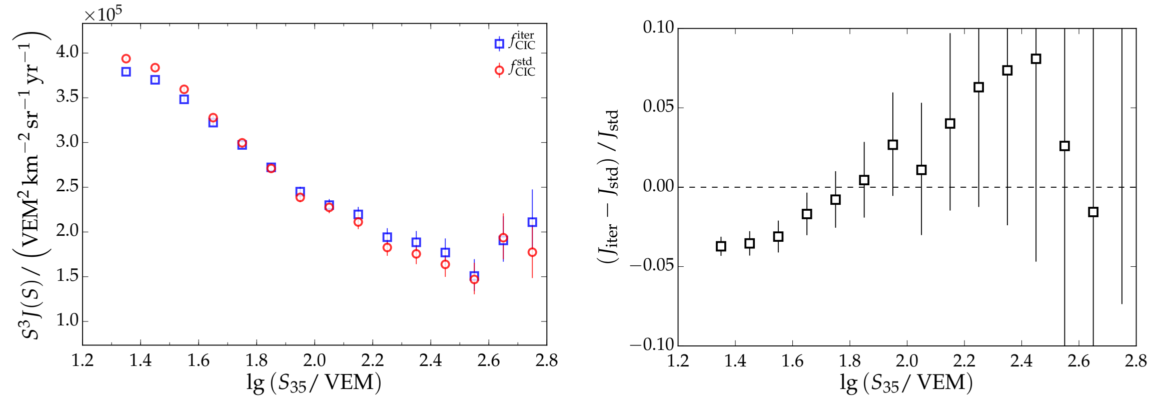

(a)

(b)

Figure 4.17: (a) The spectrum of the energy estimates as obtained with the iterative energy-dependent attenuation correction and the standard correction using $S_{35}^{\mathrm{cut}} = 40\,\mathrm{VEM}$. For both correction methods a maximum zenith angle of 60° was chosen. (b) Relative residual of the fluxes using the two different methods for correcting the attenuation.

primary energies above full efficiency prevents a composition bias in the SD data. The FD measurements have to be restricted to a fiducial FoV as described in Section 4.5.1.

4.5.1 Event selection

The event selection for the SD corresponds to the one described in Section 4.1. The data set is further reduced to golden hybrid events which fulfill a strict FD selection. The FD cuts are described in detail in Appendix B.1 and the cut sequence as used in combination with the Offline files is stated in Table B.3. The FD quality cuts serve the same purpose as the cuts applied to the SD data. They ensure the selection of data with a high-quality reconstruction and discard events which were recorded during bad operation conditions and hence are prone to biases in the reconstructed observables.

In a last step, the FD data are limited to a fiducial FoV. As depicted in Fig. 4.18, the telescopes have a limited FoV. Depending on the shower geometry, the measured X_{max}

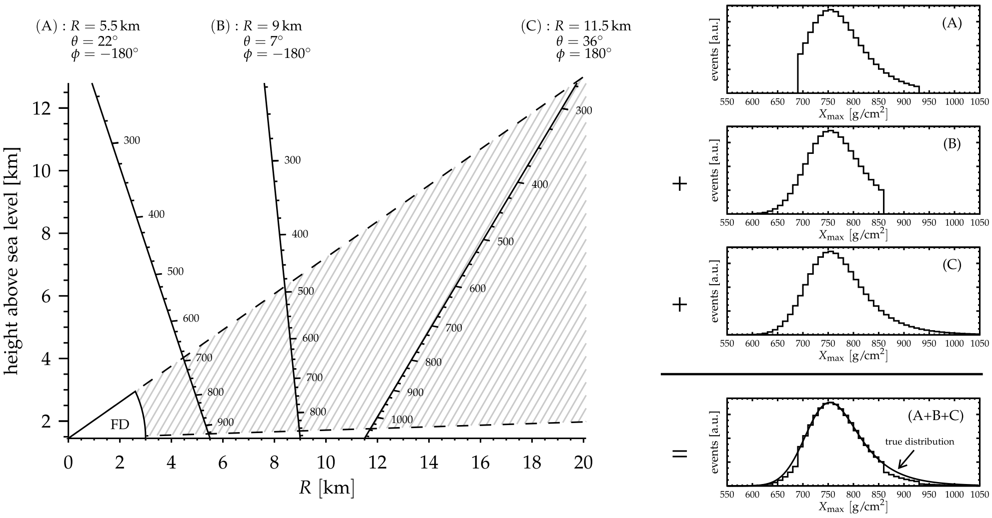

Figure 4.18: Schematic of the field of view (hatched area inside the dashed lines) of a fluorescence telescope. If a shower is detected depends on its incoming direction as well as its distance to the telescope. Three different shower geometries with different distance to the ground R, zenith angle θ and azimuth angle ϕ are depicted. The truncated X_{max} profiles are shown on the right panel. Figure taken from [31].

profiles are truncated if parts of the profiles lie outside of the FoV. Showers, for which only the rising or falling parts of the profile were measured, are discarded by the cut on the FoV. However, this cut is prone to introduce a mass-dependent selection bias. Showers develop more or less deeply in the atmosphere, depending on the mass of the primary particle. As a result, the probability of their profiles to be selected by the FoV cut differs. The fiducial FoV selection is applied to avoid a distortion of the true (yet unknown) X_{max} distribution, which is the sum of the distribution of individual primary masses. This selection ensures an equal probability of a proton or iron shower to be selected.

4.5.2 Calibration method

The energy E_{SD} of an event measured by the SD is estimated by using the simplified likelihood method as described in [98]. The key ingredient of the likelihood fit is the p.d.f.[3] $f(E_{\text{FD}}, S_{\text{SD}})$. It aims at modeling the observed event distribution and contains fluctuations due to air shower physics and detector effects. The energy of the incident particle is directly measured only by the FD and hence the events measured by the FD form the underlying distribution. Excluding all detector imperfections and shower-to-shower-fluctuations, the true event distribution is given by:

$$f_1(E, S, \theta) = \delta\left(S - S(E)\right) h(E, \theta). \tag{4.38}$$

Here, the distribution $h(E, \theta)$ is given by the cosmic ray flux multiplied by the detector aperture. The delta function includes the calibration function $S(E)$. To arrive at the actual observed event distribution, the different fluctuations need to be added to the p.d.f.. First, the shower-to-shower fluctuations that affect the SD signals at ground are taken into account:

$$f_2(E, S_{\text{sh}}, \theta) = \int_0^\infty \mathrm{d}S\, s\left(S_{\text{sh}}|S, \theta\right) \delta(S - S(E)) h(E, \theta). \tag{4.39}$$

The shower-to-shower fluctuations describe the fluctuations in the shower development. Any particle interaction implies statistical effects, hence the point of first interaction differs for

---

[3] probability density function

two identical primary particles (same energy, mass, and arrival direction). In addition, the interactions of the secondary particles within the atmosphere fluctuate. The combination of these effects is a smearing of the measured shower size around the true value. Next, the detector resolutions have to be included. This is done by adding the kernel functions $k(E_{\mathrm{FD}}|E,\theta)$ and $k(S_{\mathrm{SD}}|S_{\mathrm{sh}},\theta)$ to the p.d.f.:

$$f_3(E_{\mathrm{FD}}, S_{\mathrm{SD}}, \theta) = \int_0^{\infty} \mathrm{d}E \int_0^{\infty} \mathrm{d}S_{\mathrm{sh}} k(E_{\mathrm{FD}}|E,\theta) k(S_{\mathrm{SD}}|S_{\mathrm{sh}},\theta) f_2(E, S_{\mathrm{sh}}, \theta). \tag{4.40}$$

As a last step, the detector efficiency has to be taken into account. The efficiency of triggering ϵ depends on the signal after the detector resolution, as the resolution determines if more or less signal is measured. Including the normalization, the final p.d.f. reads now as:

$$f(E_{\mathrm{FD}}, S_{\mathrm{SD}}, \theta) = \frac{\epsilon_{\mathrm{SD}}(S_{\mathrm{SD}},\theta)\epsilon_{\mathrm{FD}}(E_{\mathrm{FD}},\theta) f_3(E_{\mathrm{FD}}, S_{\mathrm{SD}}, \theta)}{\int_0^{\pi/2} \mathrm{d}\theta \int_0^{\infty} \mathrm{d}E_{\mathrm{FD}} \int_0^{\infty} \mathrm{d}S_{\mathrm{SD}}\, \epsilon_{\mathrm{SD}}(S_{\mathrm{SD}},\theta)\epsilon_{\mathrm{FD}}(E_{\mathrm{FD}},\theta) f_3(E_{\mathrm{FD}}, S_{\mathrm{SD}}, \theta)}. \tag{4.41}$$

This full p.d.f. is computationally very expensive. Thus, some approximations are done in the following to speed up the minimization.

Including the efficiency terms allows one to include events outside of the range of full efficiency. Rather than working with efficiency curves, the standard approach is to use a step function. Once a certain value for E_{FD} is reached, the trigger efficiency jumps from 0 to 1. The exact threshold value depends on the data set. It is $3{\times}10^{17}$ eV for the SD-750 and $3{\times}10^{18}$ eV for the SD-1500. Introducing the step function simplifies the p.d.f. to:

$$f(E_{\mathrm{FD}}, S_{\mathrm{SD}}, \theta) \approx \frac{f_3(E_{\mathrm{FD}}, S_{\mathrm{SD}}, \theta)}{\int_0^{\pi/2} \mathrm{d}\theta \int_0^{\infty} \mathrm{d}E_{\mathrm{FD}} \int_0^{\infty} \mathrm{d}S_{\mathrm{SD}}\, f_3(E_{\mathrm{FD}}, S_{\mathrm{SD}}, \theta)}. \tag{4.42}$$

The next approximation concerns the treatment of the detector fluctuations k_{SD} and the shower-to-shower fluctuations. Both can be approximated with a normal distribution. More details and calculations can be found in [98, 99].

The third approximation simplifies the description of the hybrid distribution $h(E,\theta)$. As the folding of the cosmic ray flux with the FD aperture is difficult to compute, the distribution is estimated from data directly using bootstrapping. The approximated p.d.f. is:

$$h(E,\theta) \approx \frac{1}{N}\sum_i^N \delta(E - E_{\mathrm{FD}})\delta(\theta - \theta_i), \tag{4.43}$$

where i runs over the N hybrid events that fulfill the same FD cuts as the *golden hybrid* events but do not need the SD to trigger independently. The hybrid events are not cut for full efficiency in order to correctly take event migrations into account when estimating the distribution.

Combining all approximations results in the following simplified likelihood:

$$\log \mathcal{L} = \sum_k \log\left[\sum_i \frac{e^{-\frac{1}{2}\frac{(E_{\mathrm{FD},k}-E_{\mathrm{FD},i})^2}{\sigma^2_{\mathrm{FD},i}}}}{\sigma_{\mathrm{FD},i}} \frac{e^{-\frac{1}{2}\frac{(S_{\mathrm{SD},k}-S(E_{\mathrm{FD},i}))^2}{\sigma^2_{\mathrm{SD}}(S(E_{\mathrm{FD},i}),\theta_i)+\sigma^2_{\mathrm{sh}}(E_{\mathrm{FD},i},\theta_i)}}}{\sqrt{\sigma^2_{\mathrm{SD}}(S(E_{\mathrm{FD},i}),\theta_i) + \sigma^2_{\mathrm{sh}}(E_{\mathrm{FD},i},\theta_i)}}\right], \tag{4.44}$$

with k running over the golden hybrid events and i is the index for the hybrid events that are used in the bootstrap estimate. In the next section , I will discuss a necessary correction that needs to be applied to the FD energies entering the calibration. The resolutions entering the likelihood will be discussed in Section 4.5.4 and the results for both SD-750 and SD-1500 are given in Section 4.5.5.

4.5.3 Correction of reconstruction biases

Before performing the energy calibration, possible biases in the reconstruction of SD and FD events have to be studied and corrected for. For the work presented in [100], a significant bias in the reconstructed FD energies was found for SD-750 data. Comparing the reconstructed calorimetric FD energy to the Monte Carlo energy, I found a bias that ranged from about $-20\,\%$ at 10^{17} eV and $-10\,\%$ at $3{\times}10^{17}$ eV to about $-1\,\%$ at $3{\times}10^{18}$ eV. As it was unclear at that point if the full bias was present in data, the decision was made to correct only for half of the bias and add the other half as systematic uncertainty on the flux. The energy bias as well as the correction factor for half of the bias are illustrated in Fig. C.3a and Fig. C.3b, respectively.

The correction applied in this work as well as in [97] is updated with respect to the aforementioned bias correction. This is necessary due to an improvement implemented in the fit of the longitudinal profile. The Gaisser-Hillas fit was extended with a Gaussian constraint on the area over peak ratio of the profile, $k = E_\text{cal}/(\mathrm{d}E/\,\mathrm{d}X_\text{max})$. The constraint was parametrized using proton and iron showers simulated with CONEX [101] and the latest hadronic interaction models (QGSJet-II.04, Epos-LHC, and Sibyll-2.3). The final parameters are obtained by averaging over the parameters obtained for the different simulation settings:

$$k = 332.6 + 13.67\,\lg(E_\text{cal})\ \mathrm{g\,cm^{-2}}. \tag{4.45}$$

The implementation of the constraint reduces the energy bias at low energies as is illustrated in Fig. 4.19. I re-analyzed the energy bias with proton and iron showers using QGSJet-II.04 simulations from the library described in Appendix A.4. The same FD quality cuts as described in Appendix B.1 were applied to be compatible with data. The cut on the fiducial FoV differs for simulations. Here, a primary-dependent cut obtained from simulations was applied instead of the one derived from data. To parametrize the energy bias I used a 50/50 mix of high-quality proton and iron showers as a function of E_cal:

$$\Delta E = 0.052919\left[\operatorname{erf}\left(\log_{10} E_\text{cal}^\text{MC} - 17.581\right)^2 - 0.92935\right]. \tag{4.46}$$

The parameterization is visualized in Fig. 4.19. The maximum bias is on the order of $-5\,\%$ at $3{\times}10^{17}$ eV and vanishes for the highest energies. In Fig. 4.20a, the bias in the total energy is compared to the bias of the parametrization derived prior to the constrained fit. At the lower energies, it is on the same order as half of the bias from the previous parametrization. Therefore, when comparing the energy shifts in Fig. 4.20b, the difference between the shift in the uncorrected data sets in blue and in the corrected ones in black is rather small. The energy shift in the uncorrected data set is due to the improvements in the FD reconstruction of HeCo events that were implemented after the work presented in [100]. More details on the reconstruction updates are stated in [102]. Besides the updates, a change was made to the energy scales concerning the Co[4] and HEAT eyes. In an ideal case, all FD eyes would have an identical energy scale. However, due to their different locations in the shower, the energies measured in stereo events are slightly shifted. This is illustrated in Fig. 4.21. For showers measured simultaneously by Co and HEAT, the energies should be compatible when HEAT is run in downward mode, as both eyes are located next to each other and measure the same part of the showers. Nevertheless, a difference of 5.3 % is found between the two reconstructed energies. While this difference was resolved by shifting the Co energies down by 5.3 % with the argument of HEAT having the newer electronics, it was decided to reverse this correction. For the work given in [97] and follow-up analyses, the HEAT energies are rescaled upwards to match the energy scale given by Co. For simulation studies, the rescaling consists of a constant shift of $1/(1-5.3\,\%) = +5.6\,\%$. The data uses a time-dependent rescaling factor instead.

---

[4] Coihueco

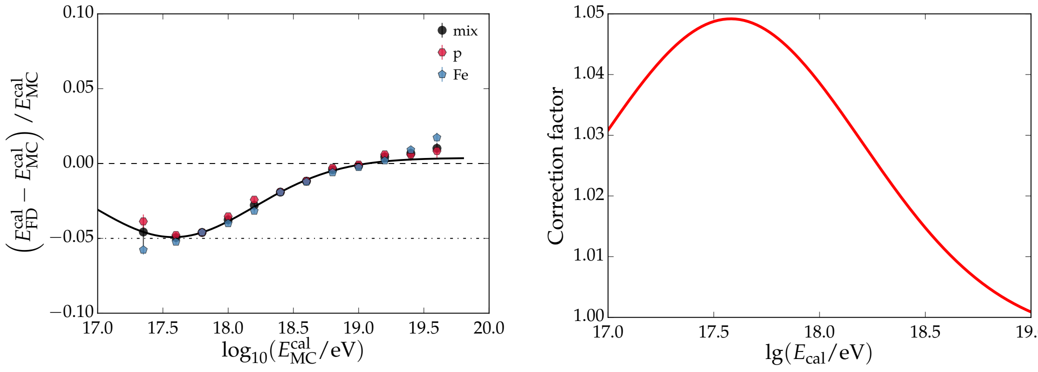

(a) **(b)**

Figure 4.19: (a) Energy bias in the calorimetric FD energy as estimated proton, iron and a mixed composition. The bias is at the 5% level at the threshold energy for full efficiency and decreases with increasing energy. The full bias correction is applied within this work and the one presented in [97]. (b) Resulting correction factor.

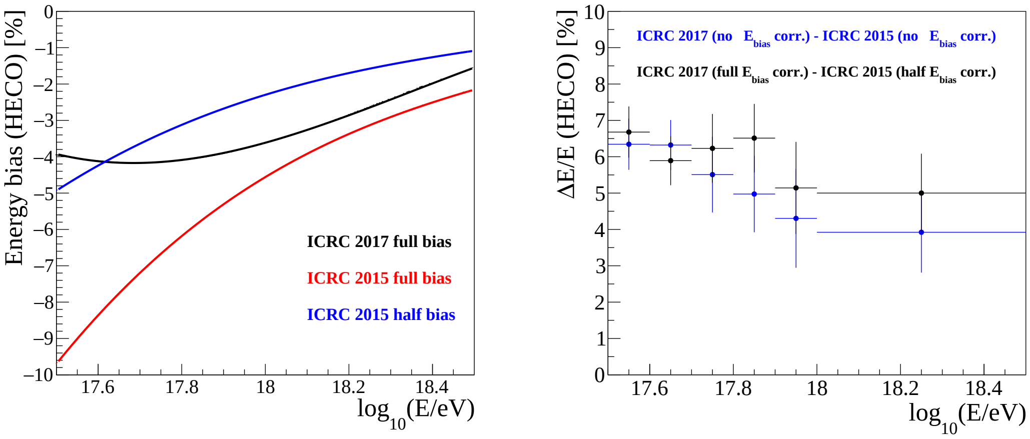

(a) **(b)**

Figure 4.20: (a) Comparison of the biases in the total FD energy. The ICRC 2017 bias has to be compared to half of the bias of ICRC 2015. The full ICRC 2015 bias was present in SD-750 simulations prior to the constrained fit of the Gaisser-Hillas profile and the energy scale was obtained by correcting $E_{\rm cal}$ for half of this bias. (b) Energy shift for HeCo events due to the improvements in the reconstruction. The shift based on the uncorrected calorimetric energies is shown in blue, in black is the one obtained after the correction [102].

4.5.4 Resolutions

The energy calibration presented in Section 4.5.2 includes the FD energy resolution as well as the resolution of the SD energy estimate. Both resolutions can be estimated from data alone through their statistical and systematic reconstruction uncertainties. The relative resolution for the FD measurements is shown in Fig. 4.22a and Fig. 4.22c for the SD-750 and SD-1500 data, respectively. The resolution is shown as function of energy and for three different zenith angle ranges. Overall, the FD resolution for both data sets shows only a slight dependence on the energy and zenith angle. In both cases, the resolution is below 10 % for most of the events as the mean values of the profiles show. An average value of 6.6 % for the SD-750 and 6.9 % gives a sound description. Taking into account the uncertainties on $E_{\rm FD}$ which are not stored

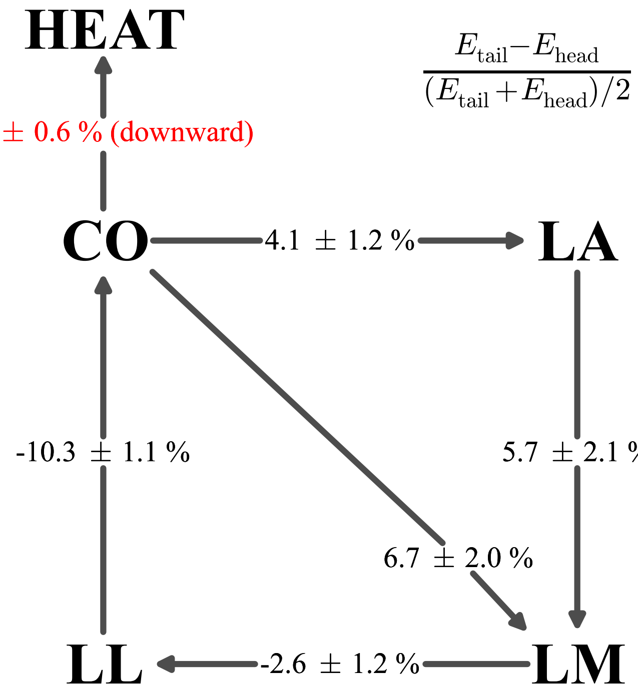

Figure 4.21: Relative energy differences as measured in stereo events among the different FD eyes. Schematic taken from [103].

in the ADST[5] data (1 % for horizontal uniformity of aerosols, 1 % for atmosphere variability, and 3 % for nightly relative calibration), the average resolutions increase to 7.4 % and 7.7 %. The relative resolutions of the energy estimators S_{35} and S_{38} are shown in Fig. 4.22b and Fig. 4.22d. In case of the SD-750, the resolution starts at a level of about 10 % at the full efficiency threshold of $3{\times}10^{17}$ eV and levels out to about 5 % for energies above 2 EeV. A dependence on the zenith angle is visible, with the highest zenith angles slightly exceeding the 10 % at the lowest energies. A similar behavior is apparent for the resolution of the SD-1500. The resolution is about 12 % at $3{\times}10^{18}$ eV and decreases to about 6 % at the highest energies. The zenith-angle dependence is less pronounced as in the case of the SD-750 data.

4.5.5 Results

The relation between the energy estimate $\hat{S}$ obtained with the SD and the energy as measured with the FD is described by a simple power law:

$$E_{\mathrm{FD}} = A \left(\frac{\hat{S}}{\mathrm{VEM}}\right)^{B} . \tag{4.47}$$

The calibration is performed individually for the SD-750 and SD-1500 data by minimizing the likelihood of Eq. (4.44). Both data sets are selected for golden hybrid events with the cuts described in Appendix B.1. This results in 1276 events in case of the SD-750 and 2661 events for the SD-1500.

The resulting calibration function for the SD-750 is shown in Fig. 4.23a together with the golden hybrid events used in the calibration fit. The data are well described by the following fit function:

$$E(S_{35}) = (14.07 \pm 0.43) \times 10^{15}\,\mathrm{eV} \left(\frac{S_{35}}{\mathrm{VEM}}\right)^{(1.000\pm0.008)} . \tag{4.48}$$

---

[5] Advanced Data Summary Tree

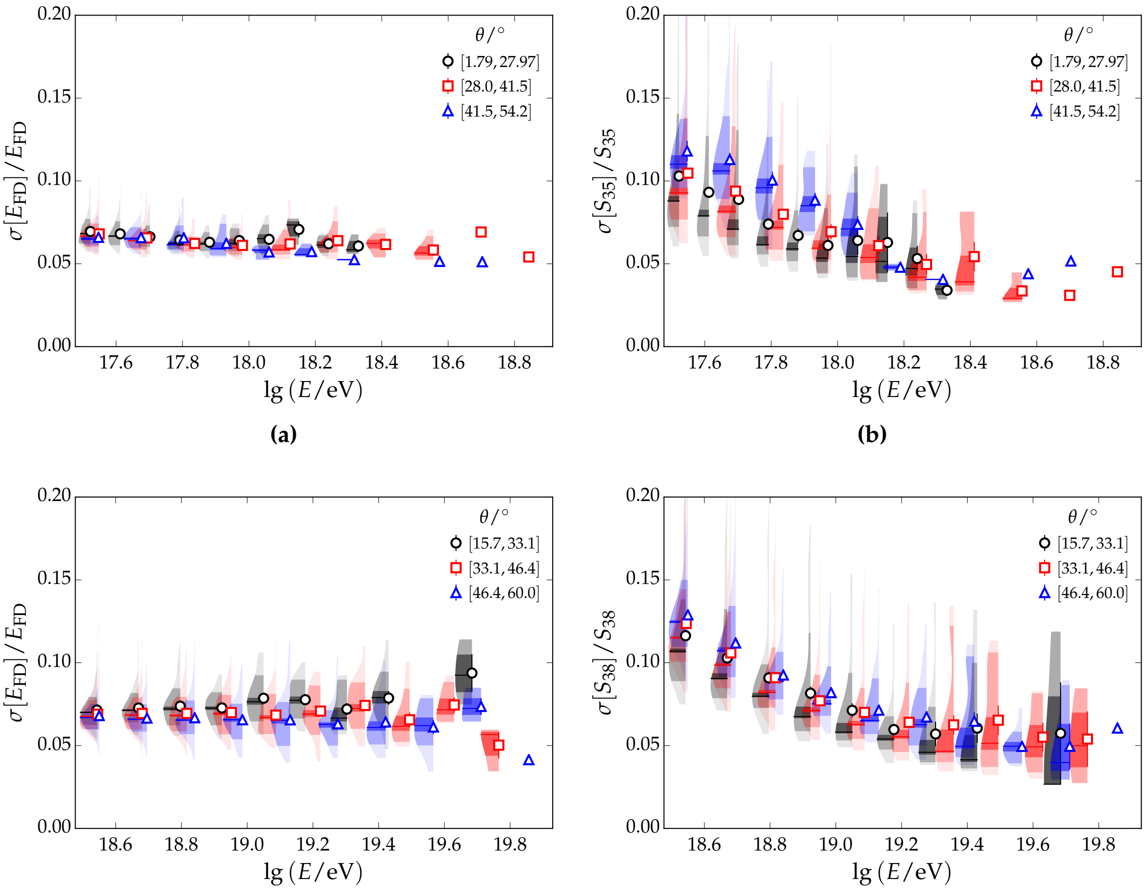

(a) **(b)**

(c) **(d)**

Figure 4.22: (a) Relative FD energy resolution for events measured with the SD-750 as function of logarithmic energy and for three zenith angle bins. A minor dependence on the energy is visible. (b) Relative resolution for the energy estimator of the SD-750. (c) Relative resolution of E_{FD} for events measured with the SD-1500. (d) Relative resolution for S_{38}. The resolution of the SD estimators show a stronger energy-dependence than the resolutions of E_{FD}.

For the shower-to-shower fluctuations, a constant value of 10 % is assumed. The energies of the golden hybrid events have been fully corrected for the bias described in Section 4.5.3. The statistical uncertainty on the calibration function is below 3 % at all energies as shown in Fig. 4.25a. For the SD-1500 data, the resulting energy calibration is:

$$E(S_{38}) = (0.178 \pm 0.003) \times 10^{18}\,\text{eV} \left(\frac{S_{38}}{\text{VEM}}\right)^{(1.042\pm0.005)} . \tag{4.49}$$

In Fig. 4.23b, the calibration function is compared to the golden hybrid data used in the calibration fit. As in the case of the SD-750, the shower-to-shower fluctuations are estimated to 10 % for all energies. The statistical uncertainty on the calibration function is depicted in Fig. 4.25b and is less than 2 % for all energies.

In Fig. 4.24, the golden hybrid data are divided into two zenith angle bins based on the reference angle. No outliers are found when looking at the data. Separate calibrations are performed on the zenith-binned data sets. The resulting calibration fits are shown in Fig. C.5 and Fig. C.6 for the SD-750 and SD-1500 data, respectively. The calibration functions obtained for the reduced set of golden hybrids are compatible within the uncertainties.

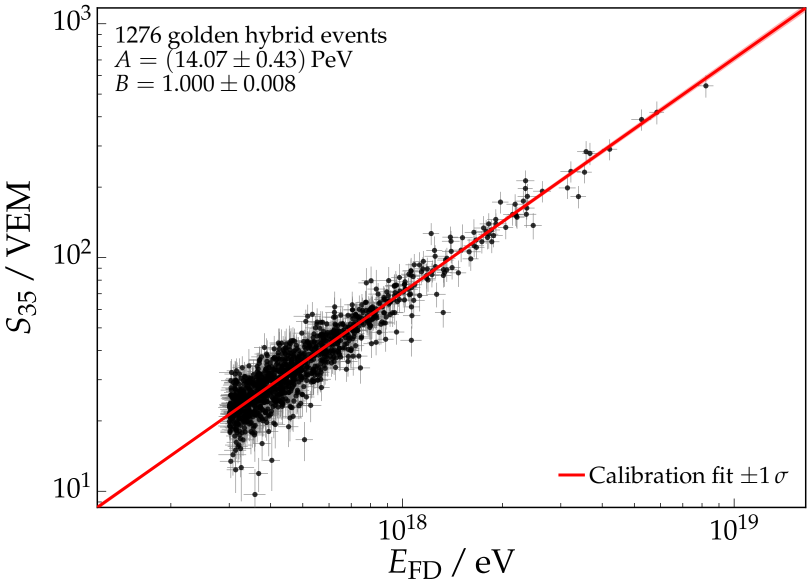

(a)

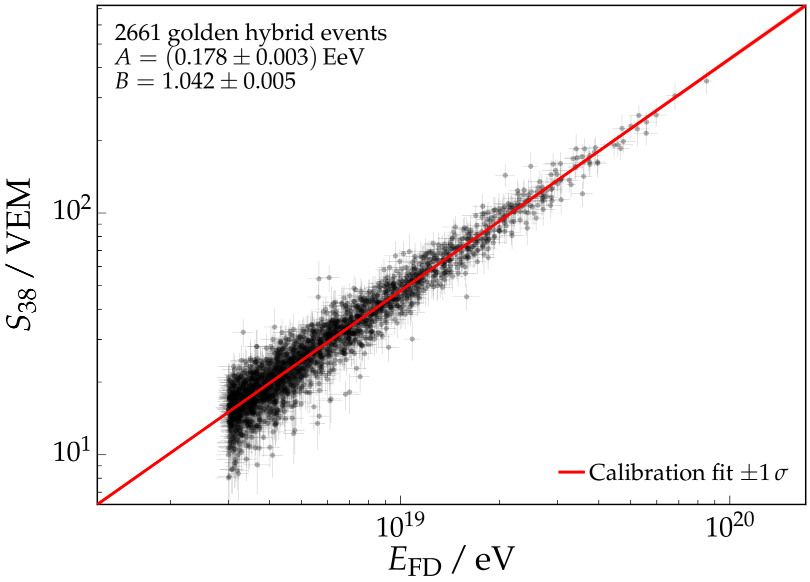

(b)

Figure 4.23: (a) Energy calibration for the SD-750. The golden hybrid events are shown in addition. The energy estimates are corrected for weather effects and the FD energies are corrected for the energy bias in the calorimetric energy as described in Section 4.5.3. (b) Energy calibration for the SD-1500. The energy estimates are corrected for weather and geomagnetic effects.

In Fig. 4.26, the quality of the energy calibration is checked by comparing the assigned SD energy to the FD energy. The relative residuals as function of E_{FD} are shown in Fig. 4.26a and Fig. 4.26c for the SD-750 and SD-1500 data, respectively. No systematic dependence on the energy is visible. In addition, the residuals are calculated as function of zenith angle in Fig. 4.26b and Fig. 4.26d, with no systematic trend being apparent.

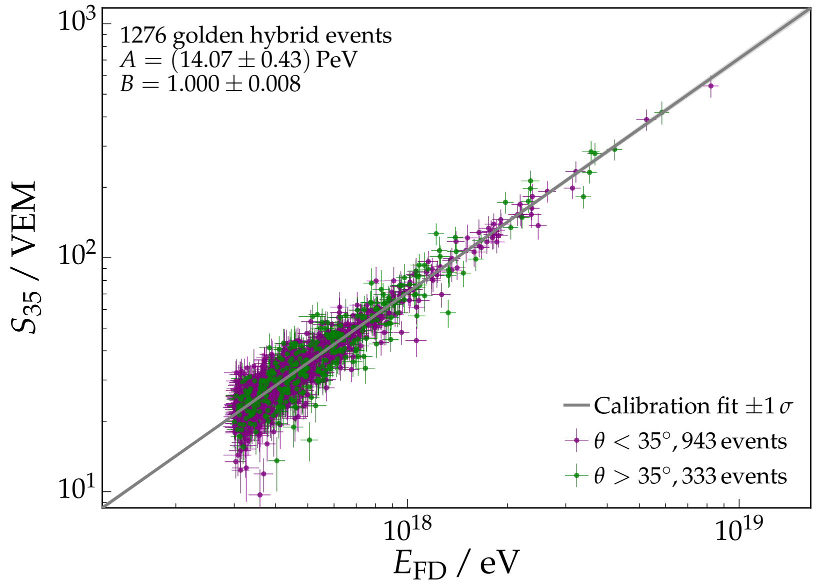

(a)

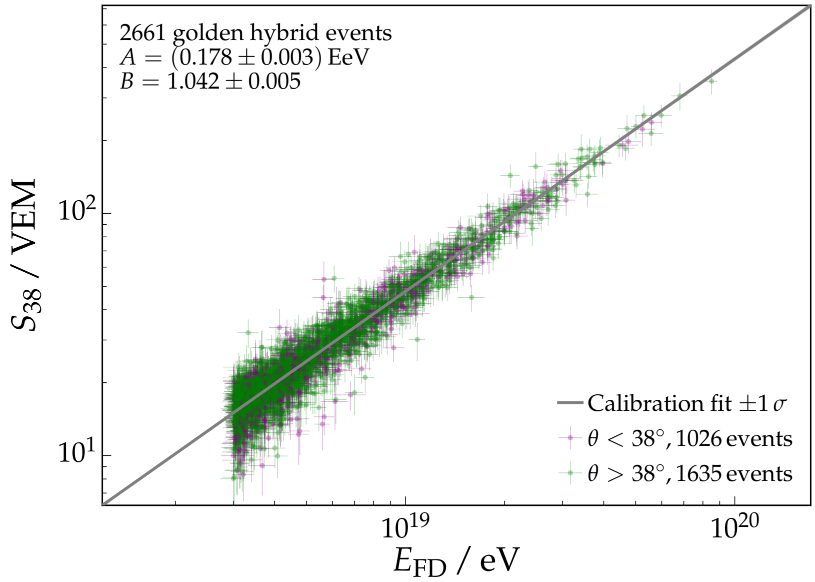

(b)

Figure 4.24: Energy calibration for the (a) SD-750 and (b) SD-1500 data. The data are divided into two zenith angle ranges. The division is done according to their respective reference angle.

4.5.6 Re-calibrating SD-750 data using a constrained fit

A validation of the energy calibration can be performed by comparing events that have been measured by both the SD-750 and SD-1500 array. The SD-750 array is a nested array within the SD-1500 and as such a subset of the stations are shared with the SD-1500. The shared stations are included in the data reconstruction of both data sets, while the nested stations participate only in the event recording of the SD-750. As a consequence, an event falling in this part of the array can fulfill the trigger conditions of both the SD-750 and SD-1500. Once both arrays triggered on the same event, the reconstructions are performed separately. Using the energy calibrations derived in Section 4.5.5, a common subset of 501 events is found with

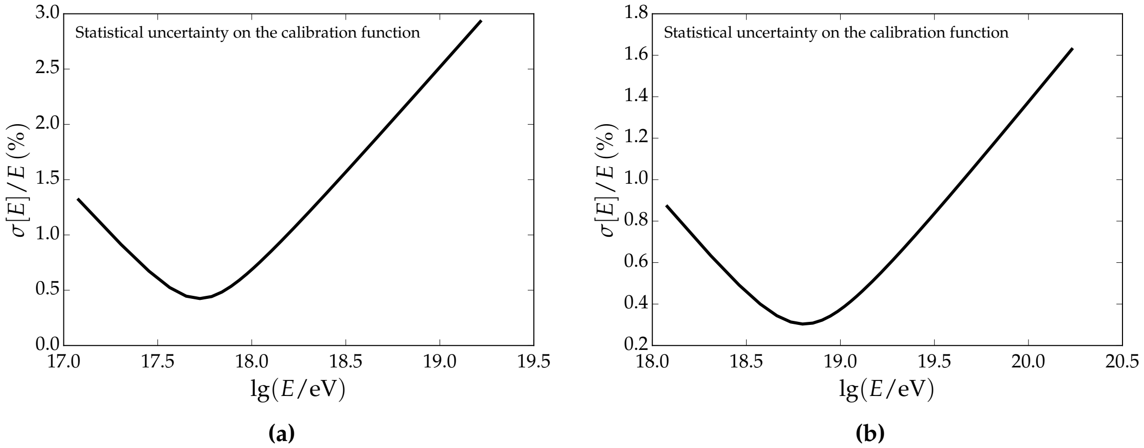

Figure 4.25: Statistical uncertainty on the calibration function as function of energy for (a) the SD-750 and (b) the SD-1500.

energies exceeding the full efficiency of $3{\times}10^{18}$ eV of the SD-1500. In Fig. 4.27a, the relative difference of the reconstructed energies for the common events is shown as function of the SD-1500 energy. Energies reconstructed with the SD-750 are systematically smaller. The bias is constant for the studied energy range and amounts to 6.3 % on average. The statistical uncertainties of the calibration fits, which are given as bands around zero, cannot account for the observed difference in the reconstructed energies.

I will follow the work of [63] to overcome this bias. The author of this work extended the energy-calibration fit of the SD-750 data by a constraint, requiring the SD-750 energies to be compatible with the energies of the common SD-1500 events. The idea behind is that the slope of the calibration function is determined by the bulk of events at lower energies. By adding the common SD-1500 events to the calibration fit, the number events with energies above 10^{18} eV to fit the slope to is increased. The constrained fit is realized by adding another log-likelihood to the one stated in Eq. (4.44). The additional log-likelihood uses the resolution of $E(S_{38})$ instead of the FD resolution. The result of the minimization of the sum of the log-likelihoods is:

$$E(S_{35}) = (13.00 \pm 0.17) \times 10^{15}\,\text{eV} \left(\frac{S_{35}}{\text{VEM}}\right)^{(1.023\pm0.003)} . \tag{4.50}$$

Comparing the parameters of this calibration function to the ones derived in Eq. (4.48) gives a difference on the order of about 2.3σ. The actual functions are shown in Fig. 4.28a, together with the golden hybrid events for the SD-750. The change in slope is clearly visible at higher energies, while the low energies are almost unaffected. The impact in the common energy range is studied by comparing the re-calibrated SD-750 energies to the SD-1500 energies, as shown in Fig. 4.27b. The difference in reconstructed energy is reduced to 1 % when using the constrained fit.

The SD-750 calibration given in Eq. (4.50) is used throughout the following analyses and the difference to the function of Eq. (4.48) is treated as systematic. In Fig. 4.29a, the flux derived with the standard calibration is compared to the one obtained from the constrained calibration fit. The following linear function describes well the flux difference:

$$\frac{\Delta J}{J} = (2.14 \pm 0.38) + (-0.12 \pm 0.09)\,\lg E. \tag{4.51}$$

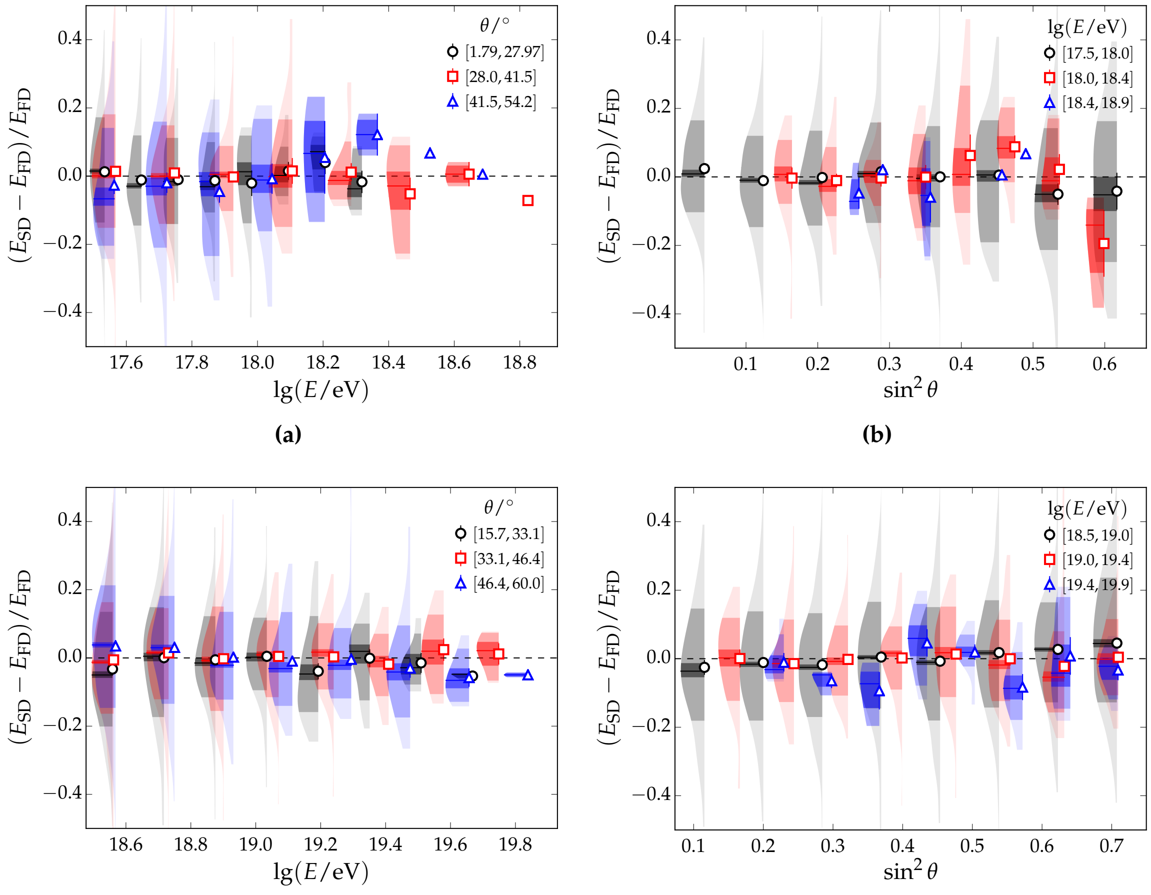

(a) **(b)**

(c) **(d)**

Figure 4.26: Energy residuals after the calibration for the SD-750 as function of (a) energy and (b) zenith. The residuals for the SD-1500 are shown in (c) and (d) as function of energy and zenith, respectively.

Half of this flux difference is used as systematic, as shown in Fig. 4.29b. At $3{\times}10^{17}$ eV, the relative systematic amounts to 2 %. The systematic vanishes at about $10^{17.82}$, where the fluxes are identical, and increases towards higher energies, up to 10 % at $10^{19.5}$ eV.

4.5.7 Calibration for the energy-dependent attenuation correction

In Section 4.4.3, the SD energy estimator was obtained using an iterative, energy-dependent attenuation correction. As the energy estimator calculated with the new method differs from the one given by the standard attenuation correction, the energy calibration has to be re-done. The same FD events as in the previous section are used and the same constant value of 10 % for the shower-to-shower fluctuations is assumed for both data sets.

The resulting energy calibration for the SD-750 data is:

$$E(S_{35}) = (14.55 \pm 0.44) \times 10^{15}\,\mathrm{eV}\left(\frac{S_{35}}{\mathrm{VEM}}\right)^{(0.992\pm0.008)}. \tag{4.52}$$

When using the constrained fit for the energy calibration as described in Section 4.5.6, the calibration parameters result in:

$$E(S_{35}) = (13.55 \pm 0.17) \times 10^{15}\,\mathrm{eV}\left(\frac{S_{35}}{\mathrm{VEM}}\right)^{(1.013\pm0.003)}. \tag{4.53}$$

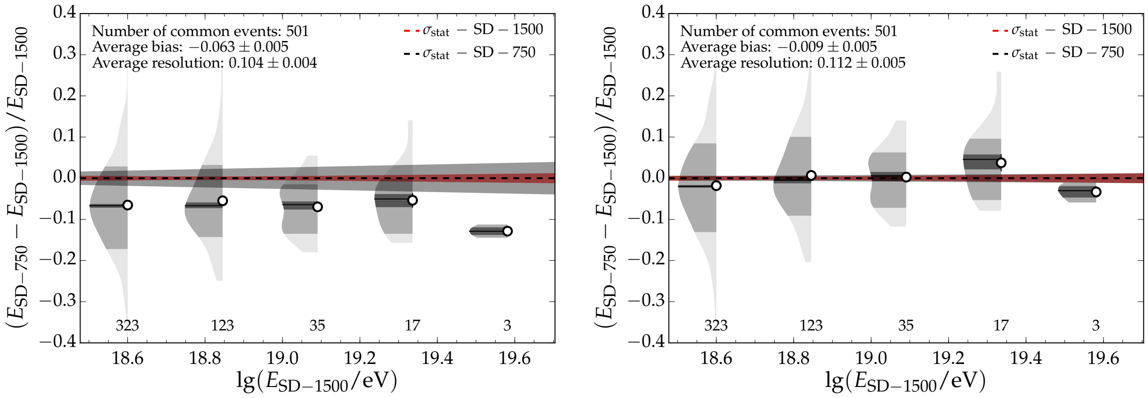

(a) **(b)**

Figure 4.27: Relative residual of the energies of events measured by both the SD-750 and SD-1500 for (a) the standard calibration derived in Section 4.5.5 and (b) the calibration extended by a constraint.

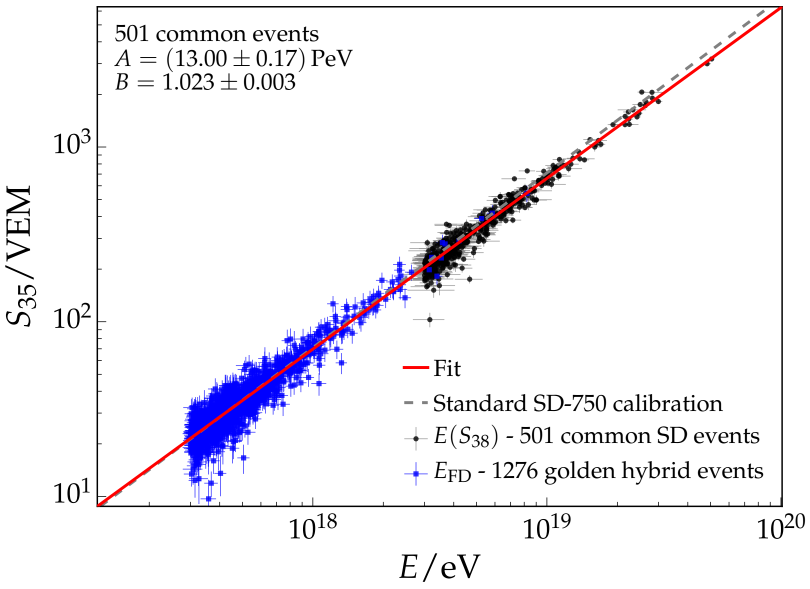

(a)

Figure 4.28: Energy calibration using a constrained fit. A subset of common events helps to constrain the energies measured with the SD-750 to the reconstructed energies of the SD-1500. The result of the standard calibration is shown in addition.

For the SD-1500, the calibration using the energy estimates corrected with the energy-dependent attenuation function leads to:

$$E(S_{38}) = (0.187 \pm 0.003) \times 10^{18}\,\text{eV} \left(\frac{S_{38}}{\text{VEM}}\right)^{(1.029 \pm 0.005)} . \tag{4.54}$$

The resulting fits are shown in Fig. 4.30. The constrained fit for the SD-750 data is shown in Fig. C.7.

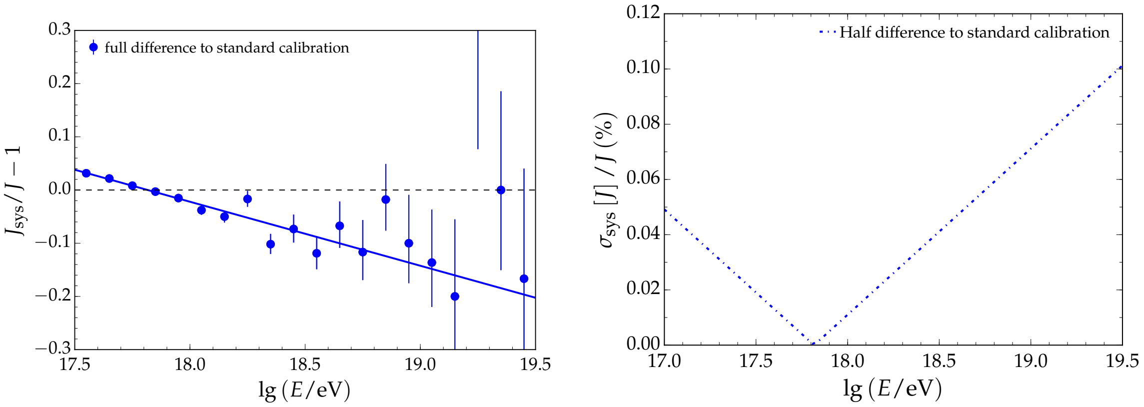

(a) **(b)**

Figure 4.29: (a) Relative flux difference due to the different calibration functions used. (b) Relative systematic on the flux from the difference in calibration. Half of the difference is propagated into the systematic.

4.6 SD energy spectrum

The previous sections described firstly the event selection, followed by the correction of the shower size estimator for the attenuation of the shower in the atmosphere and last the energy calibration of the corrected estimator, exploiting the hybrid set-up of the observatory. All these analysis steps are crucial to derive the energy spectrum of the cosmic rays.

4.6.1 Raw energy spectra

The energy spectrum of UHECRs is obtained from the measured event rate and the exposure:

$$\begin{aligned} J(E) &= \frac{\mathrm{d}N}{\mathrm{d}E\,\mathrm{d}t\,\mathrm{d}A\,\mathrm{d}\Omega} \\ &= \frac{\mathrm{d}N}{\mathrm{d}E\,\mathrm{d}\mathcal{E}}. \end{aligned} \tag{4.55}$$

The energy spectra of the raw event counts are illustrated in Fig. 4.31 as function of $\lg E$ and of the energy estimates. The spectra include energies below full efficiency and as such there is a decline visible at the lowest energies where the showers fail to trigger the arrays. The differential event counts with respect to energy and exposure are depicted in Fig. 4.32. The number of events within each bin is weighted by the respective energy interval $\mathrm{d}E = E_{\mathrm{up}} - E_{\mathrm{low}}$, where the subscripts denote the upper and lower bin edge. The 1σ statistical uncertainties are shown in addition. They are calculated as asymmetric Poisson uncertainties for bins with more than 20 events. For bins with lower event counts, two-sided Feldman-Cousins limits with a coverage of 68 % are used [104]. The upper flux limits refer to one-sided Feldman-Cousin limits with a coverage of 84 % for a zero-background event rate and no measured events. A scaling of E^3 is applied to each of the flux points to enhance the visibility of the spectral features. Both the SD-750 and SD-1500, spectra show a flattening around $10^{18.7}$ eV, called the *ankle*. While the SD-750 is lacking statistic at the highest energies, a clear and steep suppression is apparent in the SD-1500 spectrum. The spectra use the calibrations of Eq. (4.49) and Eq. (4.50) obtained for the standard attenuation correction.

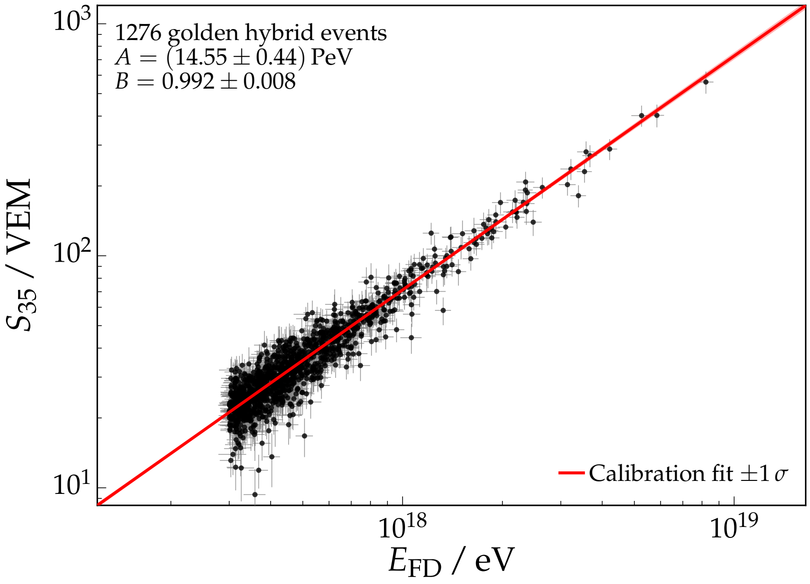

(a)

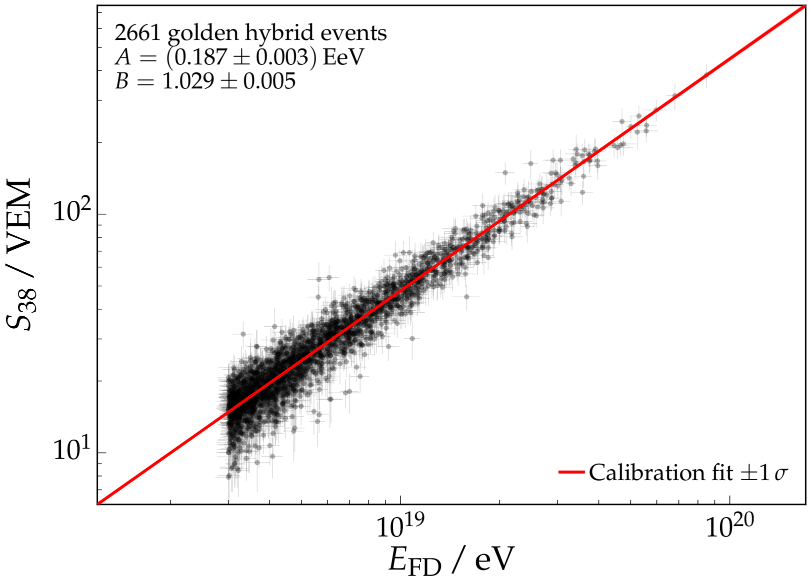

(b)

Figure 4.30: The energy estimates are obtained using an energy-dependent attenuation correction. (a) Energy calibration for the SD-750. (b) Energy calibration for the SD-1500.

4.6.2 Spectra comparison using different attenuation corrections

The spectra shown in Fig. 4.32 are compared to the ones obtained with the calibrations of Eq. (4.53) and Eq. (4.54), using the energy-dependent attenuation correction. In Fig. 4.33, the comparison of the SD-750 spectra is depicted. Both spectra use the constrained calibration fit. The spectra are re-binned at the highest energies to reduce the scatter due to statistical fluctuations. As can be seen from the residual representation in Fig. 4.33b, there is an excellent agreement between the two spectra. The comparison for the SD-1500 spectra can be found in Fig. 4.34. Looking at the residual in Fig. 4.34b, the flux as derived with the iterative attenuation correction is about 2 % lower at energies near the threshold of full efficiency. This

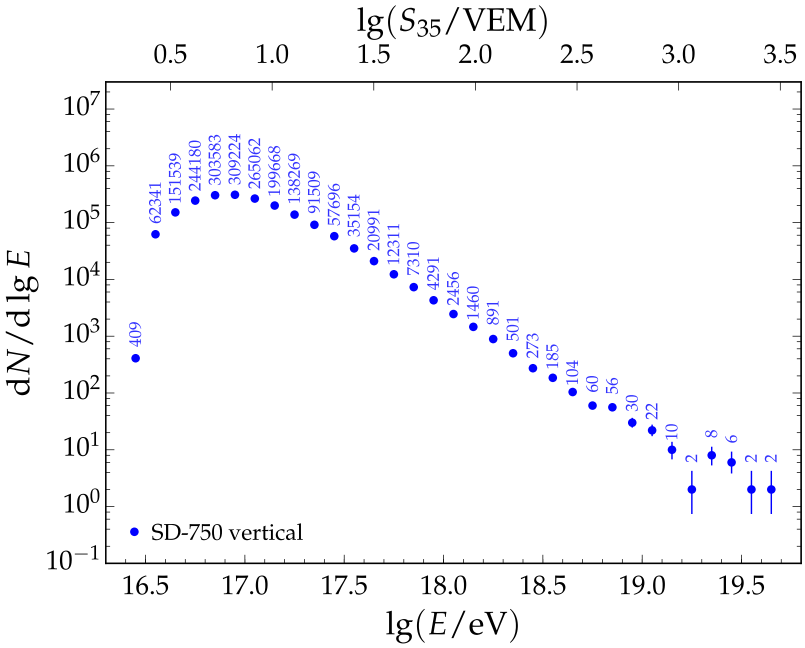

(a) SD-750 data.

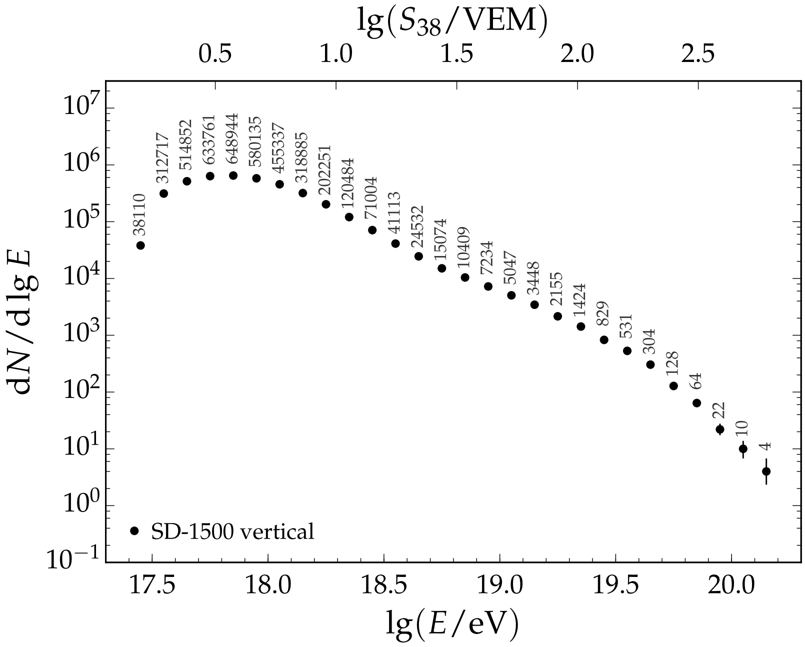

(b) SD-1500 data.

Figure 4.31: Spectra of the raw event counts as measured with (a) the SD-750 and (b) the SD-1500. The respective energy estimates are given on the top axes and the event numbers are stated above the points.

is a result of the reduced number of events at low energy estimates and high zenith angles as described in Section 4.4.3. At energies above the ankle ($\sim 10^{18.7}$ eV), the two spectra agree well within their uncertainties.

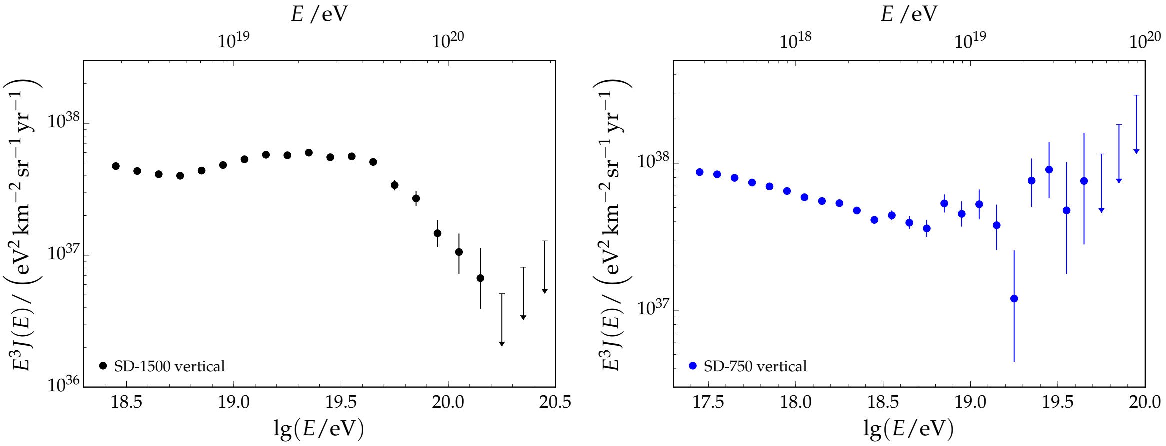

(a) Spectrum as measured with the SD-1500 **(b)** Spectrum as measured with the SD-750

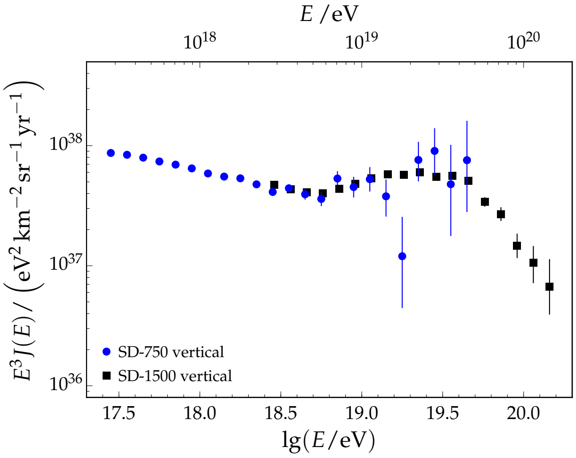

(c) Comparison of the measured spectra

Figure 4.32: Measured spectra of the (a) SD-1500 and (b) SD-750. The spectra are not corrected for migration effects. The comparison of the spectra is shown in (c). The data points of the SD-1500 include a shift towards higher energies (by 0.01 in logarithmic energy with respect to the bin center) to help the visibility.

4.7 Forward folding

The measured energy spectrum as shown in Section 4.6.1 is distorted as the energy resolution of the detector is finite. As a result, events migrate from one energy bin to another. Due to the steeply falling flux, the migration among the bins in not balanced but the migration of low-energetic events to higher energies outweighs the fluctuations from high to low energies. Therefore, the measured flux is always higher than the true flux. The true flux is per se unknown but an estimate is obtained by correcting the smeared, measured flux for the migration effects. To perform the correction a proper determination of the detector resolution is needed.

4.7.1 Detector resolutions

The total detector resolution is composed of sampling fluctuations and shower-to-shower fluctuations and can either be determined from data directly or with the help of simula-

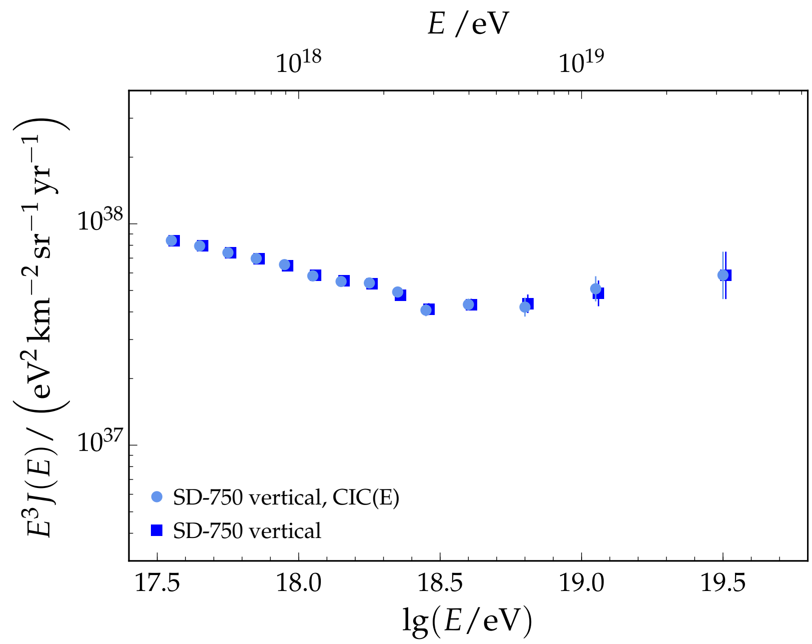

(a) Comparison of SD-750 spectra using different CIC methods

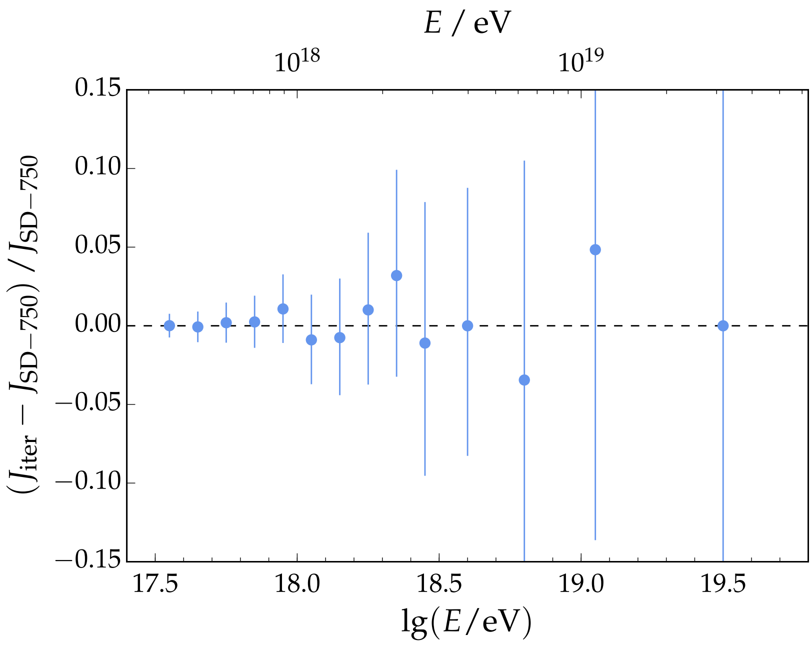

(b) Residual of SD-750 spectra

Figure 4.33: (a) The uncorrected SD-750 spectra using the standard attenuation correction (dark blue points) and the energy-dependent correction (light blue points). Both spectra are calibrated using the constrained fit described in Section 4.5.6. (b) Residual of the spectra.

tions. The sampling fluctuations are estimated on an event-by-event level by combining the statistical and systematic uncertainties emerging from the reconstruction process:

$$\sigma_\mathrm{det}^2 = \sigma_\mathrm{LDF,stat}^2 + \sigma_\mathrm{LDF,sys}^2 + \sigma_\mathrm{CIC}^2 + \sigma_\theta^2. \tag{4.56}$$

The statistical uncertainty from the fit of the LDF $\sigma_\mathrm{LDF,stat}$ contributes to the resolution as well the systematic uncertainties $\sigma_\mathrm{LDF,sys}$ from its parametrization. The slope of the LDF, β, has

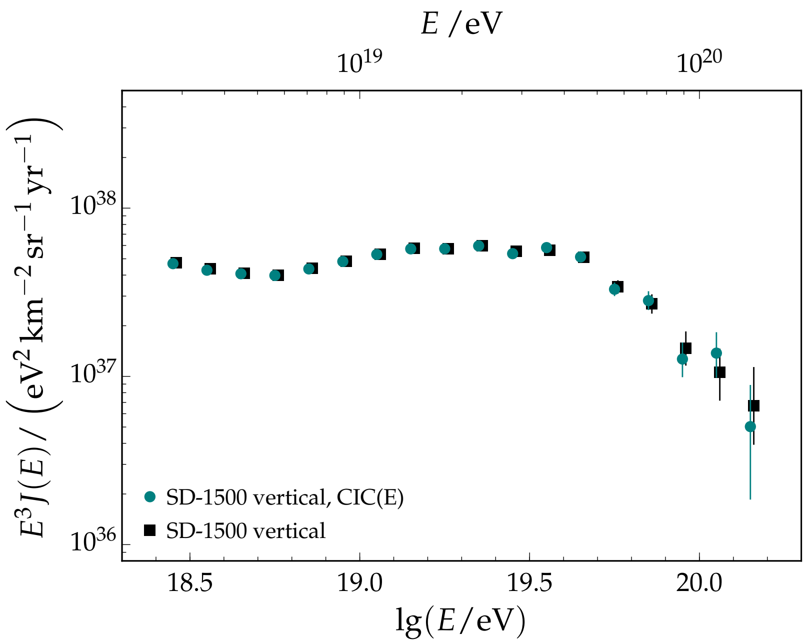

(a) Comparison of SD-1500 spectra using different CIC methods

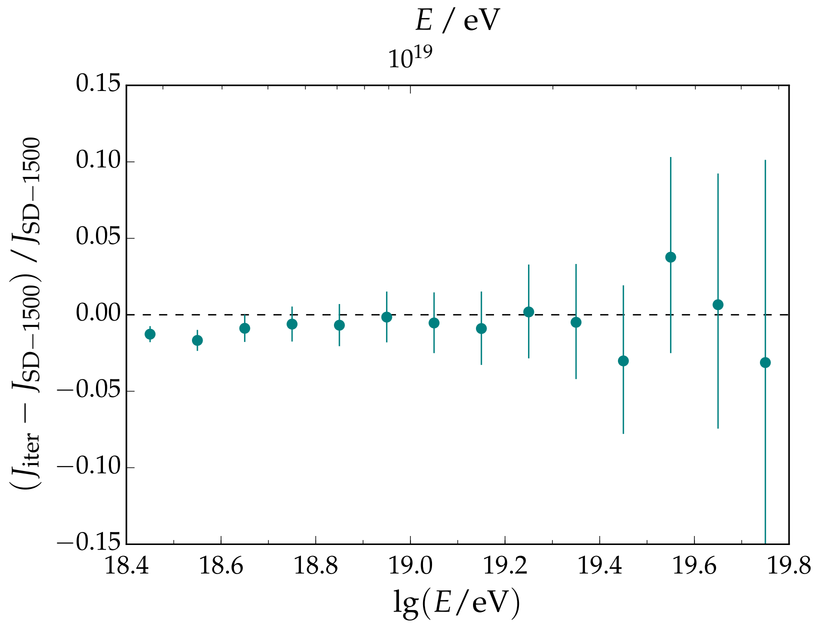

(b) Residual of SD-1500 spectra

Figure 4.34: (a)The uncorrected SD-1500 spectra using the standard attenuation correction (black points) and the energy-dependent correction (green points). (b) Residual of the spectra. The energy-dependent correction reduces the flux at lower energies on the level of 2 %.

to be fixed for events with less than five stations due to the simultaneous fit of the geometry and shower size. This leads to a systematic uncertainty in the determination of β which has to be accounted for in the uncertainty of the shower size estimation [61, 105]. Besides, the uncertainty on the attenuation function, σ_{CIC}, and the uncertainty on the reconstructed zenith angle, σ_θ, go into the total resolution. I updated the detector resolution model for the SD-1500 using the following parametrization:

$$\frac{\sigma_{\mathrm{det}}(S_{38})}{S_{38}} = 0.00832 + (0.317 - 0.440x + 7.36x^2 - 10.70x^3)\frac{1}{\sqrt{S_{38}}} \tag{4.57}$$

$$+ (0.292 + 0.426x - 6.58x^2 + 10.56x^3)\,\frac{1}{S_{38}}, \tag{4.58}$$

with $x := \lg(1/\sec\theta)$, which was derived for a previous work [71]. A comparison of the updated model with respect to the previous one is depicted in Fig. C.4.

By using the energy calibration relation $E(S)$ as well as the attenuation function $f_{\mathrm{CIC}}(\theta)$, the detector resolution is expressed in terms of energy:

$$\frac{\sigma(E)}{E} = B\frac{\sigma(S_{1000})}{S_{1000}}, \tag{4.59}$$

with B being the slope parameter of the energy calibration. The same conversion can be applied in case of the analysis of SD-750 data. In addition to the finite precision of the detector, the measured signal is distorted with respect to the true signal due to shower-to-shower fluctuations. An estimation of the fluctuations can be obtained from data when performing the energy calibration. I will use the shower-to-shower fluctuations as derived for the work presented in [97]. Here, a contribution of 10 % was determined for both the SD-750 and SD-1500 data. The total resolution is then calculated as the quadratic sum of the detector resolution and the shower-to-shower fluctuations:

$$\sigma^2_{\mathrm{tot}}(E,\theta) = \sigma^2_{\mathrm{det}}(E,\theta) + \sigma^2_{\mathrm{sh}}(E). \tag{4.60}$$

The uncertainties and probabilities included in the reconstruction process affect the resolution derived from data. There are known caveats in the reconstruction, such as that the LDF estimation does currently not include a correction for the asymmetry in the $\overline{\text{Off}}\underline{\text{line}}$ framework. Therefore, the resolution is also derived from simulations as described in Section 3.2. The resolution for the SD-1500 was obtained as:

$$\frac{\sigma\,(E)}{E} = 0.1003 + 0.442\sqrt{\frac{E_0}{E}} \tag{4.61}$$

for a mix of proton and iron showers. The resolution for the SD-750 obtained with a mixed composition is:

$$\frac{\sigma\,(E)}{E} = 0.078 + 0.165\sqrt{\frac{E_0}{E}}. \tag{4.62}$$

The derived energy resolutions for the SD-750 and SD-1500 are summarized in Fig. 4.35. For both data sets the shower-to-shower fluctuations σ_{sh} were estimated to be on the order of 10 %. They are shown as black dashed line with an uncertainty band of $1\sigma_{\mathrm{stat}}$. The shower-to-shower fluctuations have to be added in quadrature to the sampling fluctuations. The sampling fluctuations σ_{det} are obtained from Eq. (4.56) and visualized as black circular markers. They are further divided into three zenith angle bins. A slight dependence on the zenith angle is apparent, which can be attributed to the attenuation of the shower size with increasing zenith angle. The total resolution derived from data is then stated as black rectangular markers. This has to be compared to the total resolution inferred from simulations, which is depicted as black solid line with an uncertainty of 10 %. There is a good agreement between the two total detector resolutions within the stated uncertainties. For the following analysis, I will use the total resolution derived from simulations.

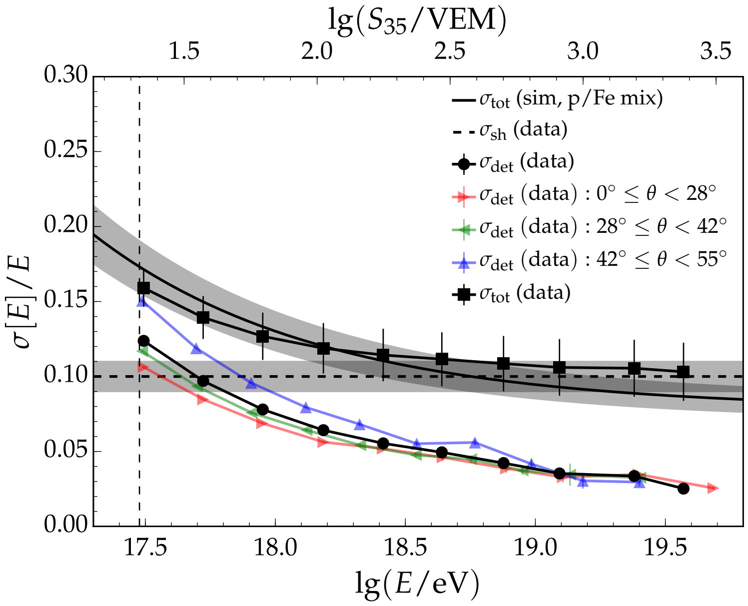

(a) SD-750

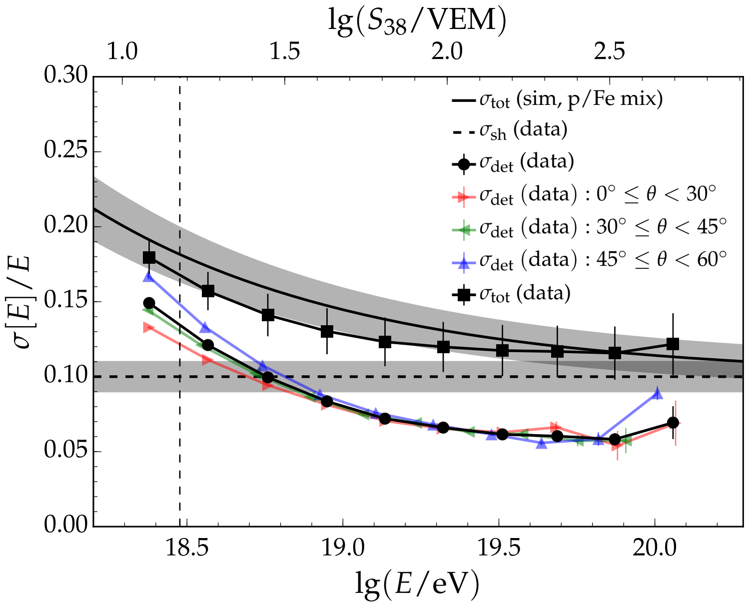

(b) SD-1500

Figure 4.35: Resolutions as derived from data and simulations for the (a) SD-750 and (b) SD-1500 arrays. The detector resolution from data is divided into zenith bins. The shower-to-shower fluctuation is given in addition. A good agreement between the total resolution derived from simulations and the combined resolution of sampling fluctuations and shower-to-shower fluctuations is apparent for both arrays. The vertical line corresponds to the respective energy of full efficiency.

4.7.2 Correction for event migration

The measured flux is smeared with respect to the true unknown one. There are various strategies to correct for the smearing. In high-energy physics, the unfolding approach is commonly used. For this method, a matrix is specified for the smearing that relates the number of true events within an energy bin to the number of observed events in the other bins. The distribution of true events is then obtained by inverting the matrix and applying it to the measured event distribution. A downside of the unfolding procedure is that small fluctuations are amplified by the inversion, leading to large fluctuations in the unfolded data [106, 107]. To overcome the large bin-to-bin fluctuations encountered in the unfolding, the regularized unfolding was introduced to damp down the oscillations [108, 109]. There are various methods for the regularization and much tuning is necessary to obtain a sound parameter set. Therefore, I make use of the forward-folding method to correct for the smearing [71]. The method uses an assumption for the true theoretical flux and folds it with the detector response:

$$J'(E') = \int \mathrm{d}E \, K\big(E'|E, \sigma(E)\big) \, J(E), \tag{4.63}$$

with the energy E' and flux J' being the measured (smeared) quantities, and (E, J) denoting the true quantities. K represents the detector kernel that describes the fluctuations inherent in the reconstruction process. A normal distribution $\mathcal{N}(E'|E, \sigma(E))$ is used with $\sigma(E)$ being the energy resolution as obtained from simulations.

The flux of the cosmic rays is binned in $\lg E$, so within each bin the measured flux is denoted as:

$$J'_i = \frac{\mathrm{d}N'_i}{\Delta E'_i \mathcal{E}_i} = \frac{1}{E'_i \log 10} \frac{\mathrm{d}N'_i}{\Delta \lg(E'_i) \mathcal{E}_i}, \tag{4.64}$$

where $\mathcal{E}_i$ is the exposure in bin i. The measured quantity

$$n'_i = \frac{\mathrm{d}N'_i}{\Delta \lg(E'_i)} \tag{4.65}$$

is fitted assuming a Poissonian distribution $\mathrm{Pois}(n'_i|\mu_i(\vec{p}))$ for the event counts. The log-likelihood is constructed as:

$$\log \mathcal{L}(\vec{p}) = \sum_i n'_i \log \mu_i + \mu_i \tag{4.66}$$

The expected number of events is given as $\mu_i = n'_i \mathcal{E}_i$. With the help of Eq. (4.63) and Eq. (4.64), the expectation within a certain bin i is written as:

$$\mu_i = \int \mathrm{d}E \, \mathcal{N}\big(E'_i|E, \sigma(E)\big) \, J(E|\vec{p}), \tag{4.67}$$

with $J(E|\vec{p})$ being the model chosen to describe the true flux. Due to computational costs, the integration is performed in $\lg E$, using the variable change $\mathrm{d}E = E \log 10 \, \mathrm{d} \lg E$:

$$\mu_i = \log 10 \int \mathrm{dlg}E \, \mathcal{N}\big(E'_i|E, \sigma(\lg E)\big) \, J(\lg E|\vec{p}) \, E. \tag{4.68}$$

In the following, the trigger efficiency is included and a possible dependence of the energy resolution on the zenith angle (e.g. as derived from data) is taken into account:

$$\mu_i = \log 10 \int \mathrm{dlg}E \int \mathrm{d}\theta \, \mathcal{N}\big(E'_i|E, \sigma(\lg E, \theta)\big) \, J(\lg E|\vec{p}) \, E \, \epsilon(\lg E', \theta) \sin\theta \cos\theta. \tag{4.69}$$

The zenith angle range is restricted to match a certain T4 trigger threshold (e.g 0.95 , 0.99), leading to an allowed zenith angle range of $[\theta_{\mathrm{low}}(E), \theta_{\mathrm{up}}(E)]$ that is dependent on the energy. Another modification is made due to the way the resolution and efficiency models are parametrized. The parametrization of the models is based on the energy estimate S with the benefit of being independent of the overall energy scale. As such, the models stay valid after a change in the energy scale. Using the relation $\mathrm{dlg}E = B\,\mathrm{dlg}S$ with the slope parameter B of the energy calibration as well as the restricted zenith angle ranges, the estimation of the number of true event counts within a certain bin i reads now as follows:

$$\mu_i = \log 10\, B \int_{\lg S_0}^{\lg S_1} \mathrm{dlg}S \int_{\theta_{\mathrm{low}}(E_i')}^{\theta_{\mathrm{up}}(E_i')} \mathrm{d}\theta\, \mathcal{N}\big(S_i'|S, \sigma(\lg S, \theta)\big)\, J(\lg E|\vec{p})\, E\, \sin\theta \cos\theta. \tag{4.70}$$

The fit is performed by minimizing the negative log-likelihood from Eq. (4.66). In each minimization step the true model is folded with the detector kernel and fitted to the measured flux to find the optimal parameters $\vec{p}$. The ratio of the true flux $J(E)$ and the smeared one of the best fit $J'(E)$ determines the bin-wise correction factor $c(E)$ that has to be applied to the measurement:

$$c(E) = \frac{J(E)}{J'(E)}. \tag{4.71}$$

In the following, the SD-750 and SD-1500 spectra are corrected with the help of the forward-folding method. The SD energy bias observed in Section 3.2 is not accounted for during the forward folding. All forward-folded SD-1500 spectra are derived without a correction for the bias. Therefore, the same forward-folding procedure is used as for the spectra presented in [97, 110, 111].

For the SD-750 data, a broken power law with a hard break at E_{ankle} is assumed as true flux:

$$J(E) = \begin{cases} a\left(\frac{E}{E_{\mathrm{ankle}}}\right)^{\gamma_1} & , \quad E < E_{\mathrm{ankle}} \\ a\left(\frac{E}{E_{\mathrm{ankle}}}\right)^{\gamma_2} & , \quad E \geq E_{\mathrm{ankle}}. \end{cases} \tag{4.72}$$

The spectral slope changes from γ_1 below the ankle to γ_2 above the ankle. The resulting fit is shown in Fig. 4.36a, together with its 1σ statistical uncertainty depicted as band. The fit parameters for the slopes and the energy of the ankle are summarized in Table 4.4. The ankle is found at 18.73 ± 0.08 in logarithmic energy, with a change in spectral slope from -3.24 ± 0.01 below this energy to -2.79 ± 0.14 above it. In addition to the unfolded spectrum, the event numbers per bin are stated above each data point. The square brackets around the points denote the total systematic uncertainty on the flux. The correction function that needs to be applied to the measured flux in order to obtain the unfolded spectrum is depicted in Fig. 4.37a. The darker shaded band represents the statistical uncertainty from the covariance of the fit. The lighter shaded band corresponds to the systematic uncertainty which arises when the resolution model is varied by ±10 %. The correction on the measured flux is highest at the lowest energies. Here, the flux needs to be lowered by about 7 %. With increasing energy, the correction becomes negligibly small.

The true flux model for the forward-folding of the SD-1500 data is a power-law like function with k smooth breaks and $k+1$ spectral slopes γ_i. The break energy is denoted as $E_{\mathrm{break},i}$:

$$J(E) = a\left(\frac{E}{E_{\mathrm{norm}}}\right)^{\gamma_1} \prod_{i=1}^{k} \frac{1 + (E/E_{\mathrm{break},i})^{-\gamma_i}}{1 + (E/E_{\mathrm{break},i})^{-\gamma_{i+1}}}. \tag{4.73}$$

The first break denotes the energy of the ankle. The fit results in a logarithmic energy of 18.80 ± 0.03 for the ankle energy and a slope of -3.28 ± 0.01 prior to it. The fit parameters for the remaining breaks and slopes are summarized in Table 4.5. The fit is shown in Fig. 4.36b on top of the unfolded spectrum. Again, the 1σ statistical uncertainty on the fit is depicted as shaded band and the event numbers per bin are stated above the data points. The correction function is shown in Fig. 4.37b. As in the case of the SD-750 data, a downward correction on the order of about 7 % is applied to the energies around the threshold of full efficiency. The correction decreases with increasing energy up to an energy of about $10^{19.6}$ eV. Above this energy, the spectrum steepens significantly and the correction increases again to the same magnitude as at the lowest energies.

The unfolded spectra are compared in Fig. 4.39. In Fig. 4.39a, the spectra are shown together with the fit to the SD-1500. The SD-750 spectrum is re-binned at the highest energies to decrease the impact of statistical fluctuations. A very good agreement of the two spectra in the overlapping energy range is visible. The compatibility is further investigated by a residual comparison as shown in Fig. 4.39b. Both spectra are compared to the expected flux as fitted to the SD-1500 spectrum. The spectra agree well within their uncertainties.

Fig. 4.38 summarizes the statistical and systematic uncertainties on the flux derived from the SD-750 and SD-1500 data. The largest uncertainties for the SD-750 depicted in Fig. 4.38a are the systematic uncertainties from the energy calibration as discussed in Section 4.5.6 and the statistical uncertainty of the calibration. The systematic uncertainty arises from the difference of the constrained calibration to the standard calibration. The statistical uncertainty is due to the low event statistic at higher energies. This uncertainty is estimated by varying the calibration parameters within their uncertainty and creating mock spectra. The spread of the randomly drawn spectra gives the uncertainty on the flux. The uncertainties attributed to the forward folding are the statistical uncertainty from the fit and the systematic uncertainty originating from the uncertainty on the energy resolution. The remaining contributions to the total flux uncertainty are the uncertainties assigned to the exposure determination (3 %) and to the shower size corrections ($\sigma_{\text{add}} = 3.5\,\%$). The latter uncertainties are also assigned to the flux of the SD-1500. As there is no systematic uncertainty for the energy calibration, the total uncertainty for the SD-1500 is smaller than the one assigned to the SD-750. The systematic uncertainties for the SD-1500 flux are below 8 % for all energies except the very highest ones, where the statistic gets poor.

The systematic uncertainty on the energy scale is the same for all SD-derived spectra. It stems from the uncertainty assigned to the FD measurement and amounts to 14 %. The individual contributions are the uncertainty on the fluorescence yield (3.6 %), the atmosphere (3.4 %÷6.2 %), the FD calibration (9.9 %), the profile reconstruction (6.5 %÷5.6 %), the invisible energy (3 % ÷ 1.5 %), and additional contributions (5 %) [112].

Table 4.4: Parameters of the fit to the SD-750 data. The SD-750 spectrum is corrected for migration effects. The systematic uncertainty (stated as second uncertainty) is obtained by varying the energy-dependent flux systematic by 1σ.

Fit parameters	
$\lg(a/\text{eV}^{-1}\text{m}^{-2}\text{sr}^{-1}\text{s}^{-1})$	$-15.410 \pm 0.002 \pm 0.006$
$\lg(E_{\text{ankle}}/\text{eV})$	$18.73 \pm 0.08 \pm 0.03$
γ_1	$-3.24 \pm 0.01 \pm 0.03$
γ_2	$-2.79 \pm 0.14 \pm 0.03$

4.8 Spectra combination

The energy spectrum as measured with Auger can be derived from different data sets. Three spectra are currently obtained from SD data (SD-750, SD-1500, SD-1500h[6]) and one from FD. The spectrum determined from the FD measurements is referred to as *hybrid* spectrum as

---

[6] 1500 m SD horizontal

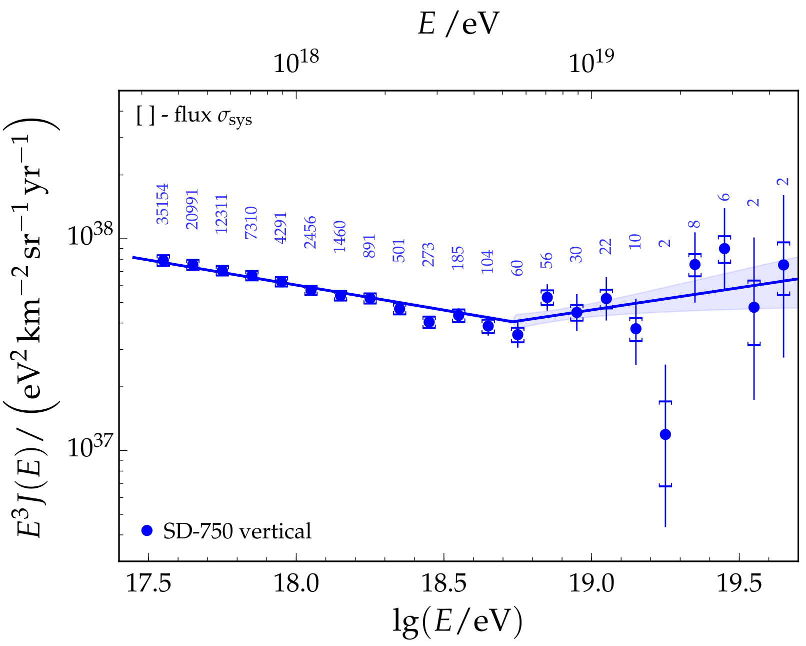

(a) SD-750 corrected flux

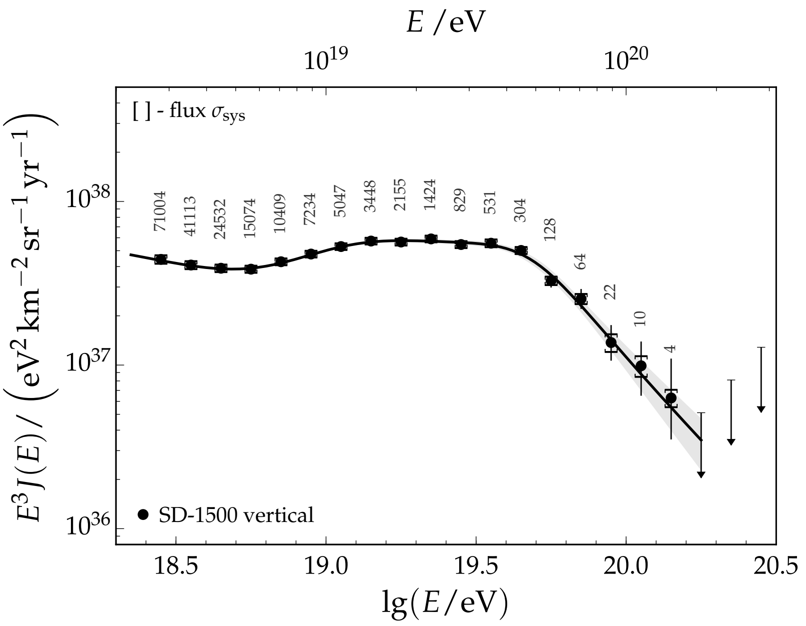

(b) SD-1500 corrected flux

Figure 4.36: Energy spectra for the (a) SD-750 and (b) SD-1500 after the correction for migration effects. The statistical uncertainty is shown as error bars, the systematic uncertainty is indicated by square brackets. The number of raw events within each bin as well as the fit model are shown in addition.

it uses at least one simultaneously triggered SD station. Within this work, the combination is only done for the two spectra obtained from the SD-750 and SD-1500 data. The spectra are combined to one spectrum using a log-likelihood method that accounts for the different

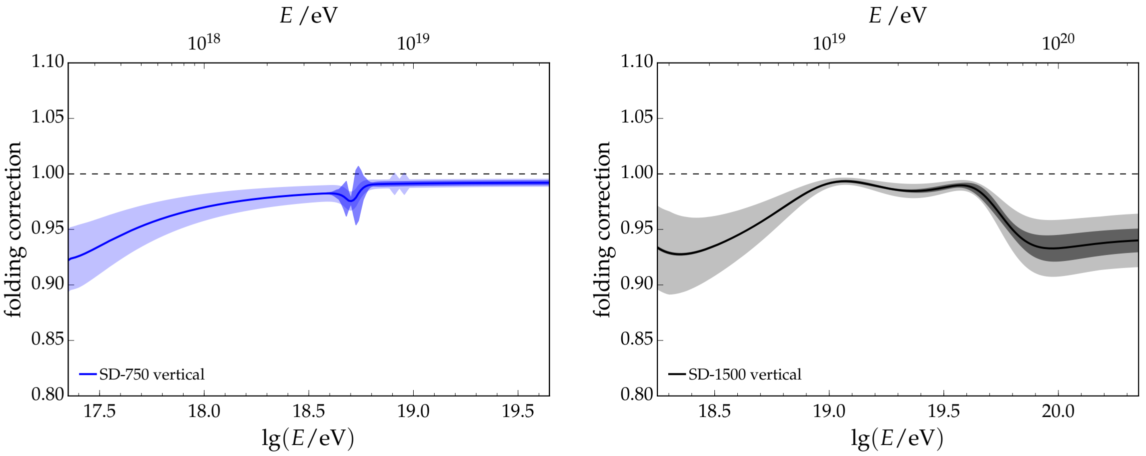

(a) SD-750 corrections

(b) SD-1500 corrections

Figure 4.37: Correction factors of the forward folding.

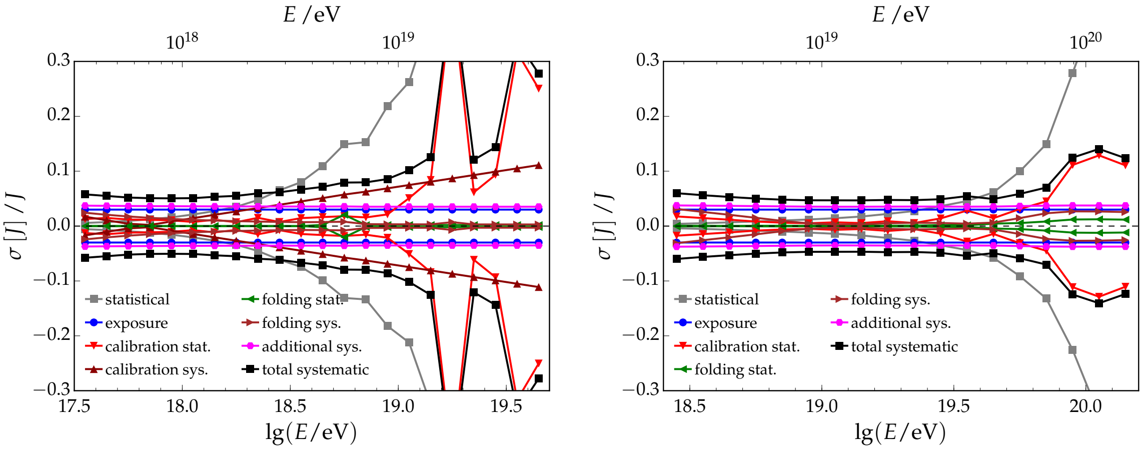

(a) SD-750 data

(b) SD-1500 data

Figure 4.38: Statistical and systematic uncertainties on the energy spectra. Details on the different contributions are given in the text.

systematic uncertainties inherent to the individual spectra. The general log-likelihood for the combination of various spectra is constructed as follows:

$$\log \mathcal{L}_{\text{comb}} = \sum_k^m \log \mathcal{L}_k^{\text{Pois}} + \log \mathcal{L}_k^{\text{Ecal}} + \log \mathcal{L}_k^{\text{Norm}}. \tag{4.74}$$

It contains the Poisson term as also used in Eq. (4.66). For a spectrum k, this reads as:

$$\mathcal{L}_{ki} = \frac{\mu_i^{n_i} \exp(-\mu_i)}{n_i!}, \tag{4.75}$$

with n_i denoting the number of measured events and μ_i the expected number in the energy bin i. In case of a pure fit to the spectrum (no forward-folding applied), the expected number of events is given by the flux model directly.

In addition, a term for the energy calibration and the normalization can be included. Within the scope of this work, the likelihood for the calibration is not taken into account. The statistical

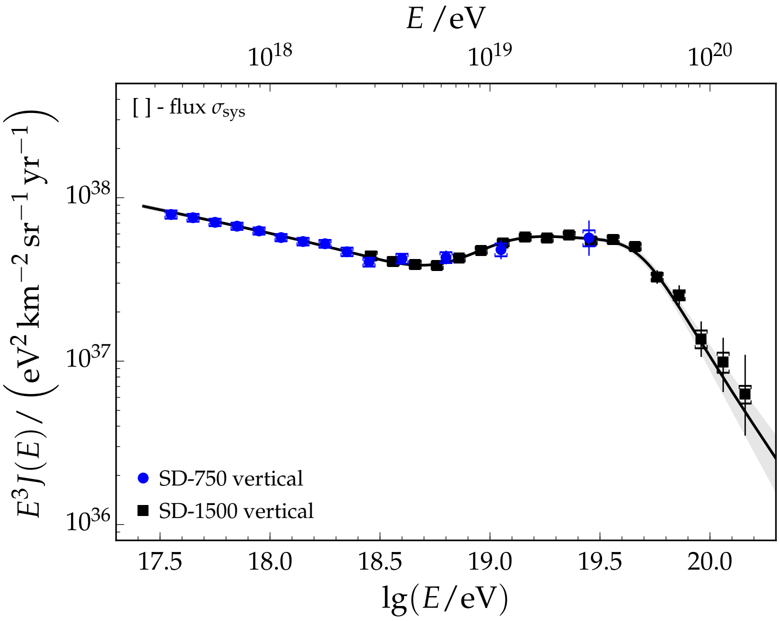

(a) Unfolded fluxes

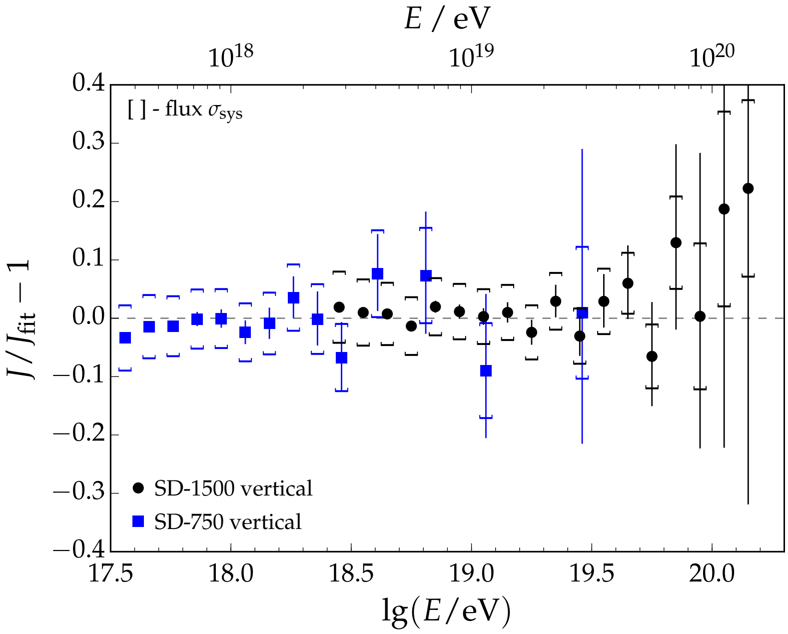

(b) Residual representation of unfolded fluxes

Figure 4.39: (a) Comparison of the spectra as measured with the SD-750 and SD-1500 corrected for migration effects. The SD-750 spectrum is re-binned at the highest energies to reduce statistical fluctuations. (b) Residual comparison of the two spectra with respect to the forward-folding fit to the SD-1500 spectrum.

uncertainty of about 1 % to 3 % on the calibration as shown in Fig. 4.25 is negligible compared to the other systematic uncertainties. The log-likelihood reduces to two contributions:

$$\log \mathcal{L} = \sum_{k=1}^{k_{\mathrm{spec}}} \sum_{i=1}^{n} \log \mathcal{L}_{ki}^{\mathrm{Pois}} + \frac{1}{2}\left(\frac{a_k - 1}{\sigma_k}\right)^2. \tag{4.76}$$

Table 4.5: Parameters of the fit to the SD-1500 data. The SD-1500 spectrum is corrected for migration effects.

Fit parameters	
$\lg(a/\mathrm{eV}^{-1}\mathrm{m}^{-2}\mathrm{sr}^{-1}\mathrm{s}^{-1})$	-17.854 ± 0.001
$\lg(E_\mathrm{ankle}/\mathrm{eV})$	18.80 ± 0.03
$\lg(E_\mathrm{break,1}/\mathrm{eV})$	19.07 ± 0.04
$\lg(E_\mathrm{break,2}/\mathrm{eV})$	19.68 ± 0.03
γ_1	-3.28 ± 0.01
γ_2	-2.21 ± 0.22
γ_3	-3.22 ± 0.05
γ_4	-4.99 ± 0.31

The first sum runs over the different spectra entering the likelihood and the second one over the number of bins of spectrum k. The total systematic uncertainty of an individual spectrum is denoted by σ_k and a_k is the overall normalization factor which is a free parameter in the fit to obtain the best combination.

The measured spectra of SD-750 and SD-1500 are corrected with the help of the forward-folding method. After applying the normalization factors on the individual spectra, the combined spectrum is calculated as the weighted average of the fluxes. For each flux point of the individual spectra, a weight corresponding to the number of measured events n_i is applied. The combination uses the following flux model:

$$\begin{aligned} J(E < E_a) &= a\left(\frac{E}{E_a}\right)^{\gamma_1} \\ J(E > E_a) &= a\left(\frac{E}{E_a}\right)^{\gamma_2}\left[1+\left(\frac{E_a}{E_\mathrm{s}}\right)^{\Delta\gamma}\right]\left[1+\left(\frac{E}{E_\mathrm{s}}\right)\right]^{-1}, \end{aligned} \tag{4.77}$$

with a denoting the flux normalization and E_s corresponding to the suppression energy at which the flux has reached half of its value when compared to an extrapolation of $J \propto E^{\gamma_2}$. The spectral indices γ_1 and γ_2 denote the index below and above the ankle, respectively, and $\Delta\gamma$ is the difference in the spectral index below and above the suppression. The resulting fit parameters are summarized in Table 4.6.

Table 4.6: Parameters of the fit to the combined SD data. The SD spectrum is corrected for migration effects.

Fit parameters	
$\lg(a/\mathrm{eV}^{-1}\mathrm{m}^{-2}\mathrm{sr}^{-1}\mathrm{s}^{-1})$	-17.87 ± 0.001
$\lg(E_\mathrm{ankle}/\mathrm{eV})$	18.72 ± 0.01
γ_1	-3.259 ± 0.005
γ_2	-2.51 ± 0.04
$\lg(E_\mathrm{s}/\mathrm{eV})$	19.58 ± 0.04
$\Delta\gamma$	2.39 ± 0.18
$a_\text{SD-1500}$	1.013 ± 0.032
$a_\text{SD-750}$	0.984 ± 0.031

The combined spectrum is shown in Fig. 4.40a, in addition to the individual spectra. The SD-750 and SD-1500 spectra are multiplied with their respective normalization factors. The fit is shown in Fig. 4.40b, together with the combined spectrum. The number of events in each bin is again stated on top of the data points. In Fig. 4.41, the combined spectrum is compared to the one derived for the work presented in [97]. The latter one is obtained from the combination of all four Auger spectra (the individual spectra are shown in Fig. C.9). There is a difference of less than 10 % visible for the lowest energies (see Fig. 4.41b). This difference is due to the usage of the constrained calibration fit for the SD-750 spectrum derived in this work. A comparison of the SD-750 spectra alone can be found in Fig. C.10. Apart from this difference in slope prior to the ankle, the spectral features are compatible. The ankle energy of the full Auger spectrum is $\lg(E_\mathrm{ankle}/\mathrm{eV}) = 18.71 \pm 0.01$, the suppression is found at $\lg(E_\mathrm{s}/\mathrm{eV}) = 19.60 \pm 0.02$, and the spectral index after the ankle is $\gamma_2 = -2.53 \pm 0.03$. These values have to be compared to the one in Table 4.6.

The log-likelihood stated in Eq. (4.74) includes only the energy-independent systematic uncertainties (see Fig. 4.38). The energy-dependent systematic uncertainties can be included in the likelihood with the help of nuisance parameters [113]. The inclusion is done by extending the likelihood of each spectrum k by a Gaussian term:

$$\begin{aligned}\mathcal{L}_k &= \prod_{i=1}^{n} \mathrm{Pois}(n_i|\nu_i)\mathcal{N}\left(\nu_i|\mu_i, \sigma(\mu_i)\right) \\ &= \prod_{i=1}^{n} \frac{\nu_i^{n_i} e^{-\nu_i}}{n_i!} \cdot \frac{1}{\sqrt{2\pi\sigma_i^2}} e^{\frac{(\nu_i-\mu_i)^2}{2\sigma_i^2}} .\end{aligned} \tag{4.78}$$

The systematic uncertainty on the flux $\sigma(\mu_i)$ allows for a variation around the expected number μ_i. The variation is denoted by the nuisance parameter ν_i in the respective energy bin i. This nuisance parameter serves as the new input for the expected number of events in the Poisson distribution. By solving the derivative of the log-likelihood

$$\frac{\partial(-\log \mathcal{L}_i)}{\partial \nu_i} = 0 \tag{4.79}$$

for the ν_i, the nuisance parameter within a bin i can be expressed by the other variables. Solving the quadratic equation and taking the positive square root gives:

$$\nu_i = \frac{1}{2}\left(\mu_i - \sigma_i^2 + \sqrt{(\mu_i - \sigma_i^2)^2 + 4n_i\sigma_i^2}\right). \tag{4.80}$$

The nuisance parameter is therefore not fitted directly. Further studies are needed to use this method for the combination procedure. The methods will be applicable not only to Auger spectra but to other flux measurements as well. This will allow an energy-dependent matching of the spectra measured by different experiments.

4.9 Investigation of declination dependence

As discussed in the following Section 4.10, there is an unresolved difference in the flux as measured by Auger and TA at the highest energies. Assuming an isotropic flux, both measurements should result in the same energy spectrum within the systematic uncertainties. The respective uncertainties on the overall energy scale of 14 % and 21 % for Auger and TA are able to cover the observed difference, except at the very high energies. As the two experiments lie on opposite hemispheres, the difference in the measured flux could also be a result of the difference in the observed sky. Before studying the overlapping parts of the sky between the two experiments in detail in the next section, the energy spectra as measured by SD-1500 and SD-750 are analyzed for a possible dependence on the arrival direction.

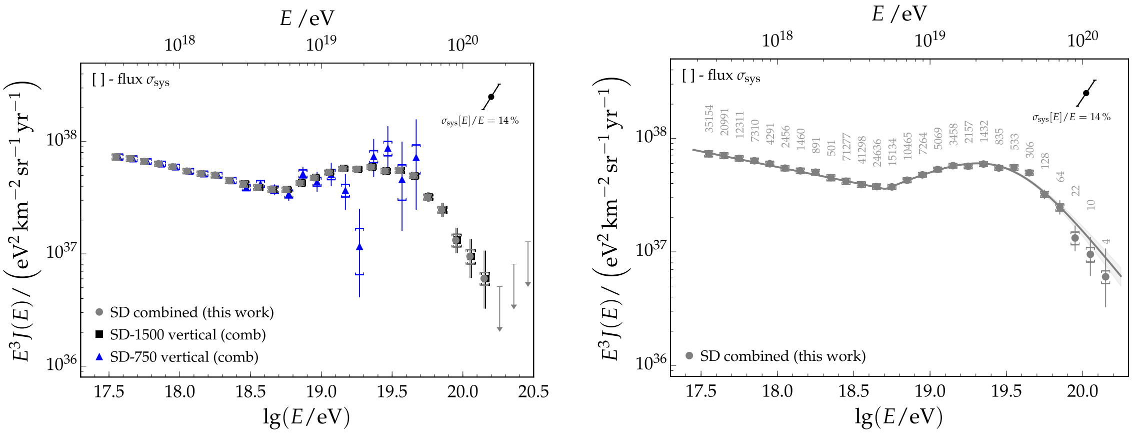

(a) **(b)**

Figure 4.40: (a) Spectra of the SD-750, the SD-1500 and the combined spectrum are shown. The individual spectra are multiplied with the normalization factors obtained during the spectrum combination. The uncertainty on the overall energy scale of Auger is indicated in the upper right corner of the plot. (b) The combined spectrum derived in this work is fitted with the model stated in Eq. (4.77).

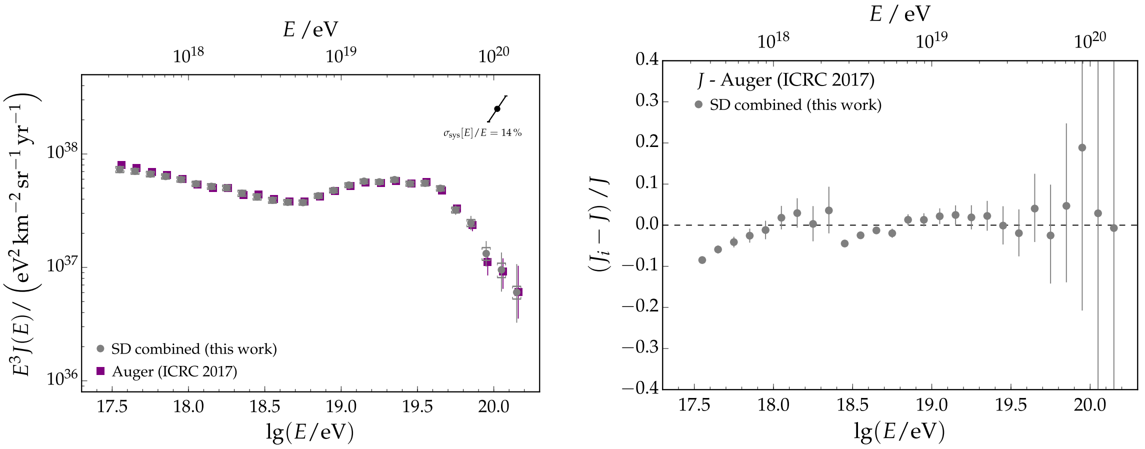

(a) **(b)**

Figure 4.41: Comparison of the combined SD spectrum derived in this work and the combined spectrum presented in [97] derived from the combination of all four Auger spectra. (b) Relative residual of the combined SD spectrum derived in this work with respect to the combined Auger spectrum.

4.9.1 Data selection

The selection of high quality events is following the one described in Section 4.1. The data sets correspond to the data published in [97]. The maximum zenith angle range of the SD-1500 data is 60°, making it possible to measure events with a maximum declination of 25°. In case of the SD-750, a valid CIC can only be performed up to 55°, therefore the maximum declination reduces to 20 degree. A summary of the two data sets is given in Table 4.7. As described in Section 4.4, the measured shower sizes of the SD-1500 and SD-750 arrays are corrected for attenuation effects in the atmosphere. The empirical correction is based on the assumption of an isotropic flux. Therefore, it is necessary to check for any discrepancy between the fluxes from different directions. If the flux from the south were different to the

Table 4.7: Overview of the SD-750 and SD-1500 data sets.

	SD-1500	SD-750
Data period	01/2004 - 12/2016	08/2008 - 12/2016
Exposure / $\mathrm{km}^2\,\mathrm{yr\,sr}$	51588	228.24
Zenith angles / °	0 - 60	0 - 55
Threshold energy E_eff / eV	3×10^{18}	3×10^{17}
Energy calibration A / EeV	0.178	0.013
Energy calibration B	1.042	1.023

one observed from the north, the application of the CIC method on the total set of events would dilute possible differences in the spectra when binned in declination. The validation of the CIC method was performed in [63, 114], using two subsamples of the data measured with the SD-1500 array. One sample covered events arriving from the north where the number of events with high declination is enriched, the other one included events stemming from the south with small declinations. No significant difference between the attenuation curves obtained from the analysis of the subsamples was found. Hence, it is valid to use the standard CIC-corrected spectra for the investigation of a possible declination dependence as done in the following.

4.9.2 Intensity spectra

To test for a possible deviation from an isotropic arrival direction, the data are divided into different intervals of declination that cover the same exposure. In case of isotropy, the distribution of the integrated number of events (i.e. intensity) above a certain energy threshold is supposed to be flat. The intensity is calculated as:

$$N(E_0) = \int_{E_0}^{\infty} \mathrm{d}E \frac{\mathrm{d}N}{\mathrm{d}E}. \tag{4.81}$$

The declination intervals of equal exposure are determined using a bisecting procedure with a relative tolerance of 0.1 %. The exposures of the respective total data sets are listed in Table 4.7. With twenty intervals in declination, each bin covers an exposure of 2579.4 km^2 yr sr in case of the SD-1500 data and 11.4 km^2 yr sr for the SD-750 data. The intensity spectra for five different energy thresholds are shown in Fig. 4.42 together with a constant fit to quantify possible deviations from a flat distribution. Besides the fitted constants and the thresholds, the values for the reduced χ^2 are stated in addition. No statistically significant deviations are found for both examined data sets. The large-scale anisotropy was studied for two energy intervals and a dipole was detected for energies above 8 EeV [25]. The expectation from the dipole is shown as boxes in Fig. 4.43. The data were divided into two declination intervals, corresponding to events coming from the southern part (−90° to −29.4746°) and the northern part (−29.4746° to 24.79°) of the sky. The event rate shows an excess of events stemming from the southern sky that agrees with the expectation of the dipole study. The study of the large-scale anisotropy uses data reconstructed with the CDAS framework. The data reconstructed by $\overline{\mathrm{Off}}\underline{\mathrm{line}}$ and CDAS are compatible with each other given the reconstruction uncertainties. However, the two reconstruction codes differ slightly in some parts. The data obtained with $\overline{\mathrm{Off}}\underline{\mathrm{line}}$ shows small deviations from the expectation derived from the CDAS data, which can probably be attributed to the slight differences between the two reconstruction frameworks.

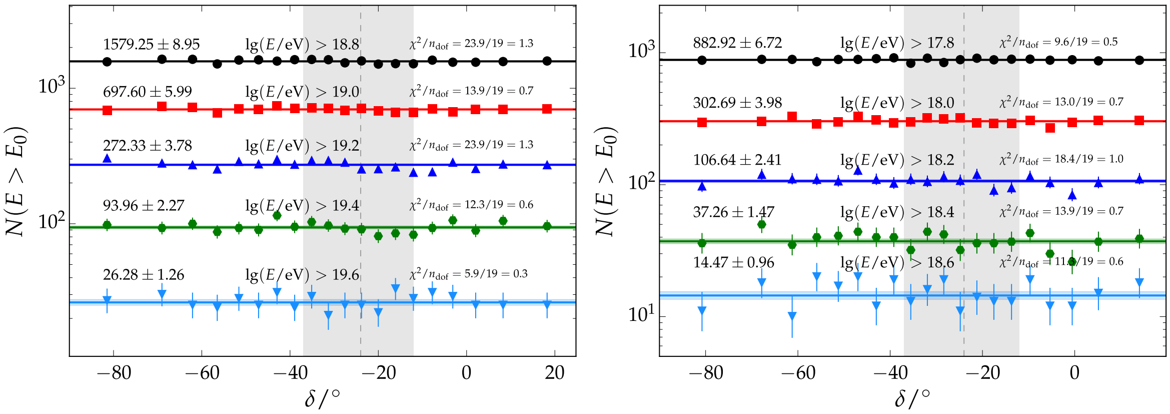

(a) SD-1500

(b) SD-750

Figure 4.42: Measured intensities as a function of declination and for different threshold energies. The intensities show no statistically significant deviation from a constant fit. The dipole at $\delta = -24°$ is indicated as dashed line, its uncertainty is shown as gray band.

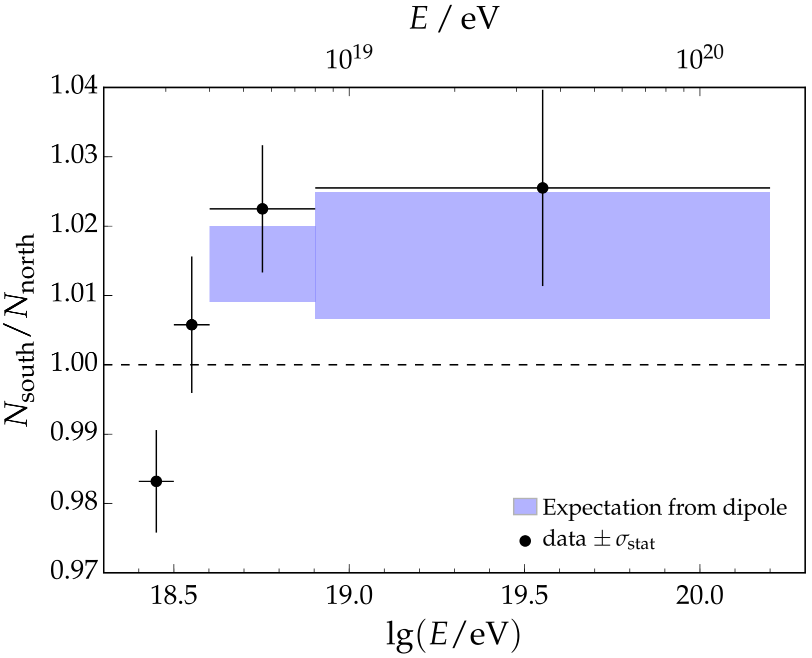

Figure 4.43: Comparison of SD-1500 event counts in two declination ranges corresponding to arrival directions from the south and north, respectively. The expectation for the two energy intervals studied for the large-scale anisotropy are shown as blue boxes [115].

4.9.3 Differential spectra

The differential flux as obtained from Eq. (5.1) is divided into different declination intervals to investigate a possible dependence on the arrival direction of the primary particles. The SD-1500 data is split into four declination bins covering the same amount of exposure, whereas the SD-750 data is only divided into three bins of equal exposure due to the lower statistic. The edges of the declination intervals chosen for the SD-1500 are –90°, –49.3148°, 29.4746°, –10.0059°, and 24.79°. The resulting energy spectra are shown in Fig. 4.44a and Fig. 4.44b. The residuals of the individual declination spectra with respect to the average

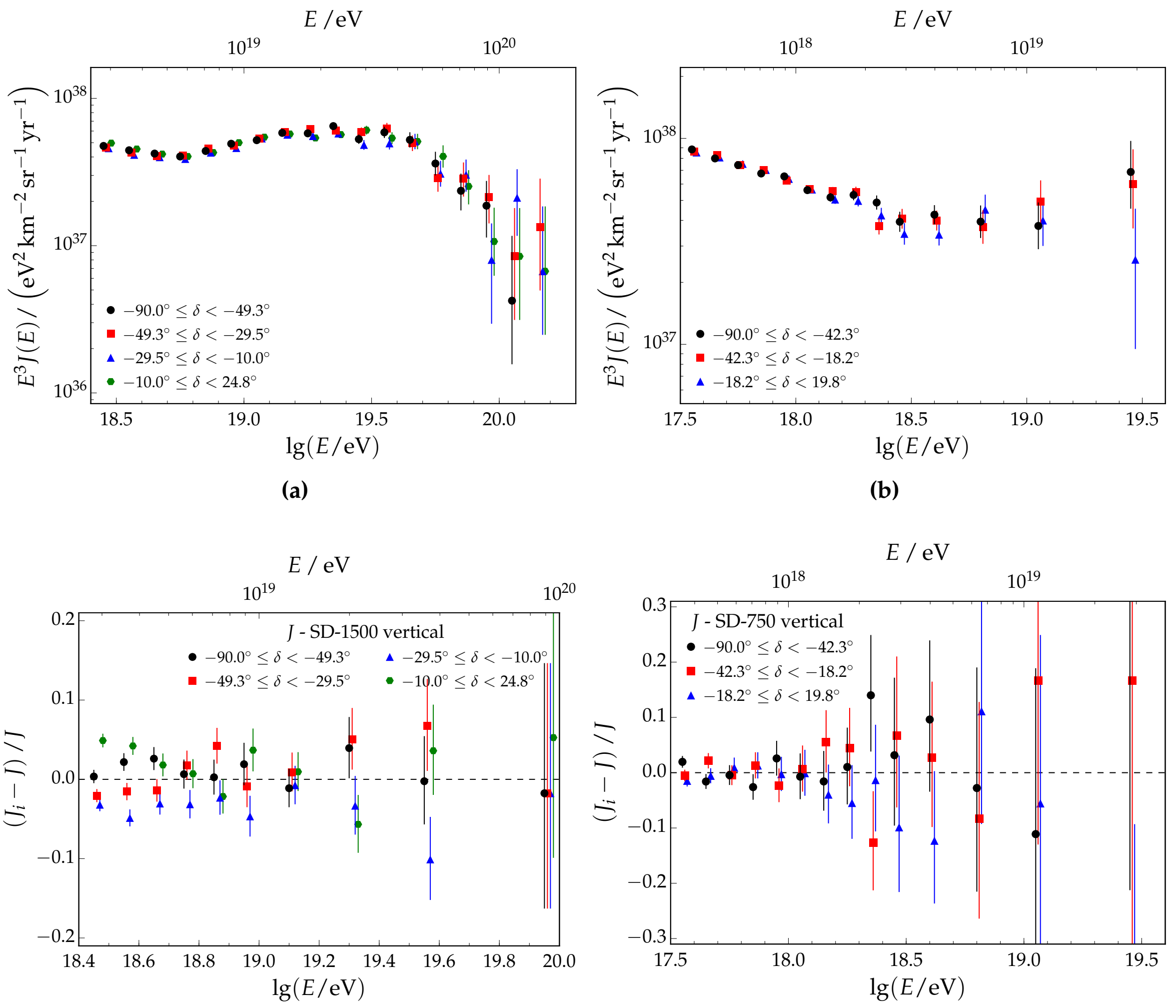

(a) **(b)**

(c) **(d)**

Figure 4.44: The measured energy spectra of (a) SD-1500 and (b) SD-750 binned in different declination intervals. The residuals with respect to the average spectra are shown in (c), (d).

spectrum not binned in declination are depicted in Fig. 4.44c and Fig. 4.44d. No statistically significant trend is apparent. To further quantify the absence of any significant deviation, a Poisson maximum-likelihood approach is used to fit the differential spectra obtained from the SD-1500 data. The fit model is comprised of a simple power law below the ankle and a power law with smooth suppression above as stated in Eq. (4.77).

The spectra are shown in Fig. 4.45 together with their fits. The individual spectra are not corrected for the smearing due to the detector effects. A comparison of the measured fluxes to the fitted ones is depicted in Fig. 4.46. The deviations of the measurements to the fits are given in units of statistical uncertainty. Given the uncertainties, the data points are compatible on the 2σ level. The uncertainties on the relative residuals are obtained from bootstrapping the energy distribution and calculating the uncertainty on the distribution a few hundred times. A closer look into the declination interval overlapping with the field of view of the Telescope Array experiment is performed in the next Section 4.10.

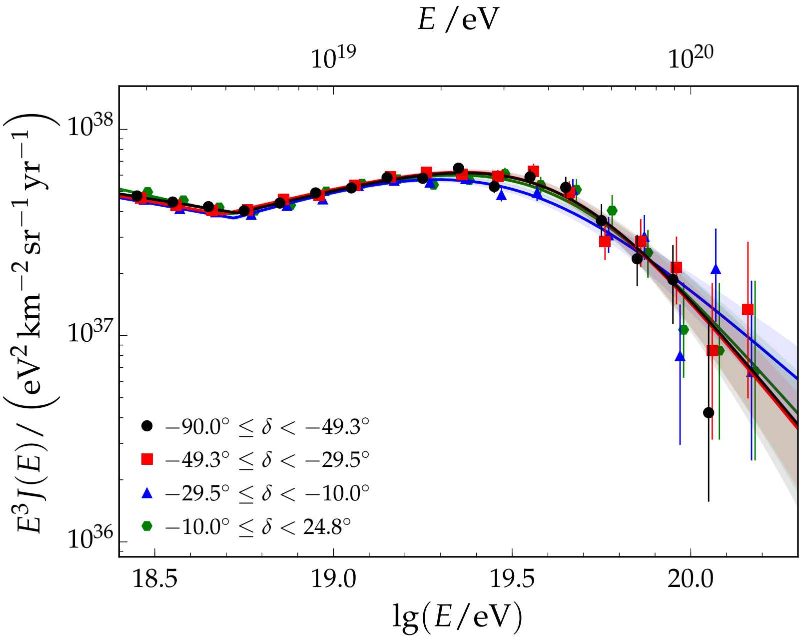

Figure 4.45: The spectrum as measured with the SD-1500 array for four different declination intervals covering equal exposures. The fits to the individual spectra are shown in addition.

4.10 Comparison to Telescope Array Measurements

Besides the Pierre Auger Observatory, the only other experiment that is able to measure the flux of UHECRs at the energies of the suppression is the Telescope Array experiment (TA), which is located in the northern hemisphere, in Millard County, Utah (USA) at a latitude of 39.3° and an altitude of about 1400 m above sea level [116]. The experiment is set up as a hybrid detector. The surface detector is composed of 507 scintillation counters spread at a distance of 1.2 km over an area of about 700 km^2. Each scintillation counter consists of two layers of 1.2 cm thick plastic scintillators with an area of 3 m^2 each [117]. Due to the scintillation counters, the SD of TA is mainly sensitive to the electromagnetic shower component, rather than the muonic component as is the case for the SD of Auger. The fluorescence detector consists of 48 telescopes distributed into three buildings located at the perimeter of the array. The data taking started in 2008, four years after the first data were taken by Auger. An overview of selected characteristics of both experiments is given in Table 4.8.

The SD energy scale of TA is determined by the FD. The SD energy estimator of TA is denoted as S_{800}. To correct for the zenith dependence, a Monte Carlo lookup table is used in TA, which connects S_{800} with the SD energy E_{SDMC}. This energy represents the reconstructed SD energy, which is then calibrated with the FD energy. In order to match the FD energies measured in hybrid events with the energy obtained from the lookup table, the SD energies have to be scaled down by $E_{\mathrm{SDMC}}/1.27$.

4.10.1 Data sets

The energy spectrum as measured by the TA-SD includes events with energies above $10^{18.2}$ eV and zenith angles up to 45°. The zenith angle range is increased to 55° when selecting only events above 10^{19} eV. With the extended zenith range, TA covers a declination range of –15.70° to 90° (whereas for $\theta < 45°$ the maximum declination in the southern hemisphere reduces to –5.70°). The TA spectra resulting from the two different zenith angle limits are

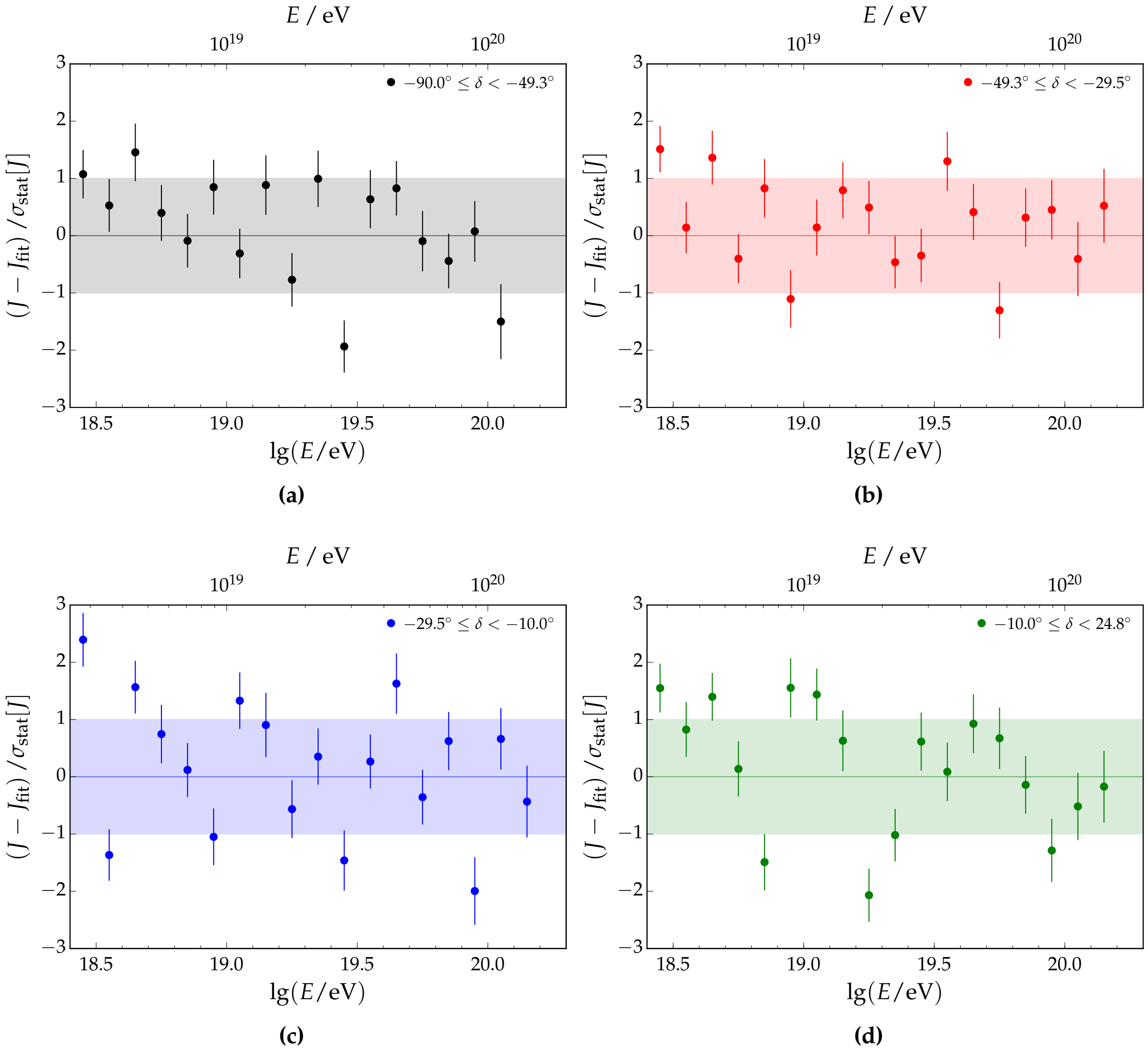

(a) **(b)** **(c)** **(d)**

Figure 4.46: The flux residuals resulting from the individual fits to the declination spectra as shown in Fig. 4.45 in units of statistical uncertainty. The data are compatible on the 2σ level.

shown in Fig. 4.49b. The spectrum using events above 10^{19} eV is divided into two declination intervals, one of them overlapping with the Auger measurements ($\delta < 24.8°$) and the other one corresponding to the TA-only declination range ($\delta > 24.8°$). An overview of the SD-1500 data set used in the comparison is given in Table 4.7.

The spectra shown in Fig. 4.49 are corrected for the smearing effects due to the detector. The SD-1500 spectrum is unfolded using the multi-smooth function of Eq. (4.73). The correction factors obtained from the unfolding of the total SD-1500 spectrum can be used to correct also the declination-binned spectra as the zenith dependence of the detector kernel is negligible. In case of TA, the corrections due to migration effects are included in the exposure. The exposure is visualized in Fig. 4.47 as function of declination for the three SD measurements of Auger and the two SD data sets of TA. The exposure for the SD-1500 data set covering declinations from −90° to 24.79° accumulates to 51 588 km^2 yr sr and the collected TA exposure for events with zenith angles extending up to 55° is 8300 km^2 yr sr. Using only events up to 45°, the exposure for TA reduces to 6300 km^2 yr sr. As can be seen from Fig. 4.48, the energy spectra of the two experiments show a clear offset in the overall energy scale. When performing a fit to the unfolded spectra, a difference in the suppression energy

Table 4.8: Overview of a selection of characteristics of Auger and TA. The detector extensions aimed at measuring low energetic showers are not included.

Detector	Characteristic	Auger	TA
SD	average latitude	–35.2°	39.3°
	average altitude	1400 m	1400 m
	surface area	3000 km^2	700 km^2
	lattice	1.5 km hexagon	1.2 km square
	detector type	water-Cherenkov	scintillator
	sensitive shower comp.	muonic	electromagnetic
	shower size estimator	S_{1000}	S_{800}
	exposure	51 588 km^2 yr sr	8300 km^2 yr sr
	max. declination range	$-90° < \delta < 24.79°$	$-15.70° < \delta < 90°$

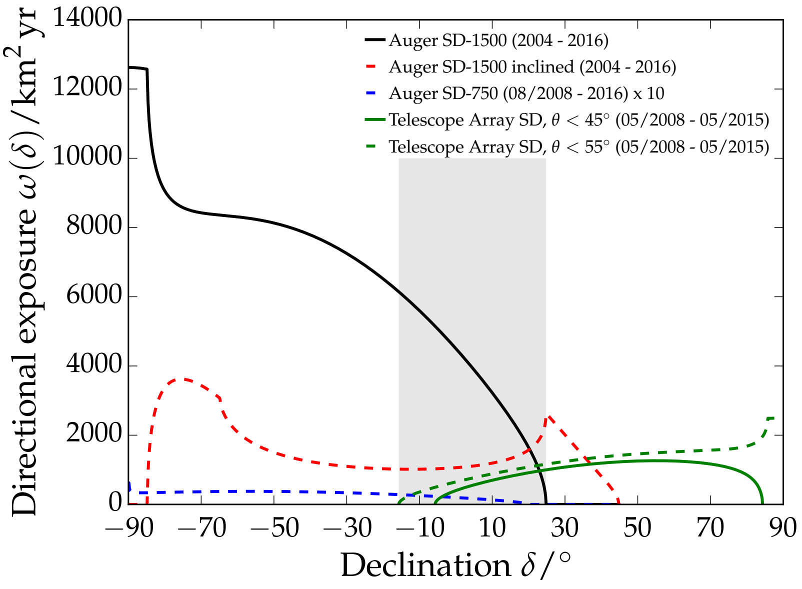

Figure 4.47: The directional exposure for Auger and TA. The Auger exposures correspond to the three SD measurements: SD-750 (blue dashed line), SD-1500 (black solid line) and SD-1500h (red dashed line). The TA exposure is shown for zenith angles up to 45 degree (green solid line) and 55° (green solid line). The common declination range of both experiments is indicated by the gray box and covers declinations from –15.70° to 24.79°.

is apparent, indicating an energy-dependent difference between the measurements. The measured suppression energy for the SD-1500 spectrum is found at $\lg(E_s/\mathrm{eV}) = 19.57 \pm 0.03$, while the fit to the TA spectrum results in a suppression energy of $\lg(E_s/\mathrm{eV}) = 19.89 \pm 0.07$. To check whether this offset in the energy scale is due to differences in the detector set up and the respective analyses or due to astrophysical effects, the spectra of both experiments are analyzed in a common declination band in the following.

4.10.2 Comparison of the Auger and TA spectra in the common declination band

The maximum declination interval that is in the field of view of both experiments is –15.70° to 24.79° when using a maximum zenith angle of 60° and 55° for Auger and TA, respectively. The SD-1500 spectra for the common declination band and the Auger-only band are depicted

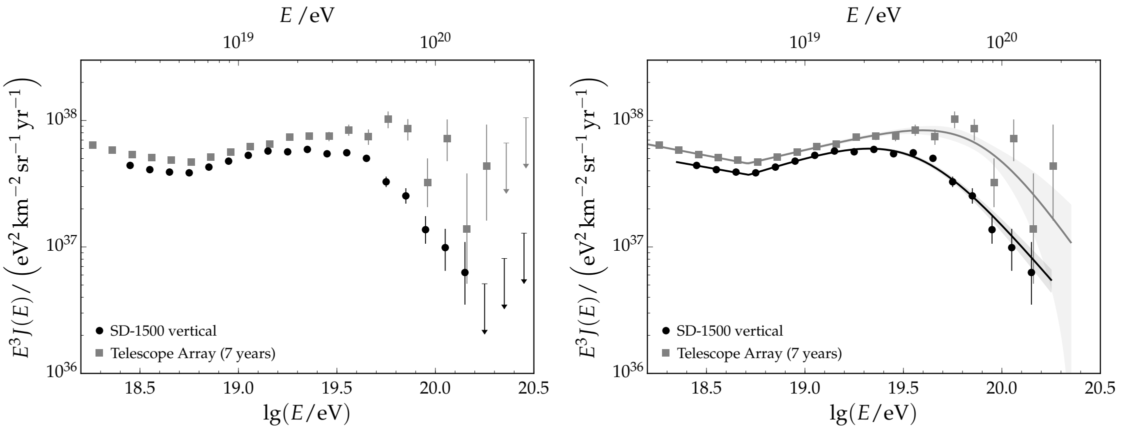

(a) **(b)**

Figure 4.48: Comparison of the SD-1500 spectrum and the TA spectrum with a maximum angle of 45°. Both spectra are corrected for the smearing due to the detector. A difference in the overall energy scale between the two measurements is apparent. The systematic uncertainty of the energy scale is 14 % for Auger and 21 % for TA.

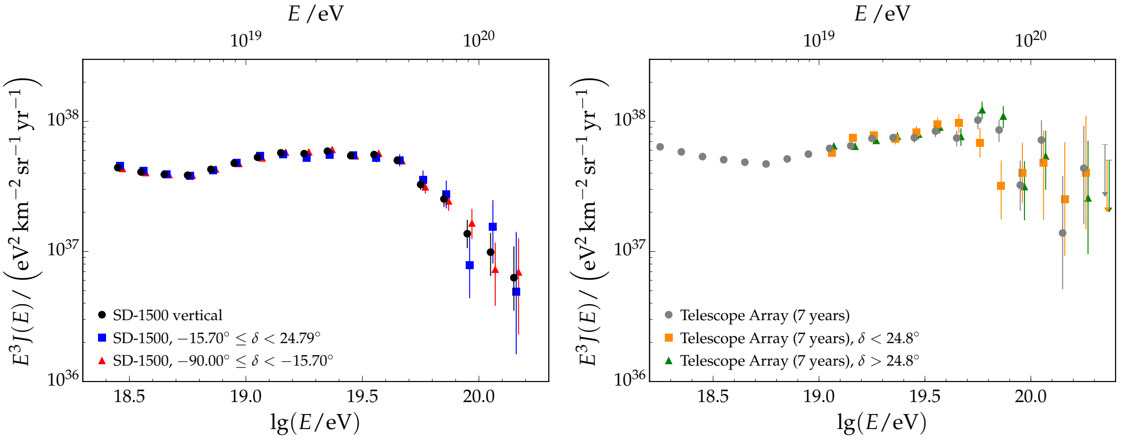

(a) **(b)**

Figure 4.49: Energy measurements by Auger and (b) TA binned in declination: (a) the SD-1500 spectrum divided into a declination band which overlaps with the field of view of TA ($-15.7° < \delta < 24.79°$) and a band which is unaccessible for TA ($-90° < \delta < -15.7°$). (b) The TA data divided into a declination range compatible with Auger ($\delta < 24.8°$) and a TA-only range ($\delta > 24.8°$).

in Fig. 4.49a. The binned spectra are in good agreement with the total SD-1500 spectrum. The declination-binned spectra measured by TA are shown in Fig. 4.49b. In [111], TA reports a difference in the position of the flux suppression when comparing the two declination spectra. The stated suppression energies are $\lg(E_{\mathrm{break}}/\mathrm{eV}) = 19.59 \pm 0.06$ for $\delta < 24.79°$, and $\lg(E_{\mathrm{break}}/\mathrm{eV}) = 19.85 \pm 0.03$ for $\delta > 24.79°$, having a statistical significance of 3.9σ [110]. To quantify the significance of the difference, the declination spectra of both experiments are fitted using two different models.

The first model (*hard model*) corresponds to the model used by TA and is comprised of three power laws E^{γ_1}, E^{γ_2} and E^{γ_3} with hard breaks at the ankle position E_a and the suppression position E_{break} [118]. The second model (*smooth model*) consists of a hard break at the ankle with a subsequent smooth suppression as introduced in Eq. (4.77). The fit method employed here is a chi-squared minimization. The fits using the hard model are shown in Fig. 4.50 for both experiments. While this model is able to describe the TA data sets well, it fails to fit the SD-1500 spectra due to the higher statistical power at the highest energies which reveals a smoother suppression region. The break energies found for TA are $\lg(E_\text{break}/\text{eV}) = 19.62 \pm 0.12$ for $\delta < 24.79°$ and $\lg(E_\text{break}/\text{eV}) = 19.85 \pm 0.06$ for $\delta > 24.79°$, which is in agreement with the results reported by TA. In Fig. 4.50c and Fig. 4.50d, the residual of the measured spectra with respect to the fit of the total SD spectrum is given in units of standard deviation. The difference in the break energy is driven by the deviation of the fluxes at about $10^{19.8}$ eV. At $10^{19.85}$ eV, the difference of the declination spectra measured by TA to the fit model describing the total TA spectrum exceeds 3σ. However, the difference in the declination spectra at $10^{19.05}$ eV is almost as significant. This difference at lower energies, where the statistic is higher, weakens the significance of the difference in the break energies.

Next, the spectra are fit with the smooth model as used by Auger. This model results in a sound description of the measured Auger spectra, as can be seen from Fig. 4.51a and Fig. 4.51c. No significant deviation from the total SD spectrum is found. While the total TA spectrum is well described by the smooth model (see Fig. 4.48b), the fit of a smooth suppression to the declination-binned spectra show larger uncertainties due to the reduced statistic.

Increasing the energies of Auger by 5.2 % and decreasing the ones of TA by −5.2 % results in a better agreement of the measured spectra at energies lower than the suppression energy. This is shown in Fig. 4.52a for the total spectra. The rescaled declination spectra are visualized in Fig. 4.52b. The residuals of the rescaled spectra are shown in Fig. 4.52c and Fig. 4.52d The applied shift is well within the energy scale systematic of 14 % and 21 %. However, the flux difference above an energy of about $10^{19.5}$ eV is not resolved by this shift.

A further comparison of the spectra is performed in the next section. Here, the spectrum calculation takes into account the differences in the directional exposures.

4.10.3 Correction for dependence on directional exposure

The energy spectrum is in principle sensitive to anisotropies. The differential flux $\Phi(\alpha, \delta, E)$ at an energy E and any incoming direction (α, δ) can be decomposed into an isotropic part, Φ_0 and an anisotropic one Φ_aniso. The expected number of events per energy unit is then calculated as:

$$\begin{aligned} \frac{\mathrm{d}N}{\mathrm{d}E} &= \int \mathrm{d}\Omega\, \omega(\delta)\Phi(\alpha, \delta, E) \\ &= \int \mathrm{d}\Omega\, \omega(\delta)\left(\Phi_0(E) + \Phi_\text{aniso}(\alpha, \delta, E)\right). \end{aligned} \tag{4.82}$$

The total exposure measured in $\text{km}^2\,\text{yr}\,\text{sr}$ is given by:

$$\mathcal{E} = \int \mathrm{d}\Omega\, \omega(\delta). \tag{4.83}$$

Using this expression, Eq. (4.82) can be modified to:

$$\frac{1}{\mathcal{E}}\frac{\mathrm{d}N}{\mathrm{d}E} = \Phi_0(E) + \frac{1}{\mathcal{E}}\int \mathrm{d}\Omega\, \omega(\delta)\Phi_\text{aniso}(\alpha, \delta, E), \tag{4.84}$$

where Φ_0 corresponds to the energy spectrum as stated in Eq. (5.1) in case of negligible anisotropies:

$$\Phi_0(E) \simeq \frac{1}{\mathcal{E}}\frac{\mathrm{d}N}{\mathrm{d}E}. \tag{4.85}$$

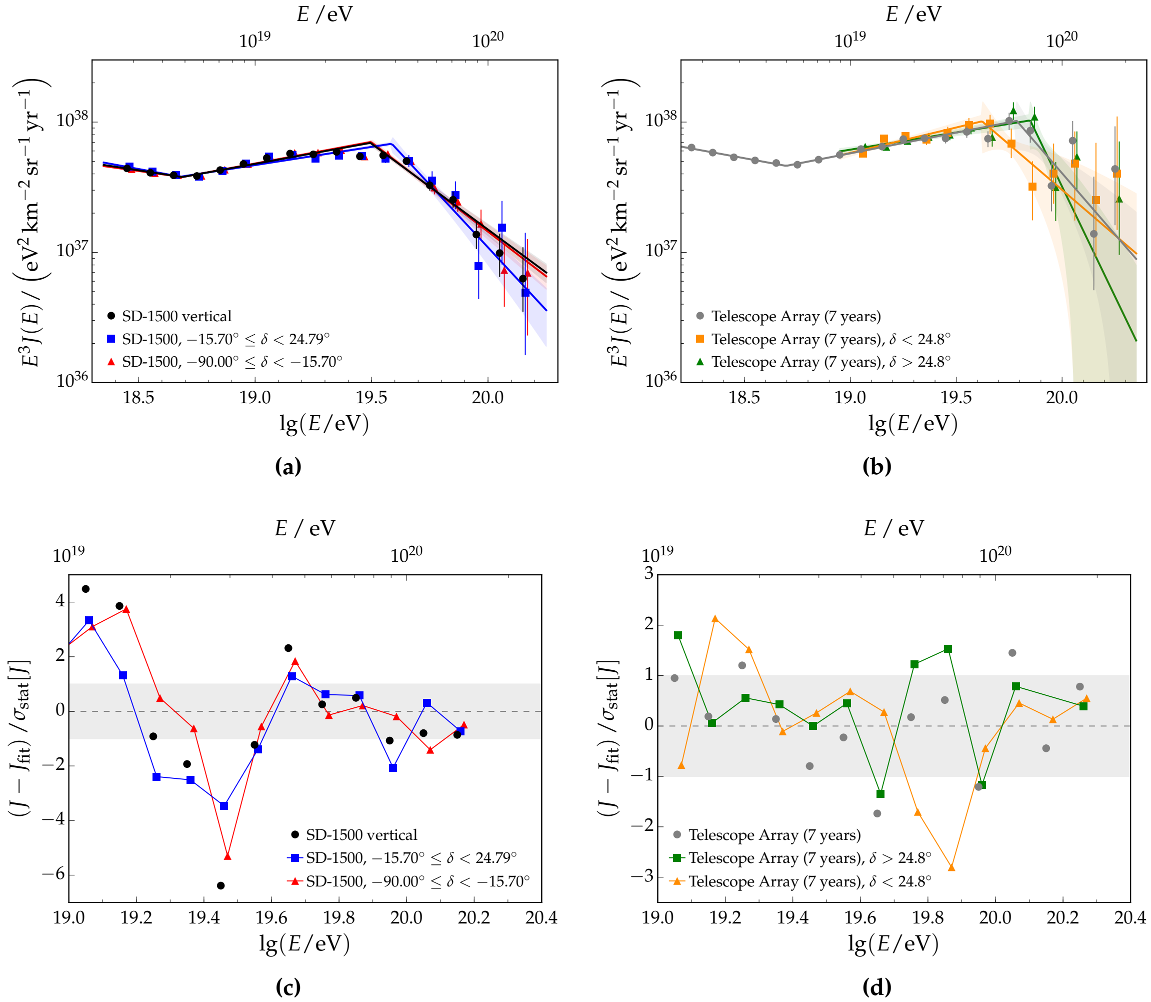

(a) **(b)**

(c) **(d)**

Figure 4.50: Comparison of the declination-binned spectra of Auger and TA to a fit model of three power laws with hard breaks. The model cannot describe the Auger spectra at the energy range of the suppression. (c), (d) Residual representation. The residuals are given in units of standard deviation. The chosen reference is the fit which describes the total spectrum. The energy range is limited to the range accessible with the declination-binned spectra of TA.

At energies above 10^{19} eV, anisotropies are likely to become non-negligible [25], leading to a dependence of the spectrum on the directional exposure $\omega(\delta)$. Therefore, when comparing the measurements of different experiments, the measured spectra will differ even when accounting for detector effects and limiting the data sets to a common field of view. To overcome the dependence on the directional exposure, the energy spectrum is recovered by considering the number of events per solid angle unit [110, 111, 119]:

$$J_{1/\omega}(E) = \frac{1}{\Delta\Omega\Delta E} \sum_{i=1}^{N} \frac{1}{\omega(\delta_i)}. \tag{4.86}$$

By weighting each event with the directional exposure of its declination, any impact due to anisotropies is corrected for. The statistical uncertainty to first order is given by:

$$\Delta J_{1/\omega}(E) = \frac{1}{\Delta\Omega\Delta E} \sqrt{\frac{N}{\mathcal{E}} \int \frac{\mathrm{d}\Omega}{\omega(\delta)}}. \tag{4.87}$$

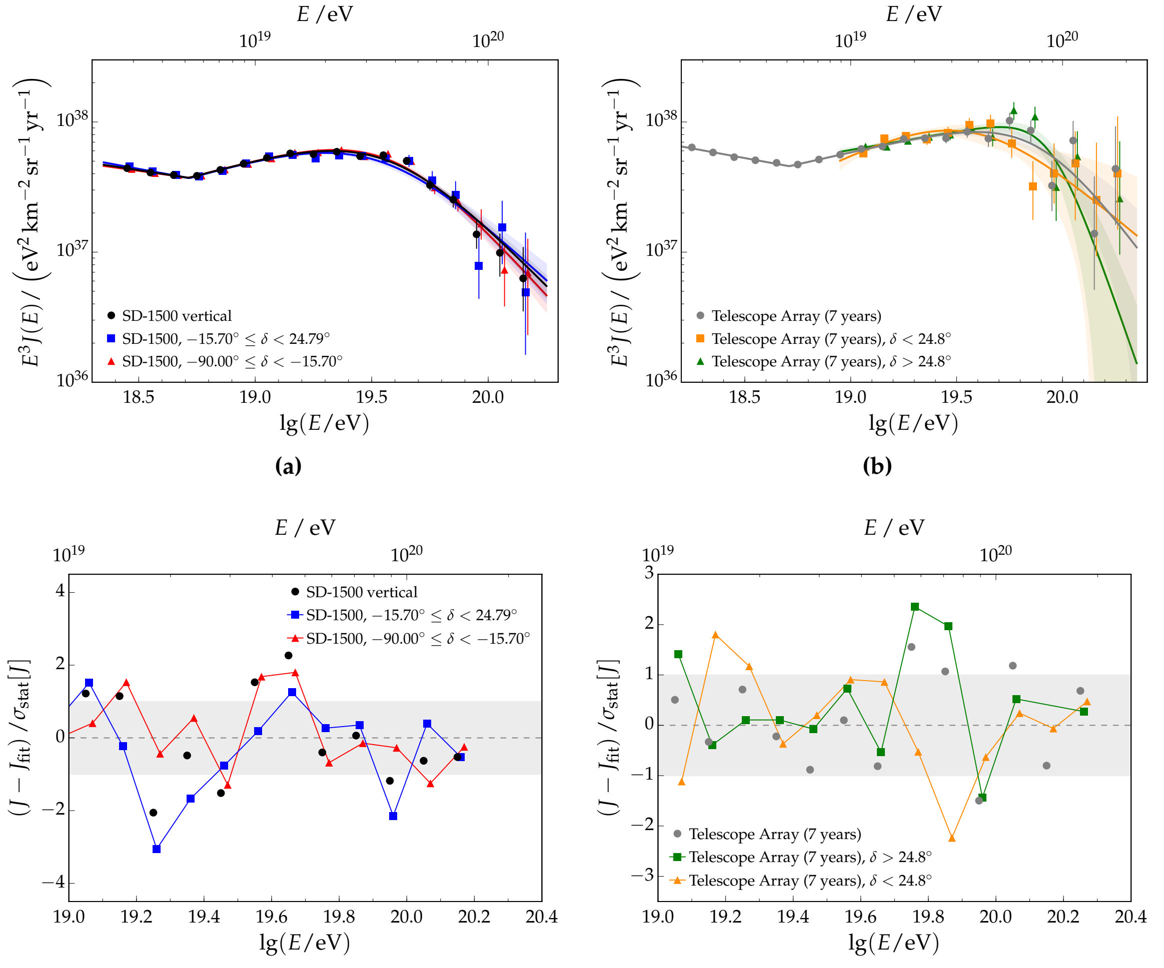

(a) **(b)**

(c) **(d)**

Figure 4.51: Comparison of the declination-binned spectra of Auger and TA to a fit model with a hard break at the ankle and a subsequent smooth suppression. While the Auger data are well-described by the model, the lower statistic of TA at the suppression favors the hard model shown in Fig. 4.50b. The residuals are given in units of standard deviation and the chosen reference fit is the one to the total spectrum.

The spectrum obtained by this $1/\omega$ method is compared to the standard approach for energies above $10^{18.9}$ eV, where effects due to possible anisotropies might start to play a role. The SD-1500 spectra calculated with the two methods are depicted in Fig. 4.53 for the full declination range of the vertical Auger data ($-90° < \delta < -24.79°$). The highest energies are re-binned to reduce scatter. As can be seen from Fig. 4.53b, both spectra agree well within their statistical uncertainties. Restricting the declination range to the common band as done in Fig. 4.54 shows a very good agreement between the two spectra estimates. Finally, the spectra obtained with both the standard method and the $1/\omega$ method are shown next to each other in Fig. 4.55 for the full sky as well as the common declination band.

A direct comparison of the spectra of Auger and TA as calculated with the $1/\omega$ method in the common declination band is depicted in Fig. 4.56a. Fitting both spectra with broken power law functions, the fitted energies for the cutoff result in $\lg(E/\mathrm{eV}) = 19.62 \pm 0.05$ for TA and $\lg(E/\mathrm{eV}) = 19.51 \pm 0.03$ for Auger, corresponding to a difference of about 1.9σ. The respective fits are shown in Fig. C.13a. Taking the ratio of the measured fluxes shows an

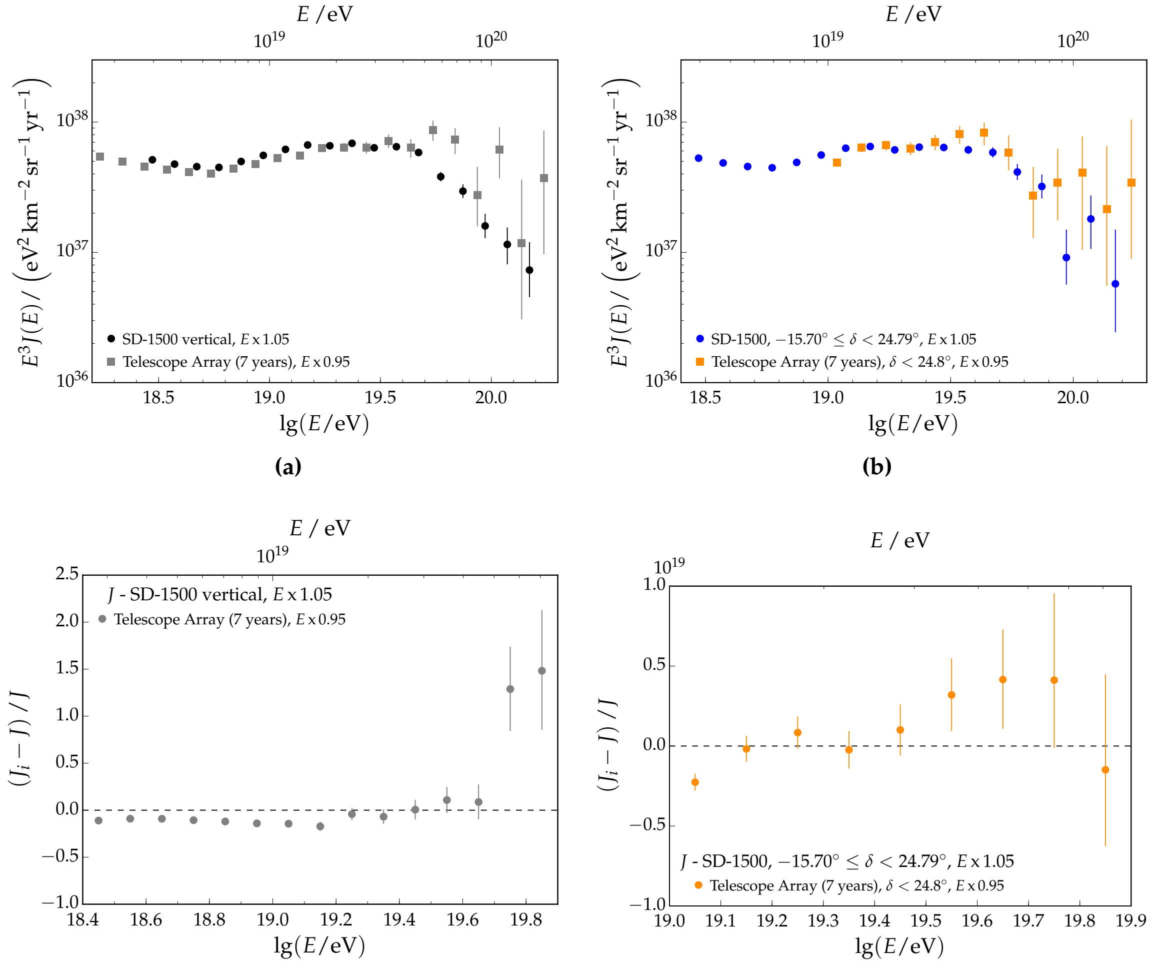

(a) **(b)**

(c) **(d)**

Figure 4.52: (a) The energy scale of Auger and TA are changed by ±5.2 %, which is well within the systematic uncertainty of the energy scales reported by both experiments. While a better agreement is reached for energies below $10^{19.5}$ eV, a large difference between the measured fluxes for the whole sky remains at the highest energies. (b) The difference in the common declination band is reduced by the shift. Residuals of the rescaled spectra for (c) the full sky and (d) the common declination band. The residuals are only shown up to an energy of $10^{19.9}$ eV due to the increased statistical fluctuations at the highest energies.

energy-dependent difference. Performing a fit with a linear dependence on the logarithmic energy gives:

$$f_{\mathrm{ratio}}(E) = (7.22 \pm 2.68) - (0.33 \pm 0.14)\,\lg E. \tag{4.88}$$

An energy-dependent difference is also present when shifting the energy scales of both experiments by ±5.2 %, as done for the spectra calculated with the standard approach. Performing a fit with broken power laws results in the cutoff energies of $\lg(E/\mathrm{eV}) = 19.592 \pm 0.063$ for TA and $\lg(E/\mathrm{eV}) = 19.531 \pm 0.021$, which is a difference of 0.9σ. The fits are shown in Fig. C.13b and the rescaled spectra are depicted in Fig. 4.56c. Fitting the residual of the rescaled spectra shown in Fig. 4.56d with the linear function results in:

$$f_{\mathrm{ratio}}(E) = (9.95 \pm 2.97) - (0.47 \pm 0.16)\,\lg E. \tag{4.89}$$

An energy-dependent difference was already apparent in the spectra calculated with the standard method. As the spectra obtained with the $1/\omega$ method are insensitive to anisotropies, the

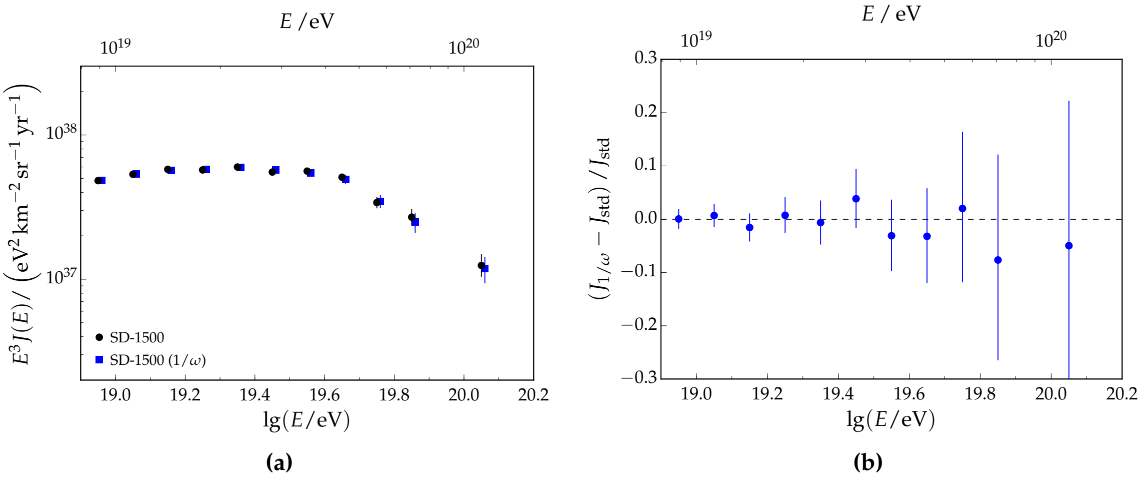

Figure 4.53: (a) The SD-1500 spectrum obtained with the the $1/\omega$ method is compared to the spectrum calculated with the standard approach. Both spectra use the full declination range for events with zenith angles below 60°. (b) Relative residual with respect to the spectrum obtained with the standard method. The $1/\omega$ spectrum is compatible with the standard calculation.

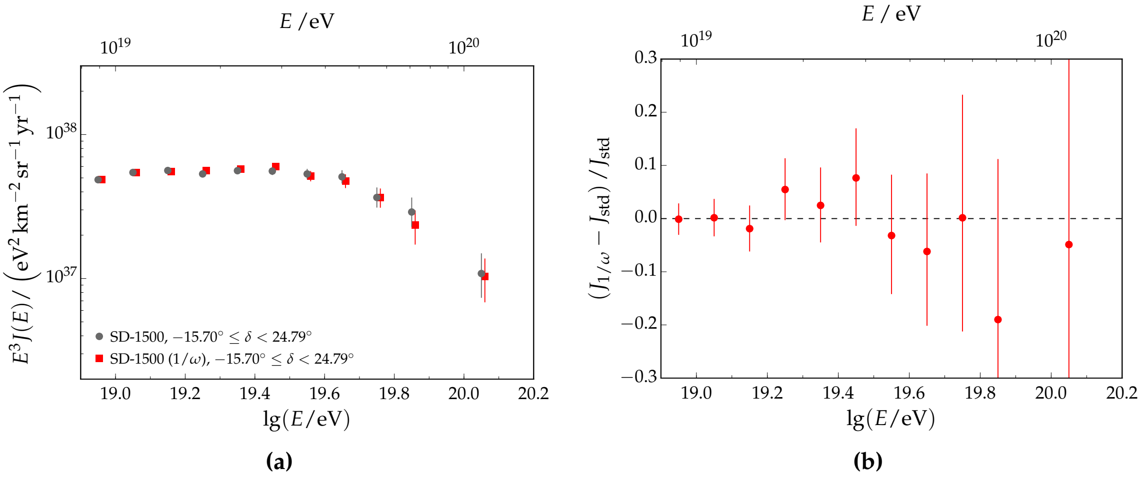

Figure 4.54: (a) Comparison of the SD-1500 spectra obtained with the two different methods. Both spectra use events of the common declination band. (b) The relative residual shows a good agreement of the spectra obtained for the common declination band.

calculated spectra have to match within their uncertainties by construction. The remaining energy-dependent flux differences indicate an experimental origin. A careful study of the systematic uncertainties, with the focus on sources for energy-dependent systematic uncertainties, is needed to help understand fully the difference between the measured spectra of Auger and TA at the highest energies. The currently reported energy-dependent systematic uncertainties of both experiments are not sufficiently large enough to explain the difference in the common declination band.

4.10.4 Conclusion

The leading experiments for the study of UHECRs to-date are the Pierre Auger Observatory and the Telescope Array experiment. Both experiments employ a hybrid design to calibrate the

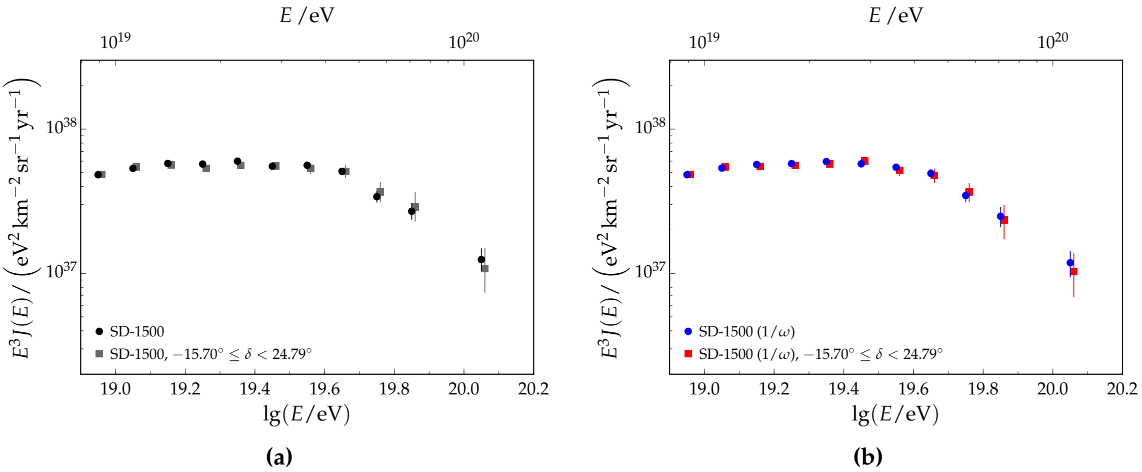

(a) **(b)**

Figure 4.55: Comparison of the spectrum of the full declination range to the spectrum obtained for the common declination range for (a) the standard calculation and (b) the $1/\omega$ method. Both methods result in compatible spectra.

SD measurements to the FD energies on an event-by-event basis. The SD of both experiments is sensitive to different shower components. While the SD of Auger is more sensitive to muons due to the employed array of WCDs, the scintillation counters of TA are more sensitive to the electromagnetic shower component. Looking at the measured energy spectra, a clear offset between the energy scales is apparent. As the two experiments are located on opposite hemispheres, they see different parts of the full sky. Hence, the difference in the energy scale between Auger and TA could either have an astrophysical or a sole experimental origin. Shifting the energies of Auger and TA by 5.2 % each (increasing the Auger energies and decreasing the TA ones), results in a reasonable agreement of the energy spectra below an energy of about $10^{19.5}$ eV. This shift is covered by the systematic uncertainties of the two energy scales (14 % for Auger, 21 % for TA). Above an energy of about $10^{19.5}$ eV, in the region of the suppression, a significant difference remains. To determine the source of the difference at the highest energies, the spectra are studied in a common declination band. The common band of $-15.7° < \delta < 24.8°$ corresponds to a declination range which is accessible to both experiments. The dependence of the exposure on the declination differs for Auger and TA, resulting in different energy spectra even though the same part of the sky is observed. To overcome this, a new spectrum calculation [110, 111] is exploited, where each event is weighted by its directional exposure ($1/\omega$ method). The $1/\omega$-spectra of Auger and TA still show a difference, which increases with energy. This indicates an experimental origin as the spectra in the common band are supposed to match. The currently reported uncertainties of both experiments are too small to account for the remaining difference. Detailed studies are needed to determine energy-dependent systematic uncertainties which are yet unknown.

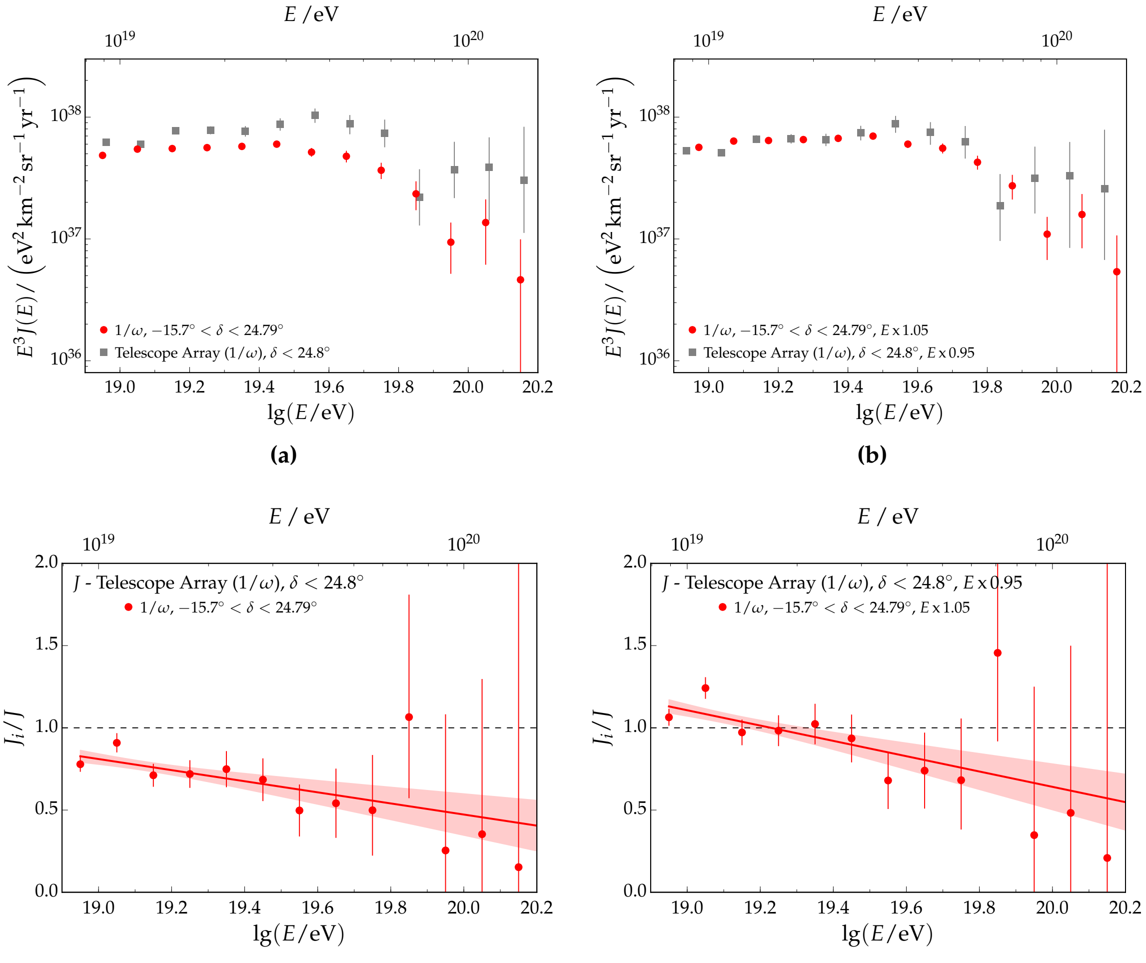

(a)

(b)

(c)

(d)

Figure 4.56: Comparison of the SD-1500 spectrum of Auger with the TA SD spectrum using (a), (c) the nominal energy scales and (b), (d) an energy shift of ±5.2 %. Both spectra are obtained with the $1/\omega$ method. An energy-dependent difference between the Auger and TA spectra is present.

CHAPTER

5

Anisotropy Imprints on the Spectrum

The study of the arrival directions of cosmic rays is crucial to elucidate the origin of the particles. Being subject to deflections in the magnetic fields, the particles lose their directional information and do not point back to their sources. However, a search for anisotropic patterns is still possible at sufficiently high energies as the deflections decrease with increasing energy. Studying the arrival directions of cosmic rays with energies above 8 EeV revealed a large-scale anisotropy. A harmonic analysis in the right ascension shows a modulation of the event rate as depicted in Fig. 5.1a. The anisotropy is well-described by a dipole pointing towards $((100 \pm 10)^\circ, (-24 \pm 12)^\circ)$ in equatorial coordinates. The smoothed event distribution is shown in Fig. 5.1b. With an amplitude of 6.5 %, it is interesting to see whether this dipole modifies the energy spectrum when analyzing different regions of the sky. To search for anisotropies on intermediate to small scales, the energy threshold has to be increased. Using events with energies above 40 EeV revealed two warm spots in the vicinity of the supergalactic plane. The warm spot in the southern hemisphere is accessible with Auger data, while the one in the northern hemisphere is seen by TA. The local significance of the overdensities is shown in Fig. 5.2. Here, the joint working group of Auger and TA performed a full-sky search for anisotropies by combining their measurements. The recent analysis used data, which is not public yet. As a member of the working group, I will perform a check for possible imprints of the warm spot on the energy spectrum in the following by only using the SD data of Auger. This is a first step towards a combined study of Auger and TA data in different regions of the sky.

5.1 Event selection

The event selection follows the one described in Section 4.1. The SD-1500h data are analyzed in addition to the vertical data of SD-1500. The SD-1500h data are covering zenith angles from 60° up to 80°. The covered declination range increases from $-90^\circ < \delta < 25^\circ$ to $-90^\circ < \delta < 45^\circ$, corresponding to a coverage of 85 % of the sky. The data from the SD-1500 array were recorded between 01 January 2004 and 31 December 2016. Each data set is cut on the energy of full efficiency. This energy corresponds to 3 EeV and 4 EeV for the SD-1500 and SD-1500h data,

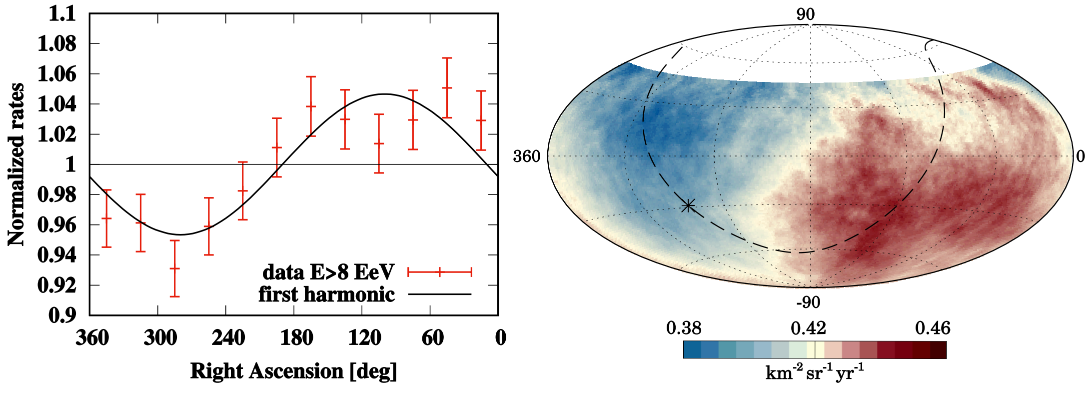

(a) (b)

Figure 5.1: (a) Normalized rate of events with energies above 8 EeV as function of right ascension. The data set contains vertical and inclined events. The solid line corresponds to the first-harmonic modulation from the Rayleigh analysis performed to study the large-scale anisotropy. The significance of the modulation is larger than 5σ [25]. (b) Sky map showing the event distribution for energies above 8 EeV in equatorial coordinates. The galactic plane is depicted by the dashed line with the galactic center marked by the asterisk (modified, original taken from [25]).

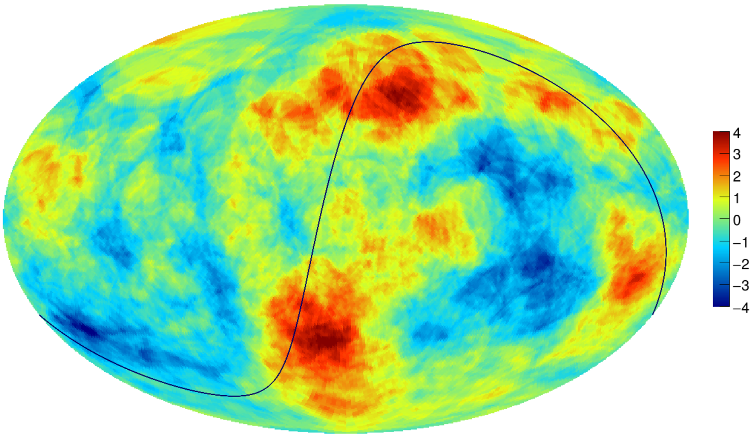

Figure 5.2: Significance map in equatorial coordinates of the joint data sets of SD-1500, SD-1500h, and Telescope Array (modified, original taken from [120]). The supergalactic plane is shown as black line, the magnitude of the local statistical significance is indicated by the color scale. Two warm spots are found along the supergalactic plane. The warm spot in the southern hemisphere is accessible with Auger data, while the one in the northern hemisphere lies in the field of view of TA.

respectively. The SD-1500 data set is corrected for the weather and geomagnetic effects on the measured shower size as discussed in Section 4.3.

In addition to the data recorded with the SD-1500 array, the data from the SD-750 array is analyzed. The maximum reachable declination is 20° due to the reduced maximum zenith angle of 55°. The energy of full efficiency corresponds to 0.3 EeV. The quality data used were recorded from the 01 August 2008 up to the 31 December of 2016.

5.2 Analytical exposure and coordinate systems

The calculation of the exposure in different coordinate systems is based on Eq. (4.12). The maximum of the exposure is at the south pole direction due to the Observatory's latitude of $l_0 = -35.2°$. For vertical events with zenith angles below 60°, the pole lies always in the field of view as is visualized in Fig. 5.3a. Here, the analytical coverage is shown in equatorial coordinates. The coverage shows a decrease from −90° up to 25° in declination, the latter one being the maximum declination reachable with events having $\theta < 60°$ (depicted as dashed line). When events up to 80° are included, the coverage will extend to 45° in declination as illustrated by the dashed-dotted line. The sky coverage for the galactic and supergalactic coordinate systems are shown in Fig. 5.3b and Fig. 5.3c.

The *equatorial* coordinate system is best suited to show the dependence of the Observatory's field of view on the location on Earth. Two measurements are used for this coordinate system, the right ascension α and the declination δ. The origin of the right ascension is defined by the vernal equinox, which denotes the position of the Sun on the first day of spring. The galactic and extragalactic coordinate systems are used to study the origin of large-scale anisotropies.

The *galactic* coordinate system uses the Sun as its origin and the fundamental plane is approximately given by the galactic plane. The galactic longitude, l, denotes the distance of an object along the plane with respect to the galactic center and the galactic latitude, b, gives the angle of the object to the north or south of the plane. As the galactic plane denotes a matter overdensity in the Galaxy, an anisotropic pattern with more events coming from the plane than from the regions above and below the plane can be expected. However, the dipole found for energies above 8 EeV points away from the plane, into the direction (233° , −13°) as visualized by the star in Fig. 5.3b, indicating an extragalactic origin.

The *supergalactic* coordinate system is set up such that the equator aligns with the supergalactic plane, which corresponds to a planar structure in the local galaxy density field. The dipole extremes lie closer to the poles in this coordinate system as visible in Fig. 5.3c.

5.3 Search for flux enhancements along supergalactic plane

A full-sky search for anisotropies becomes possible when combining the data measured by Auger and TA. This was done for the work presented in [120]. Here, the authors studied the full-sky for two different energy ranges. The first range covers the energies above the ankle up to the highest energies and corresponds to a search for large-scale anisotropy as the one reported by Auger (see Fig. 5.1). The second range focuses on energies beyond the flux suppression to search for intermediate and small-scale patterns. The latter range will be discussed in the following. The data set of Auger includes vertical and inclined events with energies above 40 EeV as measured between January 2004 and April 2017. The data of TA was taken from the beginning of 2008 up to May 2017. Due to the different energy scales of Auger and TA, the energy threshold of TA was fixed to 53.2 EeV for the search above the flux suppression. The energy shift was determined by matching the flux of Auger in TA in the common declination band. The combined data show some interesting features along the supergalactic plane. The respective significance map for a search radius of 20° is depicted in Fig. 5.2. A flux enhancement seems to be apparent for a band along the supergalactic plane. A visual inspection suggests an asymmetric band, with a slightly stronger enhancement below the supergalactic equator than above it.

In the following, the flux as measured by Auger is derived for an off-centered band around the supergalactic plane.

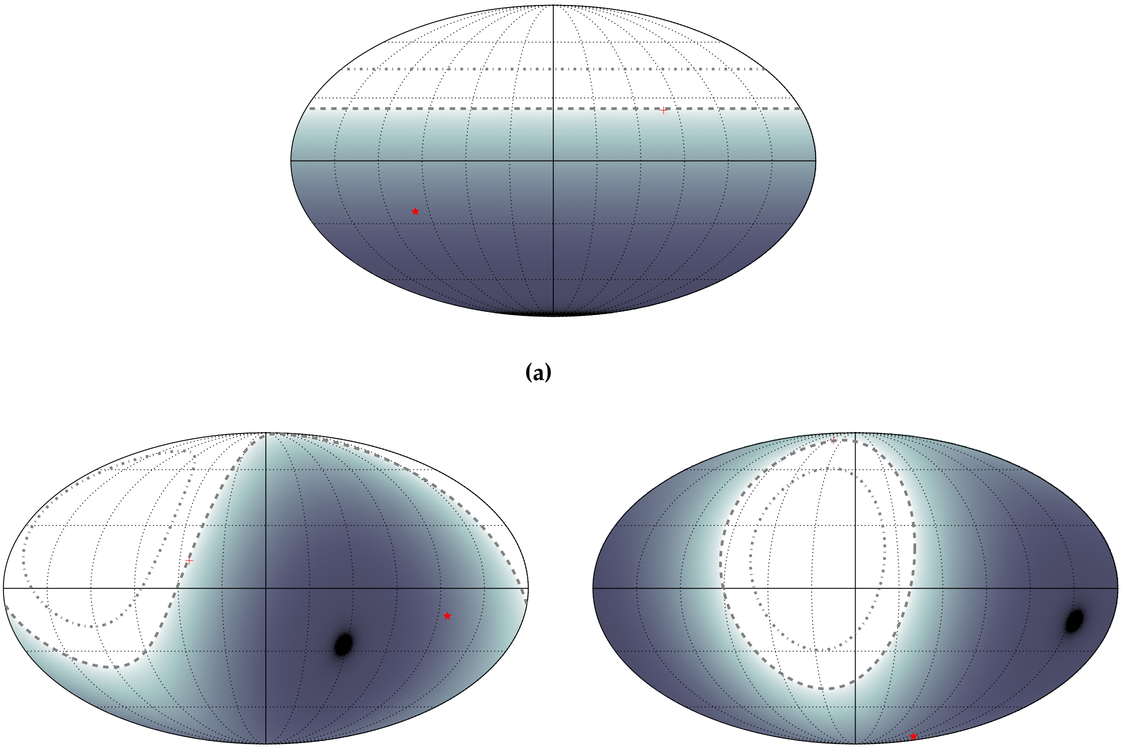
(a)

(b) (c)

Figure 5.3: Directional exposure for a zenith angle with a maximum value of 60° shown in (a) equatorial, (b) galactic and (c) supergalactic coordinates. Shown in addition is the dipole found for energies above 8 EeV with the star pointing towards the excess region. The maximum field of view is visualized by the dashed and dashed-dotted lines for events up to 60° and 80°, respectively.

5.3.1 Energy spectra in the supergalactic plane

The energy spectrum within a certain region of the sky is obtained by extending Eq. (5.1) with the contribution of the relative analytical exposure:

$$J(E) = \frac{\mathrm{d}N}{\mathrm{d}E\mathrm{d}\mathcal{E}_{\mathrm{geom}}\mathrm{d}\omega}. \tag{5.1}$$

The relative analytical exposure ω is calculated as the ratio of the analytical exposure for the particular part of the sky and the total analytical exposure using Eq. (4.12). The analysis of the energy spectrum is done with the event selection described in Section 5.1. Therefore, the data sets used in this work differ from the data sets presented in [120]. The energy spectrum is calculated in an asymmetric band with a range in supergalactic latitude of [−30°, 10°] around the supergalactic plane. The choice of the band width is based purely on visual inspection. The resulting spectra of the vertical and inclined data are shown in Fig. 5.4a and Fig. 5.4b. The spectra obtained from the events falling into the band are compared to the spectra derived from the events outside the band. To further investigate possible differences, the residuals of the spectra are built. Due to the decreased statistic when separating the data into bands, the residuals are built from the cumulative spectra. The resulting residuals are depicted in Fig. 5.4c and Fig. 5.4d for the SD-1500 and SD-1500h data. The anisotropy study of [120] uses events with energies above 40 EeV, which corresponds to a value of 19.6 in logarithmic energy. Due to the larger bin size at highest energies, only two bins in the energy spectra

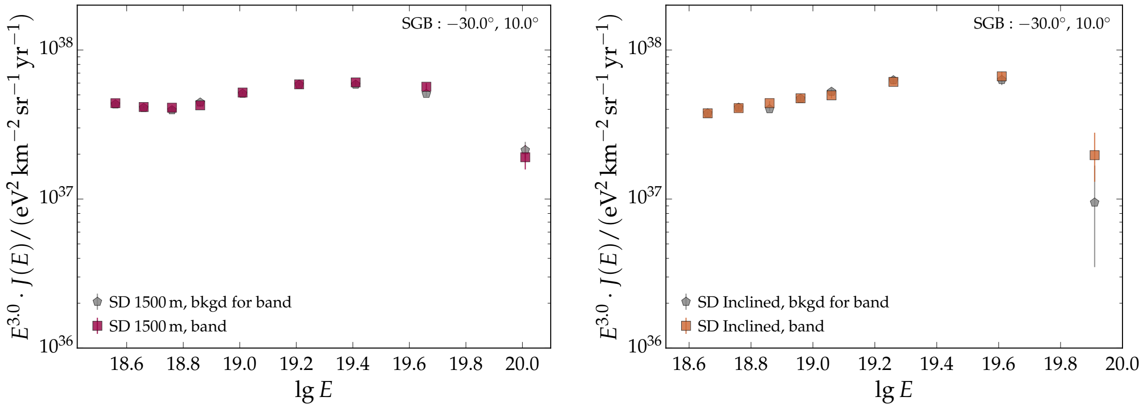

(a) SD-1500 **(b)** SD-1500h

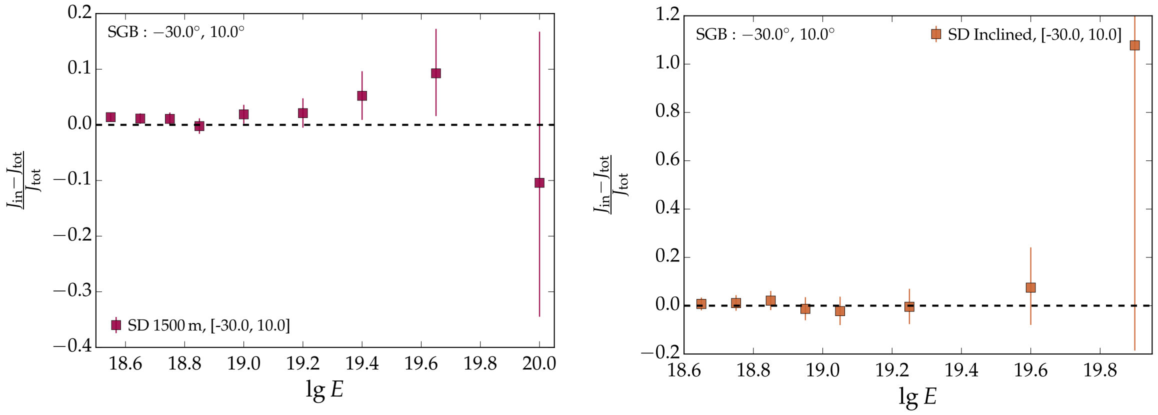

(c) SD-1500 **(d)** SD-1500h

Figure 5.4: The energy spectra of (a) SD-1500 and (b) SD-1500h are obtained for events falling into an asymmetric band around the supergalactic plane. The spectra as measured outside the band are shown for comparison. (c), (d) Residuals of the cumulative distributions. The spectra inside the band are compared to the spectra outside the band.

exceed this threshold. A flux enhancement is visible for the SD-1500 data but the difference in the flux is not significant. The SD-1500h data is compatible with no flux enhancement although there is a slight trend of an increasing flux difference at the highest energies. The reported pre-trial significances of the warm spots, which are on the order of 4 %, correspond to local significances. Due to the averaging over the whole band when determining the flux, the significance of the local overdensities are washed out in the spectrum.

While the local significance of overdensities on intermediate scales is washed out in the spectrum, the imprint of a large-scale anisotropy is expected to be larger. Motivated by the large-scale dipole depicted in Fig. 5.1, another search for an imprint of anisotropy on the spectrum is performed. The maximum imprint of the anisotropy is expected when rotating into the dipole coordinate system and analyzing the energy spectrum in bands which include the dipole extremes, as done in the following Section 5.4.

5.4 Rotation into dipole system

In order to search for an imprint of anisotropy in the spectrum, a rotation into the dipole system is performed, such that the excess region of the dipole corresponds to a declination

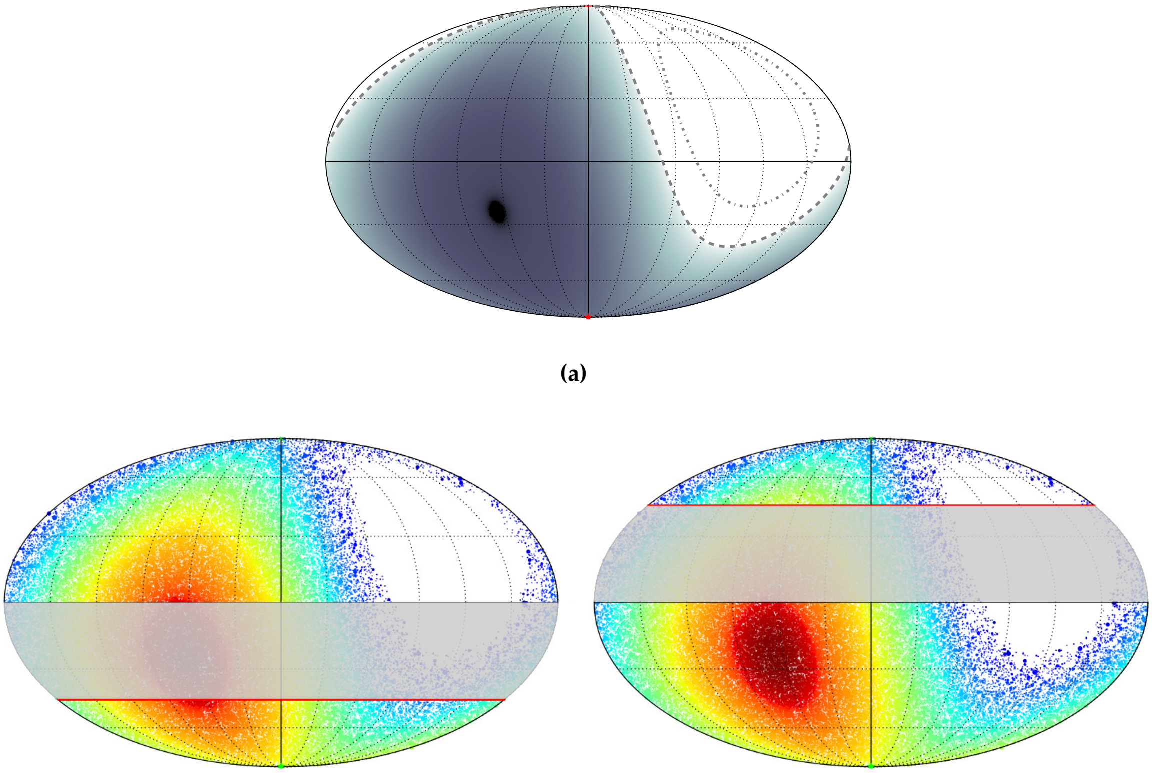

(a)

(b) **(c)**

Figure 5.5: The directional exposure in the rotated coordinate system of the dipole is depicted in (a). An example of the analyzed bands is given in (b) and (b). The sky maps show an example for the event distribution in the rotated system for events with energies above 4 EeV and zenith angles up to 80°. The color indicates the relative analytical exposure and the marker size is relative to the energy, increasing for high-energetic events. A band width of 45° in latitude starting from the respective poles is chosen for the analysis. Data lying in the gray region are neglected.

of $\delta = -90°$ and the deficit region is rotated to $\delta = 90°$. An illustration of this rotation can be seen in Fig. 5.5a where the dipole extremes lie at maximum latitudes. Being an astrophysical dipole, the intensity of the cosmic rays is always greater than zero for any region of the sky.

In the following, a band with a width of 45° in latitude starting from the poles is chosen in each hemisphere, respectively, and the flux inside the band is compared to the flux of the opposite hemisphere. Therefore, the flux in the latitude range −90° to −45° is compared to the flux obtained from the northern hemisphere with $0° < l < 90°$. This corresponds to a comparison of the band containing the excess region of the dipole to the opposite hemisphere. For the analysis of the deficit region, the latitudes are thus inverted.

An example of the event distributions is visualized in the sky maps of Fig. 5.5. For a better illustration, the sky maps show the combined data set of SD-1500 and SD-1500h with a maximum zenith angle of 80°. The color corresponds to the relative analytical exposure and the marker size indicates the energy of the events, increasing with energy. Events with arrival directions falling into the gray regions are excluded in the analysis.

5.4.1 Energy spectra of SD

The energy spectrum within a certain region of the sky is obtained with the help of Eq. (5.1). The resulting spectra for the vertical and inclined data sets are shown in Fig. 5.6. Taking the SD-1500 data as example, the spectra are determined as follows:

- *excess*: The spectrum uses events with arrival directions corresponding to a band in latitude of $[-90°, -45°]$.
- *excess, bkgd*: The spectrum is built from the events of the opposite hemisphere, hence $0° < l < 90°$.
- *deficit*: The spectrum uses events with arrival directions corresponding to a band in latitude $[45°, 90°]$.
- *deficit, bkgd*: The spectrum is built from the events of the opposite hemisphere, hence $-90° < l < 0°$.

For energies above 10^{19} eV, a slight difference between the spectra obtained in the bands and their respective reference spectrum is visible. The difference is further investigated by looking at the residuals. Due to the decreased statistics when separating the data into the different sky regions, the residuals are obtained from the cumulative spectra via:

$$R = \frac{J(E)_{\text{in}} - J(E)_{\text{tot}}}{\sqrt{\sigma^2_{\text{J,in}} + \sigma^2_{\text{J,tot}}}}, \tag{5.2}$$

with $J(E)_{\text{in}}$ denoting the flux in the excess/deficit band and $J(E)_{\text{tot}}$ referring to the flux from the respective opposite hemisphere. The corresponding uncertainties are given by the σ-terms. The maximum deviation is found for the SD-1500 data and is on the level of 4σ as shown in Fig. 5.7a. The difference vanishes at the highest energies where the statistic is poor despite the increased bin size. The SD-1500h spectra show a slightly lower difference, at the level of 3σ. However, both data sets exhibit an indication of an effect of the large-scale dipole on the spectrum. The imprint of the anisotropy on the spectrum is diluted if there are higher-order multipoles. As seen from Fig. 5.1a, the anisotropy is well-described by a dipolar modulation. However, a minor discrepancy from a pure dipole is visible at the maximum of the harmonic, which could be an indication for an underlying quadrupole deviation from isotropy.

The SD-750 spectra show a reversed trend at the lowest energies. The flux obtained from the band including the deficit is higher than the one calculated for the excess band, as depicted in Fig. 5.7c. Above an energy of about $10^{18.2}$ eV, the trend meets the one seen in the SD-1500 data and vanishes at the highest energies, where the statistic is low. The opposite trend at lower energies is an interesting observation. The origin of it remains unclear at this point. Further studies will be needed to clarify the trend.

The relative residuals of the cumulative spectra of three data sets with respect to the total flux instead of the statistical uncertainty are shown in Fig. C.14. The residuals show a flatter trend, which increases with energy. The flux differences vanish at the highest energies where the statistic is low.

5.4.2 Zenith dependence

To validate the observed dipole effect on the spectra obtained from the SD-1500 array, the data sets are further divided into two zenith bins. The reference zenith angle at which the data are split corresponds to the median angle of the respective data sets. The maximum zenith angles for the two data sets recorded with the SD-1500 array are 60° and 80°, resulting in a median angle of 38° and 68°, respectively. As can be seen from Fig. 5.8a and Fig. 5.8b, the trend stays the same. There is no indication that the seen effect of the dipole on the spectra is induced by zenith dependencies during the analysis.

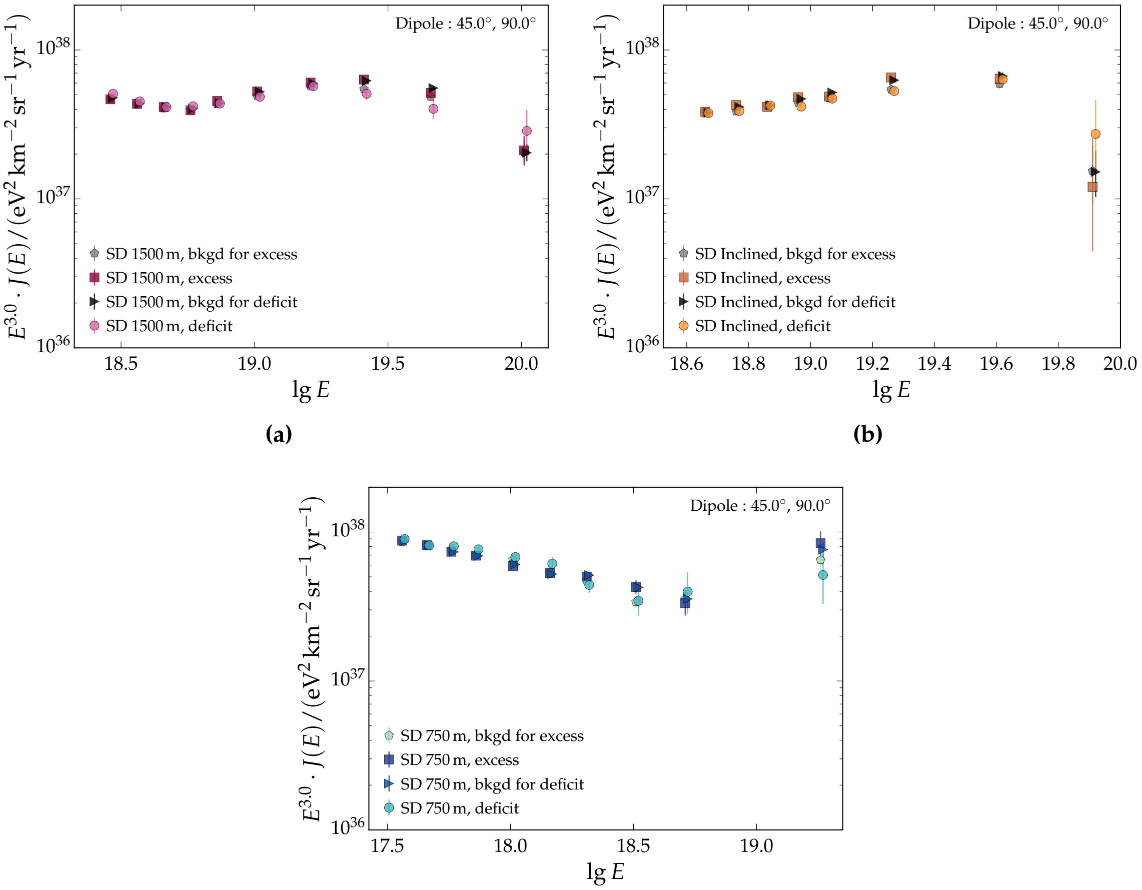

(a) **(b)**

(c)

Figure 5.6: The spectra obtained in the excess/deficit region are compared to the spectra of their respective opposite hemisphere (denoted as *bkgd*): (a) SD-1500 spectra, (b) SD-1500h spectra and (c) SD-750 spectra. The spectra are re-binned at highest energies due to the reduced statistic.

The SD-750 data is split at a reference angle of 35°. The reversed trend observed with the SD-750 remains visible when binning in zenith angle, although the effect becomes less significant. The zenith-binned distributions are depicted in Fig. 5.8c.

5.4.3 Time dependence

As a next check, the residuals of the cumulative spectra are built for different years. In Fig. 5.9, the residuals are depicted for two time intervals covering similar amounts of geometrical exposure. The dipole effect is visible for the SD-1500 data shown in Fig. 5.9a, whereas the structure of the deficit spectrum differs between the time intervals in case of the SD-1500h data. While a slight deficit is visible for the earlier years of 2004 to 2011, the trend seems to become more prominent in the later years of 2012 to 2016. This is visualized in Fig. 5.9b. The time-binned spectrum for the SD-750 data is shown in Fig. 5.9c. While the trend stays the same for energies up to 10^{18} eV, a discrepancy is visible at higher energies. The flux enhancement in the excess band is driven by the data recorded in the later years, while the decreased flux in the deficit region is dominated by the early years. This indicates a mismatch of the exposure calculation for the SD-750. A check on the detector performance is shown in Fig. C.15. It was found that the measured event rate in the early years is higher than what is

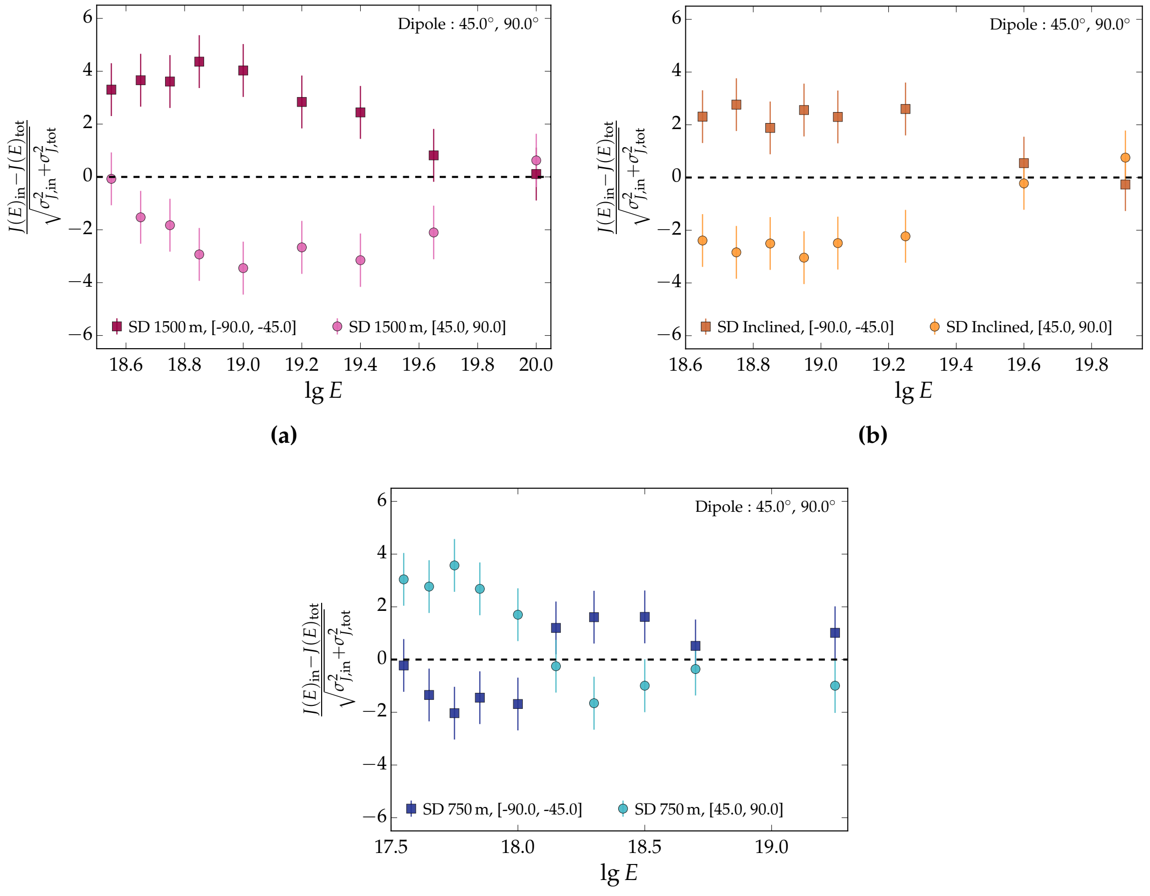

(a) **(b)**

(c)

Figure 5.7: Residuals of the cumulative distributions in units of statistical uncertainty for (a) SD-1500 data and (b) SD-1500h data. When compared to the total flux in the northern hemisphere, an excess is observed for events with arrival directions coinciding with the band on the southern hemisphere. Likewise, a deficit is visible for events from the northern dipole band. (c) The trend for the SD-750 is more complex. The trend is reversed for energies below 1 EeV, followed by a trend compatible with the two other data sets, before the difference vanishes at the highest energies.

expected from the exposure. The origin of the mismatch could not be identified and needs further investigation in the future.

5.4.4 Fit to the spectra

Fits to the spectra are shown in Fig. 5.10. The SD-1500 spectra are fitted using the model given in Eq. (4.77), whereas the SD-1500h spectra are fitted by a model without an ankle and smooth suppression. The ankle is too close to the threshold energy of full efficiency for the SD-1500h array to be studied. Hence, also the spectral index below the ankle cannot be accessed with the current SD-1500h data. The fit employs a Poisson maximum-likelihood fit. Individual comparisons of the fitted models to the spectra are depicted in Fig. C.16 and Fig. C.17. The parameters of the fits are summarized in Table 5.1 and Table 5.2 for the SD-1500 and SD-1500h spectra, respectively. A visual comparison of the fit parameters as function of the explored sky region is given in Fig. 5.11 and Fig. 5.12. The fit parameters are depicted with their respective statistical uncertainty from the fit. In addition, the solid line

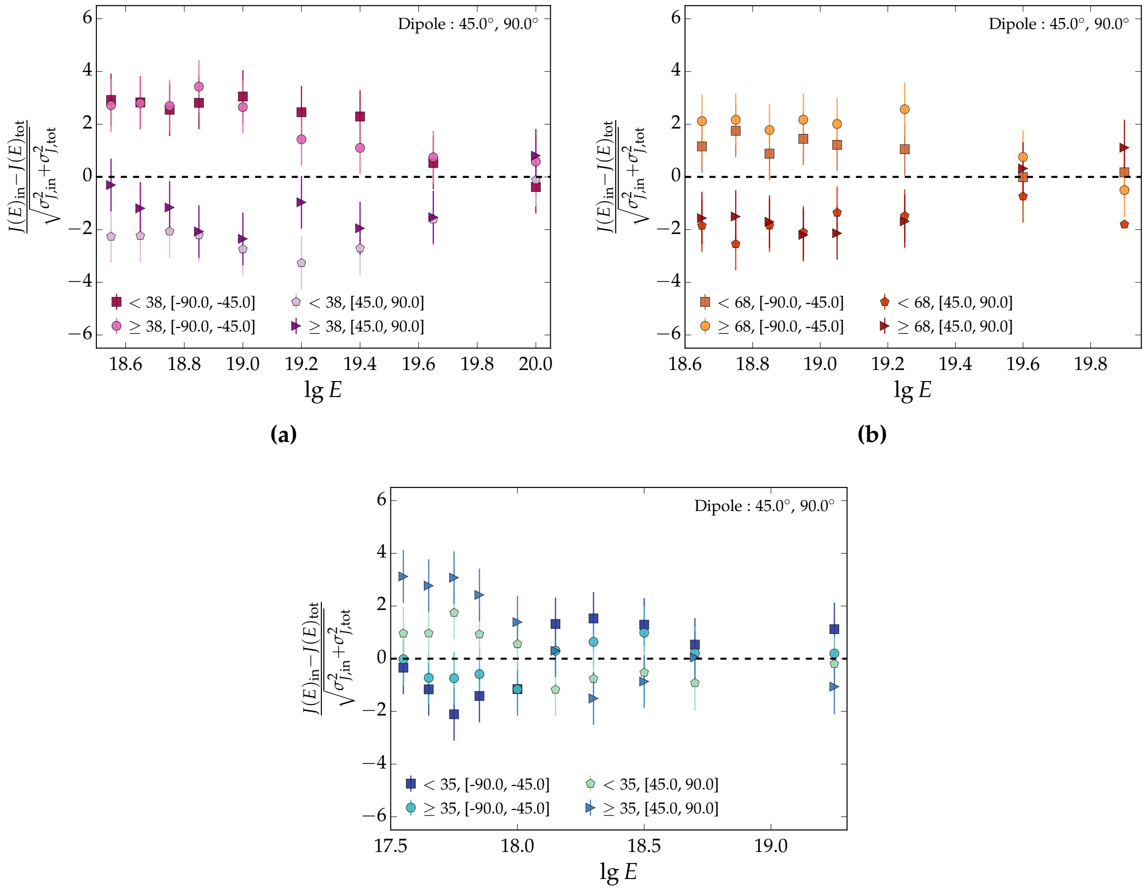

(a) **(b)**

(c)

Figure 5.8: Residuals of the cumulative event distributions binned in zenith angle. Both the (a) SD-1500 data and the (b) SD-1500h data show the same excess and deficit trend when separated in two zenith bins. The reversed trend for the SD-750 data is also visible when separating into zenith bins.

represents a linear fit to the parameters. The shaded band corresponds to the 1σ uncertainty. The two fit parameters, which show a trend for the SD-1500 spectra, are the logarithm of the flux normalization $\lg a$ and the spectral index before the ankle γ_1. Taking into account the exposure systematics of 0.03 on $\lg a$, the flux normalizations are compatible with each other. The trend in γ_1 is more distinct. However, the slope is mainly driven by the first data point, as can be seen in Fig. 5.10c. Here, residual representations are given in units of statistical uncertainty. The spectra of the bands are compared to the fit obtained for the total spectrum. Trigger effects at the threshold energy are a possible explanation of the upward trend of the first data point of the deficit spectra. A visual examination of the residual indicates a slightly higher flux coming from the excess band and a decreased flux from the deficit band when comparing the fluxes to the fit of the total spectrum. However, the differences are not statistically significant. Apart from the aforementioned deviations, no statistically significant trend is apparent in any of the other fit parameters. There is also no significant trend visible in the case of the SD-1500h spectra.

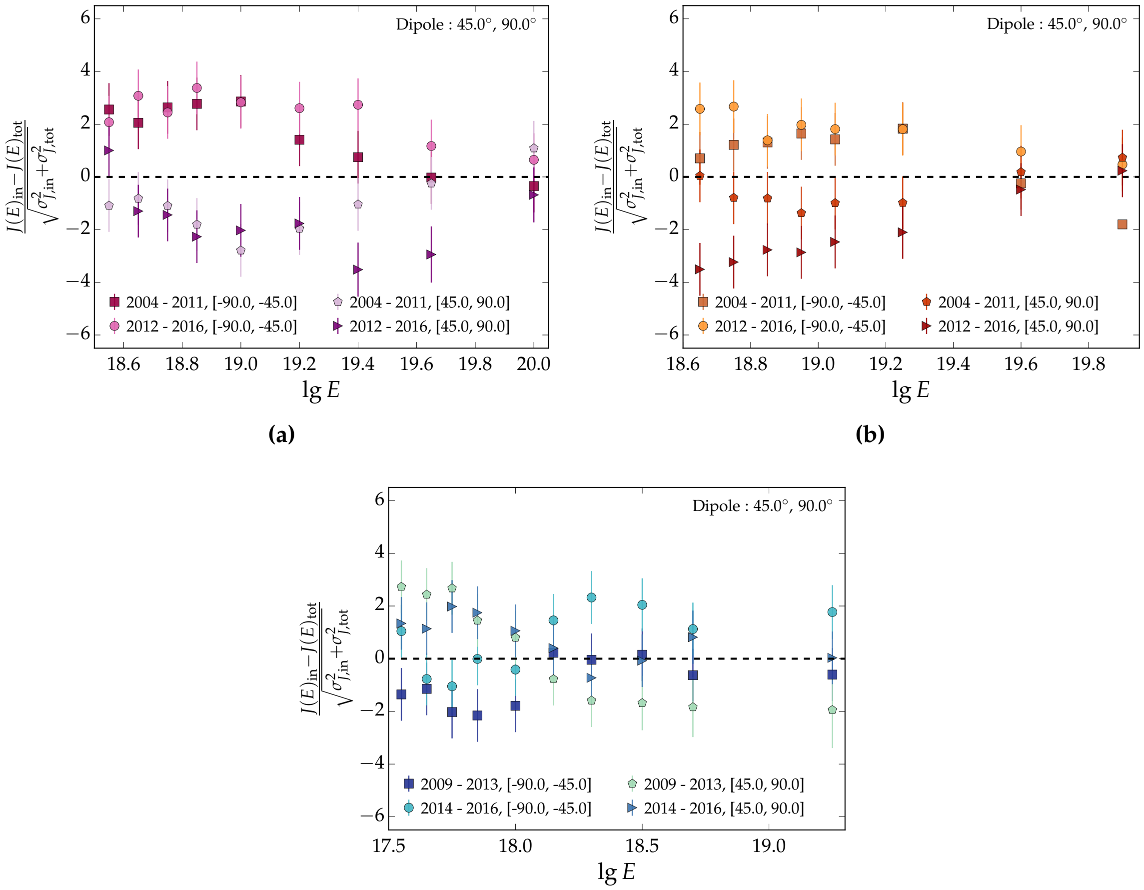

(a)

(b)

(c)

Figure 5.9: Residuals of the cumulative event distributions separated into two time intervals that cover a similar amount of geometrical exposure. An excess/deficit structure is visible for the (a) SD-1500 data, whereas the time-binned (b) SD-1500h data corresponding to the deficit region shows differences between the two time intervals. (c) The time-binned spectra of the SD-750 show a discrepancy of the trend at energies above 10^{18} eV. Details are given in the text.

5.4.5 Conclusion

The joint working group of Auger and TA performed a full-sky search for intermediate and small scale anisotropies, which revealed two warm spots along the supergalactic plane. The vertical and inclined data were investigated for possible imprints of the anisotropy on the spectrum. Analyzing the spectra in an off-centered band along the supergalactic plane resulted in a non-significant flux difference as the local overdensities of the warm spots are washed out in the spectrum calculation.

The large-scale anisotropy reported by Auger motivates the search of an imprint of the anisotropy on the spectrum. The three different SD spectra were analyzed for such an impact. The focus was put on the spectra obtained from the data recorded by the SD-1500 array, as the large-scale anisotropy was established for events above 8 EeV. A rotation into the dipole coordinate system was performed to analyze the SD data sets in different declination bands, where each band included the respective extremes of the dipole. By studying the cumulative spectra, a trend of an increased flux from the excess band and a decreased flux from the deficit band was found for both the SD-1500 and SD-1500h data. More interestingly, the trend seems to be reversed for the lower energies studied with the SD-750 data. The

Table 5.1: Parameters of the fit to the SD-1500 data. The total SD-1500 spectrum is compared to the spectra obtained in the bands which contain the dipole extremes.

Fit parameters	SD-1500	SD-1500, excess	SD-1500, deficit
$\lg(a/\mathrm{eV}^{-1}\mathrm{m}^{-2}\mathrm{sr}^{-1}\mathrm{s}^{-1})$	-17.8458 ± 0.0012	-17.849 ± 0.003	-17.823 ± 0.004
$\lg(E_\mathrm{ankle}/\mathrm{eV})$	18.716 ± 0.008	18.728 ± 0.015	18.684 ± 0.031
γ_1	-3.32 ± 0.02	-3.28 ± 0.03	-3.47 ± 0.07
γ_2	-2.55 ± 0.03	-2.46 ± 0.09	-2.58 ± 0.20
$\lg(E_\mathrm{s}/\mathrm{eV})$	19.61 ± 0.03	19.54 ± 0.07	19.54 ± 0.23
$\Delta\gamma$	2.41 ± 0.17	2.31 ± 0.31	1.77 ± 0.50

Table 5.2: Parameters of the fit to the SD-1500h data. The total SD-1500h spectrum is compared to the spectra obtained in the declination bands which contain the dipole extremes.

Fit parameters	SD-1500h	SD-1500h, excess	SD-1500h, deficit
$\lg(a/\mathrm{eV}^{-1}\mathrm{m}^{-2}\mathrm{sr}^{-1}\mathrm{s}^{-1})$	-19.313 ± 0.006	-19.292 ± 0.016	-19.346 ± 0.013
γ	-2.67 ± 0.02	-2.63 ± 0.06	-2.76 ± 0.05
$\lg(E_\mathrm{s}/\mathrm{eV})$	19.71 ± 0.03	19.65 ± 0.06	19.80 ± 0.07
$\Delta\gamma$	3.00 ± 0.41	3.00 ± 0.84	4.1 ± 2.0

difference in flux was also found when analyzing the spectra in two different zenith and time bins. The SD-1500 and SD-1500h spectra were fit to study the fit parameters as function of the declination bands. No clear significant indication is found, although some interesting structures for the spectral index before the ankle and the energies around the suppression are seen.

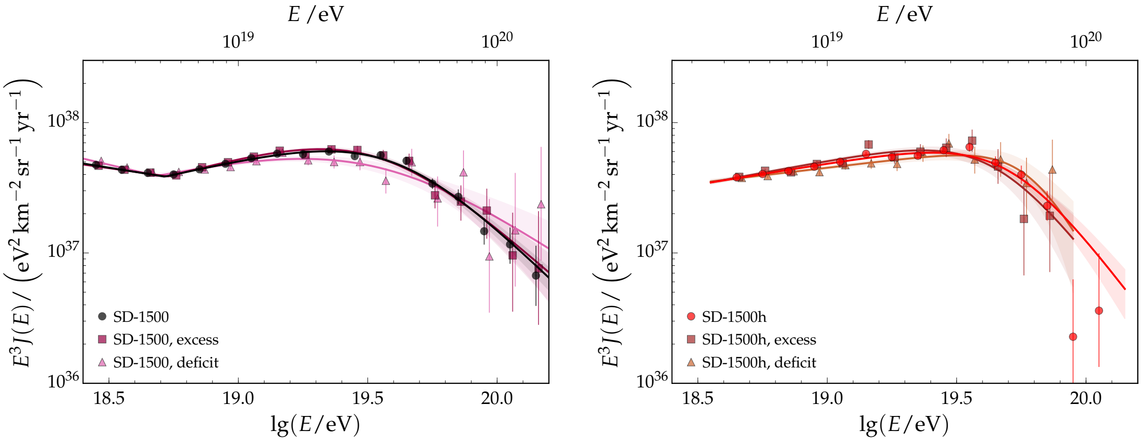

(a) SD-1500 **(b)** SD-1500h

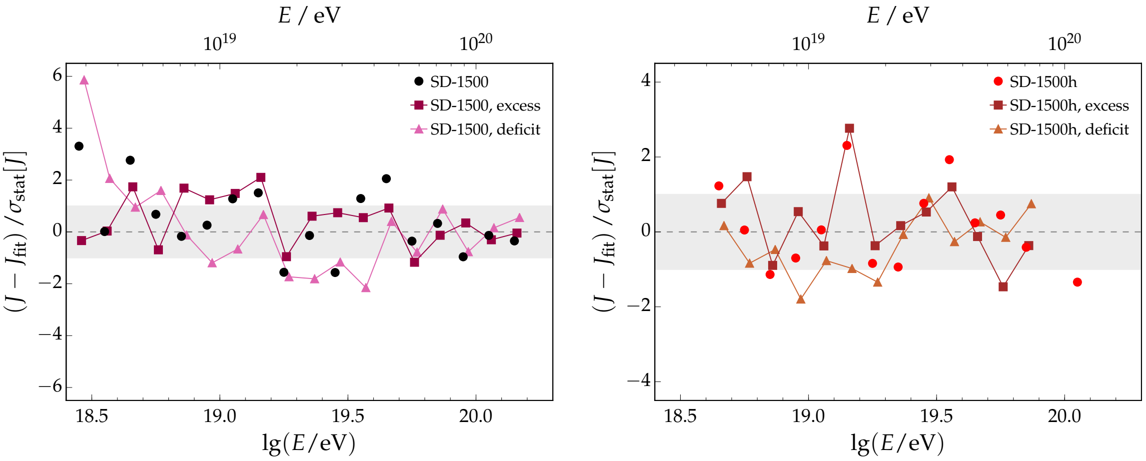

(c) SD-1500 **(d)** SD-1500h

Figure 5.10: Fit to the energy spectra obtained from the SD-1500 and SD-1500h data. (c), (d) Residual representation of the spectra in the dipole bands with respect to the fit obtained for the total field of view of Auger.

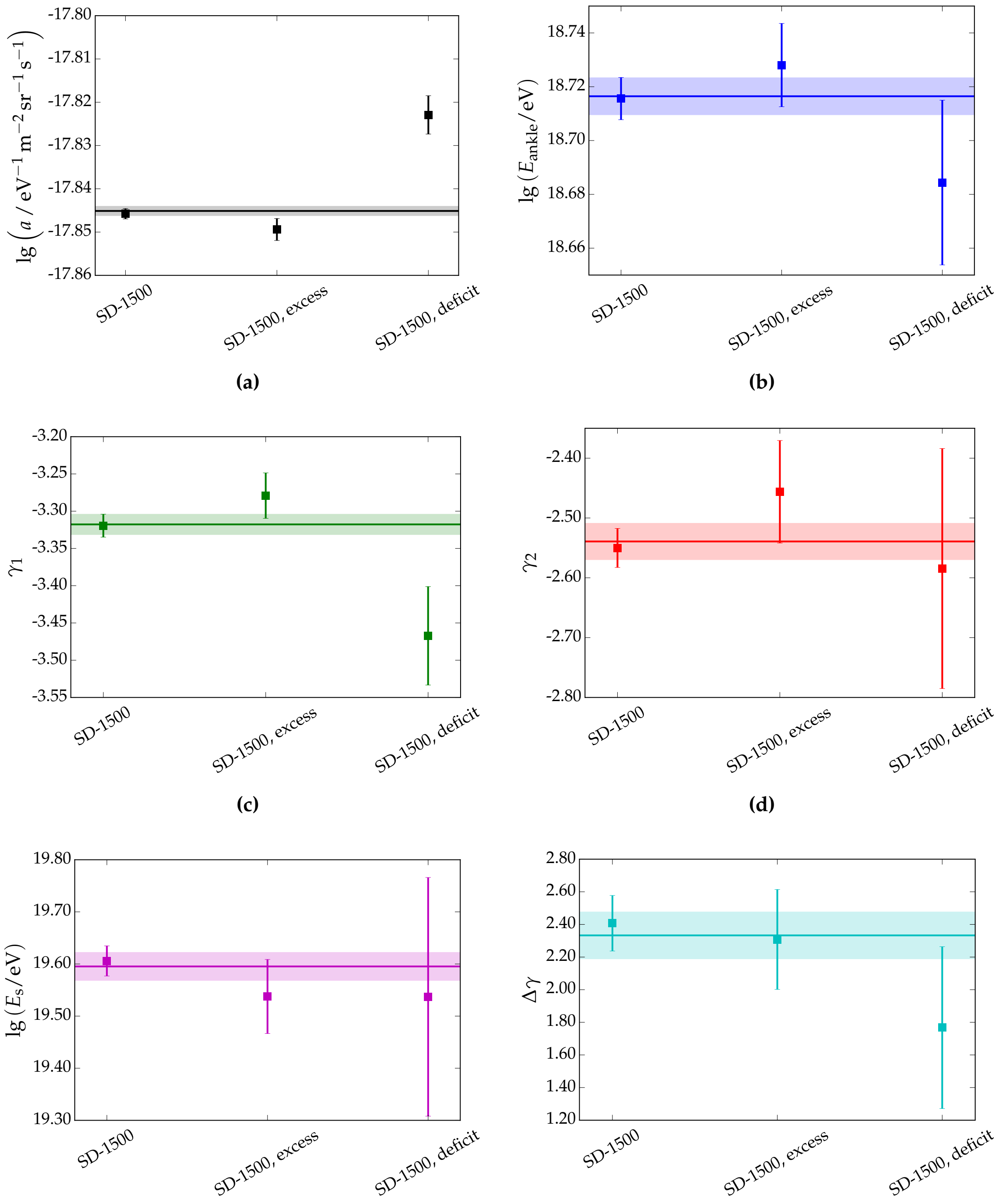

(a) (b)

(c) (d)

(e) (f)

Figure 5.11: Model parameters obtained for the fits to the different energy spectra of the SD-1500.

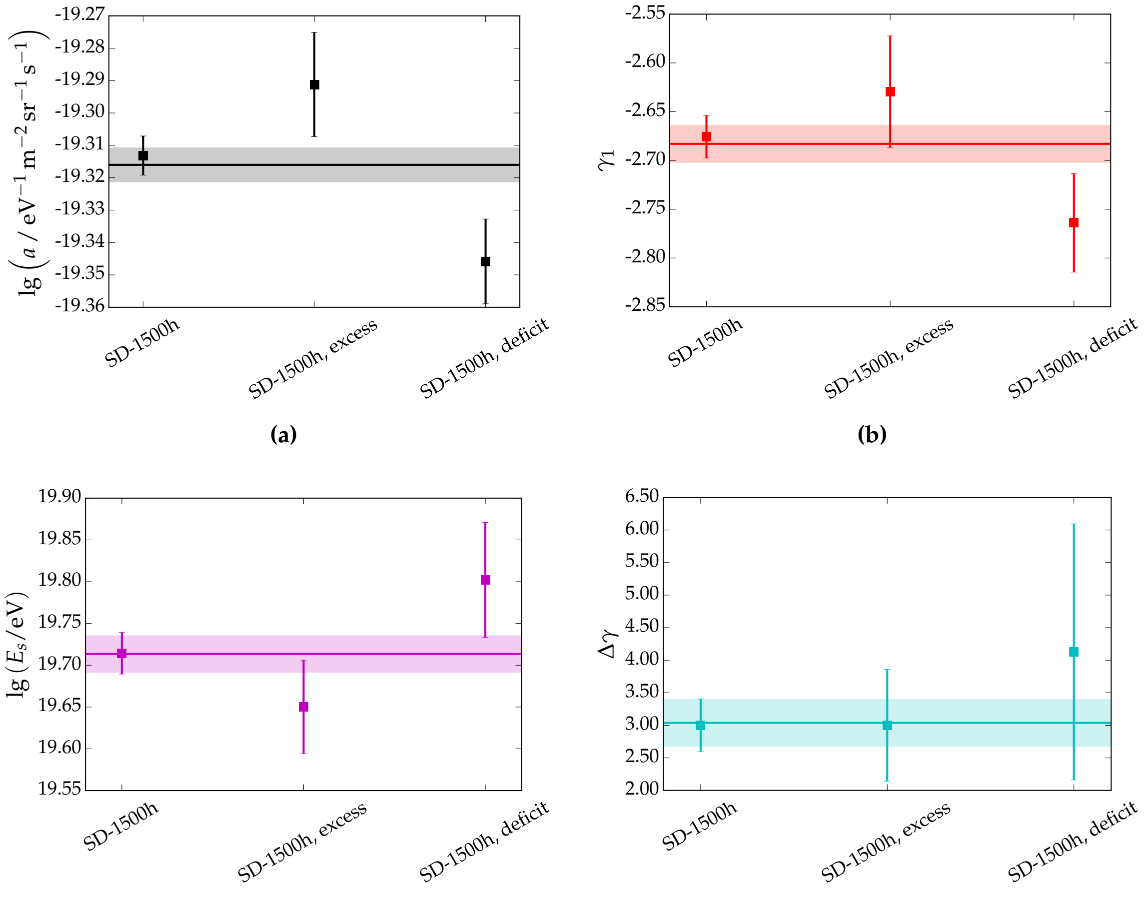

(a) **(b)**

(c) **(d)**

Figure 5.12: Model parameters obtained for the fits to the different energy spectra of the SD-1500h.

CHAPTER

6

Summary and conclusions

This thesis is focused on the energy spectrum as derived from data measured with the surface detector of the Pierre Auger Observatory. An accurate knowledge of the flux of ultra-high energy cosmic rays as function of energy is essential to help determine their origin. The major part of this work is dedicated to the measurements performed with the standard surface detector (SD-1500) and its low-energy extension, which consists of a nested detector array with half of the original detector spacing (SD-750). With a duty cycle of almost 100 % and a runtime of more than ten years, the energy spectrum is measured with unprecedented precision.

The surface detector samples the air shower at ground at certain distances. The reconstruction of the events is based on an empirically description of the lateral distribution of the signals observed in individual water-Cherenkov detectors. An expected signal at an optimal distance to the reconstructed shower axis is derived from a fit of the lateral distribution. The expected signal is a first estimator of the primary energy. While the estimator is directly linked to the primary energy, it depends on the inclination of the shower. With increasing zenith angle, the shower suffers more atmospheric attenuation. As a consequence, the expected signals of two showers with identical energies but different zenith angles will not be the same. The standard approach to correct for the zenith dependence is based on the Constant Intensity Cut method. The underlying assumption of this method is that the flux of ultra-high energy cosmic rays is to a large extent isotropic. The attenuation correction for a particular threshold energy is applied to all primary energies. A novel approach of an iterative attenuation correction was studied, which accounts for changes in the attenuation as a function of the primary energy. The shower development changes with energy, such that the ratio of the electromagnetic component to the muonic component is altered. Performing an iterative attenuation correction with different threshold energies for the SD-1500 data results in a reduction of the differential flux below the ankle of less than 2 % with respect to the flux obtained with the standard attenuation correction. Compared to the standard approach, the energy spectra agree within the systematic uncertainties, which is a confirmation for the robustness of the spectrum calculation. As the iterative attenuation correction affects mainly the events with high zenith angle and low energy, it will be of importance for future anisotropy studies with lower energy thresholds than the ones exploited at present. The novel approach shows promise to increase the maximum zenith angle range of the SD-750 data from 55° to 60°. The extended zenith angle range matches the range covered with SD-1500 data. A first energy spectrum up to 60° was derived and compared to the spectrum using the standard zenith-angle range. Both spectra agree above an energy of about $10^{17.6}$ eV. A slight discrepancy was found at the threshold of full efficiency due to trigger effects. The trigger efficiency will benefit from the future inclusion of the new station triggers in the standard event reconstruction.

The trigger efficiency for the SD-1500 array was studied for the two primaries proton and iron making use of an extensive simulation library. The energy resolution of the SD-1500 was studied with both data and dedicated simulations. The resolution deduced from simulations was updated to the latest hadronic interaction model of QGSJet-II.04 for both SD-750 and SD-1500. The measured energy spectrum is distorted due to the finite energy resolution. A correction for event migration effects was performed using the updated resolution models. The energy reconstruction of the fluorescence detector was investigated with simulated air showers. A discrepancy of the reconstructed calorimetric energy with respect to the simulated energy of −10 % at an energy of 3×10^{17} eV was found for showers recorded with the SD-750 array. These findings initiated a refined reconstruction of the longitudinal profile measured by the fluorescence detector, which reduced the bias to −5 %.

The energy spectrum derived from the SD-1500 data was compared to the flux measurements of the Telescope Array experiment. Both experiments employ a hybrid detector and are situated at about the same latitude on opposite hemispheres. The observed discrepancy in the overall energy scale could either originate from the difference in the observed sky or from differences in the experimental set-up and the applied analyses. Changing the energy scale of each experiment by 5.2 % brings the spectra in agreement for energies below $10^{19.5}$ eV. This shift in the energy scale is well within the reported systematic uncertainties on the respective energy scales (14 % for Auger and 21 % for TA). Despite the shift, a significant difference for the fluxes at energies above $10^{19.5}$ eV remains. Both Auger and TA accumulated sufficient exposures to study the flux at the highest energies in different declination bands. A common declination band from −15.7° to 24.8° was chosen to help discriminate between astrophysical and instrumental effects. In this band, both experiments observe the same part of the sky and their measured spectra are supposed to agree within uncertainties. A novel approach to calculate the energy spectrum was studied, which accounts for the different exposure dependence of Auger and TA on the declination. By construction, the derived energy spectrum is insensitive to anisotropies in the observed sky. A comparison of the spectra obtained with this new approach revealed a remaining energy-dependent difference. Based on this result, the conclusion is drawn that the flux differences in the common declination band can be attributed to instrumental effects. As a consequence, instrumental effects account for at least a fraction of the flux differences seen in the full-sky spectra. A careful study of the (energy-dependent) systematic uncertainties of both experiments is necessary in future to bring the observed spectra in agreement. A reliable comparison of the full-sky spectra will be only possible after the determination of the systematic effects.

Motivated by the large-scale anisotropy reported by Auger, a possible impact on the energy spectrum was investigated. A rotation into the coordinate system of the observed dipolar anisotropy was performed and the spectra were derived for different declination bands. The spectra including the extremes of the dipole exhibit an interesting trend with respect to the background spectrum. An increased flux is observed for the excess band, while the flux from the deficit band is lower. The trend meets the expectation of a dipolar anisotropy imprinting on the energy spectrum.

The methods developed in this thesis and the presented results build the basis for future systematic studies and a more precise determination of the energy spectrum.

List of Tables

APPENDIX

A

Monte Carlo air shower libraries

This appendix provides an overview of the simulation libraries used within this work. Additional material is given for the analyses described in Chapter 3.

The simulation libraries are created with the Corsika code to simulate air showers. All showers use an optimal thinning of level of $t = 10^{-6}$ to speed up the simulations and save some disk space without losing accuracy [121, 122]. In a thinned shower, only a subset of weighted particles are propagated to the ground. For the detector simulation, the thinning has to be reverted to obtain the particles which enter the WCDs and preserve as much of the unthinned shower information as possible. This process is called resampling [123–125]. Within the $\overline{\text{Off}}\underline{\text{line}}$ framework, the shower resampling is performed in the Cached Shower Regenerator module. The simulation libraries used in the work are both fixed in energy and zenith angle and continuous in the two observables.

A.1 Fixed library

I created this library for the analysis presented in [126]. The library consists of the two primaries proton and iron being simulated with Epos-LHC. For each primary, showers with the primary energies 10^{18} eV, $10^{18.5}$ eV, 10^{19} eV, and $10^{19.5}$ eV and the zenith angles 0°, 12°, 22°, 32°, 38°, 48°, and 56° are available. The seasonal effects on the shower development are mimicked by using monthly atmospheric models within Corsika. Each of these configurations was simulated 10 times, so that 120 unique showers are available within each energy and zenith bin. The detector simulation was only performed for SD-1500 with an ideal array as depicted in Fig. A.1a. 50 randomly distributed core positions were created and used as true core positions. In addition to the stations of the ideal array, station rings at fixed positions with respect to the shower axis were simulated. These dense stations provide the simulated detector response at exact the same positions regardless of the shower geometry and the impact point on the array. The dense stations are placed at 200 m, 400 m, 600 m, 800 m, 1000 m, 1222 m, 1494 m, 1826 m, 2232 m, and 2728 m from the shower core (Fig. A.1b). The three innermost rings contain four stations with a step size of 90° around the core, whereas the remaining rings are arranged in 45° steps. For each shower, the FD detector simulation is performed in addition.

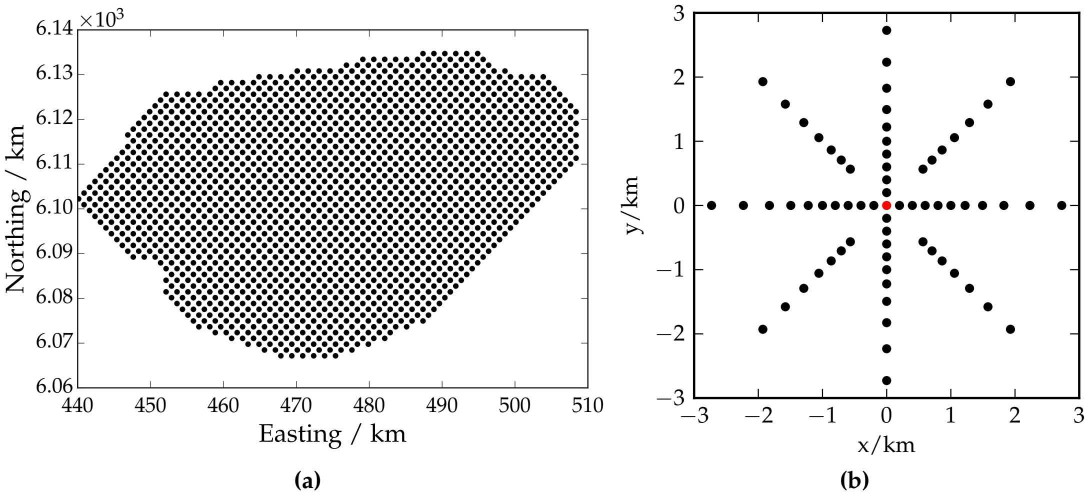

Figure A.1: (a) Schematic of an ideal SD-1500 array used for the detector simulation. Easting and northing of the stations are given on the x- and y-axis, respectively. (b) Visualization of the rings of dense stations used in the simulation. Their positions are given in the shower coordinate system.

A.2 Continuous library

A continuous library in the energy range of 10^{18} eV to 10^{20} eV with a spectral slope of E^{-1} is used [127]. The zenith angles are distributed isotropically according to $\frac{dN}{d\theta} \propto \sin\theta\cos\theta$ as seen in data using a range of 0° to 65°. The four primaries proton, helium, oxygen, and iron are available. Within the scope of this work, only proton and iron simulations are used. The CORSIKA simulations have been used to produce SD-1500 detector simulations and reconstructions. For each shower, the FD detector simulation is performed in addition.

A.3 Continuous library produced at KIT - 1

A continuous library in the energy range of $10^{16.5}$ eV to $10^{19.5}$ eV with a zenith angle distribution of $\frac{dN}{d\theta} \propto \sin\theta\cos\theta$ was produced for extensive studies of the SD-750 array. 2500 unique CORSIKA showers per decade in energy were available for both proton and iron primaries. The library was simulated with the hadronic interaction model QGSJET-II.04. Each unique shower was simulated 10 times, resulting in 75 000 showers per primary. The showers were distributed randomly onto the SD-750 array. An ideal SD-750 array as shown in Fig. A.2 is used for the detector simulation. For each shower, the full SD and FD detector simulation and reconstruction chain was performed.

A.4 Continuous library produced at KIT - 2

A continuous library in the energy range of 10^{16} eV to 10^{20} eV with a zenith angle distribution of $\frac{dN}{d\theta} \propto \sin\theta\cos\theta$ as seen in data was produced at KIT. The CORSIKA files were simulated with the new hadronic interaction model QGSJET-II.04. For the studies presented in this work, only proton and iron primaries were processed. 2000 unique showers for the energy range of 10^{16} eV to 10^{17} eV and 1000 unique CORSIKA showers for the higher energies are available. Each unique shower was simulated 10 times. The showers were distributed randomly onto

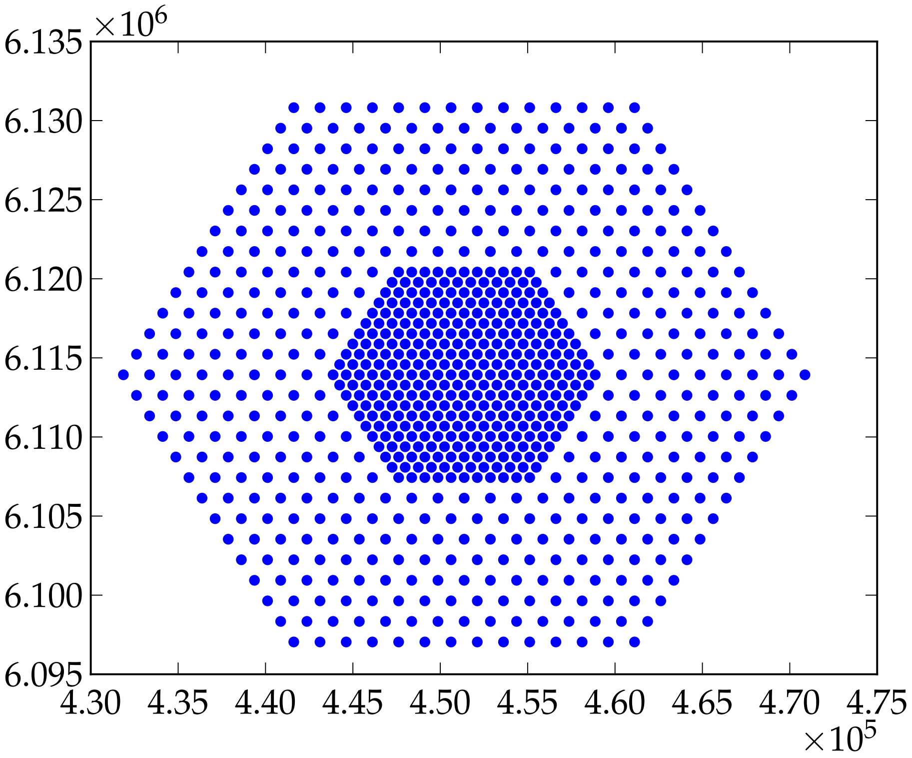

Figure A.2: Schematic of an ideal SD-750 array used for the detector simulation, represented by the inner nested stations. The stations around the nested part belong to an ideal SD-1500 array. Station positions are given in the detector coordinate system.

the SD-750 array. For each shower, the full SD and FD detector simulation and reconstruction chain was performed.

A.5 Migration matrices and energy calibration

SD-1500

Migration matrices as obtained with the library described in Appendix A.2 for QGSJet-II.04 are presented in the following. The migration matrix for the 50/50 mix of proton and iron primaries is shown in Section 3.2. The matrices derived for the pure primaries are depicted in Fig. A.3. The results for the resolution models from the direct energy calibration as performed in Section 3.2 are:

$$\frac{\sigma(E)}{E} = 0.109 + 0.433\sqrt{\frac{E_0}{E}}, \quad \text{proton} \tag{A.1}$$

$$\frac{\sigma(E)}{E} = 0.050 + 0.484\sqrt{\frac{E_0}{E}}, \quad \text{iron.} \tag{A.2}$$

The energy calibration as described in Section 4.5 was performed with the simulation sets used in Section 3.2. This serves as a crosscheck for the direct energy calibration. In Fig. A.5b,

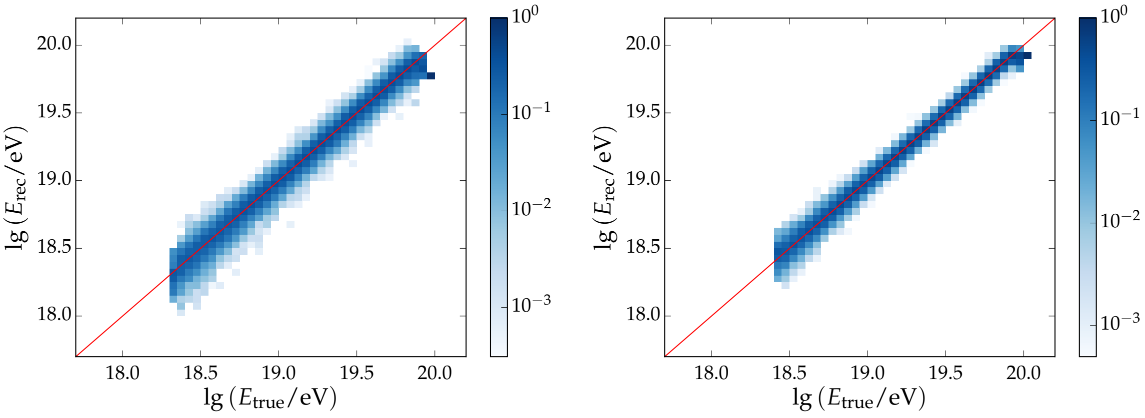

(a) proton **(b)** iron

Figure A.3: Migration matrix for SD-1500 simulations as obtained for (a) proton and (b) iron primaries.

the obtained calibrations for proton, iron, and a mixed composition are compared to the one derived from data. The resulting parameters are:

$$E(S_{38}) = (0.207 \pm 0.001) \times 10^{18}\,\mathrm{eV} \left(\frac{S_{38}}{\mathrm{VEM}}\right)^{(1.061\pm0.001)}, \quad \text{proton} \tag{A.3}$$

$$E(S_{38}) = (0.180 \pm 0.001) \times 10^{18}\,\mathrm{eV} \left(\frac{S_{38}}{\mathrm{VEM}}\right)^{(1.070\pm0.001)}, \quad \text{iron} \tag{A.4}$$

$$E(S_{38}) = (0.194 \pm 0.001) \times 10^{18}\,\mathrm{eV} \left(\frac{S_{38}}{\mathrm{VEM}}\right)^{(1.062\pm0.001)}, \quad \text{mix.} \tag{A.5}$$

SD-750

The analysis results presented in the following make use of the simulation library described in Appendix A.3. The migration matrices for proton and iron are shown in Fig. A.4. The energy resolution derived from the ansatz of a direct energy calibration as described in Section 3.2 are depicted in Fig. A.5a. The individual parameters of the resolutions for the pure composition as well as a 50/50 composition are:

$$\frac{\sigma(E)}{E} = 0.108 + 0.160\sqrt{\frac{E_0}{E}}, \quad \text{proton} \tag{A.6}$$

$$\frac{\sigma(E)}{E} = 0.484 + 0.170\sqrt{\frac{E_0}{E}}, \quad \text{iron} \tag{A.7}$$

$$\frac{\sigma(E)}{E} = 0.078 + 0.165\sqrt{\frac{E_0}{E}}, \quad \text{mix.} \tag{A.8}$$

The resolution of the SD-750 array is better for iron primaries than for proton induced showers. This is a consequence of the higher muon content of iron showers with respect to proton showers and the fact that the WCDs are more sensitive to the muonic shower component. The resolution model obtained for a mixed composition was also used to derive the flux presented in [97, 100].

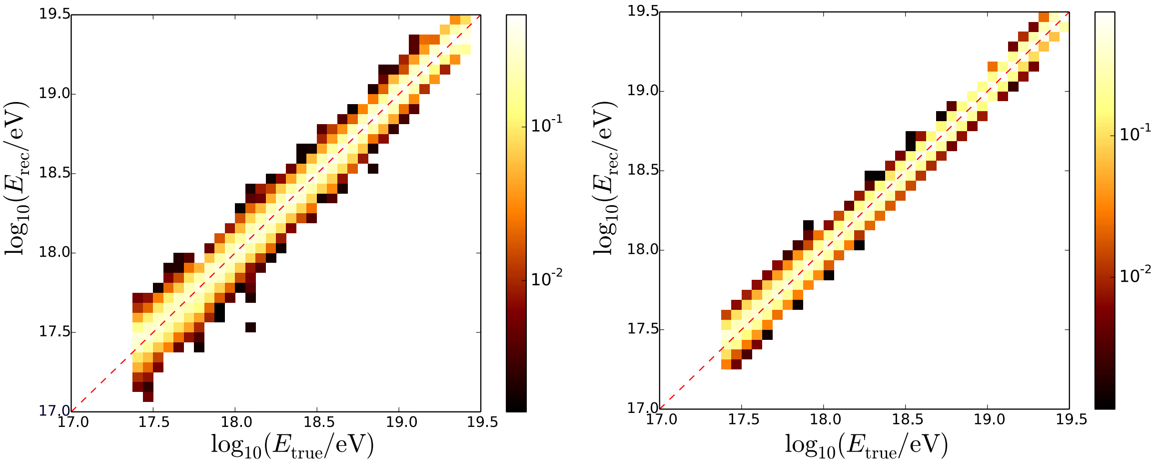

(a) proton **(b)** iron

Figure A.4: Migration matrix for SD-750 simulations as obtained for (a) proton and (b) iron primaries.

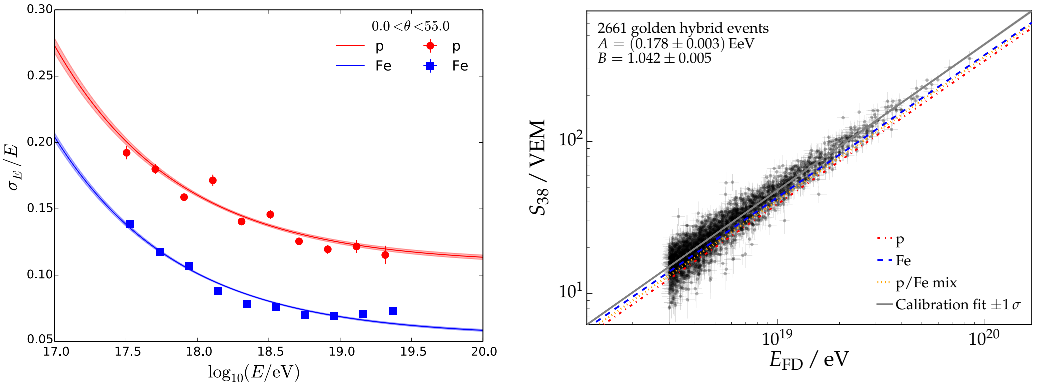

(a) SD-750 **(b)** SD-1500

Figure A.5: (a) Energy resolution as determined for the SD-750 array for proton and iron showers. (b) The energy calibration for data is compared to the calibration deduced for SD-1500 simulations using proton, iron and a mixed composition. The fit procedure for the energy calibration is the one described in Section 4.5.

A.6 FD energy and bias

The invisible energy correction for the showers produced with the library described in Appendix A.2 is based on the invisible energy derived for data. This means that the pure primaries of proton and iron are corrected with a parameterization obtained for a mixed composition. As a result, the total FD energy for proton showers is estimated too high, whereas the invisible energy assigned to iron showers is too low. This can be seen in Fig. A.6. Here, the reconstructed FD energy in simulations, which is a sum of the reconstructed calorimetric energy and the invisible energy, is compared to the true Monte Carlo energy. Due to the this offset, it was decided to use a true invisible energy correction for the analysis presented in Section 3.2.

A slight bias is found when comparing the reconstructed calorimetric energy with the true calorimetric energy. The bias shows a minor dependence on the zenith angle, as shown in Fig. A.7. The parameterization stated in Eq. (3.2) is used to correct for the bias. The bias correction is not taking into account energies below $10^{18.4}$ eV, which show an overestimation of

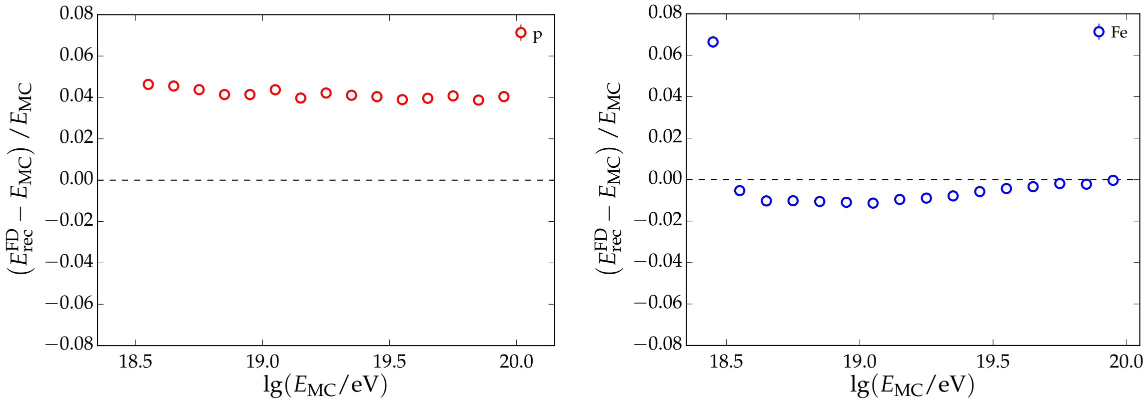

(a) **(b)**

Figure A.6: Bias in the reconstructed FD energy. The reconstructed calorimetric energy is corrected with the invisible energy as obtained in data. Due to the mixed composition in data, the correction for proton showers is too high while the correction for iron showers is too low.

the reconstructed calorimetric energy. The source of this upward fluctuation is not identified at this time.

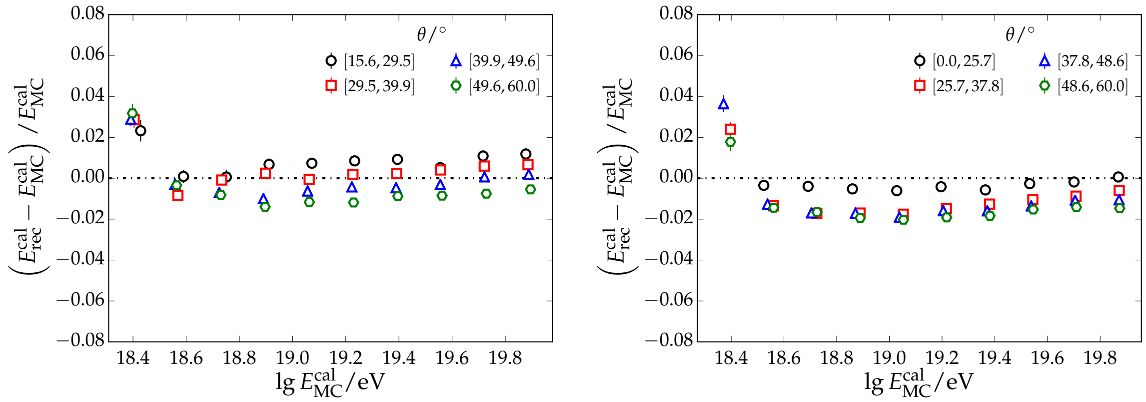

(a) proton

(b) iron

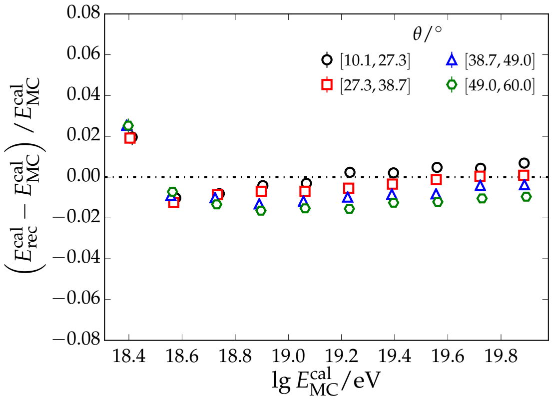

(c) mix

Figure A.7: Bias in the reconstructed calorimetric FD energy compared to the Monte Carlo one. The simulations are split in different zenith bins.

APPENDIX

B

Data sets

B.1 Data selections

This section includes the configuration files used to select ADST data. The set-up of the configuration files as used for the SD data selection are given in Table B.1 and Table B.2, the configuration file for the FD selection is given in Table B.3.

In the following, the FD cuts used for the selection of golden hybrid events in Section 4.5.1 are described in more detail. They are listed by their name as implemented in $\overline{\text{Off}}\underline{\text{line}}$ together with their associated cut value (if existent).

Reject laser events

- *!isCLF*
  The event does not correspond to a laser shot from the CLF.

- *!isXLF*
  The event does not correspond to a laser shot from the XLF.

Hardware status

- *heatOrientationUp*
  Selects events where HEAT is in upward mode. The cut has no effect on other eyes.

- *eyeCut* (100000) / (001111)
  In the first case, only events reconstructed with the merged eye HeCo are selected. This is only used for the analysis of SD-750 data. The second case selects only the four standard eyes and is applied in the selection of SD-1500 data.

- *badFDPeriodRejection*
  Rejects events that fall into a period of issues during the FD operation.

- *minMeanPixelRMSMergedEyes* (17, 6, 110000)
  Events recorded during the closing of the shutters in front of the FD are discarded

by cutting on the variance in the background light. This is smaller in case of closed shutters, hence a minimum variance is required. This cut can be only used for merged eyes which has to be stated as the second and third argument of the cut.

- *minMeanPixelRMSSimpleEyes* (17, 011111)
  Same cut as *minMeanPixelRMSMergedEyes* but for single eyes. To decide which eyes should be cut, they have to be stated as second argument.

- *!badPixels* (1)
  Rejects events which were recorded with a PMT camera that had bad calibration parameters for the pixels.

- *good10MHzCorrection*
  Events that have an imprecise GPS timing are discarded.

Atmosphere

- *hasMieDatabase*
  The atmospheric conditions have to be taken into account in order to ensure a proper energy reconstruction by the FD. The atmosphere is constantly monitored by laser shots to infer its condition. The information are stored in dedicated databases. If the database has no entries for the time of the event, it will be cut from the data set.

- *maxVAOD* (0.1)
  The aerosol content in the atmosphere is given in terms of VAOD[1]. A high amount of aerosol increases the scattering of the fluorescence light on its way to the telescope and leads to a larger uncertainty in the energy determination. Hence, only showers that traversed an atmosphere with low aerosol contamination are considered in the analysis.

- *cloudCutXmaxPRD14*
  Monitoring the atmosphere includes the measurement of the cloud coverage. Events are rejected if there are clouds detected in the direction of the shower by either the cloud camera or the GOES[2] measurements. If the height of the cloud layer as measured by the LIDARs and CLF is compatible with the field of view, the events get discarded as well.

Hybrid geometry

- *hybridTankTrigger* (2)
  Hybrid events require a triggered SD station to optimize the reconstruction. Here, the station has to fulfill a ToT trigger. This trigger type ensures that the station was not triggered by a coincidental atmospheric muon. These muons deposit a high and short signal in the station and result in a threshold trigger.

- *maxCoreTankDist* (750) / (1500)
  Maximum distance from the reconstructed hybrid core to the triggered station.

- *maxZenithFD* (90)
  Cut on the maximum reconstructed zenith angle to discard upward going events.

---

[1] vertical aerosol optical depth

[2] Geostationary Operational Environmental Satellites

- *minLgEnergyFD* (10^{-20} eV)
  In case of a failed profile reconstruction, the energy can be zero. This cut ensures to select only showers with valid reconstruction.

- *skipSaturated* Above a certain threshold of light intensity falling onto the camera, the PMTs reach saturation. As saturated pixel disable the reconstruction of the time-dependent light intensity from the shower profile, events with such pixels in the camera track are discarded.

- *minPBrass* (0.9)
  For a given FD event, the probability to have at least one SD station triggered falls below 100 % for low energetic showers. The probability for single showers to trigger at least one SD station depending on the shower geometry can be determined from proton and iron simulations. Hence, a fiducial area is obtained where the probability has to be greater than 90 % for both primaries.

- *maxPBrassProtonIronDiff* (0.05)
  The difference in the trigger probability between the two primaries has to be less than 5 % to avoid a mass-dependent selection.

Quality cuts

- *xMaxObsInExpectedFOV* (40, 20)
  The FoV of the FD telescopes is limited, so that for some showers only the tails of the longitudinal shower profile are contained in the FoV. This cut rejects showers for which the reconstructed shower maximum is not visible.

- *maxDepthHole* (20)
  Cut on events with one or more holes larger than $20\,\mathrm{g\,cm^{-2}}$ in the longitudinal profile.

- *profileChi2Sigma* (3, -1.1)
  A comparison between the χ^2 probability of the Gaisser-Hillas fit and the probability of a linear fit to the shower profile is performed. Showers with profiles that do not show a distinctive Gaisser-Hillas shape and therefore have a bad fit quality are discarded.

- *depthTrackLength* (200)
  Only showers with a minimum track length are selected to ensure a high quality Gaisser-Hillas fit.

- *xMaxError* (40)
  Events with a reconstruction uncertainty $\sigma(X_{\mathrm{max}})$ greater than $40\,\mathrm{g\,cm^{-2}}$ are discarded to ensure well-reconstructed showers.

- *energyTotError* (0.12)
  The relative uncertainty on the reconstructed total energy has to be smaller than 12 % to be selected as well-reconstructed.

- *FidFOVICRC13* (40, 20)
  Due to the limited FoV, some shower geometries depending on the incoming direction and distance to the telescope are more likely to be detected than others even though they were initiated by primaries with the same energy. An illustration is given in Fig. 4.18. On the other hand, two showers with the same geometry and energy but different incident masses differ in the position of the shower maximum. For the same energy and vertical geometry, lighter masses penetrate deeper into the atmosphere and

have a higher probability to be detected by the telescopes and survive the selection described above than primaries with higher mass. To avoid a mass-dependent selection, a fiducial FoV is introduced. Within this FoV, deep and shallow showers have an equal probability to survive the reconstruction and selection.

Table B.1: SD quality cuts for the SD-750 data.

Cut name	Cut value	Meaning
!lightning		reject events due to lightning
minRecLevel	3	select events with reconstructed LDF
maxZenithSD	55	cut on reconstructed zenith angle
T4Trigger	2	at least a 3ToT trigger configuration
T5Trigger	2	select 6T5 prior events
badPeriodsRejectionFromFile		reject events falling into bad periods
timeInterval	params: 080731 170101	cut on time range

Table B.2: SD quality cuts for the SD-1500 data.

Cut name	Cut value	Meaning
!lightning		reject events due to lightning
minRecLevel	3	select events with reconstructed LDF
maxZenithSD	60	cut on reconstructed zenith angle
T4Trigger	2	at least a 3ToT trigger configuration
T5Trigger	2	select 6T5 prior events
badPeriodsRejectionFromFile		reject events falling into bad periods
timeInterval	params: 031231 170101	cut on time range

Table B.3: FD quality cuts, usually paired with the SD-1500 quality cuts in Table B.2 for the analysis of golden hybrid events.

Cut name	Cut value	Meaning
hasMieDatabase		Information about atmospheric conditions is available
minLgEnergyFD	1e-20	
skipSaturated		Skip events that saturated the PMT camera
badFDPeriodRejection		Reject events in bad periods
!badPixels	1	Reject events with bad camera pixels
minMeanPixelRMS	17	
maxVAOD	0.1	Vertical aerosol depth below 0.1
LidarCloudRemoval	25	Cloud fraction not too large
MinCloudDepthDistance	params: -50 50	
MaxCloudThickness	100	
xMaxObsInExpectedFOV	params: 40 20	X_{max} reconstructed in expected FoV
xMaxError	40.0	
energyTotError	0.18	
profileChi2Sigma	2.5 -1.1	
maxDepthHole	20.	
maxCoreTankDist	750	
FidFOVICRC13	params: 40 20	Fiducial field of view cut (composition anti-bias cut)

APPENDIX

C

Analyses

This appendix includes supplement material to the analyses presented in the main body of the work. The material contained in the following sections is intended as crosscheck material and background information to the actual analyses. Wherever possible, the sections follow the order of the sections in the main body of the text.

C.1 Violin plots

The violin plots used within this work are discussed briefly to aid in reading the visualization. A violin plot is an extended version of a profile plot. Assuming a variable y which depends on another variable x, a general quantity of interest is the average of y in disjunct ranges of x. Therefore, the y data are binned according to x and the mean in each of the i bins is calculated. A typical profile plot displays the mean and the standard deviation. Compared to a scatter plots, profile plots often visualize underlying trends better. A downside of the profile plots is that they can easily mask bimodal distributions as Gaussian distributions. Assuming a bimodal distribution with symmetric modes on each side of a mean value. Taking the mean of this distribution results in a location of the mean value where only a few or no data points exist.

In order to combine the scatter information of scatter plots with the increased readability of profiles, the latter ones were extended to the so-called violin plots. Functions from the Python library Scipy are used to create the violin plots [128]. Their use throughout Auger should be foremost credited to [63]. The information contained in violin plots is explained with the help of example plots shown in Fig. C.1. The standard quantities of a profile plot, i.e the mean and the standard deviation of the mean, are visualized by circular markers with error bars. In addition to the mean, the median is depicted as black line. The dark shaded area around the median line corresponds to the asymmetric 1σ uncertainties of the median. The lightest gray shaded area represents the distribution of y in the different bins x_i and is called violin. To be precise, the violin plots used throughout this work correspond to one-sided violin plots. Two-sided violin plots (where one can actually see the origin of the naming convention) are also commonly used. The violins represent (rotated) kernel density estimates of the data [129, 130]. The magnitude of the violin gives the size of the p.d.f. at the

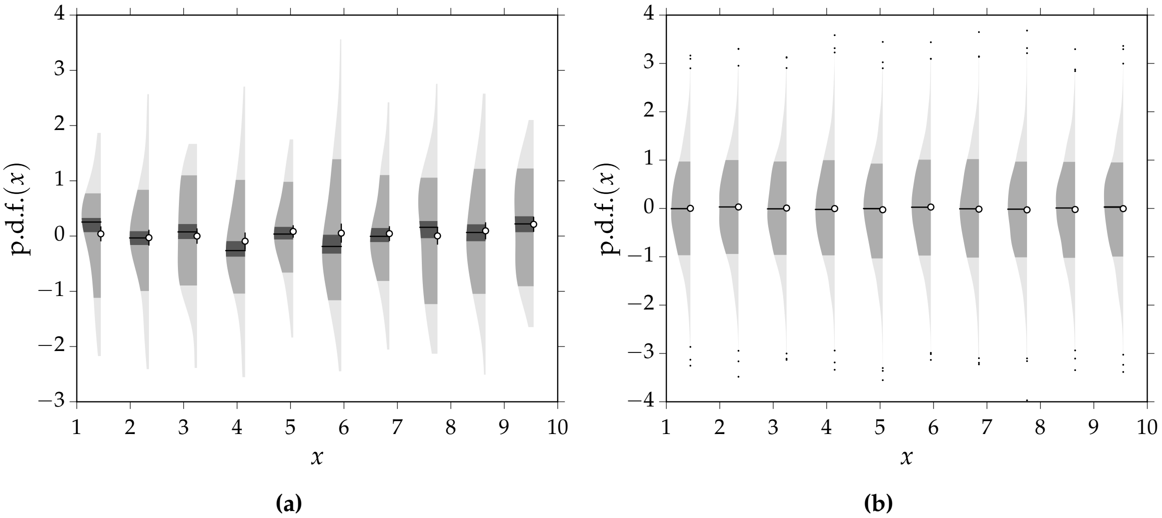

Figure C.1: Toy data distributed linearly in x between 1 and 10 and normally in y with a mean of 0 and standard deviation of 1 [63]. (a) Random draw of 500 points (x, y). The mean and median show fluctuations around the true mean. (b). Sample size of 20 000, i.e each bin includes 2000 points.

specific point. A violin extends up to 3σ (±49.9 %), represented by the lightest gray shaded area. In addition, the darker area corresponds to the asymmetric 1σ standard deviations (±34.1 %). Finally, outliers outside of the 3σ range can be visualized, if needed. Outliers are present in Fig. C.1b, whereas no outliers are included in Fig. C.1a due to the smaller sample size.

C.2 Constant intensity cut for extended zenith angle range

The constant intensity cut as presented in Section 4.4 is applied to events measured with the SD-750 up to 60°. In Fig. C.2a, the number of events with a shower size above the corresponding cut value is shown for four bins in zenith angle. Due to the increasing attenuation with increasing zenith angle, the distributions are shifted towards lower signal values. The attenuation function obtained with the constant intensity cut method is depicted in Fig. C.2c. The attenuation corrected distributions shown in Fig. C.2b lie on top of each other for smaller signals. Deviations are present for shower sizes larger than 100 VEM, indicating a failure of the correction procedure when including zenith angles above 55°.

The results presented in Section 4.4.3, which are obtained with the energy-dependent attenuation correction, show a rather flat event distribution after the correction, being compatible with the expectation of isotropy. A comparison of the event distributions above 30 VEM is depicted in Fig. C.2d. The distribution obtained for the iterative attentuation correction is compared to the standard one. The iterative method results in a event distribution which follows the expectation of isotropy, while the standard approach shows an overshoot of events at the highest zenith angles. The isotropy expectation is depicted as black line for zenith angles up to 60° and as dashed-line for a zenith-angle range up to 55°. The normalization differs due to the difference in the attenuation parameters obtained for the fits. Further studies and the inclusion of the new triggers ToTd and MoPS are needed to establish an extension of the zenith angle range.

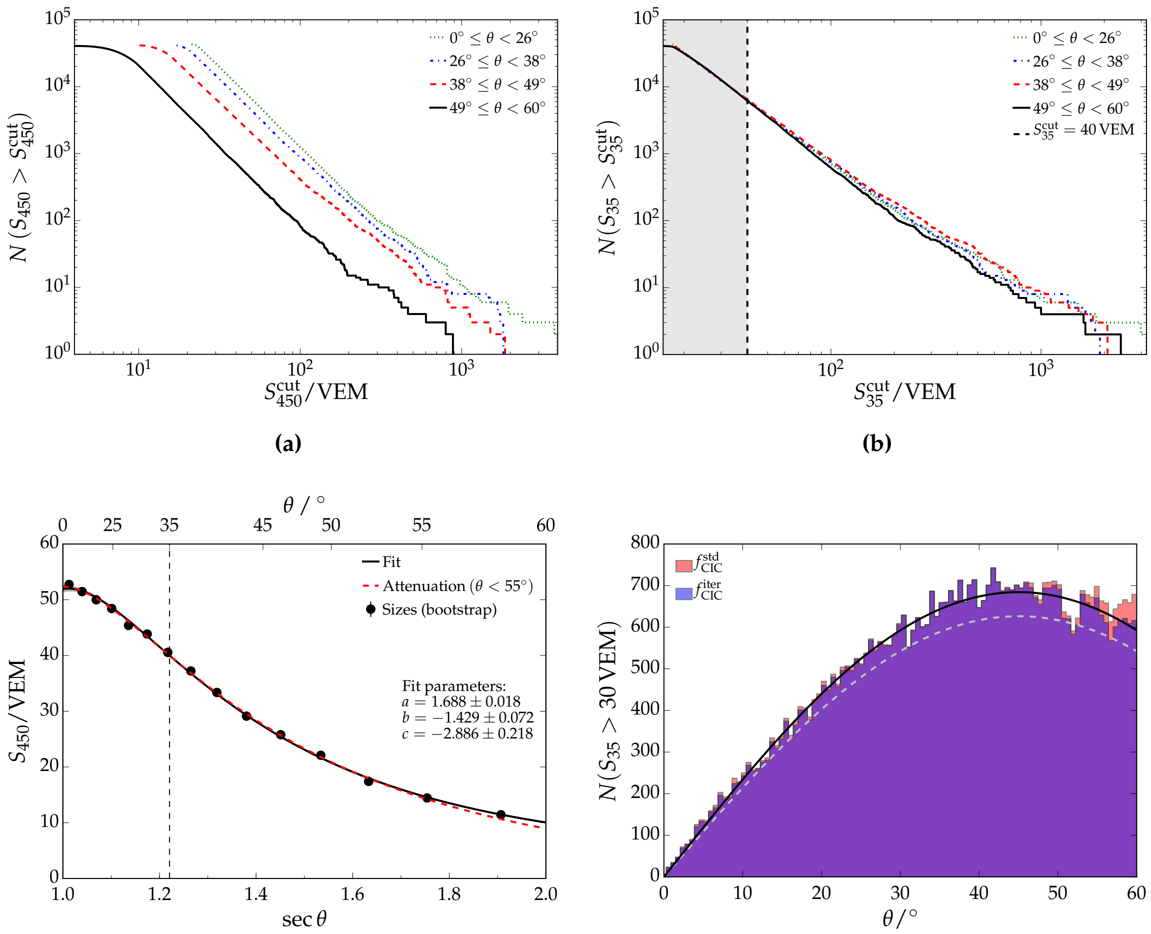

(a) **(b)**

(c) Standard CIC **(d)** Comparison of attenuation corrections

Figure C.2: (a) Number of events with a shower size exceeding the threshold value depicted on the x-axis for different zenith angle bins. The shaded area corresponds to the shower size region excluded in the fit. (b) Attenuation-corrected event distributions. (c) Attenuation function obtained for SD-750 data up to 60°. (d) Angular distribution for events above 30 VEM. The distribution for the standard attenuation correction obtained for data up to 60° is compared to the one obtained for the energy-dependent correction. The black curve shows the fit of the expected isotropic distribution, whereas the gray dashed curve is the one derived for the energy-dependent correction up to 55°.

C.3 FD energy bias and detector resolution

A significant bias in the FD energy of SD-750 simulations was found while working on the analyses presented in [100]. The difference between the reconstructed calorimetric energy and the true calorimetric energy was estimated to be on the order of −10 % at the threshold energy of 3×10^{17} eV. With increasing energy, the bias became negligible as depicted in Fig. C.3. At the time of the analysis, the origin of the bias was not identified and it was unclear whether a bias of similar size existed in data. As a result, it was decided to correct for half of the bias and use the other half as systematic on the derived flux. The resulting correction factor is shown in Fig. C.3b. Afterwards, the fit of the longitudinal profile was improved by using a constraint on the area over peak ratio of the profile. The constraint reduces the negative energy bias found in simulations significantly. The FD bias was revisited with updated

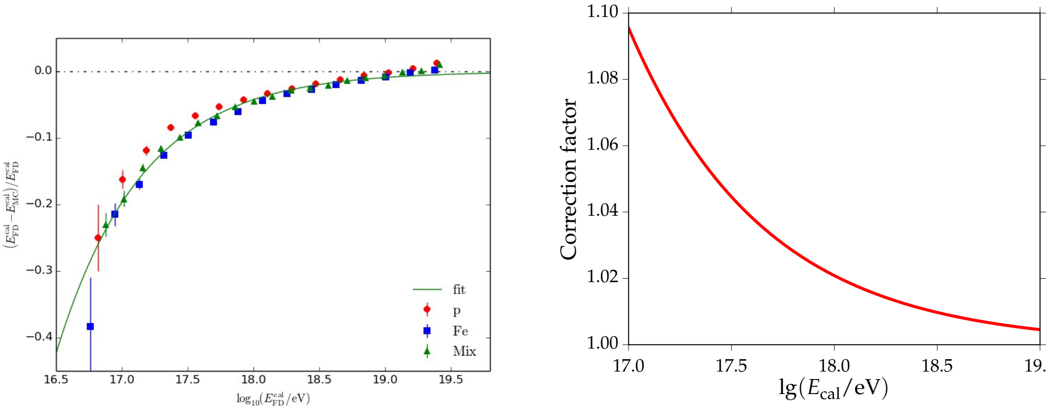

(a) **(b)**

Figure C.3: (a) Bias of the reconstructed calorimetric FD energy as observed in simulations for the SD-750 prior to the work presented in [100]. (b) The SD-750 data were corrected for half of the observed bias by the correction function given here.

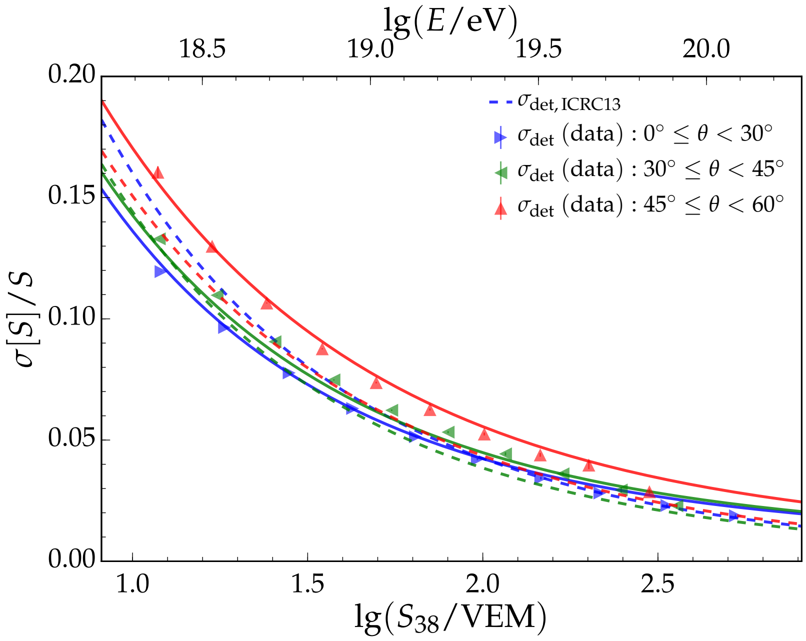

Figure C.4: Detector resolution for the SD-1500 due to sampling fluctuations. The resolution is the result of the quadratic sum of the uncertainties arising during the reconstruction. The updated parameterization (solid lines) is compared to the parameterization obtained in a previous analysis (dashed lines). The updated model shows a better description of the detector resolution when comparing it to data.

simulations. As can be seen from Section 4.5.3, the bias reduced to –5 % at the threshold energy and vanishes for energies above 10^{18} eV.

The detector resolution is revisited in this work. The updated parameterization is visualized in Fig. C.4. Here, the updated model is compared to the detector resolution calculated by using Eq. (4.56). The model to describe the resolution is the one stated in [71]. The dashed line represents the model using the parameters obtained in a previous analysis. With respect to the previous parameters, the updated model describes the data well.

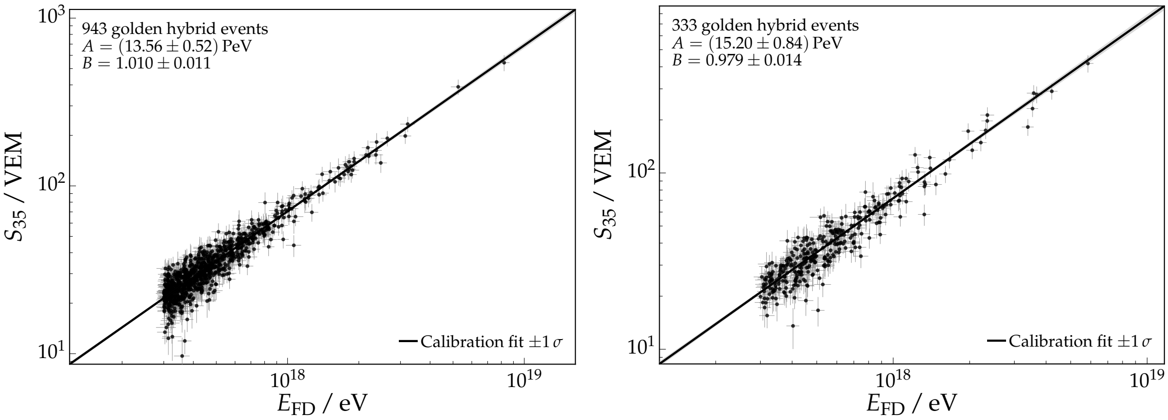

(a) $\theta < 35°$ **(b)** $\theta > 35°$

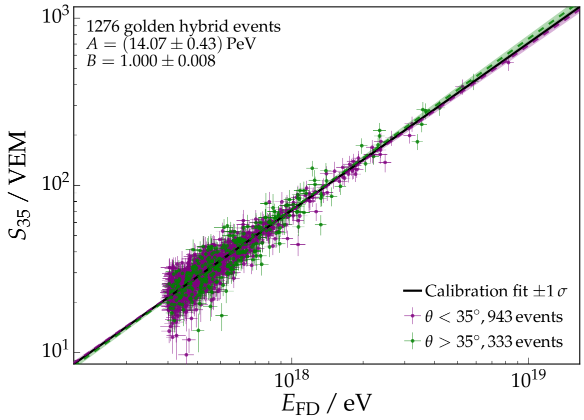

(c)

Figure C.5: Energy calibration for the SD-750 as derived for two different zenith angle bins. The calibrations agree within their uncertainties.

C.4 Energy calibration in different zenith bins

The energy calibration is performed in two zenith angle ranges. The set of golden hybrids is divided based on the reference angle θ_{ref} for the respective data set. Hence, the SD-750 data is divided into events with $\theta < 35°$ and events with $\theta > 35°$. For the SD-1500 data, the division is made at an angle of 38°.

The obtained energy calibrations for the SD-750 data sets are given in Fig. C.5. The respective energy calibration parameters are stated in the plots. The difference in the event number for the two data sets is a result of the FD acceptance. The energy calibrations are compatible within the given uncertainties, as can be seen from Fig. C.5c.

In Fig. C.6, the resulting fits of the energy calibration for the SD-1500 data are shown. Also here, the calibrations agree within their uncertainties.

C.5 Constrained calibration using the energy-dependent CIC

In order to compare the spectrum obtained with energy estimates which use the energy-dependent attenuation correction to the spectrum derived with the standard constant intensity cut method, the energy calibration for the energy-dependent correction has to be

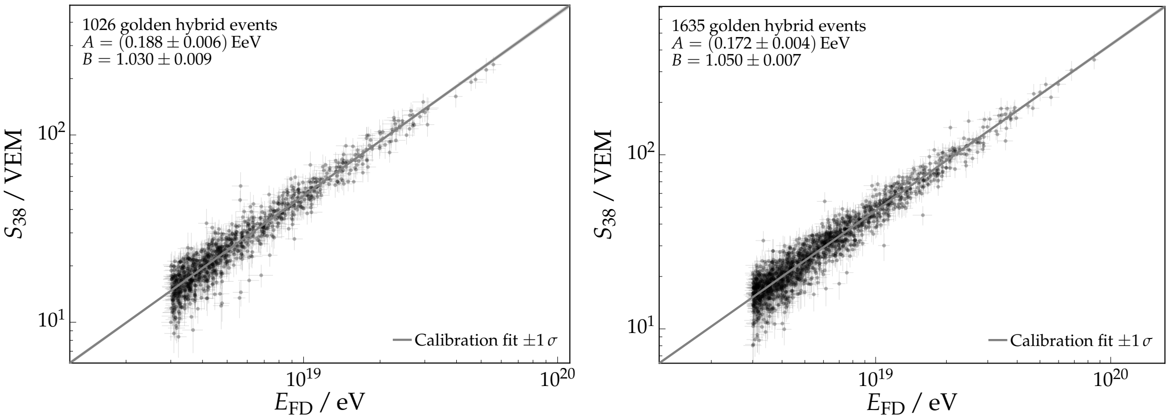

(a) $\theta < 38°$ **(b)** $\theta > 38°$

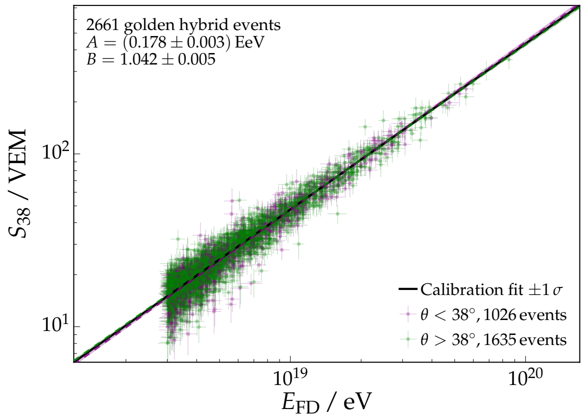

(c)

Figure C.6: Energy calibration for the SD-1500 as derived for two different zenith angle bins. The calibrations are compatible within the given uncertainties.

performed first. As is done for the analysis presented in Section 4.6, the constrained energy calibration is performed in the following. The same number of common events between the SD-750 and SD-1500 data is used. The energies measured by both arrays are depicted in Fig. C.7a. Without the constraint, the energies differ on the level of 6 % on average. Including the common events in the calibration reduces the bias to less than 1 %, as presented in Fig. C.7b. The statistical uncertainty of the calibration is given in Fig. C.7c. The resulting calibration is depicted in Fig. C.8. The parameters are stated in the top left corner.

C.6 Spectra comparison

This section provides supplement comparisons of spectra addressed in the main text. The section starts with a short overview of the four spectra derived from Auger data. The remaining part is focused on the comparison of SD-750 spectra obtained with different attenuation corrections.

C.6.1 Auger spectra

The four spectra derived from the data measured by Auger are depicted in Fig. C.9. Three spectra are obtained with the SD and one is derived from the events measured by the FD.

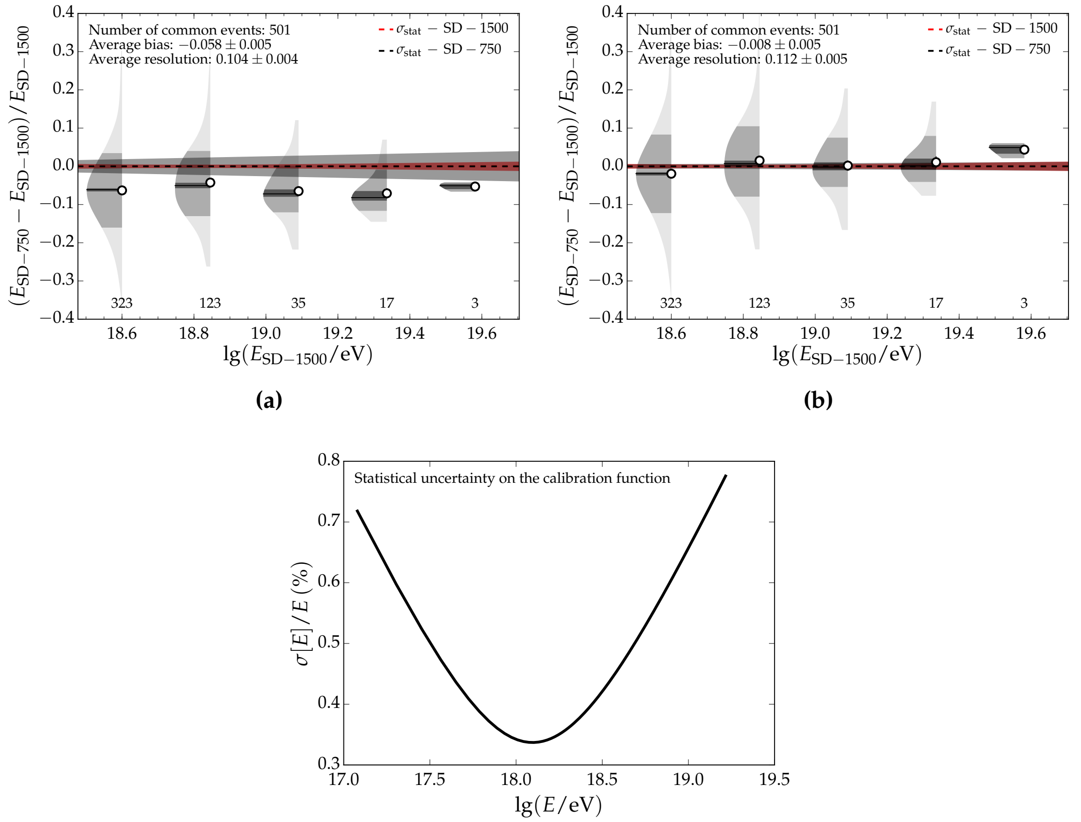

(a)

(b)

(c)

Figure C.7: Relative residual of the energies of events measured by both the SD-750 and SD-1500 for (a) the standard calibration derived in Section 4.5.5 and (b) the calibration extended by a constraint.The shower sizes of the SD-750 data were corrected with the energy-dependent attenuation function. (c) Statistical uncertainty on the calibration function using the constrained calibration.

The three SD spectra refer to the spectrum measured by the SD-750 (blue data point) and the SD-1500 array (gray and red data points). The SD-1500 data are divided into vertical ($\theta < 60°$) and inclined ($\theta > 60°$) events. The systematic uncertainty of 14 % on the energy scale is common to all four spectra.

C.6.2 Comparison of SD-750 spectra

In Fig. C.10, the SD-750 spectrum presented in [97] is compared to the one derived in this work. The difference up to a level of about 5 % is due to the different energy calibrations. The spectrum determined in this work uses the constrained calibration, where a set of common events is used in the fit to constrain the SD-750 energies to the energies measured by the SD-1500. The resulting parameters for the constrained fit are stated in Eq. (4.50), the one obtained with the standard calibration are given in Eq. (4.48).

A comparison of the SD-750 spectra obtained with the different attenuation corrections is shown in Fig. C.11. The energy calibration of both spectra is performed with the standard method described in Section 4.5. The resulting energy calibrations are given in Eq. (4.48) and Eq. (4.52) for the standard attenuation correction and the energy-dependent one, respectively. The spectrum obtained with the energy-dependent attenuation correction is compatible to the one using the standard constant intensity cut method.

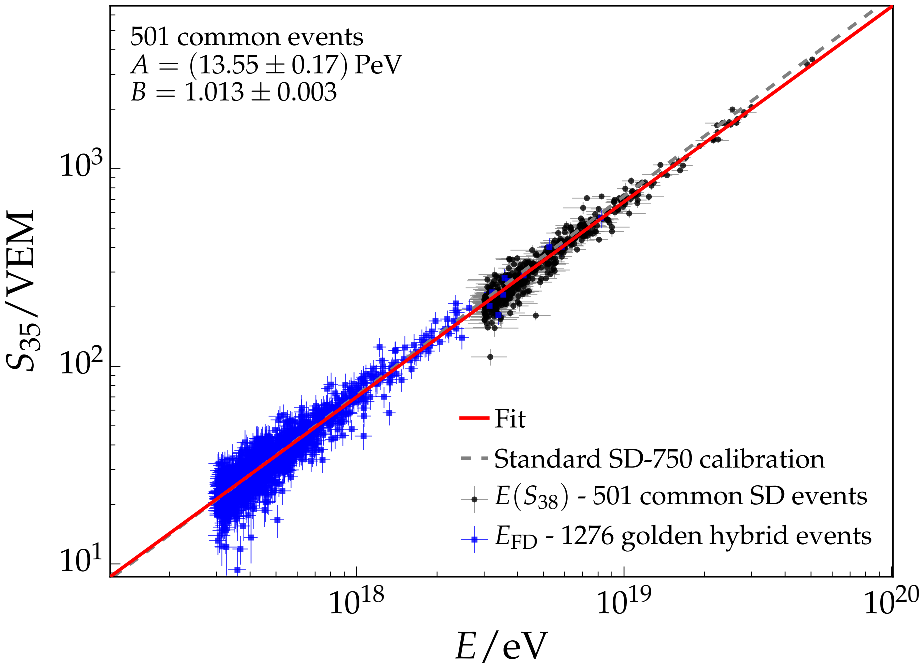

Figure C.8: Energy calibration using a constrained fit. A subset of common events helps to constrain the energies measured with the SD-750 to the reconstructed energies of the SD-1500. The result of the standard calibration is shown in addition. The data of the SD-750 were corrected with the energy-dependent attenuation function.

The SD-750 spectrum with the extended zenith angle range up to 60° is shown in Fig. C.12a in comparison to the standard one with $\theta < 55°$. Both spectra include the energy-dependent attenuation correction. The energy calibration for the extended zenith angle range results in:

$$E(S_{35}) = (14.47 \pm 0.44) \times 10^{15}\,\mathrm{eV} \left(\frac{S_{35}}{\mathrm{VEM}}\right)^{(0.993 \pm 0.008)} . \tag{C.1}$$

Compared to the standard SD-750 spectrum, the flux of the spectrum up to 60° is lower at the threshold energy. This drop in the flux is due to the reduced trigger efficiency for higher zenith angles. In Fig. C.12b, the extended SD-750 spectrum is binned in zenith angle. The decrease in the flux is driven by the highest zenith angles, as visible from the binned spectra.

The $1/\omega$ spectra as obtained for Auger and TA are fit with a broken power law in Fig. C.13. In Fig. C.13a, the fit is performed for the nominal energy scale. In Fig. C.13b, the spectra rescaled, such that the energies of Auger are increased by 5.2 %, while the energies as measured by TA are decreased by the same amount. Here, the difference in the cutoff energy of the two spectra is 0.9σ.

C.7 Search for anisotropy in the spectrum

In Fig. C.14, the relative residuals of the cumulative energy spectra are shown. The residuals are calculated with respect to the total reference flux. The trend of a flux enhancement from the excess region and a decreased flux from the deficit region remains.

The time-binned spectra of the SD-750, which are depicted in Fig. 5.9c, show a discrepancy at higher energies. The flux enhancement in the excess region is driven by the later years, while the deficit is dominated by the earlier years. To investigate the origin of the discrepancy, the event rate of the SD-750 array is studied for different years. As shown in Fig. C.15, the

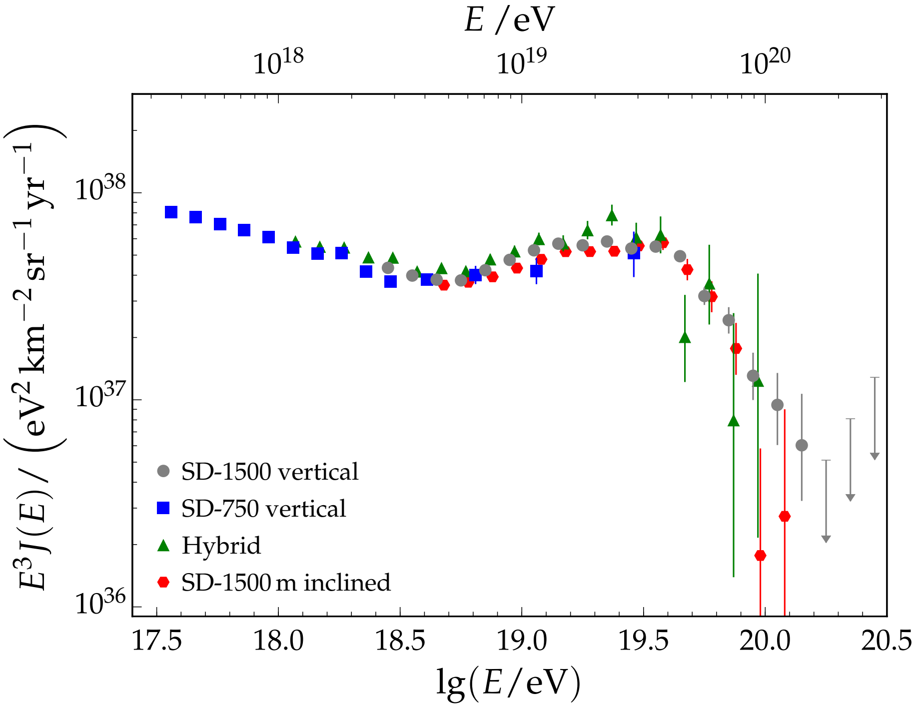

Figure C.9: The four spectra as measured by Auger. The energy spectrum obtained from the SD-750, SD-1500, SD-1500h, and hybrid data are shown [97]. All spectra share the systematic uncertainty on the energy scale (14 %).

measured event rate N is higher than the expected one $\hat{N}$ for the first years of data taking. The expected number of events is calculated from the total number of events multiplied by the fractional exposure for the respective time range. Fitting a constant to the event rate shows a difference for the first two bins, whereas the later years are compatible with a constant behavior. The number of average hexagons is shown in addition. The measured event rate is higher in the early years when the array is growing. The source of the difference between measured and expected event rate remains unclear. The exposure calculation in the early years has to be revisited in future analyses. But also the reconstruction procedure has to be checked. Due to the growth of the array, it has to be ensured that the shared stations of the SD-1500 and SD-750 and the SD-750-only stations are handled correctly when they are assigned as candidate stations to the respective array.

The SD-1500 and SD-1500h spectra are studied in Section 5.4.4 for different declination bands including the extremes of the dipole anisotropy reported by Auger. The spectra are compared to the total spectrum not binned in declination. Each of the spectra is then fit to check for a possible dependence of the fit parameters on the studied declination range. The SD-1500 spectra are fitted with a power law below the ankle and a power law with smooth suppression above the ankle. Due to the higher threshold energy for full efficiency, the ankle and the energies below it are currently not accessible with the SD-1500h data. Therefore, the spectra deduced from this data set are fitted without the ankle and a smooth suppression. The individual fits to the spectra are depicted in Fig. C.16 and Fig. C.17 for the SD-1500 and SD-1500h. The respective fit parameters are stated in addition.

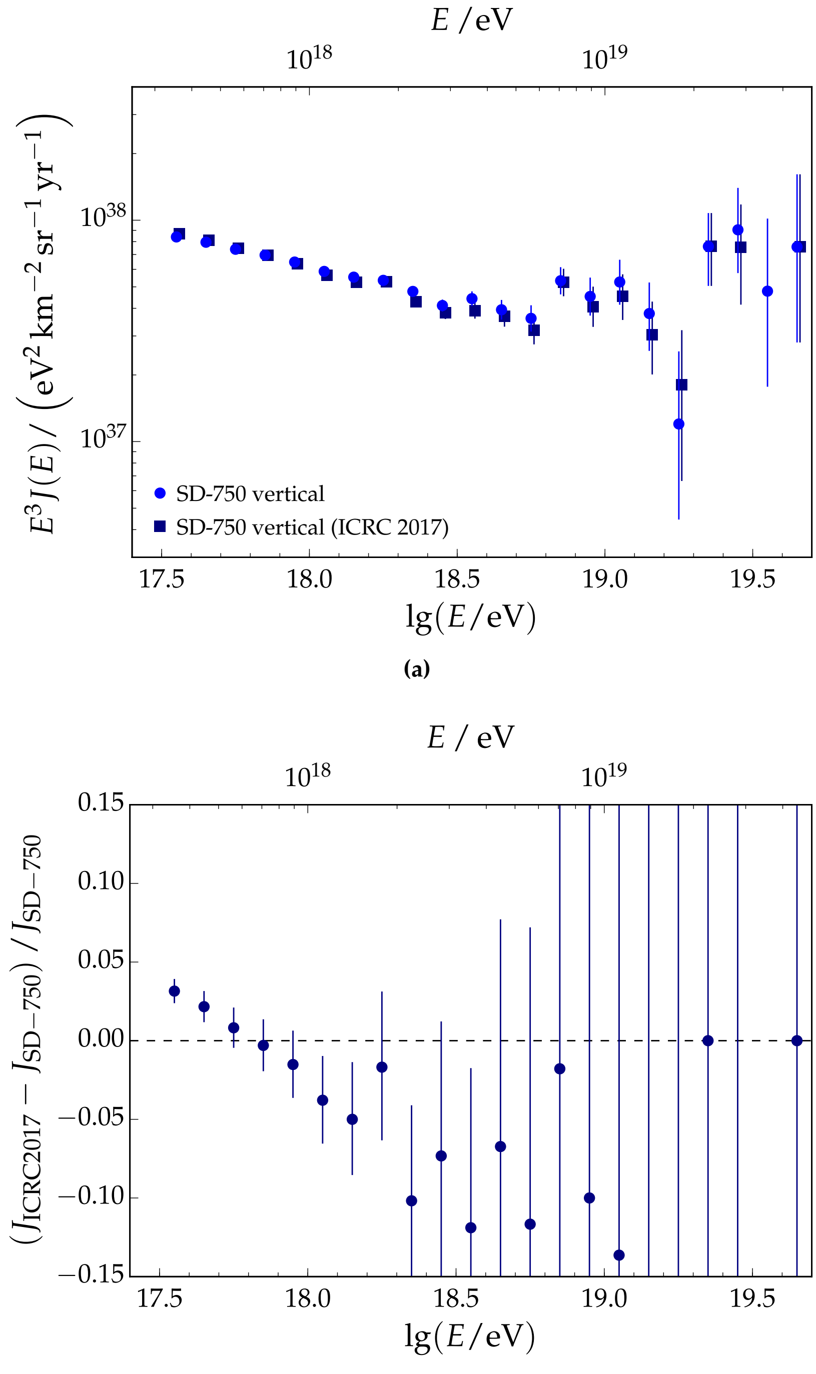

(a)

(b)

Figure C.10: The spectrum as derived for the work presented in [97] is compared to the one using the constrained calibration fit.

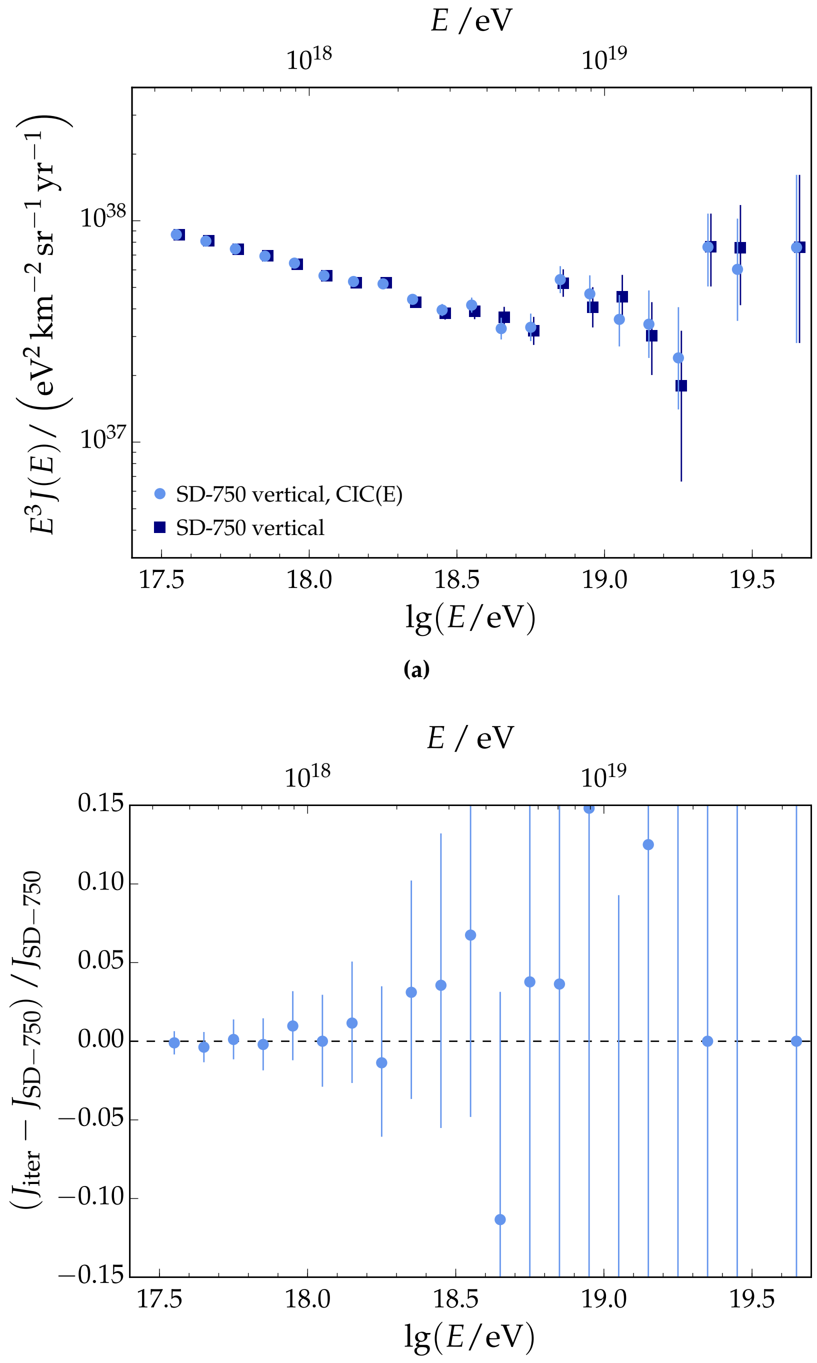

(a)

(b)

Figure C.11: The spectrum with the energy-dependent attenuation correction is compared to the one using the standard CIC method. Both SD-750 spectra use the standard calibration and not the constrained one. The spectra are very well compatible with each other.

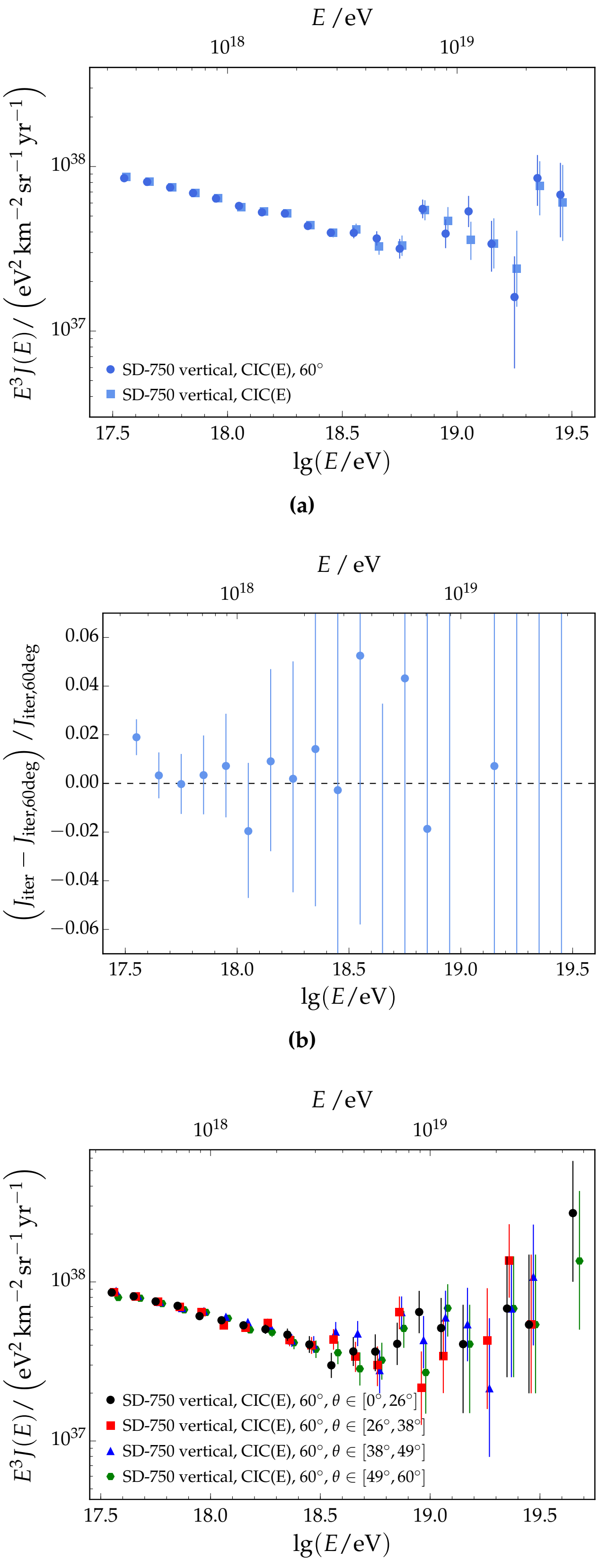

(a)

(b)

(c)

Figure C.12: Comparison of the SD-750 spectrum including zenith angles up to 60° to the spectrum obtained from the standard zenith angle range ($\theta < 55°$). The decrease in flux for the extended zenith angle range is a result of trigger effects. As can be seen from the zenith binned spectra in (b), the drop in flux is driven by the highest zenith angles.

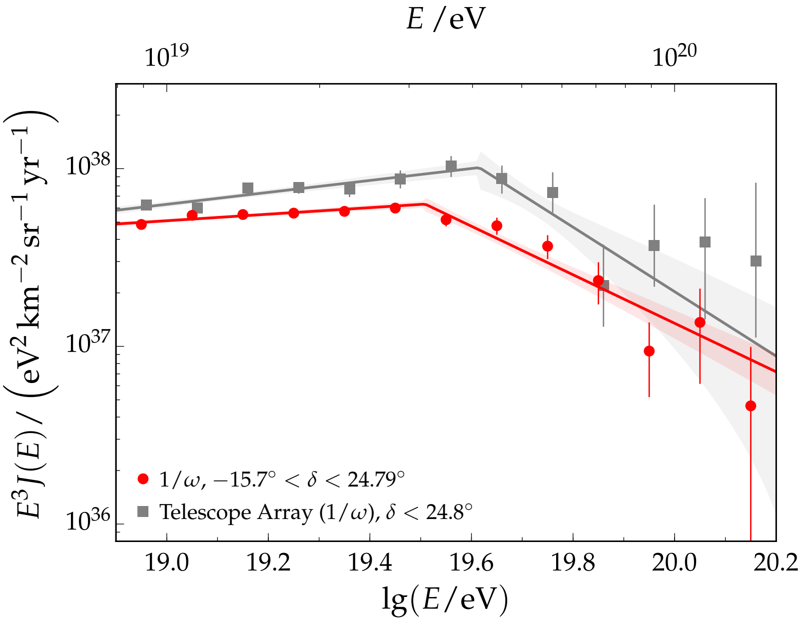

(a)

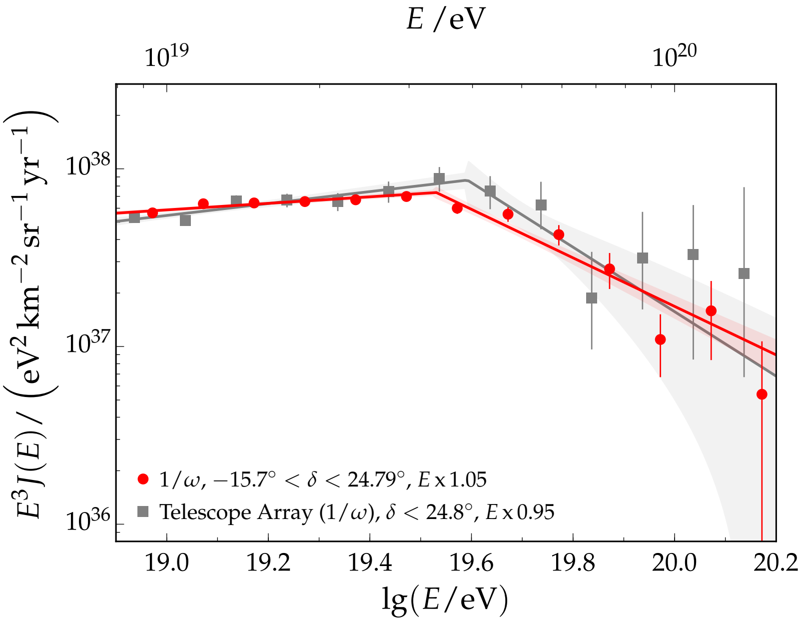

(b)

Figure C.13: (a) Fit to the $1/\omega$ spectra obtained in the common field of view of Auger and TA. (b) Both spectra are shifted by ±5.2 % and fit again with a broken power law.

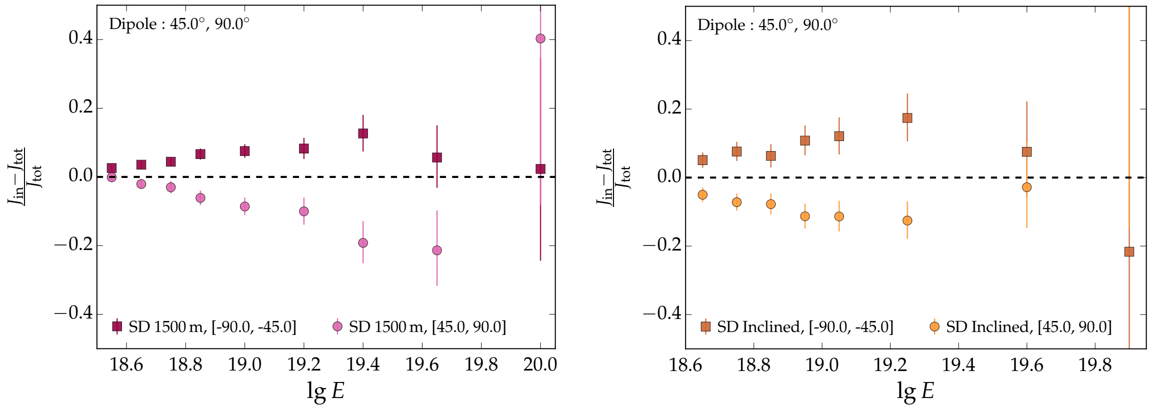

(a) SD-1500 **(b)** SD-1500h

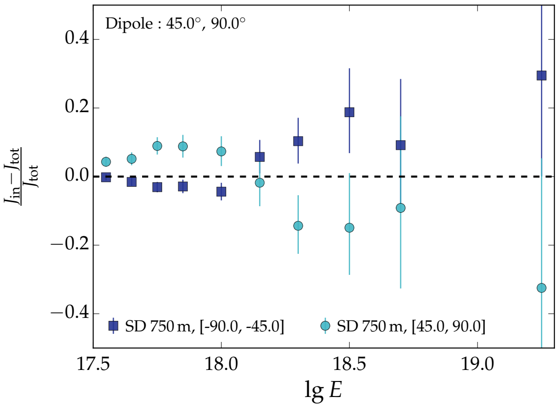

(c) SD-750

Figure C.14: Relative residual of the cumulative energy spectra as obtained from the (a) data, (b) SD-1500h data, and (c) SD-750 data.

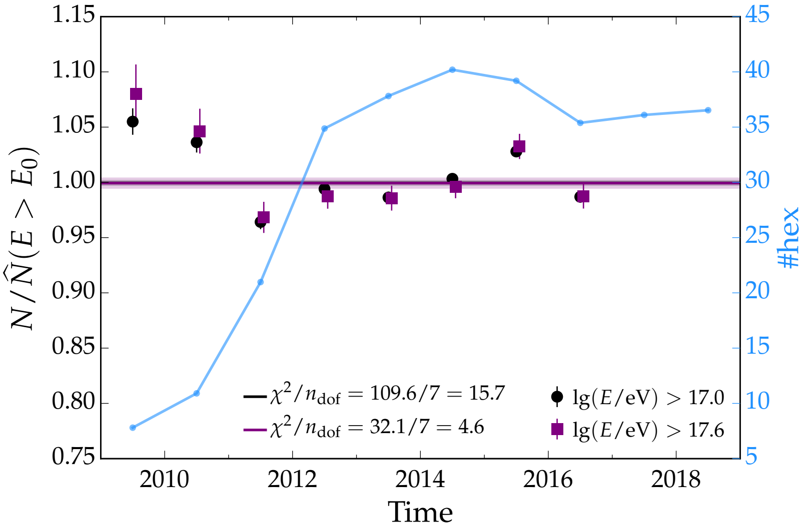

Figure C.15: Event rate as measured with the SD-750 for two different energy thresholds.

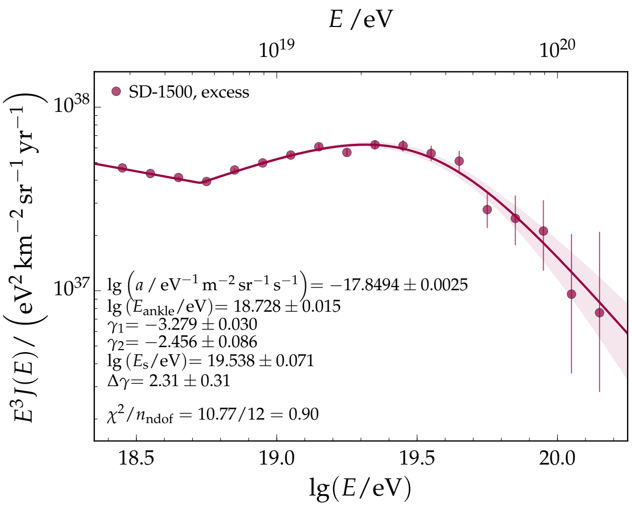

(a) SD-1500, excess

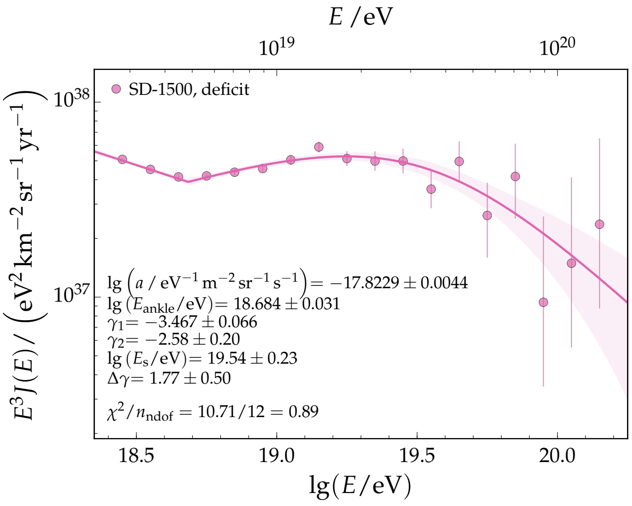

(b) SD-1500, deficit

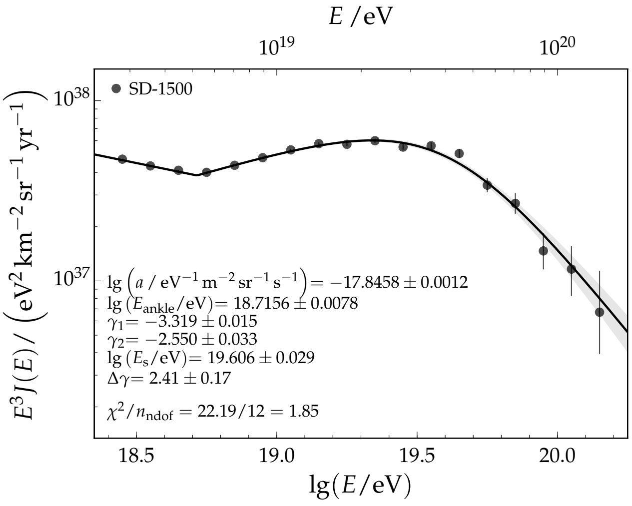

(c) SD-1500, total

Figure C.16: (a), (b) Individual fits to the spectra obtained in the bands containing the dipole extremes. (c) All-sky spectrum for events up to 60°. The fit parameters are stated in addition.

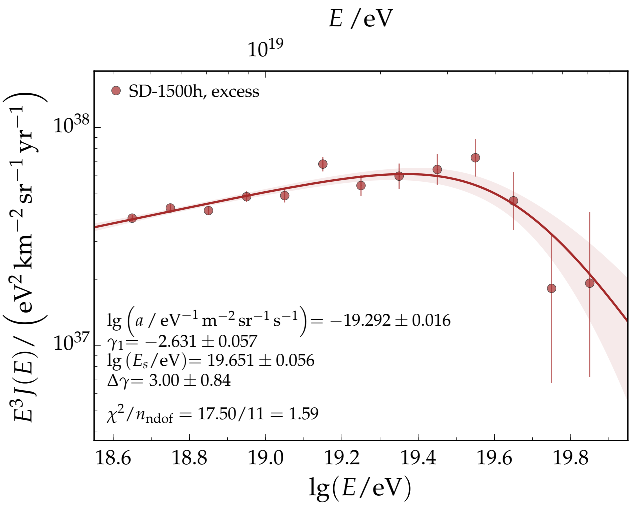

(a) SD-1500h, excess

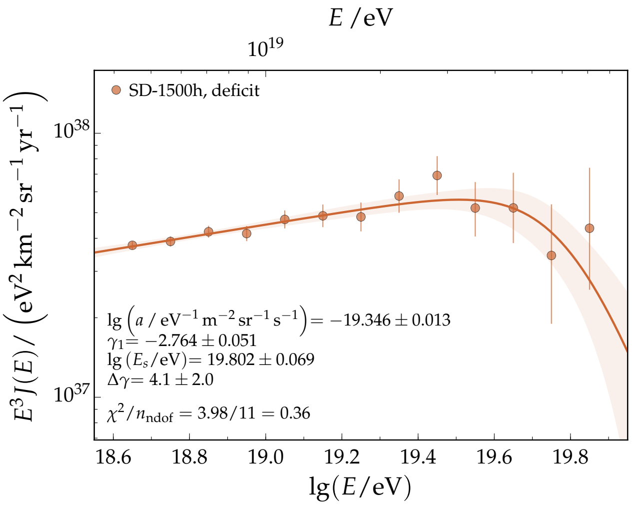

(b) SD-1500h, deficit

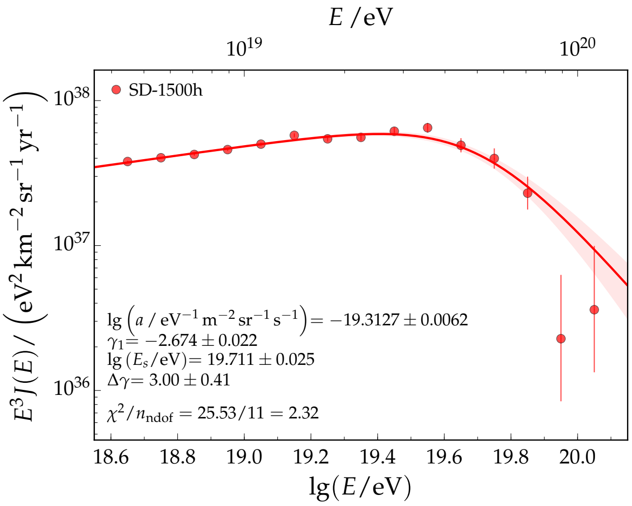

(c) SD-1500h, total

Figure C.17: (a), (b) Individual fits to the spectra obtained in the bands containing the dipole extremes. (c) All-sky spectrum for events with zenith angles starting from 60° up to 80°. The fit parameters are stated in addition.

Acknowledgments

First, I would like to express my gratitude to Prof. Johannes Blümer and the Karlsruhe School of Elementary Particle and Astroparticle Physics (KSETA) for giving me the opportunity to study the physics of ultra-high energy cosmic rays at the Institute of Experimental Particle Physics of the KIT. I am very thankful for the possibility to participate in local shifts in Argentina and visit various meetings and workshops. These experiences have been a great enrichment for my PhD thesis. I would also like to thank Prof. Günter Quast for supporting this thesis as co-referee.

I am especially thankful for the encouraging support of my advisor Dr. Markus Roth. He made it possible to find my place within the Pierre Auger Collaboration and to join interesting and fruitful tasks. A special thanks goes to Sabine Bucher for her organizing abilities and constant support.

To my friends and colleagues from Campus North and within Auger who I met throughout the years, thank you for the enjoyable atmosphere you created, the fruitful discussions, and the fun we had. I very much enjoyed our social activities, be it the movie nights in Karlsruhe, the Auger Youngster meetings (including the ones on the Christmas market) or the spontaneous nights out. Thank you to my office mates, Alex, Ariel, David, Philipp, and Sarah for your advices and support and the great times we had. Thanks to Darko for all the time you dedicate to help others. Your support and $\overline{\text{Off}}\underline{\text{line}}$ wisdom is of great benefit to the group. Thanks to Joachim, Ewa, Sebastian, Johan, and Will for always being there when I needed someone to talk to.

Thanks to Anatoli, Colin, and Felix for your encouragement, no matter which country or time zone you are in.

Many thanks goes to my friends Paul, Anna, Stefan, Tim, and Anna for always making me feel at home. Being able to share not only the fascination but also the frustration throughout this journey helped to keep me sane.

More than I could ever express, I owe thanks to my parents. You have always encouraged me to do what makes me happy and to study what interests me. Without your love and support, I could never have reached my goals.

Bibliography

[1] A. D. Angelis, N. Giglietto, S. Stramaglia, Domenico Pacini, the forgotten pioneer of the discovery of cosmic rays, arXiv:1002.2888 (2010). `arXiv:arXiv:1002.2888`.

[2] V. F. Hess, Beobachtungen der durchdringenden Strahlung bei sieben Freiballonfahrten, Phys. Z. 13 (1912) 1084.

[3] P. Auger, P. Ehrenfest, R. Maze, J. Daudin, R. A. Fréon, Extensive cosmic-ray showers, Rev. Mod. Phys. 11 (3-4) (1939) 288–291. `doi:10.1103/RevModPhys.11.288`.

[4] W. Heitler, The Quantum Theory of Radiation, third ed. Edition, Oxford University Press, Oxford, 1954.

[5] J. Linsley, Evidence for a primary cosmic-ray particle with energy 10^{20} ev, Phys. Rev. Lett. 10 (4) (1963) 146–148. `doi:10.1103/PhysRevLett.10.146`.

[6] K. Greisen, End to the cosmic-ray spectrum?, Phys. Rev. Lett. 16 (17) (1966) 748–750. `doi:10.1103/PhysRevLett.16.748`.

[7] G. T. Zatsepin, V. A. Kuz'min, Upper Limit of the Spectrum of Cosmic Rays, JETP Lett. 4 (1966) 78 – 80.

[8] N. Sakaki *et al.* (AGASA Collab.), Cosmic ray energy spectrum above 3×10^{18} eV observed with AGASA, in: Proc. 27th Int. Cosmic Ray Conf., Hamburg, Germany, 2001.

[9] D. M. Edge *et al.* (Haverah Park Collab.), The cosmic ray spectrum at energies above 10^{17} ev, J. Phys. A 6 (1973) 1612 – 1634.

[10] The High Resolution Fly's Eye Collaboration, Observation of the Ankle and Evidence for a High-Energy Break in the Cosmic Ray Spectrum, Phys.Lett.B619:271-280,2005 (2005). `arXiv:arXiv:astro-ph/0501317`, `doi:10.1016/j.physletb.2005.05.064`.

[11] P. Sokolsky for the HiRes Collaboration, Final Results from the High Resolution Fly's Eye (HiRes) Experiment, arXiv:1010.2690 (2010). `arXiv:arXiv:1010.2690`.

[12] T. Antoni, W. Apel, F. Badea, K. Bekk, K. Bernloehr, H. Bluemer, E. Bollmann, H. Bozdog, I. Brancus, C. Buettner, A. Chilingarian, K. Daumiller, P. Doll, J. Engler, F. Fessler, H. Gils, R. Glasstetter, R. Haeusler, A. Haungs, D. Heck, T. Holst, J. Hoerandel, K.-H. Kampert, J. Kempa, H. Klages, J. Knapp, K. Koehler, G. Maier, H.-J. Mathes, H. Mayer, J. Milke, M. Mueller, J. Oehlschlaeger, M. Petcu, H. Rebel, M. Risse, M. Roth, G. Schatz, J. Scholz, S. Sokhoyan, T. Thouw, H. Ulrich, B. Vulpescu, J. Weber, J. Wentz, J. Wochele, J. Zabierowski, S. Zagromski, Muon density measurements with the KASCADE central detector, Astroparticle Physics 16 (4) (2002) 373 – 386. `doi:10.1016/S0927-6505(01)00120-7`.
URL `http://www.sciencedirect.com/science/article/pii/S0927650501001207`

[13] T. Antoni, W. Apel, A. Badea, K. Bekk, A. Bercuci, J. Blümer, H. Bozdog, I. Brancus, A. Chilingarian, K. Daumiller, P. Doll, R. Engel, J. Engler, F. Feßler, H. Gils, R. Glasstetter, A. Haungs, D. Heck, J. Hörandel, K.-H. Kampert, H. Klages, G. Maier, H. Mathes, H. Mayer, J. Milke, M. Müller, R. Obenland, J. Oehlschläger, S. Ostapchenko, M. Petcu, H. Rebel, A. Risse, M. Risse, M. Roth, G. Schatz, H. Schieler, J. Scholz, T. Thouw, H. Ulrich, J. van Buren, A. Vardanyan, A. Weindl, J. Wochele, J. Zabierowski, KASCADE measurements of energy spectra for elemental groups of cosmic rays: Results and open problems, Astroparticle Physics 24 (1-2) (2005) 1 – 25. `doi:10.1016/j.astropartphys.2005.04.001`.
URL `http://www.sciencedirect.com/science/article/pii/S0927650505000691`

[14] W. D. Apel, J. C. Arteaga-Velázquez, K. Bekk, M. Bertaina, J. Blümer, H. Bozdog, I. M. Brancus, P. Buchholz, E. Cantoni, A. Chiavassa, F. Cossavella, K. Daumiller, V. de Souza, F. Di Pierro, P. Doll, R. Engel, J. Engler, M. Finger, D. Fuhrmann, P. L. Ghia, H. J. Gils, R. Glasstetter, C. Grupen, A. Haungs, D. Heck, J. R. Hörandel, D. Huber, T. Huege, P. G. Isar, K.-H. Kampert, D. Kang, H. O. Klages, K. Link, P. Łuczak, M. Ludwig, H. J. Mathes, H. J. Mayer, M. Melissas, J. Milke, B. Mitrica, C. Morello, G. Navarra, J. Oehlschläger, S. Ostapchenko, S. Over, N. Palmieri, M. Petcu, T. Pierog, H. Rebel, M. Roth, H. Schieler, F. G. Schröder, O. Sima, G. Toma, G. C. Trinchero, H. Ulrich, A. Weindl, J. Wochele, M. Wommer, J. Zabierowski, KASCADE-Grande Collaboration, Kneelike Structure in the Spectrum of the Heavy Component of Cosmic Rays Observed with KASCADE-Grande, Phys. Rev. Lett. 107 (2011) 171104. `doi:10.1103/PhysRevLett.107.171104`.
URL `http://link.aps.org/doi/10.1103/PhysRevLett.107.171104`

[15] D. Kazanas, A. Nicolaidis, Cosmic ray 'knee': A Herald of new physics?, in: 27th International Cosmic Ray Conference (ICRC 2001) Hamburg, Germany, August 7-15, 2001, 2001, pp. 1760–1763, [5,1760(2001)]. `arXiv:astro-ph/0103147`.
URL `http://www.copernicus.org/icrc/papers/ici7054_p.pdf`

[16] V. Berezinsky, Transition from galactic to extragalactic cosmic rays, arXiv:0710.2750v2 (10 2007).
URL `http://arxiv.org/abs/0710.2750v2`

[17] D. Allard, Extragalactic propagation of ultrahigh energy cosmic-rays, Astroparticle Physics 39-40 (2012) 33 – 43, cosmic Rays Topical Issue. `doi:https://doi.org/10.1016/j.astropartphys.2011.10.011`.
URL `http://www.sciencedirect.com/science/article/pii/S092765051100199X`

[18] M. Unger, G. R. Farrar, L. A. Anchordoqui, Origin of the ankle in the ultra-high energy cosmic ray spectrum and of the extragalactic protons below it (2015)`arXiv:1505.02153`.

[19] E. Kido, O. Kalashev, Telescope Array Collaboration, Constraining UHECR source models by the TA SD energy spectrum (2013)arXiv:1310.6093.

[20] Alexander Schulz *et al.* (Pierre Auger Collab.), The measurement of the energy spectrum of cosmic rays above 0.3 EeV with the Pierre Auger Observatory, in: Proc. 33rd ICRC, (2013) 27, arXiv:1307.5059, Rio de Janeiro, Brazil, 2013.

[21] R. Aloisio, V. Berezinsky, P. Blasi, Ultra high energy cosmic rays: implications of Auger data for source spectra and chemical composition, JCAP 1410 (10) (2014) 020. arXiv:1312.7459, doi:10.1088/1475-7516/2014/10/020.

[22] K.-H. Kampert, P. Tinyakov, Cosmic rays from the ankle to the cutoff, Comptes Rendus Physique 15 (2014) 318–328. arXiv:1405.0575, doi:10.1016/j.crhy.2014.04.006.

[23] The H.E.S.S. Collaboration, The exceptionally powerful tev γ-ray emitters in the large magellanic cloud, Science 347 (6220) (2015) 406–412. arXiv:http://science.sciencemag.org/content/347/6220/406.full.pdf, doi:10.1126/science.1261313.
URL http://science.sciencemag.org/content/347/6220/406

[24] A. Aab, et al., Pierre Auger, An Indication of anisotropy in arrival directions of ultra-high-energy cosmic rays through comparison to the flux pattern of extragalactic gamma-ray sources, Astrophys. J. 853 (2018) L29. arXiv:1801.06160, doi:10.3847/2041-8213/aaa66d.

[25] A. Aab, et al., Pierre Auger, Observation of a Large-scale Anisotropy in the Arrival Directions of Cosmic Rays above 8×10^{18} eV, Science 357 (6537) (2017) 1266–1270. arXiv:1709.07321, doi:10.1126/science.aan4338.

[26] A. H. Compton, I. A. Getting, An apparent effect of galactic rotation on the intensity of cosmic rays, Phys. Rev. 47 (1935) 817–821. doi:10.1103/PhysRev.47.817.
URL https://link.aps.org/doi/10.1103/PhysRev.47.817

[27] A. M. Hillas, The origin of ultra-high-energy cosmic rays, Ann. Rev. Astron. Astrophys. 22 (1) (1984) 425–444.

[28] K. Kotera, A. V. Olinto, The astrophysics of ultrahigh-energy cosmic rays, Annual Review of Astronomy and Astrophysics 49 (1) (2011) 119–153. arXiv:https://doi.org/10.1146/annurev-astro-081710-102620, doi:10.1146/annurev-astro-081710-102620.
URL https://doi.org/10.1146/annurev-astro-081710-102620

[29] A. Haungs, H. Rebel, M. Roth, Energy spectrum and mass composition of high-energy cosmic rays, Rept. Prog. Phys. 66 (2003) 1145–1206. doi:10.1088/0034-4885/66/7/202.

[30] P. Abreu, et al., Pierre Auger Collaboration, Interpretation of the Depths of Maximum of Extensive Air Showers Measured by the Pierre Auger Observatory, JCAP 1302 (2013) 026. arXiv:1301.6637, doi:10.1088/1475-7516/2013/02/026.

[31] A. Aab, et al., Pierre Auger Collaboration, Depth of Maximum of Air-Shower Profiles at the Pierre Auger Observatory: Measurements at Energies above $10^{17.8}$ eV, Phys.Rev.D (2014)arXiv:1409.4809.

[32] A. Porcelli *et al.* (Pierre Auger Collab.), Measurements of $X_{\max}$ above 10^{17} eV with the fluorescence detector of the Pierre Auger Observatory, in: Proc. 34th Int. Cosmic Ray Conf., The Hague, The Netherlands, 2015.

[33] M. Unger for the Pierre Auger Collaboration and Telescope Array Collaboration, Report of the Working Group on the Composition of Ultra-High Energy Cosmic Rays, in: Proc. 34th Int. Cosmic Ray Conf., The Hague, The Netherlands, 2015, arXiv:1511.02103.

[34] A. Aab, et al, T. P. A. Collaboration, The Pierre Auger Cosmic Ray Observatory, Nuclear Instruments and Methods in Physics Research Section A: Accelerators, Spectrometers, Detectors and Associated Equipment 798 (2015) 172 – 213. `doi:https://doi.org/10.1016/j.nima.2015.06.058`.
URL `http://www.sciencedirect.com/science/article/pii/S0168900215008086`

[35] J. Abraham, M. Aglietta, et al, Properties and performance of the prototype instrument for the pierre auger observatory, Nuclear Instruments and Methods in Physics Research Section A: Accelerators, Spectrometers, Detectors and Associated Equipment 523 (1) (2004) 50 – 95. `doi:https://doi.org/10.1016/j.nima.2003.12.012`.
URL `http://www.sciencedirect.com/science/article/pii/S0168900203033497`

[36] D. Veberič, Private Communication about current map for the Pierre Auger Observatory (03 2018).

[37] B. Keilhauer, Investigation of atmospheric effects on the development of extensive air showers and their detection with the pierre auger observatory, Ph.D. thesis, Karlsruhe University, Karlsruhe, Germany (2003).

[38] D. Ravignani *et al.* (Pierre Auger Collab.), Measurement of the energy spectrum of cosmic rays above 3×10^{17} eV using the AMIGA 750 m surface detector array of the Pierre Auger Observatory, in: Proc. 33rd Int. Cosmic Ray Conf., Rio de Janeiro, Brazil, 2013.

[39] D. Mockler, The first measurement of an energy spectrum at 0.1 EeV with the Surface Detector of the Pierre Auger Observatory, Master's thesis, Karlsruhe Institute of Technology, Karlsruhe (10 2014).

[40] S. Messina, Extension to lower energies of the cosmic-ray energy window at the Pierre Auger Observatory, Dissertation, University of Groningen (2016).

[41] J. Abraham *et al.* (Pierre Auger Collab.), The fluorescence detector of the Pierre Auger Observatory, Nucl. Instrum. Meth. A620 (2010) 227 – 251.

[42] M. Kleifges *et al.* (Pierre Auger Collab.), Extension of the Pierre Auger Observatory using high elevation fluorescence telescopes (HEAT), in: Proc. 31st Int. Cosmic Ray Conf., Lódź, Poland, 2009.

[43] S. Y. BenZvi *et al.* (Pierre Auger Collab.), The LIDAR system of the Pierre Auger observatory, Nucl. Instrum. Meth. A574 (2007) 171–184, arXiv astro-ph/0609063. `doi:10.1016/j.nima.2007.01.094`.

[44] P. Abreu, et al., Pierre Auger Collaboration, Description of Atmospheric Conditions at the Pierre Auger Observatory using the Global Data Assimilation System (GDAS), Astropart.Phys. 35 (2012) 591–607. `arXiv:1201.2276`, `doi:10.1016/j.astropartphys.2011.12.002`.

[45] F. Suarez *et al.* (Pierre Auger Collab.), The AMIGA muon detectors of the Pierre Auger Observatory, in: Proc. 33rd Int. Cosmic Ray Conf., Rio de Janeiro, Brazil, 2013.

[46] E. M. Holt (Pierre Auger Collab.), Recent Results of the Auger Engineering Radio Array (AERA), in: Proc. 35th Int. Cosmic Ray Conf., Busan, Korea, 2017.

[47] A. Aab, et al., The Pierre Auger Collaboration, Probing the radio emission from air showers with polarization measurements, Phys. Rev. D 89 (2014) 052002. `doi:10.1103/PhysRevD.89.052002`.
URL `https://link.aps.org/doi/10.1103/PhysRevD.89.052002`

[48] Aab, Alexander and others, Pierre Auger, Measurement of the Radiation Energy in the Radio Signal of Extensive Air Showers as a Universal Estimator of Cosmic-Ray Energy, Phys. Rev. Lett. 116 (24) (2016) 241101. `arXiv:1605.02564`, `doi:10.1103/PhysRevLett.116.241101`.

[49] A. Aab, et al., Pierre Auger Collaboration, Energy estimation of cosmic rays with the Engineering Radio Array of the Pierre Auger Observatory, Phys. Rev. D 93 (2016) 122005. `doi:10.1103/PhysRevD.93.122005`.
URL `https://link.aps.org/doi/10.1103/PhysRevD.93.122005`

[50] Aab, Alexander and others, Pierre Auger, The pierre auger observatory upgrade - preliminary design report (2016)`arXiv:1604.03637`.

[51] J. Abraham, et al., Trigger and aperture of the surface detector array of the Pierre Auger Observatory, Nuclear Instruments and Methods in Physics Research Section A: Accelerators, Spectrometers, Detectors and Associated Equipment 613 (1) (2010) 29 – 39. `doi:https://doi.org/10.1016/j.nima.2009.11.018`.
URL `http://www.sciencedirect.com/science/article/pii/S0168900209021688`

[52] P. Billoir, Proposition to improve the local trigger of the Surface Detector for low energy showers, Auger internal note GAP-2009-179 (2009).

[53] P. Billoir, P. Ghia, D. Nitz, R. Sato, First results of the ToTd trigger in the test hexagon, Auger internal note GAP-2011-032 (2011).

[54] P. Billoir, New proposal to improve the local trigger of the Surface Detector, Auger internal note GAP-2011-089 (2011).

[55] A. Coleman, Measurement of the Cosmic Ray Flux Above 100 PeV at the Pierre Auger Observatory , Dissertation, Pennsylvania State University (2018).

[56] D. Veberič, M. Roth, Offline reference manual: Sd reconstruction, Auger internal note GAP-2005-035, an updated version is shipped with the Offline software distribution (2005).

[57] M. Urban, D. Mockler, D. Veberič, Observer Data Set for Anisotropy Studies including 4T5 Events, Auger internal note GAP-2018-034 (2018).

[58] L. M. Bueno, P. Billoir, I. C. Maris, Signal variance for the TOTd and MoPS triggers, Auger internal note GAP-2014-035 (2014).

[59] I. C. Mariş, Measurement of the ultra high energy cosmic ray flux using data of the pierre auger observatory, Auger internal note GAP-2008-026 (2008).

[60] A. Schulz, Measurement of the Energy Spectrum of Cosmic Rays between 0.1 EeV and 30 EeV with the Infill Extension of the Surface Detector of the Pierre Auger Observatory, Master's thesis, Karlsruhe Institute of Technology (2012).

[61] T. Schmidt, I. C. Mariş, M. Roth, Fine tuning of the ldf parameterisation and the influence on s_{1000}, Auger internal note GAP-2007-106 (2007).

[62] D. Veberič *et al.* (Pierre Auger Collab.), Estimation of Signal in Saturated Stations of the Pierre Auger Surface Detector, in: Proc. 33rd Int. Cosmic Ray Conf., Rio de Janeiro, Brazil, 2013.

[63] A. Schulz, Measurement of the Energy Spectrum and Mass Composition of Ultra-high Energy Cosmic Rays, Dissertation, Karlsruhe Institute of Technology (2016).

[64] D. Heck, G. Schatz, T. Thouw, J. Knapp, J. Capdevielle, CORSIKA: A Monte Carlo code to simulate extensive air showers, Forschungszentrum Karlsruhe Report FZKA (1998) 6019.

[65] A. Fassó, A. Ferrari, J. Ranft, P. Sala, Fluka: a multi-particle transport code, CERN-2005-10 (2005), INFN/TC 05/11, SLAC-R-773 (2005).

[66] S. Ostapchenko, Monte Carlo treatment of hadronic interactions in enhanced Pomeron scheme: I. QGSJET-II model, Phys. Rev. D83 (2011) 014018. `arXiv:1010.1869`, `doi:10.1103/PhysRevD.83.014018`.

[67] T. Pierog, I. Karpenko, J. M. Katzy, E. Yatsenko, K. Werner, EPOS LHC: Test of collective hadronization with data measured at the CERN Large Hadron Collider, Phys. Rev. C 92 (2015) 034906. `doi:10.1103/PhysRevC.92.034906`.
URL `https://link.aps.org/doi/10.1103/PhysRevC.92.034906`

[68] Riehn, Felix and Engel, Ralph and Fedynitch, Anatoli and Gaisser, Thomas K. and Stanev, Todor, A new version of the event generator sibyll, PoS ICRC2015 (2016) 558. `arXiv:1510.00568`.

[69] Ostapchenko, Sergey, Cosmic ray interaction models: an overview, EPJ Web Conf. 120 (2016) 04003. `doi:10.1051/epjconf/201612004003`.

[70] X. Bertou, P. Billoir, On the origin of the asymmetry of ground densities in inclined showers, Auger internal note GAP-2000-017 (2000).

[71] A. Schulz, M. Roth, Details and technical notes on fitting the energy spectrum, Auger internal note GAP-2017-043 (2017).

[72] T. Abu-Zayyad et al., The Cosmic Ray Energy Spectrum Observed with the Surface Detector of the Telescope Array Experiment, Astrophysical Journal 768 (2013).

[73] A. Aab, et al., Pierre Auger Collaboration, Reconstruction of inclined air showers detected with the Pierre Auger Observatory, JCAP 1408 (08) (2014) 019. `arXiv:1407.3214`, `doi:10.1088/1475-7516/2014/08/019`.

[74] Aab, Alexander and others, Pierre Auger, Measurement of the Cosmic Ray Spectrum above 4×10^{18} eV Using Inclined Events Detected with the Pierre Auger Observatory, JCAP 1508 (2015) 049. `arXiv:1503.07786`, `doi:10.1088/1475-7516/2015/08/049`.

[75] C. Bonifazi, A. Letessier-Selvon, Event selection using the T5 time distribution, Auger internal note GAP-2006-042 (2006).

[76] I. Lhenry-Yvon, P. Ghia, The communications crisis in 2009: proposal for handling data between June and November, Auger internal note GAP-2010-020 (2010).

[77] P. Sommers, Cosmic ray anisotropy analysis with a full-sky observatory, Astropart. Phys. 14 (2001) 271–286.

[78] C. Bleve *et al.* (Pierre Auger Collaboration), Weather induced effects on extensive air showers observed with the surface detector of the pierre auger observatory, in: 30th Proc. Int. Cosm. Ray Conf., Merida, Mexico, 2007.

[79] C. Bleve, Atmospheric effects on extensive air showers observed with the surface detector of the pierre auger observatory, preprint submitted to Elsevier (12 2008).

[80] D. Harari, S. Mollerach, E. Roulet, On the implementation of the energy correction due to weather effects, Auger internal note GAP-2008-175 (2008).

[81] A. Remoto, S. Mollerach, E. Roulet, On the weather correction and energy calibration, Auger internal note GAP-2009-054 (2009).

[82] E. Roulet, I. Allekotte, D. Harari, S. Mollerach, On the Constant Intensity Cut and weather effects, Auger internal note GAP-2009-024 (2009).

[83] S. Mollerach, E. Roulet, O. Taborda, Revisiting the effects of weather on the air shower energy reconstruction, Auger internal note GAP-2014-047 (2014).

[84] S. Mollerach, E. Roulet, O. Taborda, Weather effects on the event rate of the Infill array, Auger internal note GAP-2014-105 (2014).

[85] P. Abreu, et al., Pierre Auger Collaboration, Large scale distribution of arrival directions of cosmic rays detected above 10^{18} eV at the Pierre Auger Observatory, Astrophys.J.Suppl. 203 (2012) 34. `arXiv:1210.3736`, `doi:10.1088/0067-0049/203/2/34`.

[86] P. Abreu, et al., Pierre Auger Collaboration, The effect of the geomagnetic field on cosmic ray energy estimates and large scale anisotropy searches on data from the Pierre Auger Observatory, JCAP 1111 (2011) 022. `arXiv:1111.7122`, `doi:10.1088/1475-7516/2011/11/022`.

[87] T. K. Gaisser, A. M. Hillas, Reliability of the Method of Constant Intensity Cuts for Reconstructing the Average Development of Vertical Showers, in: Proc. 15th Int. Cosm. Ray Conf., Vol. 8, Plovdiv, Bulgaria, 1977, p. 353.

[88] M. Healy, K. Arisaka, D. Barnhill, J. Lee, T. Ohnuki, A. Tripathi, Applying the Constant Intensity Cut to Determine Composition, Energy, and Muon Richness, Auger internal note GAP-2006-020 (2006).

[89] A. Rivera, S. Mollerach, E. Roulet, On the energy dependence of the Constant Intensity Cut, Auger internal note GAP-2009-123 (2009).

[90] H. Dembinski, M. Roth, Constant Intensity Cut method revisited: Uncertainty calculation with the Bootstrap, Auger internal note GAP-2011-074 (2011).

[91] H. Dembinski, M. Roth, Constant intensity cut: Matching the energy scales of vertical and inclined showers, Auger internal note GAP-2012-069 (2012).

[92] D. Veberič, B. Kégl, R. Engel, M. Roth, Constant Intensity Cut: Unbinned Estimation of the Signal Attenuation Function, Auger internal note GAP-2015-065 (2015).

[93] F. Fenu, A. Castellina, M. Bertaina, The effect of the Constant Intensity Cut energy dependence on the spectral shape, Auger internal note GAP-2017-034 (2017).

[94] D. Harari, S. Mollerach, E. Roulet, Fixing the zenith distribution of vertical and inclined events, Auger internal note GAP-2017-063 (2017).

[95] D. Harari, S. Mollerach, E. Roulet, The CIC for vertical and inclined events and its energy dependence, Auger internal note GAP-2018-018 (2018).

[96] D. Harari, S. Mollerach, E. Roulet, O. Taborda, The CIC for the Infill and its energy dependence, Auger internal note GAP-2018-026 (2018).

[97] F. Fenu *et al.* (Pierre Auger Collab.), The cosmic ray energy spectrum measured using the Pierre Auger Observatory, in: Proc. 35th Int. Cosmic Ray Conf., Busan, South Korea, 2015.

[98] H. Dembinski, M. Roth, A. Schulz, Energy calibration revisited: The simplified likelihood method, Auger internal note GAP-2012-090 (2012).

[99] H. P. Dembinski, B. Kégl, I. C. Mariş, M. Roth, D. Veberič, A likelihood method to cross-calibrate air-shower detectors (2015)`arXiv:1503.09027`.

[100] I. Valino *et al.* (Pierre Auger Collab.), The flux of ultra-high energy cosmic rays after ten years of operation of the Pierre Auger Observatory, in: Proc. 34th Int. Cosmic Ray Conf., The Hague, The Netherlands, 2015.

[101] T. Bergmann, R. Engel, D. Heck, N. N. Kalmykov, S. S. Ostapchenko, T. Pierog, T. Thouw, K. Werner, T. Bergmann, R. Engel, D. Heck, N. Kalmykov, S. Ostapchenko, T. Pierog, T. Thouw, K. Werner, One-dimensional Hybrid Approach to Extensive Air Shower Simulation, Astropart. Phys. 26 (6) (2007) 420 – 432, astro-ph/0606564. `doi:DOI:10.1016/j.astropartphys.2006.08.005`.
URL `http://www.sciencedirect.com/science/article/B6TJ1-4M221KN-1/2/e9f86fc88cda6ba72e1e080214b54e8d`

[102] Alan Coleman and Piera Ghia and Daniela Mockler and Ines Valiño and Valerio Verzi, Recent Improvements to the Infill Energy Spectrum, Auger internal note (in preparation).

[103] A. Porcelli, Measurement of the depth of shower maximum in the transition region between galactic and extragalactic cosmic rays with the pierre auger observatory, Ph.D. thesis, Karlsruhe Institute of Technology (2014).

[104] G. J. Feldman, R. D. Cousins, Unified approach to the classical statistical analysis of small signals, Phys. Rev. D 57 (1998) 3873 – 3889.

[105] T. Schmidt, I. C. Mariş, M. Roth, LDF systematics in S_{38} from the constant intensity cut method, Auger internal note GAP-2006-070 (2006).

[106] V. Blobel, Unfolding methods in high energy physics experiments, in: Proceedings of the 1984 CERN School of Computing, CERN 85-09 and DESY 84-111, CERN, Switzerland, 1984.

[107] V. Blobel, An unfolding method for high energy physics experiments, Tech. Rep. 02-078, DESY, arXiv hep-ex/0208022v1 (2002).

[108] V. Blobel, The RUN Manual - Regularized Unfolding for High-Energy Physics Experiments, Tech. Rep. TN361, OPAL, DESY, Germany (1996).

[109] H. P. Dembinski, M. Roth, ARU - towards automatic unfolding of detector effects, in: H. B. Prosper, L. Lyons (Eds.), Proceedings of PHYSTAT 2011 (CERN-2011-006), CERN, Geneva, Switzerland, 2011, pp. 285 – 291.

[110] AbuZayyad, Tareq and others, The Energy Spectrum of Cosmic Rays at the Highest Energies, JPS Conf. Proc. 19 (2018) 011003.

[111] Dmitri Ivanov for the Pierre Auger Collaboration and Telescope Array Collaboration, Report of the Telescope Array – Pierre Auger Observatory Working Group on Energy Spectrum, in: Proc. 35th Int. Cosmic Ray Conf., Busan, Korea, 2017.

[112] V. Verzi *et al.* (Pierre Auger Collab.), The Energy Scale of the Pierre Auger Observatory, in: Proc. 33rd Int. Cosmic Ray Conf., Rio de Janeiro, Brazil, 2013.

[113] J. S. Conway, Incorporating Nuisance Parameters in Likelihoods for Multisource Spectra, in: Proceedings, PHYSTAT 2011 Workshop on Statistical Issues Related to Discovery Claims in Search Experiments and Unfolding, CERN,Geneva, Switzerland 17-20 January 2011, 2011. `arXiv:1103.0354`.
URL `http://inspirehep.net/record/891252/files/arXiv:1103.0354.pdf`

[114] A. Schulz, H. Dembinski, M. Roth, Search for a declination dependence in the flux of cosmic rays, Auger internal note GAP-2014-013 (2014).

[115] A. Aab, et al., Pierre Auger, Large Scale Distribution of Ultra High Energy Cosmic Rays Detected at the Pierre Auger Observatory With Zenith Angles up to 80 degrees, Astrophys. J. 802 (2) (2015) 111. `arXiv:1411.6953`, `doi:10.1088/0004-637X/802/2/111`.

[116] W. F. Hanlon, Recent Results from the Telescope Array Project, Nuclear and Particle Physics Proceedings 279-281 (2016) 15 – 22, proceedings of the 9th Cosmic Ray International Seminar. `doi:https://doi.org/10.1016/j.nuclphysbps.2016.10.004`.
URL `http://www.sciencedirect.com/science/article/pii/S2405601416301857`

[117] T. Abu-Zayyad, et al., The surface detector array of the Telescope Array experiment, Nuclear Instruments and Methods in Physics Research Section A: Accelerators, Spectrometers, Detectors and Associated Equipment 689 (2012) 87 – 97. `doi:https://doi.org/10.1016/j.nima.2012.05.079`.
URL `http://www.sciencedirect.com/science/article/pii/S0168900212005931`

[118] M. Fukushima, Telescope Array, Recent Results from Telescope Array, EPJ Web Conf. 99 (2015) 04004. `arXiv:1503.06961`, `doi:10.1051/epjconf/20159904004`.

[119] O. Deligny, P. Ghia, P. Tinyakov, An Empirical Estimate of the Shift Between the Auger and Telescope Array Energy Scales, Auger internal note GAP-2015-091 (2015).

[120] J. Biteau for the Pierre Auger Collaboration and Telescope Array Collaboration, Covering the sphere at ultra-high energies: full-sky cosmic-ray maps beyond the ankle and the flux suppression, talk presented at UHECR 2018, Paris, France (2018).
URL `https://indico.in2p3.fr/event/17063/contributions/64362/attachments/50395/64305/Anisotropy_report_AugerTA_v3.pdf`

[121] D. Heck, J. Knapp, Upgrade of the monte carlo code corsika to simulate extensive air showers with energies > 10^{20} ev, Report FZKA 6097B, Karlsruhe (1998).

[122] M. Kobal, A thinning method using weight limitation for air-shower simulations, Astropart. Phys. 15 (2001) 259. `doi:10.1016/S0927-6505(00)00158-4`.

[123] P. Billoir, Reconstruction of showers with the ground array: status of the "prototype" program, Auger internal note GAP-2000-025 (2000).

[124] P. Billoir, Does the resampling procedure induce distortions in the fadc traces of the surface detector?, Auger internal note GAP-2005-109 (2005).

[125] P. Billoir, A sampling procedure to regenerate particles in a ground detector from a 'thinned' air shower simulation output, Astropart. Phys. 30 (2008) 270–285. `doi:10.1016/j.astropartphys.2008.10.002`.

[126] The Pierre Auger Collaboration, Reconstruction of Vertical Events Recorded by the Surface Detector of the Pierre Auger Observatory, in preparation.

[127] Sources of data: Napoli library, accessed: 2018-09-26.
URL `https://web.ikp.kit.edu/augeroracle/doku.php?id=auger:data#napoli_library`

[128] Scipy - A Python library for scientific calculations, `http://www.scipy.org/`.

[129] M. Rosenblatt, Remarks on some nonparametric estimates of a density function, Ann. Math. Statist. 27 (3) (1956) 832–837.

[130] S. Sheather, M. Jones, A reliable data-based bandwidth selection method for kernel density estimation, J. R. Statist. Soc. B 53 (3) (1991) 683 – 690.

Erklärung

Karlsruhe, den 14.11.2018

Erklärung der selbständigen Anfertigung meiner Dissertationsschrift

Hiermit versichere ich, dass ich die Dissertationsschrift mit dem Titel

Measurement of the Cosmic Ray Spectrum with the Pierre Auger Observatory

selbständig und ohne unerlaubte fremde Hilfe verfasst habe. Dabei habe ich keine anderen, als die von mir angegebenen Hilfsmittel benutzt.

Daniela Mockler